Four-legged snake likely a burrower *pp. 374 & 416*

Stretching out the range of conducting fibers *pp. 382 & 400*

Regulating emerging technologies *p. 384*

Science

$10
24 JULY 2015
sciencemag.org
AAAS

Unlocking the past

Ancient DNA comes of age *p. 358*

CONTENTS

386
Toward an HIV vaccine

24 JULY 2015 • VOLUME 349 • ISSUE 6246

352

NEWS

372

INSIGHTS

374 & 416
A Cretaceous snake with limbs

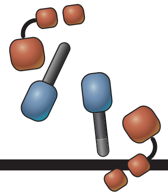

377 & 436
An autoimmunity mechanism

ON THE COVER

A researcher drills into ancient bone to extract material for DNA analysis at the Max Planck Institute for Evolutionary Anthropology in Leipzig, Germany. As the newest sequencing methods are applied to ancient samples and spread to many laboratories, ancient DNA is poised to enter its golden age, delivering stunning results ranging from the evolution of humans to that of microbes. See page 358.
Photo: © Jörg Singer

SCIENCE (ISSN 0036-8075) is published weekly on Friday, except the last week in December, by the American Association for the Advancement of Science, 1200 New York Avenue, NW, Washington, DC 20005. Periodicals mail postage (publication No. 484460) paid at Washington, DC, and additional mailing offices. Domestic individual membership and subscription (51 issues): $153 ($74 allocated to subscription). Domestic institutional subscription (51 issues): $1282; Foreign postage extra: Mexico, Caribbean (surface mail) $55; other countries (air assist delivery) $85. First class, airmail, student, and emeritus rates on request. Canadian rates with GST available upon request, GST #1254 88122. Publications Mail Agreement Number 1069624. **Printed in the U.S.A.**
Change of address: Allow 4 weeks, giving old and new addresses and 8-digit account number. **Postmaster:** Send change of address to AAAS, P.O. Box 96178, Washington, DC 20090–6178. **Single-copy sales:** $10.00 current issue, $15.00 back issue prepaid includes surface postage; bulk rates on request. The identification code for *Science* is 0036-8075. *Science* is indexed in the *Reader's Guide to Periodical Literature* and in several specialized indexes.

Science

1200 New York Avenue, NW, Washington, DC 20005
Bateman House, 82-88 Hills Road, Cambridge, UK CB2 1LQ

AAAS

SUBSCRIPTION SERVICES For change of address, missing issues, new orders and renewals, and payment questions: 866-434-AAAS (2227) or 202-326-6417, FAX 202-842-1065. Mailing addresses: AAAS, P.O. Box 96178, Washington, DC 20090-6178 or AAAS Member Services, 1200 New York Avenue, NW, Washington, DC 20005

INSTITUTIONAL SITE LICENSES 202-326-6755 **REPRINTS:** Author Inquiries 800-635-7181 **COMMERCIAL INQUIRIES** 803-359-4578 **PERMISSIONS** 202-326-6765, permissions@aaas.org **AAAS Member Services** 202-326-6417 or http://membercentral.aaas.org/discounts

Science serves as a forum for discussion of important issues related to the advancement of science by publishing material on which a consensus has been reached as well as including the presentation of minority of conflicting points of view. Accordingly, all articles published in *Science*—including editorials, news and comment, and books reviews—are signed and reflect the individual views of the authors and not official points of view adopted by AAAS or the institutions with which the authors are affiliated.

INFORMATION FOR AUTHORS See pages 678 and 679 of the 6 February 2015 issue or access www.sciencemag.org/about/authors

EDITORIAL

Rethinking graduate education

Alan I. Leshner is Chief Executive Officer, Emeritus, of the American Association for the Advancement of Science and former Executive Publisher of Science. *E-mail: alan.i.leshner@gmail.com*

All available evidence suggests that over 60% of new Ph.D.s in science in the United States will not have careers in academic research, yet graduate training in science has followed the same basic format for almost 100 years, heavily focused on producing academic researchers. Given that so many students will not join that community, the system is failing to meet the needs of the majority of its students. Many academic, governmental, and professional leaders and organizations have lamented this disconnect and have suggested worthwhile adjustments, but most of these have been minor changes in graduate course offerings. It is time for the scientific and education communities to take a more fundamental look at how graduate education in science is structured and consider, given the current environment, whether a major reconfiguration of the entire system is needed.

"...a major reconfiguration of the entire system is needed."

Some relatively new government programs and curriculum supplements are positive steps that are likely to give students greater career flexibility. For example, the Strengthening the Biomedical Research Workforce Program from the U.S. National Institutes of Health supports innovative approaches to help biomedical graduate training better reflect the range of career options that students might pursue. Individual institutions are also working on the problem. As one example, the Massachusetts Institute of Technology offers a Global Entrepreneurship Bootcamp to help students learn innovation-driven entrepreneurship through hands-on learning experiences with successful entrepreneurs. However, these efforts are limited in scope and primarily take the form of adding offerings to an already overcrowded curriculum. What is needed is a fundamental system analysis and reconfiguration that results in graduate training programs that are better designed to meet the diverse career needs of today's students. One of the last system-level reviews was in 1995, when the U.S. National Academies' Committee on Science, Engineering, and Public Policy published a report* calling for a reshaping of graduate education to reflect the evolution of careers in science and science-dependent fields. Some experiments and much discussion, but not much real progress, ensued. It is time to do that scale of analysis again and include an action plan for making the recommended changes.

Making such fundamental change may encounter substantial resistance. After all, the current system does produce first-rate academic scientists and does meet the needs of faculty who depend on graduate students as research assistants. The system also works for the very best graduate students at the top research universities, whose career paths often do point toward academia. Indeed, because the current approach has generated one of the strongest academic scientific enterprises in the world, there will be understandable reluctance to tinker with success. "Do no harm while doing good" will have to be a mantra of any system redesign.

This scale of change has been tackled before, with substantial success, in related fields. The U.S. National Academy of Engineering's Educating the Engineer of 2020 project recommended dramatic changes in undergraduate engineering education, many of which have been implemented. The Vision and Change in Undergraduate Biology Education project organized by the U.S. National Science Foundation and the American Association for the Advancement of Science, and involving a large number of other scientific organizations, has similarly been directed toward major changes in the way biology is taught to undergraduate students, and many other initiatives are under way. The experiences of both projects are cause for optimism.

Leaders from the scientific, academic, industry, and government communities will have to work together to mount a project of this scope, develop an action plan, and monitor its progress. No group can do it alone. The benefits for the science students of the future will be well worth the collective effort.

– Alan I. Leshner

*www.nap.edu/catalog/4935.

10.1126/science.aac9592

PHOTOS: (TOP RIGHT) DAVID SHARPE; (INSET) HXDBZXY/ISTOCKPHOTO.COM

NEWS

"The doctor is saying you are gravely ill."

Oceanographer Jeff Severinghaus, to the Associated Press, on the findings of last week's *State of the Climate in 2014* report, which showed the year had the highest average global surface temperatures on record.

IN BRIEF

Chile and the Canaries to share gamma-ray observatory

The array (artist's rendition shown) will detect radiation by gamma rays striking the atmosphere.

The governing board of the world's largest and most powerful gamma-ray observatory has announced its selection of the two sites that will host the Cherenkov Telescope Array (CTA). The sites, in Chile's Atacama Desert and La Palma island in the Canary Islands, were chosen ahead of rival sites in Namibia and Mexico for the northern and southern portions of the CTA, a €297 million facility that will allow astrophysicists to study some of the most energetic phenomena in the universe, from the origin of cosmic rays to particle acceleration around black holes. Each site is already home to major astronomical facilities. The board, made up of representatives from 14 of the project's 31 member countries, did not give final approval for the site selection—that is the job of the CTA Council—but it did vote to start formal negotiations with the European Southern Observatory (ESO), which operates the Paranal Observatory in Chile, and Spain. http://scim.ag/CTAsite

AROUND THE WORLD

U.S. education bills advance

WASHINGTON, D.C. | Science education advocates are holding their breath now that the U.S. Senate and House of Representatives have passed revisions to the No Child Left Behind Act, which has governed federal education policy since 2002. Both bills (H.R. 5 and S. 1177) would retain an annual testing regimen for reading and math and would measure a student's progress in science once each during elementary, middle, and high school. The Senate version, approved last week, also contains programs to promote STEM (science, technology, engineering, and math) education. However, the House bill, passed on 8 July, doesn't require states to do anything with the results of the tests. It would also prohibit the federal government from promoting any national standards, including fledgling ones for science. STEM advocates fear the science provisions could be horse-traded away in upcoming negotiations on a final bill.

Institute honors HIV pioneer

AMSTERDAM | One year ago, the missile attack on Malaysia Airlines flight 17 (MH17) ended the life of Joep Lange, a towering figure in the world of HIV/AIDS and global health. Now, the new Joep Lange Institute aims to bring the researcher's characteristic combination of research and on-the-ground action to bear on health problems in developing countries. It will open its doors in Amsterdam later this year, supported by some $20 million from various private sources in the United States. Lange was instrumental in convincing pharmaceutical companies in the mid-1990s that a cocktail of drugs was the best way to fight HIV; once those cocktails proved successful, Lange advocated for bringing them to the millions of HIV-infected people in developing countries. In the last decade of his life, Lange became interested in increasing access to health care in general—by setting

IMAGE: COLLABORATION CTA

up health insurance plans in Africa, for instance—and driving down poverty. http://scim.ag/LangeInst

Nigeria hits 1-year polio mark

ABUJA | Nigeria has hit a milestone: The country's last known case of wild polio was exactly 1 year ago. Before sounding the all-clear, the World Health Organization's (WHO's) Global Polio Eradication Initiative (GPEI) must finish analyzing stool samples collected through 24 July, a task they expect to complete by September. If no virus is found, WHO will remove Nigeria from its list of polio-endemic countries where transmission of the wild virus has never stopped. That will leave two countries on the list (down from more than 125 in 1988): Afghanistan and Pakistan. Vaccine-derived polio viruses still circulate in Nigeria, a consequence of using live oral vaccine, which will begin to be phased out in 2016. And the risk that the wild virus lurks in the strongholds of jihadist group Boko Haram in northeastern Nigeria is "not zero," although unlikely, says Hamid Jafari, GPEI's director. Until the final data are in, he says, the country is "on eggshells."

A health official gives a child polio vaccine in Nigeria.

Arctic nations sign fishing ban

OSLO | The five nations ringing the Arctic Ocean have signed a declaration to prevent unregulated commercial fishing within the ocean's high seas—the unclaimed waters that don't fall within 370 kilometers of any country's coastline. Commercial fishing is not yet a reality in the Arctic Ocean, but the rapidly retreating sea ice has prompted the five nations—Canada, Denmark (via Greenland), Norway, Russia, and the United States—to agree to a moratorium on commercial fishing until the ocean's fish stocks have been studied and a science-based management plan can be established. The five countries stated in the declaration that they would authorize their fleets to conduct future commercial fishing only once international standards are in place; they also agreed to establish a joint scientific research program to study the region's ecosystems.

BY THE NUMBERS

65

Number of countries that will require "game-changing" strategies to meet the World Health Organization's goal of three doses of diphtheria-tetanus-pertussis vaccine for 90% of their children.

123

Number of potential medicines for Alzheimer's disease that were halted in clinical trials between 1998 and 2014. Four medicines were approved in that time.

11%

Reduction in U.S. CO_2 emissions between 2007 and 2013—a drop driven primarily by the economic recession, scientists say (*Nature Communications*).

Diamondback moths are crop pests with increasing resistance to insecticides.

Genetically modified moth fathers sire defective daughters

Scientists may have found a way to limit damage done to vegetable crops by diamondback moths by altering the DNA of some of the insects. The U.K. company Oxitec genetically modified male moths to have a "self-limiting" gene that causes them to produce female offspring that die before they, in turn, can reproduce. As the males mate with females in the wild, the idea goes, populations of the insect should decline over time. Now, the technique has been shown to work in confined greenhouse conditions, Oxitec-funded researchers report in a study published last week in *BMC Biology*. The moths, which eat cabbage, broccoli, and other crucifers, cause an estimated $5 billion in damage worldwide each year. The technique could one day offer farmers pest control methods that are nontoxic and pesticide-free, the researchers say.

PHOTOS: (TOP TO BOTTOM) AP PHOTO/SUNDAY ALAMBA; DAVID MARQUINA REYES/FLICKR

IN DEPTH

Ice mountains of Pluto's Norgay Montes range tower 3500 meters above nearby plains.

PLANETARY SCIENCE

Scientists ponder an improbably active Pluto

New Horizons delights researchers with stark vistas and perplexing puzzles

By **Eric Hand**

Last week, 4.7 billion kilometers from Earth and just a shade past that distant world known as Pluto, a little plutonium-powered spacecraft torqued itself around and sent home a 15-minute message. Waiting on the receiving end was Alice Bowman, the serenely composed operations manager for NASA's $720 million New Horizons mission.

In other missions, the engineers who designed the spacecraft or maneuvered it safely down to the surface of an alien planet have been the celebrities. On New Horizons, Bowman became a hero by ensuring that the probe's complex flyby came off without a hitch. Moving 60 times faster than a passenger jet, New Horizons was tearing through space too quickly for Pluto's weak gravity to reel it into orbit. The craft had just one chance to observe Pluto and its moons as it passed within 12,500 kilometers of Pluto's surface. It had to execute more than 20,000 computer commands over 9 days and, for 22 climactic hours, could not waste time and processing power by swiveling around to communicate with Earth. The 15-minute call home, which began at 8:52:37 p.m. EDT on 14 July, was the mission controllers' first chance to learn whether the probe had survived its moment of closest approach. A collision with just a speck of orbiting dust could have derailed the entire endeavor.

Bowman peered at her computer console in the mission control room at Johns Hopkins University Applied Physical Laboratory (APL) in Laurel, Maryland. Her subordinates relayed the contents of the message: The spacecraft was on its target trajectory. Most important, its memory banks were chock-full of scientific data. "We have a healthy spacecraft," she declared. "We are outbound from Pluto."

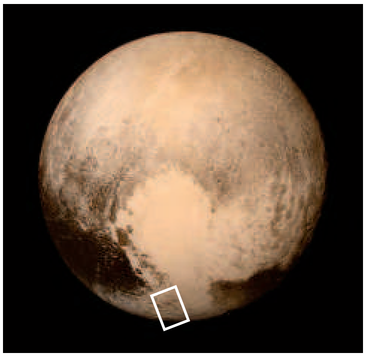

Norgay Montes (box) flanks Pluto's bright "heart," 1600-km-wide Tombaugh Regio.

With that, the spacecraft spun around and went back to work, observing Pluto's dark side by the reflected light of its moon Charon. The craft's handlers took a brief break. Clad in black mission polo shirts, the New Horizons team marched into an APL auditorium for a victory lap, waving American flags on little sticks. Bowman was beaming. The audience rose to give her a standing ovation. She tucked her thumb across her right hand and flashed nine fingers at the crowd: a "nine-fingered salute," in honor of Pluto's former status as the solar system's ninth planet. Alan Stern, the mission's indefatigable principal investigator and a Pluto champion in the years leading up to the spacecraft's 2006 launch, said he had three words for the world: "We did it."

With the flyby complete and the data trickling home, mission scientists focused on a new challenge: making sense of an unexpectedly complex and dynamic body. A Pluto image released on the day of closest approach revealed a world the color of a peach, mostly smooth but also pocked with cliffs and craters. Just as images from the Hubble Space Telescope had hinted more than a decade earlier, Pluto displayed three distinctly colored regions. At its heart was a heart—a bright beacon of nearly white ice. Girdling the heart, around Pluto's equator, were darker terrains, perhaps enriched in organic residue left behind as the ice sublimed away. At the pole was a medium-bright region found to be rich in methane ice.

To planetary scientists, a varied surface means a body has hosted some kind of activity. And activity of any sort is a surprise on Pluto, which receives a minuscule dose

PHOTOS: (TOP TO BOTTOM) NASA/JOHNS HOPKINS UNIVERSITY APPLIED PHYSICS LABORATORY/SOUTHWEST RESEARCH INSTITUTE; NASA

of solar energy and is so small that it should long ago have lost any internal heat leftover from its formation or given off by radioactive elements in its interior. To explain what might be creating the patches, the team bandied two kinds of explanatory theories: top down and bottom up.

Top-down mechanisms would sculpt the surface from above. Pluto's thin atmosphere harbors winds blowing at a meter or two per second, strong enough to erode its surface. What's more, many ices on Pluto—methane, nitrogen, and carbon monoxide—are volatile. They can sublime directly into the atmosphere without melting when the surface warms in the course of Pluto's seasonal cycle, driven by its sidelong tilt and elongated orbit. When temperatures drop, they can condense out of the atmosphere as frost, creating bright patches while concealing other features.

For some geoscientists, bottom-up mechanisms are more provocative: They raise the possibility that Pluto's interior has somehow remained warm and active billions of years after its formation. Internal heat could send molten blobs of material to the surface, driving geysers or even watery volcanoes that could spew fresh ices onto the surface. That scenario gained support when an early close-up picture revealed mountains, some 3500 meters high, composed of water ice. At Pluto temperatures, water ice is the bedrock: too solid to flow or sublime. So the presence of ice mountains implies that deep forces pushed them up. At the same time, surrounding plains of ice were remarkably crater-free—suggesting that another process had paved them over.

As a first approximation, researchers estimated that the surfaces were 100 million years old—a mere blip in geological time—and that resurfacing could still be happening today. As the team peered closer, other hints of internal activity emerged. One image showed wind-blown streaks of material emanating from dark spots just a few kilometers across—a sign of possible geysers, although the team was not yet ready to announce a definite discovery.

Still, Mike Brown, a planetary astronomer at the California Institute of Technology in Pasadena, doubts that Pluto is geologically active today. "It's a pretty astounding claim, and their evidence for that is pretty weak," he says. The top-down mechanisms are powerful enough to explain everything scientists see, Brown says. The ice mountains could easily be ancient, not young, he says, and the plains could hold craters masked by thick frosts accumulating from above. Pluto's exceptionally strong seasons are enhanced by feedback loops in which, for example, dark patches absorb more heat, accelerating the loss of ice. Brown expects the heart—named Tombaugh Regio after Pluto's discoverer—to sublime away in the coming years.

As for the potential geysers, he thinks there may be less to them than meets the eye. "They're totally superficial," he argues—like those found on Neptune's moon Triton. Triton is thought to be a captured object from the Kuiper belt, the throng of icy worlds to which Pluto also belongs. When the Voyager 2 spacecraft flew past Triton in 1989, it discovered active geysers, but most planetary scientists think they are quite shallow—fueled by sunlight that penetrates clear surface ice and drives a small greenhouse effect that melts deeper ice.

New Horizons team members view new images at mission control.

PHOTO: NASA/BILL INGALLS

"I think the solar system saved the best for last."

Alan Stern, New Horizons principal investigator

Pluto's moon Charon could prove key to resolving the riddle. The radioactive fires stoked by isotopes in its interior should have gone out even before those on larger Pluto. And Charon lacks an atmosphere and the volatile ices that can camouflage craters in frost. Yet early images show that it, like Pluto, is strikingly unblemished, especially in its southern hemisphere; this suggests youthfulness, and recent resurfacing. What could be driving it?

One possible solution: The giant impact thought to have formed Pluto and Charon—and given both bodies an enormous dose of heat—might not have occurred in the solar system's early days, 4.5 billion years ago, as most scientists thought. Instead, the cataclysm could have been more recent, which would have allowed more heat to persist up until now.

Bill Bottke, an impact expert at Southwest Research Institute in Boulder, Colorado, is skeptical. Scars in Charon's northern hemisphere suggest that the moon is old, he notes. What's more, potential impactors have become increasingly rare over solar system history, making giant impacts later in time more difficult to explain, Bottke says. "I don't like the probabilities," he says.

Francis Nimmo, an embedded collaborator on the mission from the University of California, Santa Cruz, is toying with another scenario for heating Pluto's interior. "I'm beginning to wonder now whether there's some form of tidal heating we've missed," he says. For example, he is considering a second big impact on Pluto that would have knocked it into a noncircular orbit around Charon. As gravitational forces slowly rounded out that ellipse, they could have kneaded both bodies' interiors, providing an additional heat source. But Nimmo worries that only an improbably large impact would have supplied enough heat.

More clues may be lurking in the gigabits of data still stored on board New Horizons. Because of the vast distances and the spacecraft's low-power radio antenna, it returns data at speeds of just a few kilobits per second. (A decent Internet connection today is a thousand times faster.) Only 1% to 2% of the encounter data have been retrieved, and it will take 16 months to get it all down.

For now, Stern is savoring the moment, which came 50 years to the day after NASA's Mariner 4 spacecraft flew past Mars and returned the first picture from another planet. No matter that Pluto is now classified as a dwarf planet. "I think the solar system saved the best for last," Stern says. ■

With additional reporting by Richard A. Kerr.

Published by AAAS

HUMAN GENETICS

New mystery for Native American origins

Rival papers compete to explain surprising link to Australia and Melanesia

By Michael Balter

The Americas were the last great frontier to be settled by humans, and their peopling remains one of the great mysteries for researchers. This week, two major studies of the DNA of living and ancient people try to settle the big questions about the early settlers: who they were, when they came, and how many waves arrived. But instead of converging on a single consensus picture, the studies, published online in *Science* and *Nature*, throw up a new mystery: Both detect in modern Native Americans a trace of DNA related to that of native people from Australia and Melanesia. The competing teams, neither of which knew what the other was up to until the last minute, are still trying to reconcile and make sense of each other's data.

"Both models … see in the Americas a subtle signal from" Australo-Melanesians, notes *Science* co-author David Meltzer, an archaeologist at Southern Methodist University in Dallas, Texas. "A key difference is when and how it arrived in the New World." The *Nature* team concludes it came in one of two early waves of migration into the continent, whereas the *Science* team concludes it came much later, and was unrelated to the initial peopling.

DNA suggests this ancient Brazillian was related to today's Native Americans, despite its skull resembling Australo-Melanesian skulls.

For the *Science* paper, nearly 4 years in the making, researchers sequenced 31 complete and 79 partial genomes from people in North and South America, Siberia, and Oceania. They compared these with previously sequenced genomes of three ancient skeletons: the 24,000-year-old Mal'ta child from Siberia, the 12,600-year-old Anzick child from Montana, and the 4000-year-old Saqqaq individual from Greenland. The team examined the genetic differences among their samples to determine how long ago various populations diverged, using the ancient genomes to calibrate this DNA clock. They concluded that all Native Americans, ancient and modern, stem from a single source population in Siberia that split from other Asians around 23,000 years ago and moved into the now-drowned land of Beringia. After a stop of up to 8000 years in Beringia—slightly shorter than some researchers have suggested—(*Science*, 28 February 2014, p. 961)—they spread in a single wave into the Americas and then split into northern and southern branches about 13,000 years ago (see map).

That's a largely familiar picture of the migration, albeit with much more precise dating. But the *Science* team also found a surprising dash of Australo-Melanesian DNA in some living Native Americans, including those of the Aleutian Islands and the Surui people of Amazonian Brazil.

Some anthropologists had previously suggested an Australo-Melanesian link. They noted that certain populations of extinct Native Americans had long, narrow skulls, resembling those of some Australo-Melanesians, and distinct from the round, broad skulls of most Native Americans. In the so-called Paleoamerican model, Walter Neves of the University of Sao Pãolo in Brazil and Mark Hubbe of Ohio State University, Columbus, argue that these people descended from an early wave of migration that was separate from the one that gave rise to today's Native Americans, and drew on a different source population in Asia. A similar claim was made for the Kennewick Man, the iconic 8500-year-old skeleton from Washington state, but was refuted when his genome was published by this team last month: He is related only to Native Americans (see http://scim.ag/ancientone).

The *Science* results also counter the Paleoamerican model. When the team sequenced the DNA of 17 individuals from the extinct South American populations with the distinctive skulls, they found no trace of Australo-Melanesian ancestry. "The analysis refutes a very simplistic view of [skull] variation," comments anthropologist Rolando Gonzalez-Jose of the National Scientific and Technical Research Council in Puerto Madryn, Argentina.

So how did living South Americans get a

The long odyssey of the first Americans

One study concludes that Native Americans arrived in a single wave of migration (purple), then split into two subgroups; the Arctic Inuit arrived in a later migration.

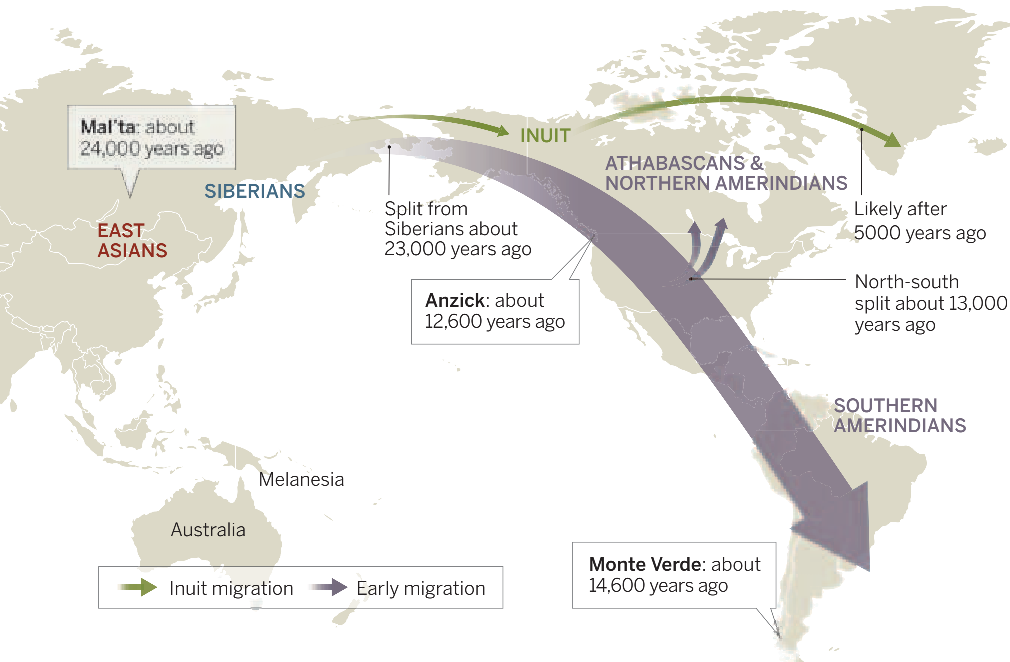

dose of this Australo-Melanesian DNA? "A possible explanation is that the connection reflects more recent gene flow," says *Science* co-lead author Eske Willerslev of the University of Copenhagen. By that he doesn't mean boats crossing the Pacific, as some researchers had speculated earlier. Instead, Willerslev contends that the ancestors of some of today's South Americans might have mixed with Asian populations related to today's Australo-Melanesians and carried those genes into the Americas during a well-established later wave of migration from Asia that also peopled the Aleutian Islands (*Science*, 13 January 2012, p. 158).

Hubbe, however, counters the study could have missed telltale DNA in the ancient populations because its sample size is "extremely small." Geneticist David Reich of Harvard Medical School in Boston and leader of the *Nature* team agrees, noting that the genomes from the 17 ancient relict populations are incomplete and provide very low coverage.

His own paper also finds this mysterious Australo-Melanesian DNA in some of the same modern populations but reaches a different conclusion about its source. His team analyzed partial genome sequences of 106 Native Americans from 25 populations in Central and South America, and compared them with DNA data from 197 populations from outside the Americas. They found that some Amazonians, including the Surui people, shared about 1% to 2% of their ancestry with present-day native people from Australia, New Guinea, and the Andaman Islands. Differences in the shared DNA suggest this ancestry did not come directly from these populations, the team concluded, but through a now extinct population they call "Population Y" that may have lived somewhere in East Asia and contributed genes to both very early Paleoamericans and to Australo-Melanesians. Because the Amazonian groups are only distantly related to Population Y, the team concludes that this represents an ancient rather than recent genetic contribution that arrived in an early "pulse of migration" to the Americas.

And yet Reich says his data, like those of the *Science* team, clash with the classic Paleoamerican model, which postulates a major, more direct genetic contribution from Australo-Melanesians. In that sense, Reich says, "the two papers are not in disagreement."

Researchers agree that more genomes from modern and ancient Native Americans are needed to unravel the mysteries. For now, says anthropologist Jennifer Raff of the University of Texas, Austin, the two papers throw open an "incredibly exciting" window on the ancestors of today's Native Americans, as they sat poised to enter the New World. ■

HIV/AIDS

Child fights HIV to a draw

After 12 years off treatment, a young woman has had remarkable—and unexplained—control of her infection

By **Jon Cohen** *in Vancouver, Canada*

In 1996, a baby infected with HIV at birth was started on anti-AIDS drugs. But at age 6, against the advice of doctors, her family stopped treatment. Twelve years later, the young French woman is still healthy, with no detectable virus in her blood. Her unusual case, reported Monday at an international AIDS conference in Vancouver, Canada, may hold clues that help other HIV-infected people control their infections without antiretroviral (ARV) drugs and offer insights to AIDS vaccine developers.

The case adds a wrinkle to earlier reports of "elite controllers" who effectively thwart their HIV infections without ever receiving ARVs, as well as "posttreatment controllers" like the "Mississippi baby," who stopped taking ARVs at 18 months of age and appeared virus-free for more than 2 years. In 2013, many researchers thought that child was "cured," but HIV came back strong after 27 months off treatment.

It is clear that the French woman is not cured: Investigators have found strong signals of HIV DNA in her immune cells and can readily induce them to produce virus, says Asier Sáez-Cirión, a viral immunologist at the Pasteur Institute in Paris who reported on her case. But she is the first documented HIV-infected child to go off treatment and remain in remission for this length of time. "We don't know why this happened," Sáez-Cirión says.

Some clues may come from a group of people infected by HIV as adults, known as the VISCONTI cohort, who went off ARVs and did not have the virus return for many years. As Sáez-Cirión and colleagues described in the March 2013 issue of *PLOS Pathogens*, the 14 adults were diagnosed shortly after they became infected, began ARVs immediately, and stayed on them for an average of 3 years. At the time of that publication, the average person had been off ARVs for 7 years.

Bad start, good finish

People who control HIV infections after stopping treatment have higher viral loads at the start

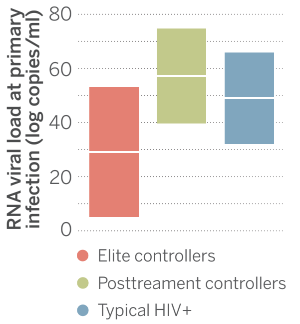

DATA: ADAPTED FROM FIGURE 2 OF A. SÁEZ-CIRIÓN *ET AL./PLOS PATHOGENS* (2013)

The people in the VISCONTI cohort look strikingly different from elite controllers, who, despite never receiving treatment, do not develop high virus levels, even in the first weeks of infection. Although no single factor explains the ability of elite controllers to rein in HIV, many are genetically predisposed to make high levels of the CD8 lymphocytes that eliminate infected cells.

Posttreatment controllers, like the people in VISCONTI, have high virus levels shortly after infection and their immune systems rapidly deteriorate. Paradoxically, many have a genetic background that predisposes them to a weak adaptive immune response to the virus.

Sáez-Cirión thinks they may be receiving help instead from the innate immune system, which may be strong enough to contain HIV if people have very small reservoirs of viral DNA. Members of the VISCONTI cohort may fit this bill because treatment began so quickly after infection. Another, somewhat counterintuitive, possibility is that the weak immune response in posttreatment controllers helps limit the size of the reservoir before the drugs are even started. HIV preferentially targets and infects CD4 white blood cells that help fight infections. A weak CD4 response to HIV means fewer targets for it to infect. A third possibility: Some posttreatment controllers are infected with a weaker mutant of HIV.

Anthony Fauci, who heads the U.S. National Institute of Allergy and Infectious Diseases, says he's intrigued by the new French case and how it fits together with the Mississippi child. "There's something about the immune system of a very young person," Fauci says. "The Mississippi child was a tickler for us, and I wouldn't throw it out the window—27 months is a long time. Maybe, somehow, the way that child kept the virus under control is the same as the new case. I have an entirely open mind." ■

Published by AAAS

U.S. Secretary of Energy Ernest Moniz and his Iranian counterpart, Ali Akbar Salehi (left), negotiated many of the nuclear deal's scientific dividends.

NUCLEAR DIPLOMACY

Iran nuclear deal holds 'goodies' for scientists

Researchers to collaborate at repurposed nuclear facilities

By **Richard Stone**

When Iran agreed last week to dismantle much of its nuclear infrastructure, it won more than the promise of relief from crippling sanctions. If the agreement survives strong opposition in the U.S. Congress, Iran can expect a rapid expansion of scientific cooperation with Western powers. As its nuclear facilities are repurposed, scientists from Iran and abroad will team up in areas such as nuclear fusion, astrophysics, and radioisotopes for cancer therapy. For scientists on both sides, "these things are the goodies," says Stephan Klement, the European Union's lead technical negotiator in the talks.

To the six world powers that sat across the table from Iran over 2 years of talks, the signal achievement of the Joint Comprehensive Plan of Action, signed in Vienna on 14 July, is that it would slow Iran's "breakout time"—the time needed for it to produce enough fissile material for one bomb—from an estimated 2 to 3 months today to at least a year. That meant blocking Iran's four pathways to nuclear weapons: the Natanz and Fordow centrifuge facilities, which enrich uranium; the Arak heavy water reactor, which makes plutonium; and hidden facilities that might use other technologies, such as uranium enrichment with lasers.

Negotiators had to find a way to reach that goal without requiring Iran to shutter a single nuclear site—a "red line" for Iran's leaders. In the case of the Arak reactor, for example, Iran agreed to work with the international community to redesign it to run on low-enriched uranium. That would greatly restrict plutonium production, and Iran pledged to ship all spent fuel out of the country for the reactor's lifetime.

A bigger headache was the fate of some 19,500 centrifuges for enriching uranium hexafluoride gas at Natanz and Fordow. Under the action plan, most centrifuges will be mothballed. Iran will continue to run 5060 of its first-generation centrifuges at Natanz to enrich uranium to 3.67% of the fissile isotope uranium-235, far below the 20% threshold considered weapons-grade.

Iran's R&D effort to develop more advanced centrifuges was no less contentious. "That was a main concern of ours, and our most time-intensive effort," says Klement, a theoretical physicist and lawyer. Iran won a concession that it could continue to tinker with four of its more advanced centrifuge models and use computer modeling and simulations to explore new types of centrifuges. James Acton, a nonproliferation expert at the Carnegie Endowment for International Peace in Washington, D.C., regards the concession as a weakness of the action plan. Nevertheless, he adds, "on balance that's an acceptable price to pay" for what he calls a "good agreement."

Iran did give ground on a related issue. U.S. negotiators were intent on preventing Iran from pursuing laser enrichment, a new route to fissile material that would be easier to hide than ranks of centrifuges. Iran agreed to limit its enrichment R&D to gas centrifuges for the next 10 years. "Iran understood that was an important priority," says Istanbul-based Ali Vaez, a senior analyst with the International Crisis Group.

Negotiators were left with one more dilemma: the fate of the 3000 centrifuges at Fordow, the other uranium enrichment site. They hit on "a creative solution," says Steven Miller, director of the international security program at Harvard University's Belfer Center for Science and International Affairs. Uranium enrichment at Fordow will cease entirely and Iran will convert the underground facility into an international nuclear, physics, and technology center.

Negotiators squabbled over just how to do that, Vaez says, because "the Iranians wanted to keep centrifuges at Fordow spinning." The world powers agreed that Iran could retain 1044 centrifuges at Fordow; 348 will be reconfigured with Russia's help to produce stable isotopes for industry, and the rest will remain idle. Russian scientists have visited Fordow in recent weeks and plan to alter some centrifuges to produce iridium-191; adding a neutron to it at Arak would make iridium-192, which is used in gamma cameras to check for structural flaws in metal. The iridium will also contaminate the centrifuges, rendering them unusable for enriching weapons-grade uranium.

Both sides strived to identify other research that could be carried out in Fordow's cramped space. "It's not a great work environment. Not a suitable place to do many things," Klement says. One idea is to install a small linear accelerator for basic research in nuclear physics and astrophysics. Iran has agreed to invite proposals for collaborative projects at Fordow and host an international

PHOTO: CARLOS BARRIA/POOL PHOTO/AP IMAGES

workshop to review them. "We want to have concrete activity there as soon as we can," Klement says.

To offer Iran one more dividend to tout to its domestic audience, the agreement also calls for exploring cooperation in other areas of science, such as neutrino astronomy and fusion research, and "facilitating contribution of Iran" to the International Thermonuclear Experimental Reactor, or ITER. Because Iran has scant expertise in fusion research and the facility is already being built in France, its initial participation may consist of sending visiting scholars to ITER-associated fusion laboratories.

Certain nuclear research will be off-limits. Iran agreed to refrain from studying metallic uranium or plutonium—the raw material for nuclear weapons—for a decade. Some experts are surprised that Iran accepted a blanket prohibition because uranium metal has other uses—for example, in conventional weapons that take advantage of uranium's high density to breach armor and in basic physics research. Still, if Iranian scientists are intent on such research, they could probably get away with it, says Siegfried Hecker, a plutonium specialist at Stanford University in Palo Alto, California. "I don't see how you can monitor uranium metallurgy research on a relatively small scale in laboratories."

As "amazingly detailed" as the action plan is on many technical questions, Acton says, "I don't think one should underestimate the challenges of a seven-way partnership." A joint commission created to oversee implementation must approve the Arak redesign, for example, and put its imprimatur on R&D at Fordow. Eliminating the covert pathway, meanwhile, will rely on intrusive inspections and unprecedented oversight of Iran's purchases for its nuclear program.

As Iranian and U.S. nuclear scientists begin to mix, both sides could learn much from each other, says Robert Rosner, a theoretical physicist at the University of Chicago in Illinois and former director of Argonne National Laboratory. "It's an incredibly long time since we built any nuclear reactors," he says. "Iran has world-caliber scientists and engineers, and they have been in the thick of doing that."

It wouldn't be surprising if Iran's nuclear scientists are skittish at first about engaging, Miller says. Several of the nation's key nuclear scientists were assassinated, presumably by foreign agents, after Iran's once-clandestine nuclear program emerged from the shadows a decade ago. "Iran naturally became hypersensitive about access to its scientists," Miller says. But those dark days may soon be over. "When scientists get together," Rosner says, "differences always fall away." ■

ASTRONOMY

Web billionaire bankrolls search for alien signals

Yuri Milner hopes that $100 million can answer one of humanity's most enduring questions

By **Daniel Clery**

Are we alone in the universe? Russian Internet entrepreneur Yuri Milner wants to know—and he is willing to pay for an answer. Milner has pledged $100 million for a 10-year effort to detect signals from other civilizations in the universe, a project that has drawn high-profile support. "It's time to answer the question of whether there is life beyond Earth," physicist Stephen Hawking told a 20 July press conference at the Royal Society in London, where Milner announced the plan. In addition, the project will throw a lifeline to budget-strapped radio telescopes, and it will develop new technology to monitor 10 billion radio frequencies simultaneously.

Astronomers have used radio telescopes since the 1960s to listen for extraterrestrial signals that could not be produced by natural phenomena. The effort struggled after Congress axed U.S. public funding for the search for extraterrestrial intelligence (SETI) in the early 1990s; since then, the nonprofit SETI League has continued the effort with help from private donors.

10 billion

Estimated number of Earth-sized exoplanets at lukewarm temperature in the Milky Way

184,000

Number of DVDs worth of data Breakthrough Listen will produce in 24 hours

The new project, dubbed "Breakthrough Listen," will boost SETI funding fivefold and "take the search for intelligent life in the universe to a whole new level," Milner says. It will be 50 times as sensitive as previous efforts, cover 10 times more of the sky, and keep two of the world's leading radio telescopes busy. The new money will buy 20% of the total observing time on the 100-meter-wide Green Bank Telescope in West Virginia for the next decade and 25% of the observing time on the 64-meter Parkes Radio Telescope in New South Wales, Australia, for the next 5 years—a boon to the telescopes, both of which are under threat of budget cuts. The project will also use the 2.4-meter Automated Planet Finder Telescope at the Lick Observatory on Mount Hamilton near San Jose, California, to search for laser signals from other worlds.

Milner is estimated to be worth $1.8 billion, amassed through investments in companies such as Facebook, Twitter, Spotify, and Groupon. In 2012, he became a benefactor of science through the Breakthrough Prizes, with individual awards of $3 million, the largest in the world. His new project aims to survey the plane of the Milky Way, focusing on the closest million stars to Earth. It will also scan 100 nearby galaxies. The observations will produce some 10 gigabytes of data per second, far too much to store in raw form; instead, the data will be processed on the fly using a new signal processing system to be developed by a team at the University of California, Berkeley, led by renowned exoplanet-hunter Geoff Marcy.

Other surveys, such as by NASA's Kepler satellite, have suggested that there may be as many as 10 billion Earth-sized exoplanets at tolerable temperatures in the Milky Way alone. "I'd bet my house that [somewhere] in the nearest 100 star systems there are single-celled life forms flourishing," Marcy says. Of course, Breakthrough Listen can only detect life forms that have developed technology and started broadcasting. "Intelligence is the great unknown. It may be very rare," Hawking says. "We only have to look in the mirror to see that it is very fragile and prone to self-destruction."

"SETI is a perfect area for private funding," says Albert Zijlstra, director of the Jodrell Bank Centre for Astrophysics in Manchester, U.K., who is not involved in the project. Conventional research funding is hard to secure, he says, "because of the exceedingly small chance of success, and partly because it is more exploration than science." But everyone wants to know the answer, says U.K. Astronomer Royal Martin Rees, who will head the project's advisory committee. "It's a huge gamble, of course, but the payoff will be so enormous." ■

FEATURES

NEW LIFE FOR OLD BONES

After a stormy adolescence, the field of ancient DNA enters its golden era

From this 45,000-year-old thighbone from Ust'-Ishim, Siberia, researchers managed to sequence the oldest genome of our species.

PHOTO: © ALEXANDER MAKLAKOV

By **Elizabeth Culotta**

With reporting from **Ann Gibbons**, **Elizabeth Pennisi**, *and* **Gretchen Vogel** *in Jena, Germany*

When Kelly Harkins's Ph.D. work on ancient tuberculosis reached an impasse in 2012, she turned to the wider research community. She left her lab at Arizona State University (ASU) and headed for the University of Tübingen in Germany for 4 months. There, in the lab of archaeogeneticist Johannes Krause—a convivial setting where everyone went to lunch together—she heeded her adviser's advice to "be a sponge." She learned how to apply sophisticated next-generation DNA sequencing techniques to ancient tissue samples. "Then I came home and taught it all to the grad students at ASU," she says. The precise, centuries-old microbial sequences her team gleaned from the samples led to a surprising conclusion: ancient tuberculosis in the New World likely came from marine mammals (see http://scim.ag/tuberculosisseals).

Harkins's experience couldn't be more different from that of the researcher who may have done the most to create the field of paleogenetics, Svante Pääbo. As a grad student in the early 1980s in a virology lab in his native Sweden, Pääbo wanted to analyze DNA from ancient mummies to find out whether modern Egyptians were closely related to ancient pharaohs. But he feared that his adviser would think the project a fool's errand. So he pursued it only on nights and weekends. "It was a side project different from my 'real' doctoral work, and I did it secretly," Pääbo says. "I was alone."

But Pääbo and a handful of other pioneers learned as they went, inventing ways to apply the DNA sequencing revolution to tissues ravaged by time. They succeeded beyond all expectation, eventually retrieving the entire genomes of Neandertals and other kinds of ancient humans and transforming the picture of human evolution (see p. 362). Researchers have also delved into the genomes of ancient animals—the oldest so far is a 700,000-year-old horse (see http://scim.ag/horsegenome)

Young researchers have flocked to the lab of Johannes Krause to learn the latest methods for extracting and analyzing DNA from ancient samples.

But extracting and analyzing degraded DNA molecules was so tricky that for years it remained the exotic province of a few high-profile labs.

No longer. As sequencing and sample preparation technologies improve and researchers from fields outside paleoanthropology realize just how much ancient DNA can tell them, the method is being applied to everything from the peopling of Europe to how plants and pathogens respond to climate change. "We now see something of an explosion," Pääbo says. "Ancient DNA is about to become a normal tool … an integrated part of many projects … much like carbon dating is already."

"There's a revolution," agrees Krause, who recently moved from Tübingen to Jena, Germany, to co-direct a new Max Planck Institute on the Science of Human History. "The techniques are available to everybody. You can work with a small lab and publish high-profile publications. You don't need fancy equipment, you need know-how. And that know-how is spreading."

After the first ancient DNA successes in the late 1980s, the field struggled with contamination, as the genetic material from modern bacteria or a technician's finger masqueraded as ancient DNA (*Science*, 13 February 2009, p. 866). At first, researchers relied on the polymerase chain reaction (PCR) to amplify and sequence the tiny bits of DNA that survive in ancient samples. But PCR preferentially amplifies longer molecules, which are more likely to be modern contaminants. As spectacular claims of DNA from dinosaurs, Native Americans, and insects in amber turned out to be due to contamination, even Pääbo says he almost gave up on ancient human samples.

Then next-generation sequencing was developed. Today, researchers can simultaneously sequence millions of DNA fragments and so sometimes produce an entire genome in a single day. This high-throughput method both sped up sequencing and brought costs down, although equipping an ancient DNA facility remains expensive. The method also gave ancient DNA researchers a new weapon against contamination. Next-gen sequencers don't rely only on PCR to reconstruct molecules. And the new methods analyze sequences so that the tell-tale fingerprint of ancient DNA—a preferential degradation of certain nucleotide bases—can be recognized. Sequences lacking that pattern are likely modern contamination, and can be identified and discarded. "You still have to worry about contamination," Harkins says, "but a little piece of the fear is assuaged."

All these advances, plus new sample preparation techniques that make the most of whatever DNA is left in a fossil, al-

Ancient DNA's growth spurt

The number of papers with "ancient DNA" in the title, abstract, or keyword has soared in the past 20 years.

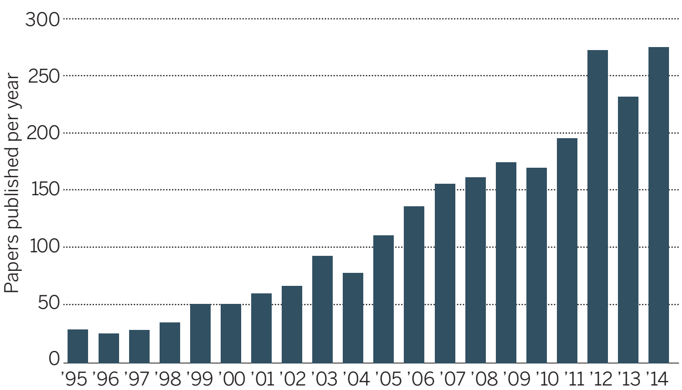

PHOTO: © JÖRG SINGER; GRAPH SOURCE: THOMSON REUTERS' WEB OF SCIENCE

lowed researchers to sequence complete ancient genomes from our ancestors and archaic humans (*Science*, 17 December 2010, p. 1616). "Fifteen years ago, I would never have thought that it would become possible to sequence genomes of extinct hominins to a quality similar to that of present-day people," says Pääbo, whose lab applied next generation techniques to sequence the full nuclear genome of Neandertals in 2010 and to get high quality coverage in 2012 (*Science*, 31 August 2012, p. 1028).

As more labs become able to exploit ancient DNA, they're applying it to new questions. These newcomers "can start doing things that I couldn't even dream of," such as looking at genomes of hundreds or thousands of individuals, says evolutionary geneticist Hendrik Poinar of McMaster University in Hamilton, Canada. "We are in a golden era of ancient DNA analysis."

A tally of papers with "ancient DNA" in the title, abstract, or keyword shows that the output rose from 30 papers published in 1995 to 275 published in 2014, according to data from Thomson Reuters' Web of Science, which indexes more than 12,000 of the most influential peer-reviewed journals. About 14 papers, most reporting the complete genomes of archaic humans, form a cluster of highly cited research that Thomson Reuters analysts call a "research front." The average publication date of those papers is only 2013, suggesting a new field with a young foundational literature.

Even as ancient DNA analysis becomes more powerful and standardized, researchers are identifying new places to find old sequences. The dense petrosal bone of the ear preserves DNA surprisingly well, as does plaque on teeth, which opens up whole arenas of inquiry into ancient diet and microbiomes. Other researchers are simply sequencing the DNA found in scoops of ancient soil or ice to reconstruct past ecosystems (see p. 367). Still others are exploring how to tease out ancient DNA from specimens found in the tropics, where heat and humidity attack the molecule (see p. 370). And a handful of researchers are looking on the horizon at what may be the next big technology—sequencing ancient proteins (see p. 372).

For now, however, paleogenetics rules, attracting even researchers in distant fields. "I'm not that interested in ancient DNA per se—I'm primarily interested in diseases of people who are still alive," says microbiologist Pushpendra Singh, now a visiting scientist at the National Hansen's Disease Program in Baton Rouge. But he and his then-postdoc adviser, Stewart Cole of the Swiss Federal Institute of Technology in Lausanne in Switzerland, wanted to understand why so few people in Europe today have leprosy compared with 1000 years ago. Had *Mycobacterium leprae* evolved to become less virulent over time?

PODCAST

Listen to a podcast with Elizabeth Culotta at http://scim.ag/AncientDNApod

So Singh, too, made the trek to Tübingen to learn ancient DNA prep in Krause's lab. The team was eventually able to sequence five medieval samples, including one with exceptionally well-preserved DNA. With Cole, Krause, and others, he showed that *M. leprae's* genome in medieval times was essentially the same as it is now. Another factor—perhaps reduced coinfection with other diseases or the evolution of a protective mutation—must explain leprosy's decline in Europe (*Science*, 12 July 2013, p. 179).

Other labs are exploring questions ranging from the relations between the ancient Minoans and Mycenaeans to the family trees of potato blight. "I'm contacted every week asking for advice," Krause says.

All the same, a handful of elite labs with big funding still lead the field. These "tycoons," as Krause calls them, develop new techniques and tackle the most difficult problems. "Our strategy is to go to the things that are hard—to the edge of the technology," says Pääbo, who has challenged his team to sequence the genomes of 100 individuals at least 30,000 years old in the next 5 years. "We're sort of calling it the '100 archaic genomes' project," he says. The fragmentary DNA in such old specimens often is sequenced 20, 30, or 40 times—at a cost of about $2000 or more per copy—to be reliable. "It's still very expensive to do this well," says population geneticist Rasmus Nielsen of the University of California, Berkeley.

Contamination remains a nagging worry. Now, "everyone thinks they can have a go with ancient DNA," says molecular evolutionist Alan Cooper of the University of Adelaide in Australia. "But next generation sequencing doesn't remove the issues of contamination." He fears the same kind of high profile claims and mistaken results that plagued the field in the 1990s, especially as more labs try their hand. Pääbo agrees: "It's still hard to do this right. It's a big commitment—you have to have a clean room and full-time people working on this."

Harkins's generation also faces the problems typical of a booming field, including intense competition. "There are at least five labs working on mammoth genetics and genomics, and the same is true for Bronze Age humans," Krause says. But Harkins, for one, says there are plenty of scientific challenges to go around. "We can look at population level questions, immune-related loci on the nuclear genome—we could do this or this or this," she says. "This field is great." ■

Susanna Sawyer follows strict protocols in the clean room at the Max Planck Institute for Evolutionary Anthropology in Leipzig, Germany, in order to avoid contaminating samples with her own DNA.

PHOTO: © JÖRG SINGER

Archaeologists David Anthony and Dorcas Brown measure a skeleton from the Russian steppe whose 5000-year-old DNA revealed close ties with Europeans.

REVOLUTION IN HUMAN EVOLUTION

As it smashes disciplinary boundaries, ancient DNA is rewriting much of human prehistory

By **Ann Gibbons**

At 6:30 p.m. on a blustery March evening in Boston, most of the researchers on the second floor of Harvard Medical School's New Research Building were at a beer hour, but David Reich's lab was still bustling. Molecular biologist Nadin Rohland was working late, trying to finish sequencing 390,000 bases of DNA from each of 92 Bronze Age human bones. The samples had been streaming in from archaeologists, and she was hustling to keep up. "We're really busy," Rohland said as she prepared equipment for the next day's round of sequencing.

Next door, postdocs from three countries sat at their large computer screens, trying to figure out how to analyze sequences faster. "Exactly a year ago, we had DNA from one farmer from Germany, one farmer from Luxembourg, and two or three hunter-gatherers," said Iosif Lazaridis from Greece. "Suddenly we had 50. Now it's in the 100s—I don't know if we've crossed the thousands." Pontus Skoglund, from Sweden, joked: "There's too much data!"

Just 5 years ago, extracting and deciphering a single fossil's genome—and making sure the result was not muddied by contamination with modern DNA—was a titanic effort. Now, thanks to technological breakthroughs that have vastly accelerated sequencing and made the results more trustworthy, DNA researchers the world over are awash in data (see p. 359). The result is a series of revelations about humanity's past. Ancient DNA has led to the discovery of new types of ancient humans and revealed interbreeding between our ancestors and our archaic cousins, which left a genetic legacy that shapes our health and appear-

PHOTO: © DREW GURIAN

Published by AAAS

ance today. And because investigators can now sequence entire ancient populations, as Reich's lab is doing, ancient DNA is adding layers of complexity to the story of how ancient populations migrated and mixed across the globe. "The whole field is exploding in terms of its impact," says Christina Warinner of the University of Oklahoma, Norman. "The data that's coming out is completely rewriting what we know about human prehistory."

The findings are forcing a shotgun marriage between ancient DNA specialists and other researchers trying to unravel the past, including anthropologists, archaeologists, and population geneticists. For them, the technique poses unsettling challenges as well as opportunities. Ancient DNA has contradicted prevailing views—that the invention of farming reflected the spread of ideas rather than people, for example. But it is also enabling these scientists to answer questions they could not previously address, and many are now seeking collaborations with ancient DNA researchers. "Before 2010 I didn't know anything about DNA," says archaeologist David Anthony of Hartwick College in Oneonta, New York, who provided bone samples of ancient herders from Russia to Reich's lab. "I've had to ramp up my knowledge—ancient DNA is becoming a tool for archaeology almost like radiocarbon dating."

Such collaborations aren't always easy. Despite their interest, archaeologists, for example, are still outsiders to the world of DNA, says archaeogeneticist Johannes Krause of the Max Planck Institute for the Science of Human History in Jena, Germany. "Archaeologists can't analyze that kind of data," he says. "And they aren't completely in charge anymore." But they can't ignore the burgeoning new field. "The new data can rewrite history."

WHEN PALEOANTHROPOLOGIST Chris Stringer was a 22-year-old grad student in the early 1970s, he took his calipers to museums around Europe, applying a new, systematic measurement procedure to all the skulls of Neandertals and modern humans he could get his hands on. Traveling in a battered Morris Minor, with long hair, barely enough cash to stay in youth hostels, and a modern human skull as passenger, he sometimes aroused suspicion. Some researchers at first refused access to fossils, and the Czech police searched his belongings, saying that his visit was of "no value to the people of Czechoslovakia." In Rome, thieves stole the modern human skull.

But Stringer persevered, carefully measuring the rare bones. He noted that Neandertals had long, low skulls with pronounced brow ridges and projecting midfaces, whereas the younger modern humans had globular skulls and flat faces. He concluded that Neandertals in Europe were not the ancestors of modern humans there, as was then widely believed, but a separate species that had been completely replaced by modern humans. That put him at odds with researchers who focused on different anatomical traits and thought that Neandertals had interbred with our ancestors, and even were members of our own species, *Homo sapiens*.

The infighting went on for years. Meanwhile, paleogeneticist Svante Pääbo of the Max Planck Institute for Evolutionary Anthropology in Leipzig, Germany, took a different, risky route to answering the question: He studied DNA from Neandertal fossils. First, he had to overcome the problems of contamination—Stringer, for one, had left a trail of his own DNA on fossils across Europe. But Pääbo and his colleagues ultimately managed to create a composite genome from three female Neandertals and compare it with modern human DNA. The team found that Neandertals did indeed have a genome distinct from our own—but that living Europeans and Asians had inherited 1% to 3% of their DNA from Neandertals (*Science*, 7 May 2010, p. 680).

That genetic legacy meant that Stringer's view of the fossils was incomplete: Neandertals had interbred with modern humans at least once. More recent ancient DNA analyses suggest that such interbreeding happened at least three times, probably 37,000 to 85,000 years ago in the Middle East and Europe (*Science*, 22 May, p. 847). One modern human who lived in Romania roughly 40,000 years ago even had a great-great-great-grandparent who was a Neandertal, Pääbo's team reported in June.

The same year Pääbo's team published the Neandertal genome, it sequenced a sliver of a fossil pinky bone from Denisova Cave in Siberia and found genetic evidence of a new kind of human, related but not identical to Neandertals. The team called them Denisovans and found that they, too, had mixed with modern humans so that Melanesians carry up to 5% Denisovan DNA (*Science*, 26 August 2011, p. 1084).

Although ancient DNA proved Stringer wrong about interbreeding among our ancestors, he embraces the new results. As anthropologist Marcia Ponce de León of the University of Zurich in Switzerland puts it, "ancient DNA answers questions that morphology alone cannot answer conclusively—and raises questions that have never been asked before."

Ponce de León, who specializes in state-of-the-art morphological analyses, notes that that lesson emerged yet again earlier this year, when she and others reanalyzed the skull and sequenced the genome of Kennewick Man, an 8500-year-old skeleton found on the shore of the Columbia River in Washington state. Some scientists had argued that Kennewick's long, low skull resembled those of Polynesians or the Ainu people of Japan rather than the broader, rounder skulls of today's Native Americans. They suggested that Kennewick Man might

Excavations of a Bronze Age settlement in Russia's Samara Valley unearthed dozens of skeletons, including an adult male (above). Their DNA is helping reveal the origins of Europeans and Asians.

PHOTOS: © DAVID W. ANTHONY (2)

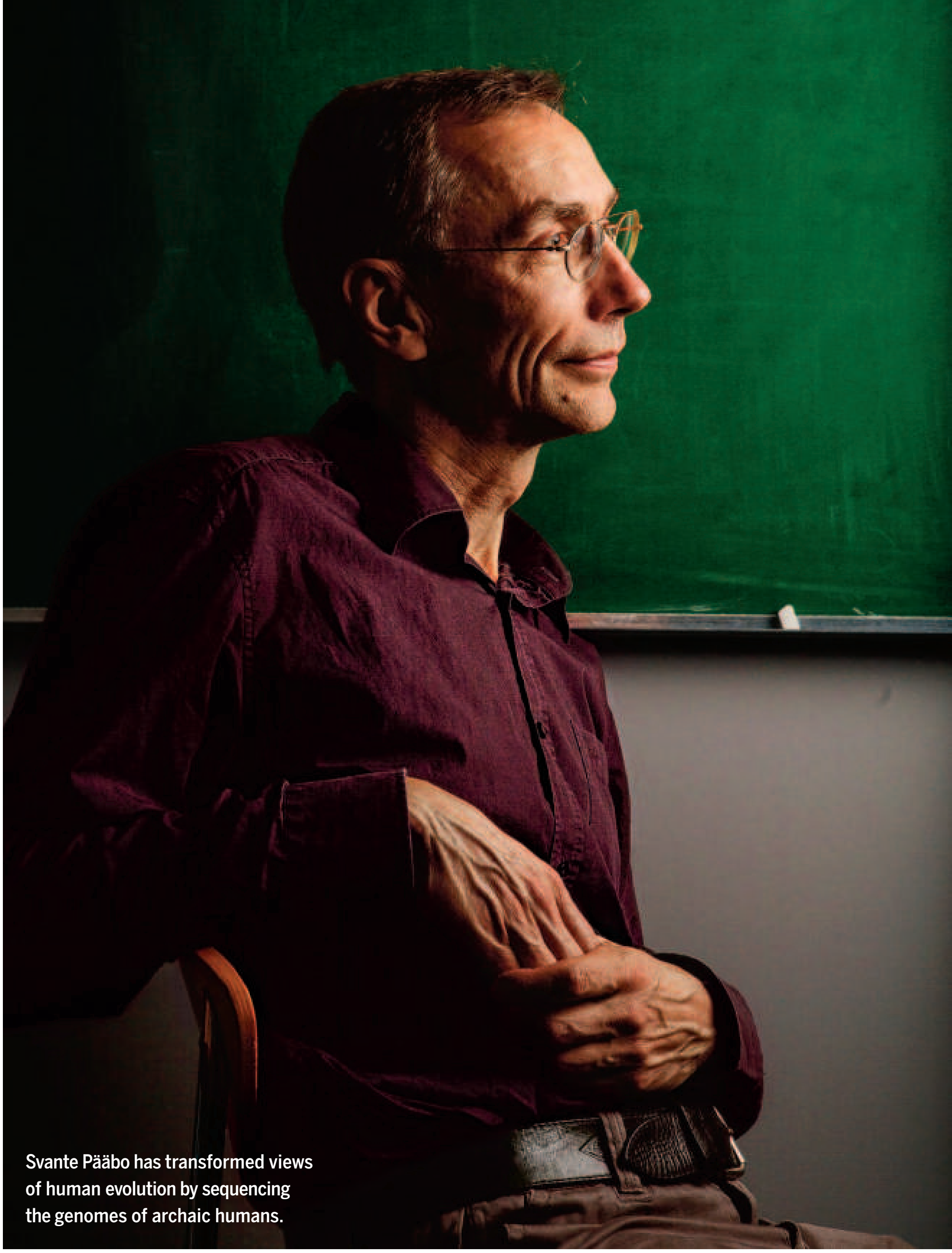

Svante Pääbo has transformed views of human evolution by sequencing the genomes of archaic humans.

PHOTO: © ROB CLARK/INSTITUTE

have been part of an early wave of migration to the Americas and only distantly related to today's Native Americans; their anatomical research influenced court decisions preventing the reburial of the bones according to Native American customs.

Ponce de León and others confirmed the anatomical differences seen in Kennewick Man's skull. But in the same study, evolutionary biologist Eske Willerslev of the University of Copenhagen and others found that Kennewick Man's genome shows that he was closely related to Native Americans, including at least one of the five tribes that originally fought to rebury him. "Ancient DNA analyses provide thousands of independent, often neutrally evolving, features per individual," Ponce de León says. "In morphology, we typically have comparatively few features, which are highly interdependent and only partially reflect the genome."

All the same, Stringer cautions, "it's not time to throw away the artifacts and fossils." They yield insight into ancient people's activities that genes just can't provide. "No amount of ancient DNA would tell us whether the Neandertals buried their dead, or whether the ancestors of Australasians used boats to reach New Guinea and Australia," he says.

WHEN POPULATION GENETICIST Joshua Akey was a graduate student in the 1990s, his fieldwork involved sitting in front of a computer and downloading data on the genes of living people. He was scanning for genes that had been targets of natural selection, and he succeeded: He and his colleagues analyzed variation in the genomes of the 270 people collected by the International HapMap Project and spotted 174 genes, including two linked to cystic fibrosis and diabetes, that apparently had been shaped by natural selection. "I remember thinking how cool it was to be able to use patterns of variation in contemporary individuals to learn about what influenced our ancestors' ability to survive and reproduce," says Akey, now at the University of Washington, Seattle.

He recalls, though, that "all the data could fit in an Excel spreadsheet." That's because living people preserve only a fraction of the genetic diversity of ancient ones. "Population geneticists were trapped in time—they could only look at what was here today," Skoglund says. Now he, Akey, and others can look deep into the past by analyzing the genetic makeup of people who lived long ago. "It seems like science fiction to be able to generate large amounts of sequence data from individuals who lived 30,000, 40,000, 50,000 years ago," Akey says.

As soon as these investigators post sequences from ancient people into public databases, the data feed whole schools of evolutionary researchers downstream, who fish for signs of evolution and adaptation in our genomes. Population geneticists who have never measured a fossil and computational biologists who have never worked in a clean room now sit at their computers unraveling the complex genetics of what made us modern.

Today, Akey continues to seek genes that were favored or weeded out by natural selection. But now he's on the alert for something that hadn't been on his radar before: genes that our ancestors lifted from archaic humans. Adaptation is usually a slow process, as beneficial mutations often require hundreds or thousands of generations to spread through a population. But the Neandertal and Denisovan genomes have shown that in some cases our modern human ancestors were able to take an evolutionary shortcut: As they spread around the globe, they met other kinds of humans who were already adapted to the local environment. By breeding with them, our ancestors were able to snag beneficial genes.

"We're figuring out how interactions with Neandertals and Denisovans helped our ancestors survive," Akey says. Such "adaptive introgression" has been well documented in plants and bacteria. Its importance in human evolution was highlighted last year, when researchers discovered that Tibetan highlanders had inherited a "superathlete"

gene variant called *EPAS1* from Denisovans. This ancient variant, which helps Tibetans use oxygen more efficiently, was found in Denisovans but not in Neandertals or other people around the world, according to work by population geneticist Rasmus Nielsen of the University of California (UC), Berkeley, and his Chinese collaborators.

Other archaic genes helped our ancestors resist disease. "When modern humans started dispersing around the globe, they encountered unique pathogens that archaic humans were better adapted to," Akey says. Luckily for modern humans, they picked up some immune genes from Neandertals, such as a version of *STAT2*, a gene involved in the interferon response that fights viral infections; moderns also acquired different types of human leukocyte antigen genes, which help the immune system detect foreign invaders. Researchers are now trying to figure out just how these archaic gene variants change immune function, but the effect must have been beneficial: The DNA record shows that these genes spread rapidly through Europeans and Asians.

A sliver of pinky bone from Denisova Cave generated a high-quality genome.

Neandertals, whose ancestors had at least 200,000 years to adapt to Europe's gray skies and frigid winters, also bequeathed some skin genes to the modern humans they encountered, including a gene called *BNC2*, which is associated with light skin in Europeans and allows skin to synthesize more vitamin D. (Many of today's Africans, whose ancestors didn't mingle with Neandertals, do not carry these gene variants.) Akey's team also found that Neandertals contributed other genes that protect skin against abrasion or water loss (*Science*, 28 February 2014, p. 1017). These chunks of archaic DNA have provided "a rich reservoir" of genes that have allowed Europeans and Asians (including the ancestors of Native Americans) to adapt rapidly to various environmental conditions, according to a June report in *Nature Reviews Genetics* by Nielsen and Fernando Racimo of UC Berkeley.

Not all such archaic genes are beneficial: Mayas in Mexico, some Native Americans, and about 25% of Asians retain an allele from Neandertals that boosts their risk for diabetes. The gene variant plays a role in the breakdown of fats and may have been beneficial when diets were lean and our ancestors needed to store fat efficiently. Also, several independent studies have noted that long stretches of the modern genome are archaic "deserts" lacking any Neandertal or Denisovan signal. Researchers suspect that natural selection weeded out deleterious archaic genes in these regions, and the DNA here may be what distinguishes us from those archaic people. "This has the potential to contribute to our understanding of what makes modern humans modern," Akey says.

To date, Pääbo has assembled a catalog of about 31,000 base-pair changes, or single nucleotide polymorphisms (SNPs), in which modern humans carry a different version from Neandertals and Denisovans. Several teams are doing lab work in stem cells and mice to try to figure out what some of these genes do (*Science*, 3 July 2015, p. 21).

The revolution in ancient studies has brought Akey full circle—back to scanning data from living humans: He is now col-

The most wanted genomes

Genomes from ancient humans in these artists' reconstructions could reveal much about our evolution but remain just out of reach—for now

Homo floresiensis, aka "the hobbit"

Found in Liang Bua cave on the Indonesian island of Flores in 1998, this hominin was just over 1 meter tall but has sparked an outsize controversy. Many think the bones represent an amazingly tiny species of ancient human, but a few researchers say the hobbit, who lived as recently as 18,000 years ago, is a diseased member of our own species. DNA sequencing could put that argument to rest, and reveal any kinship with other archaic humans. But independent efforts have so far failed to retrieve any genetic material from the hobbit bones.

Homo heidelbergensis

In the 1990s, archaeologists found the remains of about 32 archaic people with large brows and short, compact bodies in a cave in northern Spain. Many researchers thought that the 440,000-year-old fossils were ancestral to the Neandertals. But in 2013, researchers at the Max Planck Institute for Evolutionary Anthropology in Leipzig, Germany, managed to sequence the mitochondrial genome from a *H. heidelbergensis* legbone, and found it looked more like that of another ancient group, the Denisovans. Max Planck researchers are now trying to sequence its nuclear genome to check this puzzling result.

Homo erectus

This iconic human ancestor, the first with a notably enlarged brain, lived 1.8 million to 1 million years ago, so sequencing its DNA seems a bit like science fiction. But researchers are eager to do so, because it is thought to be ancestral to later hominids, including Neandertals, Denisovans, and modern humans. Comparing *H. erectus* with its descendants could show what these three types of humans once had in common, how they have diverged, and the stepwise changes that led to *H. sapiens*. To glimpse *H. erectus*'s genome, researchers are now analyzing long stretches of very old DNA in its descendants.

Published by AAAS

Who's who of ancient genomes

Some of the best known nuclear genomes sequenced from human ancestors across the Northern Hemisphere.

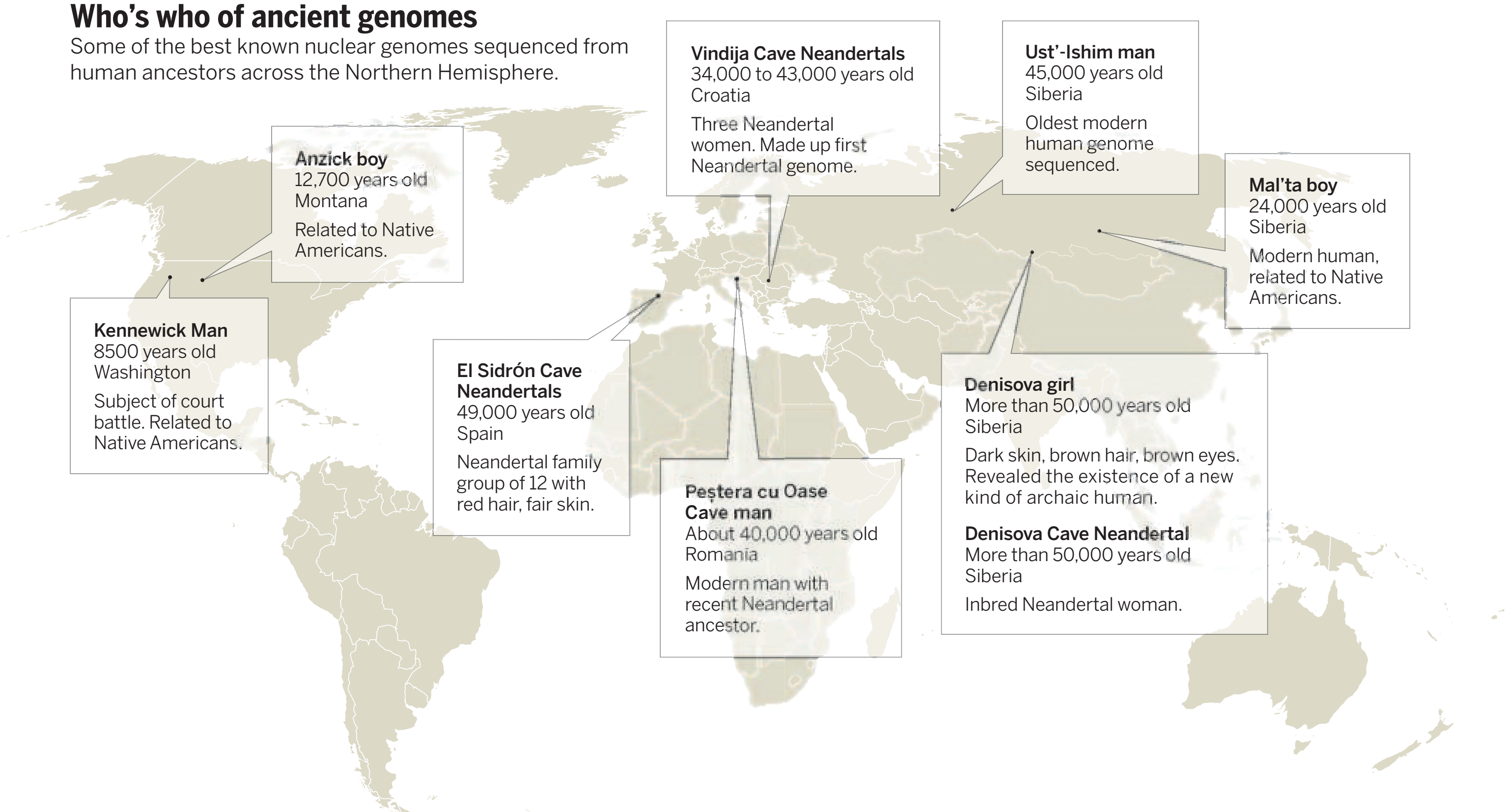

laborating with researchers worldwide to see whether archaic versions of genes boost the risk of schizophrenia, diabetes, and autoimmune disorders. For better or worse, "we're all amalgamations of the past, with little bits and pieces of DNA that originated all over the world and, in some cases, from different species," Akey says.

FOR ARCHAEOLOGIST ANTHONY, in contrast, ancient DNA is a tool for unveiling ancient populations—in particular, a mysterious group of tall young herders he has excavated from beneath earth mounds in the Samara Valley of Russia. He and Dorcas Brown, his wife and research partner, used all the tricks of their trade to probe how these elite members of the Yamnaya herding culture lived and died about 5000 years ago. With their Russian collaborators, they measured bones, analyzed isotopes, and examined their grave goods. Finally, the pair sealed bone fragments of the Yamnaya into plastic bags and stored them on a shelf.

But Anthony was haunted by all he still didn't know about the nomads who moved across the northern steppe on horseback. "I wanted to know their eye color, skin color, hair color," he says. "And were the people buried in these elite graves related to each other?"

So when he got a phone call in 2013 from a colleague of Reich's who was seeking bones for DNA analysis, he agreed to let the researchers grind up small samples of the Yamnaya's limb bones for sequencing. To quickly probe their population history and appearance, Reich's team sequenced not the full genomes but a set of 390,000 key SNPs from each of 69 ancient Europeans and Asians, including nine Yamnaya. The results, published in February, showed that the Yamnaya were the source of a massive migration of herders who swept into the heartland of Europe on horseback about 5000 years ago—and that most Europeans can trace at least some of their ancestry to this group. Anthony got some of his questions answered: The Yamnaya had brown eyes, brown hair, and light skin. And the people in the elite graves were members of the same clan, showing that family ties influenced status. "One of the wonderful things about ancient DNA is that it gives these old samples new life," he says.

Sometimes, though, the results can be hard for archaeologists to handle. "When we circulated the final version of our paper, the European archaeologists who had given us samples were distressed," Reich says. They were startled when the genetic data showed the Yamnaya from the Russian steppes were the ancestors of the Corded Ware people in Germany, because it seemed to echo an erroneous idea about Aryan culture propagated by the Nazis. But once archaeologists realized that the genetic evidence was "unambiguous," they added cautionary notes and signed onto the paper, Reich says.

DNA repeatedly shows that people who live in a place today rarely are related to those who lived there thousands of years earlier. "People in every inhabited continent 10,000 years ago looked different to people in these same regions today," Stringer says. For example, when Willerslev's team sequenced the genome of a 24,000-year-old Siberian boy from Mal'ta in 2013, it found no genetic connection to anyone living in Central Asia today. But the Mal'ta boy was related to Kennewick Man and Native Americans, suggesting that he represented an ancient source population for migrations of Paleoindians to the Americas.

Anthony hopes ancient DNA will help him continue to learn about the Yamnaya. Could these elite herders drink alcohol? Did their dogs travel with them? To answer such questions, ancient DNA researchers need data from many more archaeological sites. So at the last annual meeting of the Society for American Archaeology, Anthony could be found recruiting samples for Reich's lab. There are "samples lying all over Europe and North America, in labs sitting in the dark," he says.

Most archaeologists, he says, are happy to be asked. "People are excited that their samples could be a source of ancient DNA." ■

MAP: M. ATAROD

LOST WORLDS FOUND

Sugar cubes of buried soil reveal how ecosystems warmed after the last ice age

By **Elizabeth Pennisi**

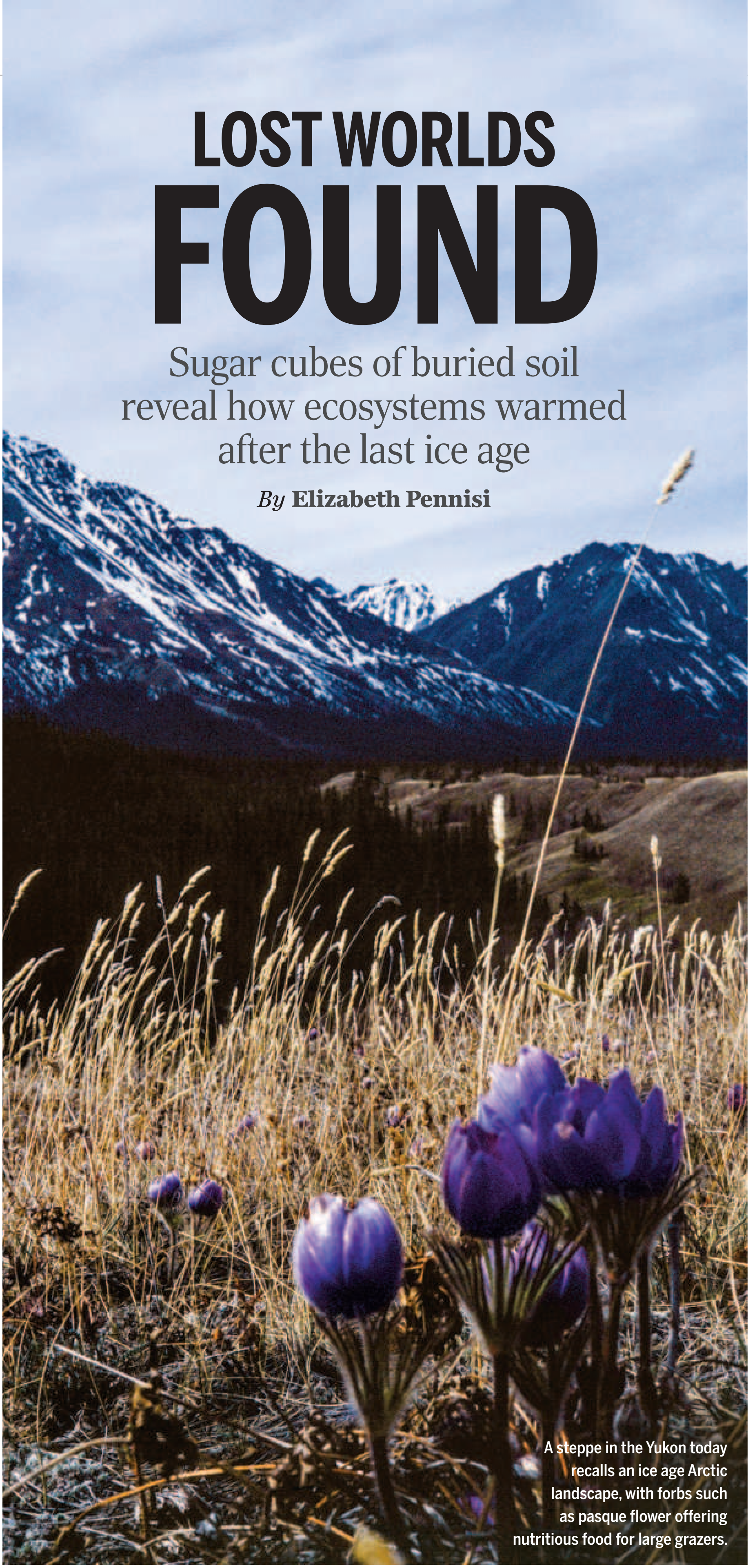

A steppe in the Yukon today recalls an ice age Arctic landscape, with forbs such as pasque flower offering nutritious food for large grazers.

PHOTO: © SCOTT ARMBRUSTER

If time travel were possible, big game hunters would be clamoring to visit the Yukon during the last ice age. About 30,000 years ago, mammoths with 3-meter tusks and shaggy coats nosed about with bison, woolly rhinos, muskoxen, and small horses, while lions, short-faced bears, and scimitar-toothed cats lurked in the background. But the vast Pleistocene game park had vanished by 10,000 years ago. The great beasts were long gone, replaced by familiar elk and moose, with lynx and grizzlies as predators.

For decades, scientists have debated why these megafauna disappeared from the Arctic and much of the rest of the world. Did a fluctuating climate drive species to extinction? Or did humans, in their relentless expansion across the globe, kill off the big game in an ancient hunting spree?

Now, ancient DNA data have entered the fray, most recently in the form of molecules scooped directly from samples of soil or ice. By sequencing whatever DNA emerges from even a thimbleful of ancient soil, researchers are reconstructing ancient ecosystems as far back as 700,000 years ago with astonishing clarity. A single sample of so-called environmental DNA (eDNA), combining sequences from plant and animal detritus as well as microbes, can provide an inventory of ancient species, filling gaps in conventional fossil and pollen records. The method "could revolutionize our understanding of [ancient] ecosystems by giving us … a full picture of the food web from the ground up," says geologist Fred Longstaffe of Western University in London, Canada.

In a landmark paper published in *Nature* last year, for example, researchers using eDNA discovered that in the Arctic, the big herbivores' favorite foods—tasty herbaceous plants like marsh marigolds and alpine forget-me-nots—grew ever scarcer as Earth warmed after the last glacial age. That points to climate as a factor in the extinctions. A paper using ancient DNA and detailed climate records, published online this week in *Science* (http://scim.ag/Cooperetal), goes further, suggesting that bouts of rapid warming disrupted ecosystems and slammed the megafauna even before the last great warming. The finding "is going to overturn the human versus climate debates," says lead author Alan Cooper of the University of Adelaide in Australia, "and serves as a grim warning about climate warming."

When it comes to eDNA, researchers are still working out how to date samples and avoid contamination, and the research is most developed for Arctic environments. But the data also illuminate how the post-

Published by AAAS

In northern Greenland, Eske Willerslev took samples from sediments and from megafauna like this muskox for DNA extraction.

PHOTO: © KURT KJER

glacial thaw transformed other landscapes, such as temperate forests, with implications for today's warming world.

"Every time molecular data comes into a field, it shakes the field up," says paleoecologist Jason McLachlan of the University of Notre Dame in Indiana. "Now it's happening in paleoecology. ... There isn't any paleoecologist in the world who hasn't thought about using ancient DNA."

IN THE 1980s, microbiologists using new techniques for extracting and analyzing DNA found they could get a snapshot of existing species in a sample of soil or seawater by simply collecting and sequencing its DNA en masse, without bothering to try to isolate and culture the microbes themselves. Then evolutionary geneticists successfully applied the method to the past. For example, Eske Willerslev of the University of Copenhagen took eDNA from 2000- and 4000-year-old cores from the polar ice caps. His team melted ice from cores, filtered out DNA, and used DNA tags called primers to pull out all the copies of part of a gene known to vary among species. They were able to identify 57 groups of plants, fungi, and animals.

After that proof of principle, permafrost seemed the next logical target, as this permanently frozen soil has proved to be a great preservative of DNA in bones. At the time, others "told me it was a most stupid idea," Willerslev recalls. But in a sugar cube–sized permafrost sample from northeastern Siberia, he found DNA from "all kinds of plants, bison, horses, bears, mammoths, even lemmings." Hendrik Poinar, now an evolutionary geneticist at McMaster University in Hamilton, Canada, extended the method to a cave in the Arizona desert in 2003. There, a quarter-century of digging and the removal of 2 tons of dirt had unearthed fossils of two dozen species, from giant sloths to condors, dating back 40,000 years. Poinar sequenced eDNA from less than a thimbleful of soil and managed to identify 12 species—half of the excavation total.

Environmental DNA comes from urine, feces, hair, skin, eggshells, feathers, and even the saliva of animals, as well as from the decaying leaves and fine rootlets of plants. Most of this DNA degrades in hours or weeks, destroyed by bacterial or fungal enzymes. But bacteria sometimes take up the molecules, preserving fragments intact inside their cells, Willerslev says. Much more DNA binds to clay, humic acid, or other charged particles that shield it from enzymatic attack.

Traditional species surveys of modern water and soil suggest that eDNA can give a good picture of biodiversity. In rivers, for example, "you can find all the life in the rivers just in a single sample," says Pierre Taberlet, an ecologist at the CNRS Alpine Ecology Laboratory in Grenoble, France. And because fossils are rare, eDNA may bring surprises: Poinar found DNA from a woolly rhinoceros—a species never before found in the New World—in ancient Yukon permafrost.

By allowing investigators to survey entire ecosystems, eDNA is revealing how glacial climate shifts affected both plants and animals. In last year's *Nature* study, Willerslev, Taberlet, Cooper, and others collected 200 samples of soil from around the Arctic. They divided the samples into three periods: From about 50,000 to 25,000 years ago, when climate fluctuated sharply; from 25,000 years ago to 15,000 years ago, a consistently cold period when glaciers were at their peak; and from 15,000 years ago to today, when Earth emerged from the last ice age.

The researchers extracted DNA from the soil samples and then used specially designed probes to pull out and sequence DNA from particular species of plants, mammals, and also nematodes, which can serve as indicators of soil moisture and vegetation. Finally, they sequenced DNA from fossilized guts and stools of ancient mammals.

They found that before and during the peak glacial period, herbaceous plants called forbs, such as anemones and forget-me-nots, dominated a dry and dusty Arctic landscape (*Science*, 28 February 2014, p. 961). Large mammal herbivores such as mammoths were also common then, and the gut and stool contents showed that the forbs were a mainstay of these animals' diets. As glaciers melted and the climate grew warmer and wetter, however, forbs became rare. Less-nutritious grass and shrubby plants took hold. That's when eDNA and other indicators show that the big grazers declined as well, Willerslev says. Thus, he says, "it's tempting to say it's the loss of the main food source that led to the extinction of these animals."

Cooper's new study, which offers far better time resolution, suggests that even before the end of the ice age, brief bouts of warming caused repeated local extinctions of the megafauna. The study uses a variety of climate records to create an astonishingly fine-grained picture of temperature fluctuations on timescales of as little as a decade over the past 50,000 years. The researchers tracked extinctions across Eurasia and Alaska using the bones of large mammals such as mammoths and bears.

They found that species went locally extinct whenever the weather warmed—whether humans were present or not.

For example, in North America the giant short-faced bear was already gone before humans arrived about 13,000 years ago. In Eurasia, many big animals persisted after modern humans showed up 44,000 years ago, surviving for thousands of years longer and then disappearing during repeated sudden warming events. Animals first hit by warming might have been particularly vulnerable to hunting, Cooper says, but "climate is doing much of the damage before humans arrived."

Researchers who think humans drove these extinctions welcome the new data from eDNA and other studies. But they still think climate is secondary. "Having this layer of information tuned to this chronology and showing warming is important and a great start," says paleoecologist David Burney, retired director of conservation at the National Tropical Botanical Garden in Kalaheo, Hawaii. "But it by no means lets humans off the hook." He thinks humans repeatedly made recovery impossible for struggling species, either by hunting them or by interrupting migrations and feeding.

ENVIRONMENTAL DNA STUDIES have flourished in the Arctic, where cold, dry conditions help preserve DNA. But an even richer source of eDNA may come from lakebeds in temperate latitudes, long a source of information about ancient ecosystems. Because lake sediments are deposited in annual layers, they can be precisely dated, and they preserve microscopic fossils and pollen. But pollen may not reveal the species or even genus of plants, and its records are stacked in favor of those plants that produce masses of windborne pollen. With eDNA, "we can reconstruct the ecosystem to a way greater resolution," Poinar says.

To explore the method's potential, McLachlan, Poinar, and Candice Lumibao, now a postdoc at the University of Minnesota, Twin Cities, sampled three Michigan lakes. Pollen data had suggested that beech trees colonized the landscape only about 1500 years ago, 7000 years after ice age glaciers receded. But the eDNA points to small pockets of beech trees in Michigan as early as 5000 years ago. "They may have moved north earlier than we thought they did," McLachlan says.

That finding is echoed in another eDNA lake sediment study by Willerslev's team. Many researchers had thought that spruce and other trees disappeared from Scandinavia during glacial times, and then expanded back once the climate warmed. But an eDNA study in Norway and Sweden showed that one lineage of spruce persisted in small pockets even when most of the country was covered with ice (*Science*, 2 March 2012, p. 1083). Thus, this species had a leg up on revegetating the landscape once the ice was gone.

Both studies show that eDNA tracks early appearances of species better than pollen. They "suggest that trees were poised to repopulate glaciated areas much earlier than researchers had once thought," McLachlan says, a result that could have implications for understanding how fast today's trees will be able to adjust to global warming. This level of detail "is going to be a game changer for global change biology," he adds.

Willerslev's Arctic data, too, send a message for today's warming era: Before the last glacial maximum, the Arctic ecosystem seemed to bounce back from climate fluctuations. But after that glacial peak, the forbs and the ecosystem as a whole never returned to their former state, likely because too many species completely disappeared. That's a warning, Willerslev says. Even if warming was halted today, there is no guarantee that "we will return to the same vegetation cover." The eDNA in just a teaspoon of soil may be enough to tell future generations whether his prediction was correct. ■

Prospecting for genetic gold

By **Elizabeth Pennisi**

From muddy cliffs in Canada's Yukon territory, where miners flush out gold-laden gravel, Beth Shapiro is netting a different sort of treasure: DNA from thousands of mammoth, bison, horse, and other mammal bones. Her goal is to paint a picture of the animal community here during the past 80,000 years—and see how their genes changed as the environment shifted. "We want to watch evolution as it happened," she says. In addition to extracting DNA from the bones, she and her colleagues are analyzing environmental DNA taken directly from the soil (see main story, p. 367). Thus, she plans to capture both genetic changes and the environmental shifts that drove them.

DNA from hundreds of samples will help Beth Shapiro track animals' evolutionary responses to climate change.

Shapiro, an evolutionary biologist at the University of California, Santa Cruz, has been working with her team outside Dawson City—the epicenter of the 19th century Klondike gold rush—since the 1990s. Mining has exposed fossils and layers of volcanic ash, which have been dated with radiometric methods. Geologists now have an exquisite catalog of well-dated layers, so Shapiro can pin down the ages of fossils back to before 40,000 years ago, the limit of radiocarbon dating.

Her colleague, Hendrik Poinar of McMaster University in Hamilton, Canada, has already sieved environmental DNA from the sediments. But that eDNA is in tiny fragments, whereas fossil bones chilled in permafrost may yield nearly complete genomes. Thanks to the ever-shrinking cost of sequencing, Shapiro can analyze hundreds of individuals per species, recording changes through time in the frequency of specific gene variants, such as those involved in digestion or immunity. Such shifts may have helped large ruminants such as bison cope with climate warming and cooling and the resultant changes in vegetation and pathogens. The project's first papers are expected next year. ■

VIDEO Watch Beth Shapiro in action at http://scim.ag/AncientDNAvid

For example, in North America the giant short-faced bear was already gone before humans arrived about 13,000 years ago. In Eurasia, many big animals persisted after modern humans showed up 44,000 years ago, surviving for thousands of years longer and then disappearing during repeated sudden warming events. Animals first hit by warming might have been particularly vulnerable to hunting, Cooper says, but "climate is doing much of the damage before humans arrived."

Researchers who think humans drove these extinctions welcome the new data from eDNA and other studies. But they still think climate is secondary. "Having this layer of information tuned to this chronology and showing warming is important and a great start," says paleoecologist David Burney, retired director of conservation at the National Tropical Botanical Garden in Kalaheo, Hawaii. "But it by no means lets humans off the hook." He thinks humans repeatedly made recovery impossible for struggling species, either by hunting them or by interrupting migrations and feeding.

ENVIRONMENTAL DNA STUDIES have flourished in the Arctic, where cold, dry conditions help preserve DNA. But an even richer source of eDNA may come from lakebeds in temperate latitudes, long a source of information about ancient ecosystems. Because lake sediments are deposited in annual layers, they can be precisely dated, and they preserve microscopic fossils and pollen. But pollen may not reveal the species or even genus of plants, and its records are stacked in favor of those plants that produce masses of windborne pollen. With eDNA, "we can reconstruct the ecosystem to a way greater resolution," Poinar says.

To explore the method's potential, McLachlan, Poinar, and Candice Lumibao, now a postdoc at the University of Minnesota, Twin Cities, sampled three Michigan lakes. Pollen data had suggested that beech trees colonized the landscape only about 1500 years ago, 7000 years after ice age glaciers receded. But the eDNA points to small pockets of beech trees in Michigan as early as 5000 years ago. "They may have moved north earlier than we thought they did," McLachlan says.

That finding is echoed in another eDNA lake sediment study by Willerslev's team. Many researchers had thought that spruce and other trees disappeared from Scandinavia during glacial times, and then expanded back once the climate warmed. But an eDNA study in Norway and Sweden showed that one lineage of spruce persisted in small pockets even when most of the country was covered with ice (*Science*, 2 March 2012, p. 1083). Thus, this species had a leg up on revegetating the landscape once the ice was gone.

Both studies show that eDNA tracks early appearances of species better than pollen. They "suggest that trees were poised to repopulate glaciated areas much earlier than researchers had once thought," McLachlan says, a result that could have implications for understanding how fast today's trees will be able to adjust to global warming. This level of detail "is going to be a game changer for global change biology," he adds.

Willerslev's Arctic data, too, send a message for today's warming era: Before the last glacial maximum, the Arctic ecosystem seemed to bounce back from climate fluctuations. But after that glacial peak, the forbs and the ecosystem as a whole never returned to their former state, likely because too many species completely disappeared. That's a warning, Willerslev says. Even if warming was halted today, there is no guarantee that "we will return to the same vegetation cover." The eDNA in just a teaspoon of soil may be enough to tell future generations whether his prediction was correct. ■

Prospecting for genetic gold

By **Elizabeth Pennisi**

From muddy cliffs in Canada's Yukon territory, where miners flush out gold-laden gravel, Beth Shapiro is netting a different sort of treasure: DNA from thousands of mammoth, bison, horse, and other mammal bones. Her goal is to paint a picture of the animal community here during the past 80,000 years—and see how their genes changed as the environment shifted. "We want to watch evolution as it happened," she says. In addition to extracting DNA from the bones, she and her colleagues are analyzing environmental DNA taken directly from the soil (see main story, p. 367). Thus, she plans to capture both genetic changes and the environmental shifts that drove them.

DNA from hundreds of samples will help Beth Shapiro track animals' evolutionary responses to climate change.

PHOTO: © MATHIAS STILLER

Shapiro, an evolutionary biologist at the University of California, Santa Cruz, has been working with her team outside Dawson City—the epicenter of the 19th century Klondike gold rush—since the 1990s. Mining has exposed fossils and layers of volcanic ash, which have been dated with radiometric methods. Geologists now have an exquisite catalog of well-dated layers, so Shapiro can pin down the ages of fossils back to before 40,000 years ago, the limit of radiocarbon dating.

Her colleague, Hendrik Poinar of McMaster University in Hamilton, Canada, has already sieved environmental DNA from the sediments. But that eDNA is in tiny fragments, whereas fossil bones chilled in permafrost may yield nearly complete genomes. Thanks to the ever-shrinking cost of sequencing, Shapiro can analyze hundreds of individuals per species, recording changes through time in the frequency of specific gene variants, such as those involved in digestion or immunity. Such shifts may have helped large ruminants such as bison cope with climate warming and cooling and the resultant changes in vegetation and pathogens. The project's first papers are expected next year. ■

VIDEO Watch Beth Shapiro in action at http://scim.ag/AncientDNAvid

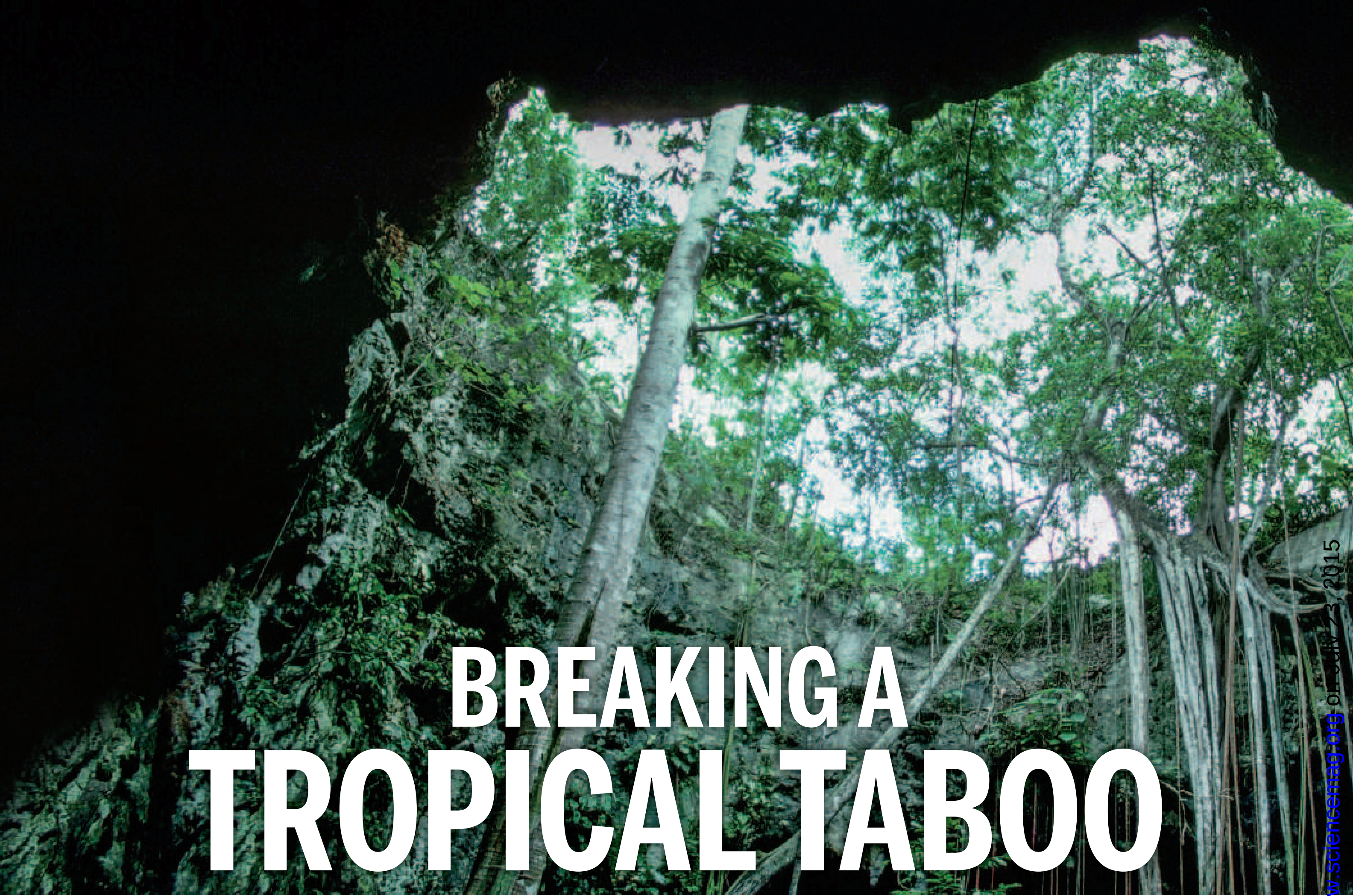

BREAKING A TROPICAL TABOO

Most ancient DNA comes from frigid environs. Can new methods sample hot and humid locales? *By* **Lizzie Wade**

When Tania Gutiérrez García packed up 40 rodent jaws in a package smaller than a shoebox and headed to Canada in 2009, she was pretty sure she was setting herself up for disappointment. A doctoral student in biology at the National Autonomous University of Mexico in Mexico City, she had wrangled an invitation to spend 3 months at a premier ancient DNA lab at McMaster University in Hamilton, where she would work alongside scientists who were then sequencing the woolly mammoth genome. Gutiérrez's own goal was to extract ancient DNA from the rodent bones, which ranged from about 12,000 to 4000 years old, and so reconstruct their family trees.

But even in a lab where once outlandish dreams were coming to pass, her project seemed a long shot. The mammoth samples had been found in the Arctic permafrost, where consistently cold, dry conditions are known to best preserve ancient DNA. Gutiérrez's rodents had died in the hot, humid Yucatán Peninsula. She wasn't even sure there was any DNA left in their bones. But the rat jaws ended up delivering a surprise, and raised hopes that ancient DNA can answer questions that once seemed beyond its ken.

Much of the world's biodiversity, including that in our own family tree, evolved in the tropics. Ancient DNA from those latitudes could resolve the origins of the strange megafauna that once dominated South America and Australia (see p. 372) and settle the controversy over whether Indonesia's diminutive *Homo floresiensis*, known as the "hobbit," was an odd species of hominid or a diseased modern human. But when Gutiérrez went to Canada, nearly all attempts to retrieve ancient DNA from tropical locales had failed.

That's because DNA degradation is a fact of life and chemistry. DNA is a notoriously weak molecule, explains Hendrik Poinar, the evolutionary geneticist who runs the McMaster lab. Exposure to water or oxygen can rip apart the chemical bonds that hold the double helix together. When an organism is alive, cells quickly repair such damage. But after death, chemical processes can wreak havoc, chopping DNA into tiny strands, sometimes only a few bases long. A severely degraded sample is little more than "alphabet soup," says Michael Bunce, a paleogeneticist at Curtin University, Perth, in Australia.

For decades, scientists have assumed that the only place to find viable ancient DNA was in cold, dry environments. Freezing temperatures slow chemical reactions and inhibit microbial activity that can eat away cells and expose the fragile DNA inside. And dryness should reduce water's attack on DNA's molecular bonds.

Experience seemed to bear out those assumptions. Impressive, verifiable results began to pour in from cold environments beginning in the early 2000s. One team successfully sequenced a 700,000-year-old horse genome from the Yukon—the oldest genome to date—while others retrieved the complete genome of a new type of human from a sliver of pinky bone in Denisova Cave in Siberia.

PHOTO: © RICHARD A. COOKE/CORBIS

Loltun Cave's cool climate may have shielded ancient DNA in animal bones from the worst of the Yucatán's heat.

PHOTO: © CINDI RAYAS

Meanwhile, high-profile tropical efforts like sequencing the hobbit ended in heartbreak.

With all that in mind, Gutiérrez wasn't surprised when students in the McMaster lab laughed at her plans for the tiny rodent jaws, which had been excavated in the late 1970s and 1980s from a limestone cave system in the Yucatán called Loltun and had sat in storage in Mexico City ever since. She figured she had a 90% chance of returning to Mexico empty-handed. But the bones had a few features that kept her focused on that 10% chance of success.

First, she found that she could crack apart the delicate jaws to reach the roots of the rodents' teeth, which is "one of the most likely places to find ancient DNA," she says. For example, University of Copenhagen paleogeneticist Hannes Schroeder was able to analyze DNA from the tooth roots of three 17th century enslaved individuals unearthed on the Caribbean island of St. Martin. His team extracted enough DNA to trace each person's ancestry back to a specific region of West Africa, they wrote this spring in the *Proceedings of the National Academy of Sciences*.

Gutiérrez also knew her samples had a leg up because the rodents were preserved in a limestone cave. Caves—if they're deep enough—are usually much cooler than the surface, and the temperature inside tends to stay steady. And limestone, a buffer, can prevent DNA from being eaten away by acidic soil. "Cave sites are phenomenal" for DNA preservation, Poinar says, noting Denisova in Siberia and Sima de los Huesos or the "Pit of Bones" in Spain, which has yielded the most ancient hominid DNA so far.

At McMaster, Gutiérrez used the reigning technology of the time, centered around the polymerase chain reaction (PCR), to amplify sequences of DNA. She managed to extract six overlapping fragments of ancient DNA, totaling 666 base pairs, from 12 jaws. Comparing the rodents' sequences with DNA from living relatives, she was able to craft a family tree of Yucatán rodents and publish her work last summer in *Biology Letters*; she, Poinar, and their co-authors called the work "an unprecedented success" for a tropical ancient DNA sample.

"It's amazing," agrees Ross MacPhee, a paleontologist at the American Museum of Natural History in New York City who has tried unsuccessfully to extract ancient DNA from South American fossils. "It just goes to show what we don't know about DNA preservation."

Still, says Alan Cooper, a molecular evolutionist at the University of Adelaide in Australia, there are "an enormous number of sites which prove the rule" that DNA decays quickly in the tropics. Cooper himself tried and failed to extract DNA from the hobbit bones. If Gutiérrez's results are confirmed, "something very extraordinary" must be going on in Loltun, he says. "Why is this site doing something no other site can do?"

A slow trickle of results like Gutiérrez's are persuading some scientists that Loltun may not be a fluke. Even exposure to water—a sure-fire way to destroy DNA in the lab—hasn't turned out to be a death knell. "Water is very bad if you're dealing with free DNA," says Morten Allentoft, a paleogeneticist at the University of Copenhagen. "But when [DNA] is preserved inside a bone or a tooth, I'm not so sure that water actually matters that much." He's worked with outstanding DNA samples from ancient humans found in lakes in Denmark, Allentoft says.

"If you had asked me 5 years ago" whether some environments had zero chance of yielding ancient DNA, "I probably would have said yes," Bunce adds. "But now I would say that the only way to absolutely determine [whether a sample will yield ancient DNA] is to have a go at it."

All the same, the tropics will probably never yield genetic sequences as old as those found in the Arctic, Bunce and others say, because DNA simply breaks down faster in warmer climates. In certain conditions, even a few centuries can wreak genetic havoc. Schroeder, for example, got only 3% genome coverage from the St. Martin slave bones, which were less than 400 years old. Next-generation sequencing technologies are "very good at making the most out of what is left," Cooper says. "But the question comes back to, what is left?"

Still, relatively recent DNA from the tropics can answer plenty of interesting questions. The dodo, driven extinct in the 17th century, may fall within the limit, Cooper says. Meanwhile, Schroeder and his colleagues are attempting to extract and sequence ancient DNA from a member of the extinct Taíno tribe, who lived in the Caribbean before Christopher Columbus arrived. They hope to shed light on how and when people arrived in the Caribbean, one of the last regions of the world to be populated by humans. And Schroeder's collaborator, María Ávila, a postdoc at Stanford University, hopes to use ancient DNA from 16th and 17th century skeletons to study the African slave trade's effect on the population genetics of Mexico.

Today, Gutiérrez's initial analysis is already outdated, because methods centered on PCR have been superseded by next-generation sequencing, which allows scientists to analyze shorter fragments of DNA and helps them rule out contamination with modern sequences. So she returned to McMaster with her rodent samples in 2011. So far she has used the newer technology to sequence more than 2000 contamination-free base pairs. Poinar predicts the final results "will be impressive."

Next, Gutiérrez, who is now a professor at the University of Guadalajara in Mexico, plans to try to extract DNA from other ancient animals buried in Loltun, such as shrews or perhaps pre-Columbian horses. "They don't laugh at me anymore," she says with a smile. ■

Tania Gutiérrez García painstakingly extracted DNA from the tooth roots of rodents buried up to 12,000 years ago.

PROTEIN POWER

Paleoproteomics hustles to catch up with its more developed cousin

By **Robert F. Service**

While working out his theory of evolution, Charles Darwin was flummoxed by fossils of a pair of bizarre, extinct animals from South America. The horse-sized *Macrauchenia* looked like a cross between a camel and an elephant; *Toxodon* resembled a rhinoceros with the head of a hippo. Ever since, Darwin and his successors have puzzled over where these 12,000-year-old mammals belong in the evolutionary tree of life. Were they relatively close kin to African elephants, as *Macrauchenia*'s trunklike snout suggests? Or had they branched off on their own odd evolutionary trajectory long ago?

Researchers tried to solve the puzzle by isolating DNA from the fossils, but the warm South American climate had degraded the genomes (see p. 370). Then, earlier this year, an answer came from a more resilient ancient molecule: protein. A team led by Ian Barnes, an evolutionary biologist at the Natural History Museum in London, isolated and sequenced collagen—the most abundant protein in bone—from 48 fossils of the animals. The researchers compared it with collagen from a variety of modern animals and found that *Macrauchenia* and *Toxodon* represent their own vanished lineage: Their closest living relatives are horses and rhinos, but they likely split from that group way back in the early Eocene, some 55 million years ago. *Macrauchenia*'s trunk must have evolved independently from that of elephants.

Barnes's study did more than just solve an evolutionary mystery. It also demonstrated the research potential of ancient protein, which has some advantages over its more famous cousin, ancient DNA. For starters, tissues are made up of protein. "There is tons of it compared to DNA," Barnes says. So proteins need not be amplified during analysis, as is often done with DNA, and researchers are less likely to mistake a contaminant for the real thing. Proteins also resist the ravages of time far better than fragile DNA. "Protein sequencing has the potential to look a lot further back in time," maybe even millions of years ago, says Matthew Collins, a paleoproteomics expert at the University of York in the United Kingdom.

The odd trunks of South America's extinct *Macrauchenia*, reconstructed in this painting, bewildered biologists for more than a century.

In addition to solving Darwin's conundrum, ancient proteins have already illuminated a few far-flung corners of ancient life, helping diagnose a severe bacterial infection in a 500-year-old Incan mummy and identify the cattle proteins used to glue a 3500-year-old Chinese sculpture. The method appears particularly promising in archaeology, where it can reveal the diets and lifestyles of past cultures, illuminating which plants and animals

ILLUSTRATION: DANIEL ESKRIDGE/STOCKTREK IMAGES/CORBIS

people used and how they used them. "This field is going great guns at the moment," Collins says.

Still, the technique has a long way to go before it reaches the maturity of paleogenetics, chiefly because methods to sequence amino acids lag behind DNA sequencing. And dedicated funding for ancient protein work remains miniscule. "I don't think we're quite there yet," says paleoproteomics leader Peggy Ostrom of Michigan State University in East Lansing. But "we've made enormous progress over the last 15 years."

Ancient proteins tantalized researchers well before DNA did. In 1954, a team led by Philip Abelson, a physicist then with the Carnegie Institution of Washington (and a former editor of *Science*), detected amino acids—the building blocks of proteins—in fossils, including fossilized fish more than 300 million years old. But the researchers couldn't sequence the amino acids or identify the proteins they came from.

The first protein sequencing technique arrived in the 1960s, but it required destroying large amounts of precious samples. Today, modern mass spectrometry methods can sequence minuscule amounts of proteins. These tools chop a protein into short fragments called peptides, weigh the peptides to fingerprint their amino acid makeup, and compare them to reference peptides to identify them.

This approach, known as shotgun proteomics, was developed primarily to enable biomedical researchers to flag rare proteins associated with human diseases. Because disease-related proteins can be 10 orders of magnitude scarcer than common proteins, instrument makers have continually refined their machines to detect vanishingly small amounts of protein—exactly what is needed to spot rare remnants of intact proteins in a sea of degraded organic matter.

"It's been a story of slow technology improvements," Collins says. "We've ridden on the back of that." In a 2006 proof of principle, Ostrom and her colleagues used their new mass spectrometry tools to obtain the full sequence of an intact protein—osteocalcin, a protein found in bones and teeth—from a 42,000-year-old horse fossil from a cave in Wyoming.

Even with a complete skull of a *Toxodon*, researchers couldn't classify the extinct mammal until ancient proteins revealed its family tree.

Besides harnessing protein sequences to explore evolutionary relationships, researchers have used them to probe ancient diets and gene expression—areas where proteins may be more revealing than DNA. For example, one project explores when and where people began consuming milk products. All human infants can digest lactose, a sugar found in milk, but only some populations have evolved the ability to digest lactose as adults. To track which cultures consumed animal milk, archaeologists have sought storage pots with milk residues, and ancient DNA researchers have begun to track the lactase persistence gene in modern and recent populations.

Now, biochemist Enrico Cappellini of the University of Copenhagen and colleagues have found a direct way to track who consumed what in the Bronze Age: The researchers analyzed proteins caught in calcified dental plaque. In a paper in *Scientific Reports* last year, the team reported success at using a whey protein called β lactoglobulin (BLG) as a direct marker for consumption of milk and soft cheeses made from ruminants like cows and goats. The researchers found that the presence of the BLG protein in ancient dental plaque largely matched DNA data on lactose tolerance in living people from the same regions. And BLG could even distinguish among proteins from cattle, sheep, and goats, says Collins, who was part of the team.

In the same paper, Cappellini and his colleagues analyzed the remains of medieval Norse colonies in Greenland, whose founders arrived with their cattle, sheep, goats, and pigs in 983 C.E. during a warm period. Archaeological evidence suggests that the Norse struggled to maintain their herding way of life as the Little Ice Age began around 1300 C.E. and the growing season shortened. By analyzing proteins from the settlers' dental plaque, the researchers were able to show that early settlers relied heavily on milk from domesticated animals. But by the time the settlements were abandoned in the 15th century, the Norse had largely shifted their diet to one based on fish.

Such successes are just the beginning. Other reports have revealed the ancient production of sourdough bread and kefir cheese in Bronze Age China, and identified periodontal disease in the teeth of medieval monks in Dalheim, Germany. Some studies have even suggested that new methods can spot intact proteins from dinosaurs up to 80 million years old (*Science*, 1 May 2009, p. 578). These studies have yet to be confirmed by independent labs. But if that happens, paleoproteomics may shine a new spotlight onto the ancient past. ■

Medieval Norse in Greenland tried to maintain their ways, including building Christian churches like this one. But proteins in their teeth show that they eventually gave up European-style dairying and ate fish instead.

PHOTO (FROM TOP): © COLIN KEATES/DORLING KINDERSLEY LTD./CORBIS; © PETER ESSICK/AURORA PHOTOS/CORBIS

INSIGHTS

Silence or destruction by microRNA *p. 380*

Conducting fibers that don't fade in the stretch *p. 382*

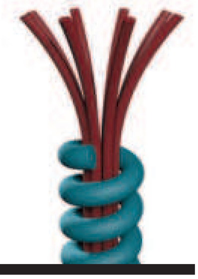

PERSPECTIVES

PALEONTOLOGY

Four legs too many?

A long-bodied fossil snake retains fore- and hindlimbs

By **By Susan Evans**

A classic Gary Larson cartoon shows a robed and bearded figure rolling out clay strips, with the caption: "God makes the snake." Body elongation was certainly fundamental in the evolution of snakes from lizards, as was the shrinking and ultimately the loss of limb pairs (limb reduction). However, informative early fossils are rare, and many details of the transition remain unresolved. A remarkable fossil described on page 416 of this issue by Martill *et al.* (*1*) brings fresh perspective to the debate. The aptly named *Tetrapodophis* combines a snakelike body with fore- and hindlimbs bearing five well-developed digits (see the illustration).

Snakelike bodies evolved several times through geological history. Among amniotes (reptiles, birds, and mammals), they occur only in Squamata, the group comprising lizards and snakes. Within Squamata, however, this body form has arisen independently at least 26 times (*2*) (see the figure). Body elongation is always correlated with limb reduction (*2*), and the forelimbs are usually lost first (*Bipes* and *Bachia* are rare exceptions). One explanation is that as the body lengthens, coordination of limb movements becomes increasingly difficult. Moreover, a serpentine body moves most effectively by lateral undulation, a movement in which limbs can become a hindrance, especially in narrow spaces. Researchers have identified a threshold body length at which limb

Department of Cell and Developmental Biology, University College London, London, UK. E-mail: s.e.evans@ucl.ac.uk

A four-limbed snake from the Cretaceous. Artist's impression of *Tetrapodophis*, which retains four limbs, each with five digits, in an elongated body with 160 precaudal vertebrae.

ILLUSTRATION: JULIUS CSTONYI

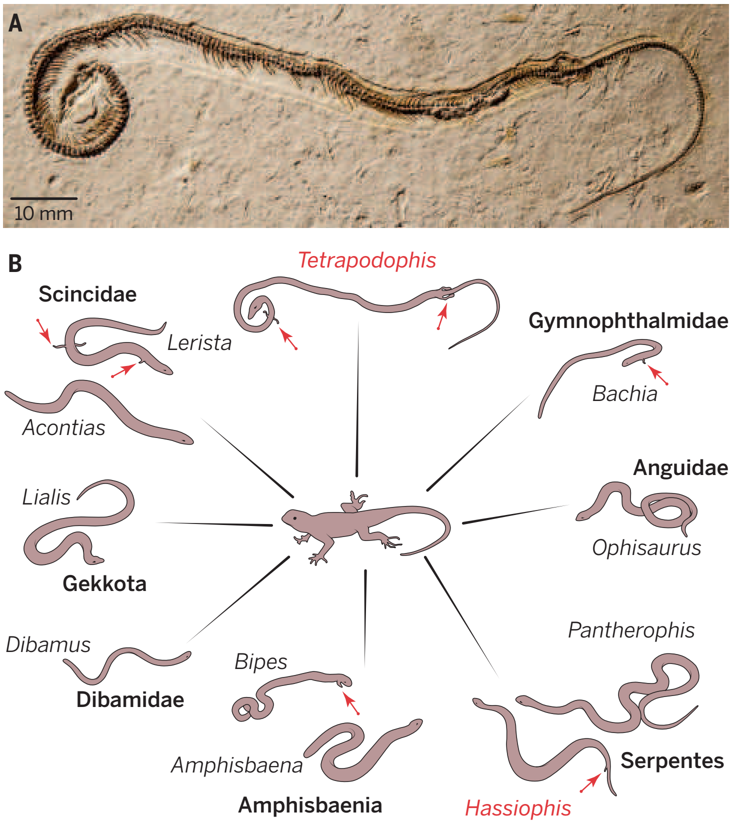

Limbs or no limbs. (**A**) Martill *et al*. report the discovery of a four-limbed snake, *Tetrapodophis amplectis*, from the Cretaceous. (**B**) Schematic showing independent development of the long bodied, limb-reduced body plan among squamates (not to scale).

reduction begins, and no known squamate with more than 70 precaudal (before-tail) vertebrae retains four complete limbs (*2*). *Tetrapodophis* (*1*), with around 160 precaudals, is therefore exceptional.

Efforts to reconstruct the evolutionary stages in the snake body plan are hampered by a lack of consensus on snake relationships and ancestral lifestyle. Analyses using molecular data group snakes with terrestrial lizards like iguanas and Komodo dragons (Iguania and Anguimorpha) (*3*) and generally hypothesize a burrowing or semiburrowing ancestry (*1*–*3*). However, some analyses that include anatomical characters place them with extinct Cretaceous (~100 to 66 million years ago) marine lizards, the mosasaurs (*3*, *4*). This has prompted the suggestion of a marine swimming ancestry for snakes (*4*).

Molecular divergence estimates date snake origins to the Jurassic (~150 million years ago) (*5*), but the earliest uncontested fossils are isolated vertebrae from the mid-Cretaceous (~113 million years ago) of North America (*5*). These vertebrae come from terrestrial deposits but are otherwise fairly uninformative. More instructive are several articulated skeletons or partial skeletons from slightly younger (~100 million-year-old) deposits. The largest set consists of several related marine snakes from the Middle East, North Africa, and southern Europe. These fossil snakes have 140 to 155 precaudal vertebrae and a short tail. They show no trace of forelimbs or shoulder girdle but do have small hindlimbs; only one [*Haasiophis* (*6*)] preserves digits. The relationships of these limbed marine snakes remain controversial, but many analyses (*1*, *3*, *6*, *7*) nest them among modern snakes, rather than nearer the base of the snake evolutionary tree. This implies either that hindlimbs were reduced more than once within snakes, or that the limbs redeveloped in some lineages (6).

A second set of early fossil snakes comes from terrestrial deposits in South America. The most complete, 95-million-year-old *Najash* (*7*), resembles the fossil marine snakes in having small hind legs without preserved digits but is more primitive (*1*, *7*). *Tetrapodophis* is also from South America, and from a deposit that yields a mix of freshwater and terrestrial species, but it is older (~113 million years old). Martill *et al.* (*1*) place it on the stem of the snake evolutionary tree, below *Najash* and close to another early terrestrial snake, the North American *Coniophis*, represented by vertebrae and attributed jaw elements.

Whereas fossils can yield information on the sequence of anatomical changes involved in any major transition, developmental biology helps to explain how these changes occurred. Evolution of the snake body form combined axial elongation, limb loss, and reduced regionalization (*8*, *9*). Whether and how these components are linked developmentally remains uncertain. In all vertebrate embryos, individual vertebrae develop from segments (somites) that form at regular intervals. To increase vertebral numbers, somite formation must either continue for longer or occur at a faster rate. Snakes use both strategies (*8*). Individual vertebrae then acquire positional identity along the body axis through the overlapping expression domains of *Hox* genes. In a typical tetrapod, the boundaries between major vertebral regions (such as the neck and the trunk) coincide with *Hox* gene expression boundaries.

In a pioneering study of *Python* development, Cohn and Tickle (*10*) reported a marked expansion of the typical Hox expression domains, particularly those normally associated with the neck-trunk boundary. They argued that the neck had been lost in snakes and that this loss disrupted the molecular signals required for forelimb positioning and outgrowth. However, in another snake, *Pantherophis*, the Hox expression domains, although expanded and without sharp boundaries, retain a regionalized pattern comparable to that of lizards with a distinct neck (*9*, *11*). A parallel study of vertebral anatomy across a wide range of snakes (*12*) revealed a similar regionalized pattern, implying that snakes have a neck of 10 to 12 segments.

Like that of a lizard, the vertebral column of *Tetrapodophis* has distinct regions, including 10 to 11 short-ribbed neck vertebrae adjacent to the tiny forelimbs. This neck length is within the range of some generalized terrestrial lizards and matches that proposed by the developmental (*9*, *11*) and anatomical (*12*) studies. Thus, as in long-bodied lizards, elongation of the snake skeleton occurred in the trunk region and not the neck. Moreover, if *Tetrapodophis* is correctly interpreted as a stem-snake, that elongation preceded loss of the forelimbs.

Love them or loathe them, snakes have long fascinated humans. The combined efforts of paleontology and developmental biology have gone some way toward unraveling the early history of snakes, but many questions remain as to their origins, relationships, character evolution, and ancestral lifestyle. Resolution of these questions depends, ultimately, on the recovery of further fossils and their thorough and objective analysis. ■

REFERENCES

1. D. M. Martill *et al.*, *Science* **349**, 416 (2015).
2. M. C. Brandley, J. P. Huelsenbeck, J. J. Wiens, *Evolution* **62**, 2042 (2008).
3. T. W. Reeder *et al.*, *PLOS ONE* **10**, e0118199 (2015).
4. M. W. Caldwell, *Zool. J. Linn. Soc.* **125**, 115 (1999).
5. J. J. Head, *Palaeontol. Electronica* **18**, 1 (2015).
6. E. Tchernov, O. Rieppel, H. Zaher, M. J. Polcyn, L. L. Jacobs, *Science* **287**, 2010 (2000).
7. S. Apesteguía, H. Zaher, *Nature* **440**, 1037 (2006).
8. C. Gomez *et al.*, *Nature* **454**, 335 (2008).
9. J. M. Woltering *et al.*, *Dev. Biol.* **332**, 82 (2009).
10. M. J. Cohn, C. Tickle, *Nature* **399**, 474 (1999).
11. N. Di-Poï *et al.*, *Nature* **464**, 99 (2010).
12. J. J. Head, P. D. Polly, *Nature* **520**, 86 (2015).

10.1126/science.aac5672

PHOTO: (A) D. M. MARTILL/UNIVERSITY OF PORTSMOUTH; ILLUSTRATION: (B) P. HUEY/SCIENCE

MICROBIAL ECOLOGY

Making methane down deep

Scientists find active life 2.5 km beneath the sea floor

By **Julie A. Huber**

The global ocean is Earth's largest biome, which extends into the sediments and igneous crust below the oceans. The abundance of microbial life beneath the sea floor is at least comparable to that in the oceans (*1*), but this biome remains poorly understood. The ramifications of a massive buried biosphere are important on a global scale, with sub–sea-floor microbes playing a crucial role in carbon sequestration, element cycles, and Earth's evolution, and likely encompassing staggering metabolic and genetic diversity. On page 420 of this issue, Inagaki *et al*. (*2*) report that even at almost 2.5 km beneath the sea floor, microbial life is not only present and compositionally distinct from that in shallower sediments, but also producing methane.

Investigations of sub–sea-floor life have tended to focus on marine sediments, which are relatively easy to collect and study compared to basement rocks and fluids. Advances in sampling techniques and contamination assessment (*3*), cell quantification (*4*), and biosignature detection (*5*) have expanded the ability to identify diverse microbial communities of Bacteria, Archaea, and even Eukarya in marine sediments at great depths (*6*). These methods have also helped to confirm the often very low metabolic activity of these microbes beneath the sea floor (*7*–*9*). Even in some of the most carbon-poor ocean sediments, small communities of oxygen-respiring organisms can persist for tens of millions of years (*10*, *11*). When Kallmeyer *et al*. included the cell concentrations from these energy-starved sediments in global estimates of sub–sea-floor sedimentary microbial abundance, they found that it was roughly equal to the microbial abundance in the oceans; variations in abundance were strongly correlated with sedimentation rate and distance from land (*1*). However, given the diversity of depositional settings and associated microbial life in the worlds' oceans, existing paradigms about what other environmental or biological properties or processes control the extent and variety of life in the sub–sea-floor are likely to evolve as new habitats are explored.

Inagaki *et al*. now extend our understanding of life deep within the sea floor by studying an unusual sequence of marine sediments in the Western Pacific continental margin offshore the Shimokita Peninsula of Japan. Using a riser drilling system aboard the research vessel R/V *Chikyu*, the deepest scientific borehole to date was drilled to examine the abundance, taxonomic composition, and biosignatures of sub–sea-floor microbial communities in sediments from 400 to almost 2500 m beneath the sea floor (see the figure). In this setting, coastal wetland sediments were moved offshore during subsidence and then buried by more typical marine sediments. Over 20 million years, organic-rich coal layers formed more than a kilometer deep in the sediments.

Using fluorescence image-based quantification, the authors detected microbial cells in every sample that they examined, down to less than 100 cells per gram of sediment. They then used a novel probability-based contamination correction to remove those organisms likely not to be indigenous sub–sea-floor residents. Based on this correction, the authors predict less than 1 cell per gram of sediment as some depths—the lowest cell abundances ever estimated for deep sediments.

However, depth is only part of the story. In coal-bed layers, cell abundances were higher, and multiple lines of isotopic and biomarker evidence indicate that methane in these layers has been generated by hydrogen-utilizing archaea. These results suggest that despite the low biomass levels in the deep sediments, cells persist, are active, and can potentially be stimulated by energy sources such as hydrogen or organic matter derived from the coal-bearing sediments. To further test whether methane-producing archaea were present in the coal layers, the authors enriched for these organisms in the laboratory using pulverized coal layers as the primary inoculum and energy source. They confirmed activity of the archaea via isotopic tracers and also identified a gene sequence affiliated with methanogens, providing additional support for the suggestion that deeply buried microbes are using energy in the coal

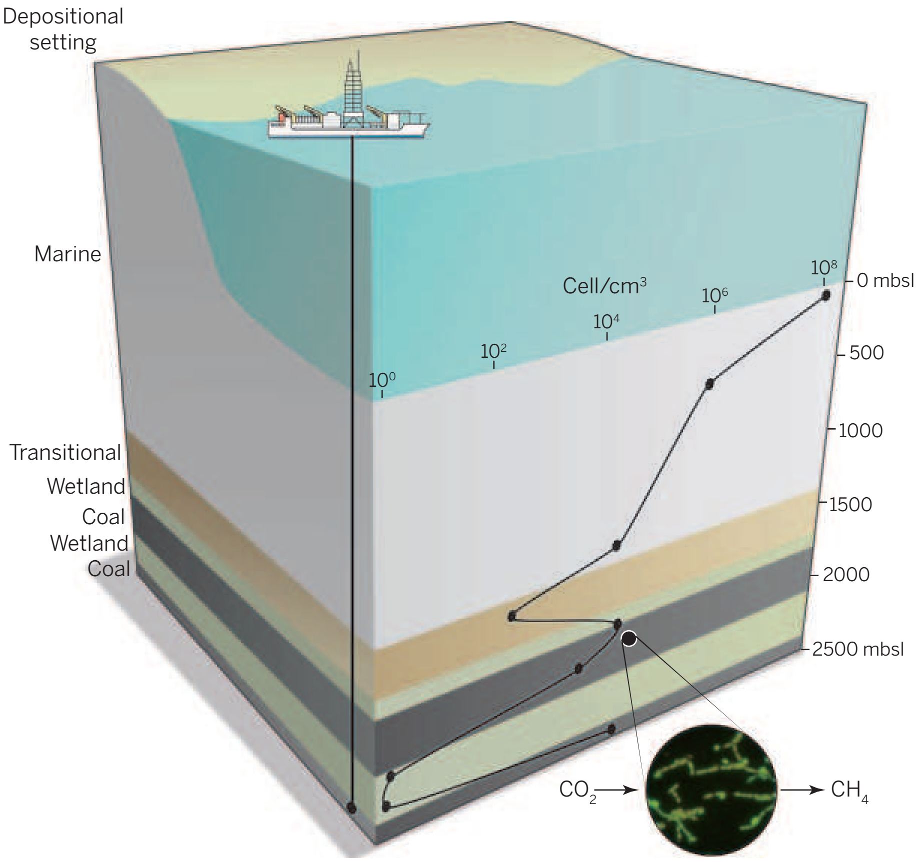

Life at depth. Inagaki *et al*. have found microbial cells in samples at depths of 400 to 2500 m in the world's deepest scientific borehole at the Shimokita Peninsula of Japan. Cell counts rise in coal beds associated with deeply buried coastal wetland sediments. Methane in the coal beds bears a biological signature, suggesting active microbial life.

ILLUSTRATION: P. HUEY/SCIENCE

Josephine Bay Paul Center, Marine Biological Laboratory, Woods Hole, MA 02543, USA. E-mail: jhuber@mbl.edu

layers to make methane.

Molecular analysis of the deeply buried coastal wetland sediments indicates that they are taxonomically distinct from microbial communities in shallower (less than 400 m below sea level) marine sediments. The latter are the most commonly studied part of the sub–sea floor. The sequences obtained from the deep habitats instead bear similarity to those seen in wetland and forest soils. It remains unclear whether these deep communities retain the community structure of the original depositional setting or have been selected for under sub–sea-floor conditions over millions of years. Future studies should explore what physiological and metabolic features, if any, are selected for in those deeply buried organisms that enable them to survive and metabolize.

Inagaki *et al.*'s results extend the depth of the marine deep biosphere, but they do not reach the limits; organisms were detected in all samples via microscopy, DNA, or other biomarkers. This is perhaps not surprising given that temperatures never exceeded ~60°C, well within the growth range of many microbes, and that both hydrogen and carbon are plentiful energy sources, particularly in the coal-bed layers. Why so little, life, then? Is it difficulties with biomolecule repair, as the authors suggest, or something else like porosity or pressure? Uncovering what limits the biomass in this unusual environment will certainly be a focus of future studies. Genomic reconstruction of the organisms in the different depositional layers may also help to reveal whether deeply buried microorganisms harbor fundamental traits that differ significantly from those of their shallow or terrestrial counterparts.

Marine sediments are the best-explored biome in Earth's subsurface, and Inagaki *et al.*'s report marks the deepest detection of active life to date. However, we have barely scratched the surface of the igneous crust beneath those sediments to determine the extent and diversity of life in the rocks and the fluids that move through the sea floor. We still have a long way to go in uncovering and understanding microbial life deep beneath the sea floor. ■

REFERENCES

1. J. Kallmeyer, R. Pockalny, R. R. Adhikari, D. C. Smith, S. D'Hondt, *Proc. Natl. Acad. Sci. U.S.A.* **109**, 16213 (2012).
2. F. Inagaki *et al.*, *Science* **349**, 420 (2015).
3. F. Inagaki *et al.*, *Integr. Ocean Drill. Progr. Prelim. Rep.* **337** (2013).
4. Y. Morono *et al.*, *ISME J.* **3**, 503 (2009).
5. D. A. Stolper *et al*, *Science* **344**, 1500 (2014).
6. M.-C. Ciobanu *et al.*, *ISME J.* **8**, 1370 (2014).
7. W. D. Orsi *et al.*, *Nature* **499**, 205 (2013).
8. S. D'Hondt *et al.*, *Science* **295**, 2067 (2002).
9. R. J. Parkes *et al.*, *Nature* **436**, 390 (2005).
10. H. Røy *et al.*, *Science* **336**, 922 (2012).
11. S. D'Hondt *et al.*, *Nat. Geosci.* **8**, 299 (2015).

10.1126/science.aac6673

IMMUNOLOGY

Moving CTLA-4 from the trash to recycling

Individuals lacking a protein expressed in T cells have low CTLA-4 and develop autoimmunity

By **David M. Sansom**

To prevent immune responses to our own bodies, a series of immune checkpoints exist. Cytotoxic T lymphocyte antigen–4 (CTLA-4) operates the earliest checkpoint controlling whether or not T cells respond to antigen. Manipulation of CTLA-4 has recently gained enormous attention in the field of tumor immunotherapy (*1*). However, in its day-to-day activities, CTLA-4 prevents autoimmune targeting of tissues (*2*), though the precise mechanism of action and critical controls influencing CTLA-4 function are still emerging. On page 436 in this issue, Lo *et al.* (*3*) provide evidence that an intracellular protein, lipopolysaccharide-responsive and beige-like anchor protein (LRBA) controls CTLA-4 expression and thereby influences immune self-tolerance.

T and B lymphocytes possess a vast array of antigen-specific receptors designed to recognize constantly changing microbial challenges. One consequence of this immense flexibility of target recognition is the ever-present threat of unintentionally targeting our own tissues. Because this problem cannot be solved by simply restricting target recognition (*4*), a series of regulatory checkpoints exist that determine whether immune responses ensue following antigen recognition. Principal among these is an elaborate system involving two related receptors (CD28 and CTLA-4) on T cells that share two ligands (CD80 and CD86) on antigen-presenting cells (*5*). Interaction of CD28 expressed on the surface of conventional T cells with its ligands "costimulates" T cell responses, in conjunction with antigen recognition, via the T cell receptor. This is critical for T cell activation (which in turn also helps antibody production by B cells). By contrast, CTLA-4 acts as a negative regulator whose functional impact appears to be predominantly (but not exclusively) mediated via regulatory T (T_{reg}) cells (*2*, *6*).

Loss of T_{reg} cells due to mutations in the transcription factor Foxp3 causes the early-onset autoimmune syndrome immunodysregulation, polyendocrinopathy, and enteropathy, X-linked (IPEX) (*7*). Recently, heterozygous mutations in CTLA-4 have been reported that also result in T_{reg} cell impairment and immune dysregulation with some similarities to IPEX, albeit with later onset and incomplete penetrance (*8*, *9*). Lo *et al.* report that patients with biallelic disruption of LRBA also develop early-onset autoimmunity. Somewhat surprisingly, both CTLA-4 and LRBA mutations were identified within cohorts of patients suffering from common variable immune deficiency (CVID) due to accompanying defects in antibody production. Although LRBA deficiency has previously been recognized as having similarities to IPEX (*10*), Lo *et al.* directly link

> ***"...interaction between CTLA-4 and LRBA appears to occur in recycling endosomes (expressing the marker Rab11), suggesting that LRBA rescues CTLA-4 from entering the lysosome..."***

LRBA to CTLA-4 expression and function, thereby demonstrating its role in controlling a major pathway of T_{reg} cell function.

CTLA-4 is continually internalized by T cells via endocytosis, and is predominantly found in intracellular compartments. Its endocytosis is driven by an interaction with the clathrin adaptor protein–2 (AP-2) complex and like many endocytic proteins, after internalization, CTLA-4 can be either recycled back to the plasma membrane or targeted for degradation in lysosomes (*11*). The purpose of this intracellular behavior remained elusive until it was found that CTLA-4 can physically capture and remove its ligands from antigen-presenting cells, subsequently degrading them in lysosomes—a process called transendocytosis (*12*). This suggests a mechanism whereby CTLA-4 suppresses

Institute of Immunity and Transplantation, University College London, Royal Free Hospital, London, UK. E-mail: d.sansom@ucl.ac.uk

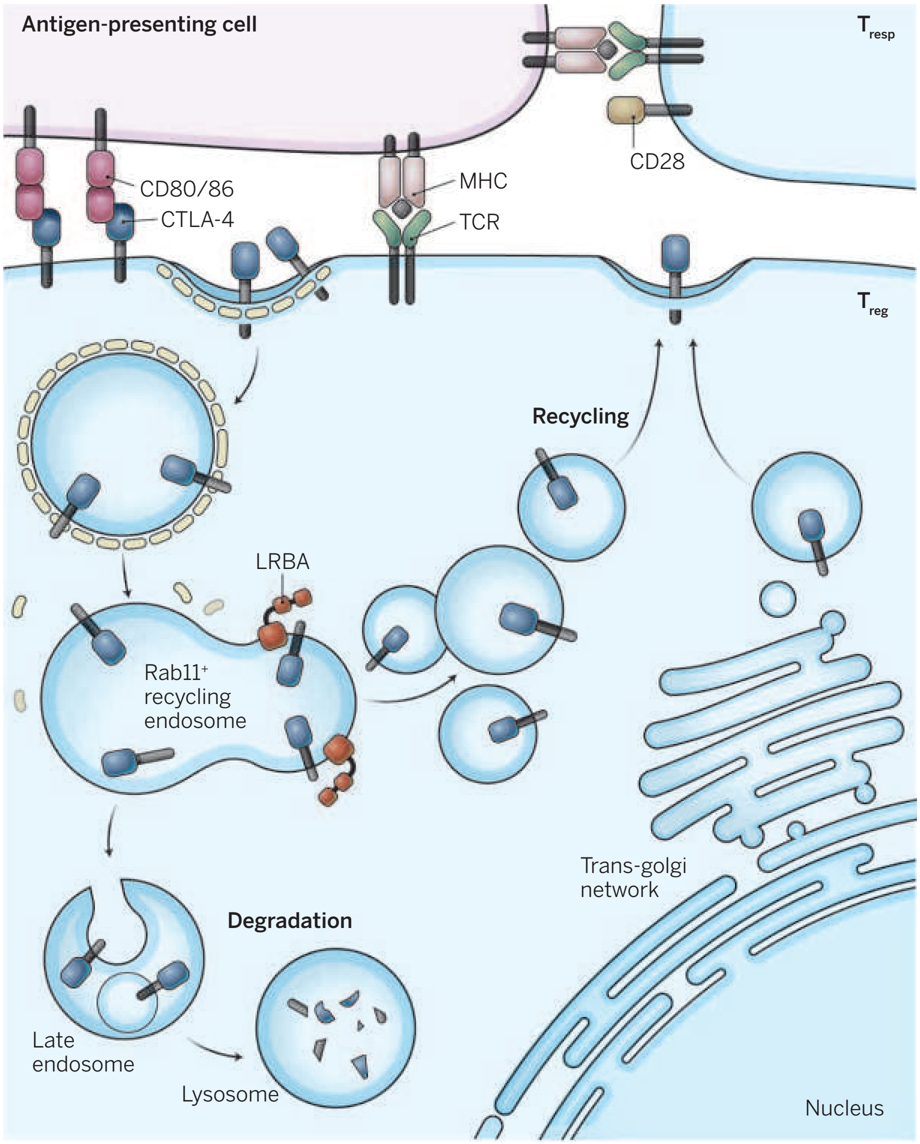

Directing traffic. CTLA-4 is constitutively internalized from the surface of T_{reg} cells in clathrin-coated pits, and encounters LRBA in recycling endosomes. Interaction with LRBA rescues CTLA-4 from a lysosomal fate, thereby maintaining high amounts of CTLA-4 trafficking to the cell surface for ligand (CD80 and CD86) removal. Effective ligand removal from the antigen-presenting cell restricts CD28 costimulation of conventional T cells, maintaining immune self-tolerance. MHC, major histocompatibility complex; TCR, T cell receptor; T_{resp}, responder T cell.

T cell responses by controlling ligand availability for CD28. Accordingly, where CTLA-4 is present in sufficient amounts, ligand levels on antigen-presenting cells are restrained and CD28 costimulation is limited. By contrast, where ligand removal by CTLA-4 is insufficient, or in settings where ligand expression is increased, T cell activation is triggered. Thus, the amount of CTLA-4 available at the cell surface appears crucial in preventing costimulation of T cells that possess self-reactive T cell receptors (*13*).

So how does LRBA influence CTLA-4? Lo *et al.* show that loss of LRBA substantially increases degradation of CTLA-4 in lysosomes, revealed by the use of lysosomal inhibitors such as chloroquine. This interaction between CTLA-4 and LRBA appears to occur in recycling endosomes (expressing the marker Rab11), suggesting that LRBA rescues CTLA-4 from entering the lysosome pathway and likely increases its recycling (see the figure). The authors further show that this interaction requires a specific Tyr-Val-Lys-Met (YVKM) motif in the CTLA-4 cytoplasmic domain. There is still relatively little information on the precise function of LRBA. However, the data strongly suggest that it is a scaffold or adaptor protein involved in vesicle traffic—its large size, multidomain architecture, intracellular localization, and homology to trafficking-related proteins support such a role (*14*, *15*). Thus, loss of LRBA allows routing of CTLA-4 to lysosomes, impairing CTLA-4–dependent T_{reg} cell function, consistent with the IPEX-like features seen in patients lacking LRBA.

Strikingly, patients with LRBA deficiency respond well to abatacept. This drug is a fusion protein containing the extracellular domain of CTLA-4. By binding to CD80 and CD86, abatacept blocks the availability of these ligands for CD28. Abatacept, in effect, replaces natural CTLA-4 function, with the caveat that CD80 and CD86 ligands are covered up by the drug rather than physically removed from the surface of antigen-presenting cells. Responsiveness to abatacept also provides insight as to whether memory T cells require costimulation via CD28. Upon re-exposure to an antigen, memory T cells rapidly initiate cell-mediated immunity. Patients lacking LRBA have highly expanded subsets of memory T cells, yet respond to abatacept with a reduction in this population.

Studies on LRBA and CTLA-4 deficiency highlight the finely balanced and quantitative nature of the CTLA-4 immune checkpoint. As identified by Lo *et al.*, the degree of loss of LRBA correlates with the defect in CTLA-4 expression, potentially resulting in variability in disease outcome and suggesting the possibility that heterozygous mutations in LRBA may also predispose to autoimmunity. Similarly, some individuals with heterozygous *CTLA-4* mutations remain healthy whereas others succumb to disease (*8*, *9*), indicating that interactions with other genes (e.g., *LRBA*) or environmental factors affect this "tipping point." Accordingly, insights from these single-gene defects bring into focus how multiple subtle expression changes in the same pathways can, in aggregate, confer important functional effects, as is likely to be the case in the development of more common autoimmune diseases such as type I diabetes and rheumatoid arthritis. ■

REFERENCES

1. P. Sharma, J. P. Allison, *Science* **348**, 56 (2015).
2. L. S. Walker, D. M. Sansom, *Nat. Rev. Immunol.* **11**, 852 (2011).
3. B. Lo *et al.*, *Science* **349**, 436 (2015).
4. K. A. Hogquist, S. C. Jameson, *Nat. Immunol.* **15**, 815 (2014).
5. H. Bour-Jordan *et al.*, *Immunol. Rev.* **241**, 180 (2011).
6. K. Wing *et al.*, *Science* **322**, 271 (2008).
7. E. d'Hennezel, K. Bin Dhuban, T. Torgerson, C. A. Piccirillo, *J. Med. Genet.* **49**, 291 (2012).
8. D. Schubert *et al.*, *Nat. Med.* **20**, 1410 (2014).
9. H. S. Kuehn *et al.*, *Science* **345**, 1623 (2014).
10. L. M. Charbonnier *et al.*, *J. Allergy Clin. Immunol.* **135**, 217 (2015).
11. O. S. Qureshi *et al.*, *J. Biol. Chem.* **287**, 9429 (2012).
12. O. S. Qureshi *et al.*, *Science* **332**, 600 (2011).
13. W. Ise *et al.*, *Nat. Immunol.* **11**, 129 (2010).
14. J. W. Wang, J. Howson, E. Haller, W. G. Kerr, *J. Immunol.* **166**, 4586 (2001).
15. A. R. Cullinane, A. A. Schäffer, M. Huizing, *Traffic* **14**, 749 (2013).

10.1126/science.aac7888

CHEMISTRY

Catalysts by Platonic design

Sophisticated shape-controlled design is yielding ever more active nanocatalysts

By **Peter Strasser**

Around 360 BCE, in his work *Timaeus*, the Greek philosopher Plato elaborated on the four elements as the basic components of our cosmos: earth, water, air, and fire. He argued that each element consists of small, highly symmetric corpuscles—the cube for earth, the tetrahedron for fire, the icosahedron for water, and the octahedron for air. The faces of the latter three corpuscles consist of equilateral triangles, which—according to Plato—allows air, water, and fire to interconvert. Plato would likely be thrilled to learn that, as recently confirmed by Huang *et al.* (*1*), nanoscale Pt-Ni octahedra are the catalytically most active known material for converting air (molecular oxygen) into water and fire (thermal energy). On page 412 of this issue, Zhang *et al.* (*2*) show that octahedral and cubic hollow shells of just a few atomic Pt layers are also versatile catalysts, with the octahedral shells particularly active for oxygen reduction. Such tiny metallic octahedra may one day become the building blocks of electrodes for electrochemical energy conversion.

The electrochemical process of reducing molecular oxygen to water, i.e., the oxygen reduction reaction (ORR), follows

$$O_2 + 4H^+ + 4e^- \rightarrow H_2O,\ \Delta E^0 = +1.23\ V_{SHE}$$

where ΔE^0 is the standard half-cell potential. This conversion poses a fundamental scientific challenge for electrochemical energy conversion and storage. As a four-electron process, the ORR is slowed down by kinetic energy barriers between the reactive chemical intermediates (*3*). In 2007, Stamenkovic *et al.* reported exceptionally high catalytic ORR reactivity for a thermally annealed Pt-Ni alloy surface with a well-defined (111) orientation (*4*). Since then, many groups have tried to design nanoscale Pt-Ni alloy particles with octahedral shapes, which exclusively expose (111)–oriented surface facets. Such Pt-Ni nano-octahedra should maximize the catalyst performance/cost ratio (*4–6*).

The race for catalytically active nano-octahedra (*7–11*) quickly reached performance/cost ratios 30 times higher than those of Pt benchmark catalysts (see the first figure) (*12*). But in 2014, Chen *et al.* reported the discovery of an even more active familiy of catalysts consisting of nickel-depleted Pt-Ni nanoframe catalysts (*13*). Their Pt performance/cost ratios exceeded that of conventional Pt catalysts by a factor of almost 60.

The nanoframes held on to the ORR activity record for about 12 months before being overtaken again by Pt-Ni nano-octahedra. In *Science* recently, Huang *et al.* (*1*) report preparation and ORR reactivity of bimetallic Pt-Ni nano-octahedra doped with d-block metals. The performance/cost ratios of molybdenum-doped Pt-Ni nano-octahedra with about 8-nm edge length (see the second figure, panel A) were almost 70 times higher than those of benchmark Pt catalysts.

The origin of the exceptional performance of surface-doped nano-octahedra, as well as the spatial elemental distribution of Pt, Ni, and Mo atoms, remains elusive. However, computational data suggest that Mo atoms under oxygen atmospheres prefer surface sites near the vertices of the nano-octahedra. There, they are believed to modify the binding strength of reactive intermediates while forming stable Mo-Pt and Mo-Ni bonds (*1*).

Zhang *et al.* now report the synthesis of catalytically active octahedral and cubic Pt nanoparticles. The nanoparticles are not solid but instead are hollow nanocages entirely enclosed by either {111} facets (octahedra, see the second figure, panel B) or {100} facets (cubic particles). Unlike earlier studies on shape-selected Pt-Pd bimetallic core-shell nanoparticles (*14*), the authors managed to carefully dissolve the metallic core without compromising the well-defined thickness and composition of a Pt shell that is a mere atomic layer thick. The study provides experimental and computational insights into the atomic-scale mechanism by which the Pd metal atoms dissolve across angstrom-scale vacancies formed by initial Pd dissolution.

What is more, the authors show that the nanocages are catalytically active. They pick the ORR to compare the catalytic efficacy of the hollow Pt cubes and octahedra. Catalytic activities are higher for the eight-faceted hollow octahedra than for the cubes, although the absolute activity of both significantly trails that of solid Pt-Ni octahedra (*1*).

The studies in (*1*, *2*) testify to the high level of control and craftsmanship that now exist in chemical preparation of nanoscale metal particles with defined three-dimensional shape. They highlight the opportunities offered by harnessing the geometric structure sensitivity of catalysts. Future investigations

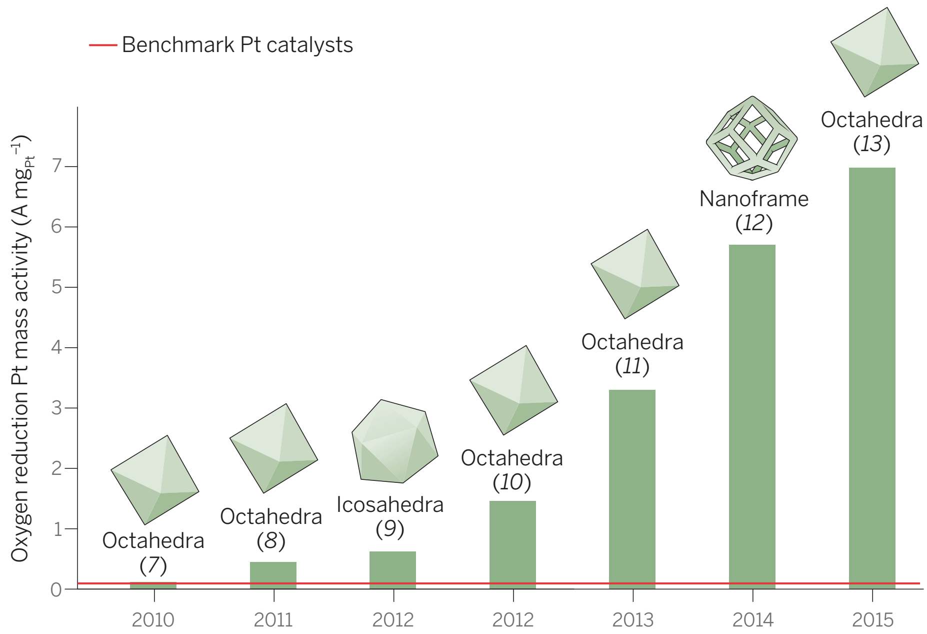

Going from strength to strength. Ever rising performance/cost ratios for Pt nanoparticles with octahedral shapes.

ILLUSTRATION: ADAPTED BY P. HUEY/SCIENCE

Department of Chemistry, Chemical Engineering Division, Technical University Berlin, Berlin 10623, Germany. E-mail: pstrasser@tu-berlin.de

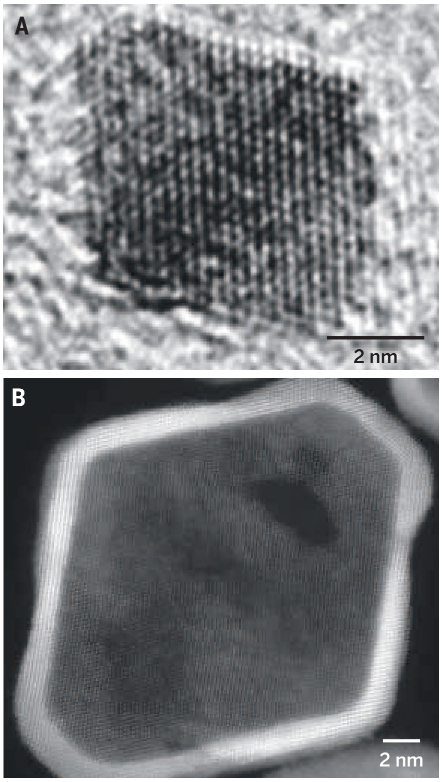

The importance of being octahedral. Huang *et al.* (*1*) recently showed that molybdenum-doped Pt-Ni nanoparticles with octahedral shapes (**A**) are highly active catalysts for the conversion of molecular oxygen to water. Zhang *et al*. have created hollow Pt octahedra (**B**) that are also catalytically active for this reaction.

of the morphological and compositional stability of shaped catalysts under realistic conditions will show whether the octahedral shapes can compete with their dealloyed cuboctahedral Pt-Ni core-shell alloy siblings (*15*). The latter have surpassed the U.S. Department of Energy Commercialization targets of 2017 for stability and activity under realistic fuel cell conditions, showing higher stability but lower activity than the octahedra (*16*). Such tests remain to be done for the octahedra to show if they can be used in applications such as fuel cells or air batteries. ■

REFERENCES

1. X. Huang *et al.*, *Science* **348**, 1230 (2015).
2. L. Zhang *et al.*, *Science* **349**, 412 (2015).
3. I. E. L. Stephens *et al.*, *Energy Environ. Sci.* **5**, 6744 (2012).
4. V. R. Stamenkovic *et al.*, *Science* **315**, 493 (2007).
5. H. A. Gasteiger, N. M. Marković, *Science* **324**, 48 (2009).
6. L. Gan *et al.*, *Science* **346**, 1502 (2014).
7. J. Wu *et al.*, *J. Am. Chem. Soc.* **132**, 4984 (2010).
8. J. Zhang *et al.*, *Nano Lett.* **10**, 638 (2010).
9. J. Wu, A. Gross, H. Yang, *Nano Lett.* **11**, 798 (2011).
10. C. Cui *et al.*, *Nano Lett.* **12**, 5885 (2012).
11. C. Cui *et al.*, *Nat. Mater.* **12**, 765 (2013).
12. S.-I. Choi *et al.*, *Nano Lett.* **13**, 3420 (2013).
13. C. Chen *et al.*, *Science* **343**, 1339 (2014).
14. X. Wang *et al.*, *Nat. Commun.* **6**, 10.1038/ncomms8594 (2015).
15. L. Gan *et al.*, *Nano Lett.* **13**, 1131 (2013).
16. B. H. Han *et al. Energy, Environ. Sci.* **8**, 258 (2015).

10.1126/science.aac7861

GENE REGULATION

Breakers and blockers—miRNAs at work

MicroRNAs mediate silencing through messenger RNA degradation and translation repression

By **Elisa Izaurralde**

MicroRNAs (miRNAs) are small, ~22-nucleotide-long noncoding RNAs. They silence the expression of messenger RNAs (mRNAs) containing complementary sequences (*1*). The human genome encodes ~1500 miRNAs, each with the potential to bind hundreds of different mRNAs (*1*). miRNAs regulate many biological processes, and the dysregulation of their expression is linked to various human diseases, including cancer (*1*). To exert their repressive function, miRNAs associate with the Argonaute family of proteins (AGOs) to form the core of miRNA-induced silencing complexes (miRISCs) (*1*) (see the figure). In animals, miRISCs silence mRNA expression at two levels, by preventing protein production (translation) and inducing mRNA degradation. Over the past decade, progress has been made in our understanding of the mechanism by which miRISCs induce mRNA degradation, but the question of how miRISCs repress translation remains elusive.

miRISCs were originally thought to repress protein synthesis without detectable changes in mRNA abundance. However, work from many laboratories has established that miRISCs degrade their mRNA targets, thereby reducing protein synthesis, at least in part, indirectly (*1–3*). Nevertheless, the possibility that a fraction of targets were regulated only at the translational level without changes in mRNA levels could not be ruled out, raising concerns that an unknown fraction of targets would be overlooked if only mRNA levels were monitored (*2*, *3*). Mechanistically, mRNA degradation was thought to represent a secondary effect of the inhibition of translation, with the primary effect of the miRISC being interference with protein synthesis.

These issues have been in part addressed with the advent of ribosome profiling, which maps the position of translating ribosomes on mRNAs at a global level (*2*, *3*). Ribosome profiling analyses combined with simultaneous detection of mRNA amounts did not yield evidence of a large number of targets that are regulated exclusively at the translational level. These studies revealed that mRNA degradation is the dominant effect of miRNA-mediated regulation at steady state, accounting for most (66 to 90%) of the repression observed in cultured mammalian cells (*2*, *3*).

The mechanism by which miRNAs degrade their mRNA targets occurs through a cellular pathway—the 5′-to-3′ mRNA decay pathway—which also degrades bulk mRNA (*1*). miRISCs recruit the cellular machinery involved in this pathway to the mRNA target, thereby accelerating its degradation. mRNA degradation is initiated by deadenylation, the removal of the polyadenylate tail at the 3′ end of the mRNA. Deadenylation is catalyzed by the consecutive action of two deadenylase complexes: the PAN2-PAN3 complex and the CCR4-NOT complex (see the figure). Following deadenylation, the cap structure that protects the mRNA 5′ end is removed by the decapping enzyme DCP2 in complex with additional cofactors. Decapping makes the mRNA 5′ end accessible to the major cytoplasmic exonuclease XRN1 that degrades the mRNA from the 5′ end (*1*, *4–6*).

The Argonaute proteins of the miRISC recruit the two deadenylase complexes to the mRNA. They do so indirectly, through their interaction with a protein of the GW182 family (*1*, *4–6*). GW182 proteins (also known as TNRC6 proteins in vertebrates) are conserved in animals. These proteins are mainly unstructured and contain multiple glycine (G) tryptophan (W) repeats. They use these repeats to bind to Argonaute proteins and subunits of the PAN2-PAN3 and the CCR4-NOT deadenylase complexes, thereby bridging their interaction (*4–6*).

Structures of human Argonaute-2 (AGO2) bound to miRNAs (*7*), as well as of AGO2 and subunits of the deadenylase complexes (PAN3 and NOT9) bound to tryptophan residues (*8–10*), have revealed how miRISCs recognize target mRNA, and subsequently how GW182 proteins bridge the interaction between Argonaute proteins and the

Department of Biochemistry, Max Planck Institute for Developmental Biology, Spemannstrasse 35, D-72076 Tübingen, Germany. E-mail: elisa.izaurralde@tuebingen.mpg.de

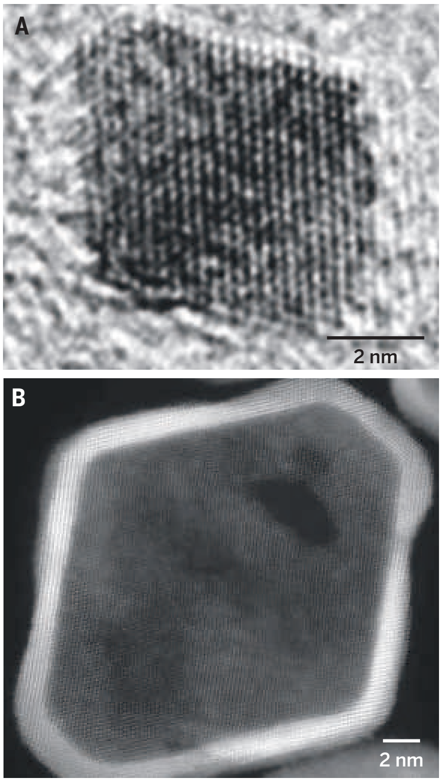

The importance of being octahedral. Huang *et al.* (*1*) recently showed that molybdenum-doped Pt-Ni nanoparticles with octahedral shapes (**A**) are highly active catalysts for the conversion of molecular oxygen to water. Zhang *et al*. have created hollow Pt octahedra (**B**) that are also catalytically active for this reaction.

of the morphological and compositional stability of shaped catalysts under realistic conditions will show whether the octahedral shapes can compete with their dealloyed cuboctahedral Pt-Ni core-shell alloy siblings (*15*). The latter have surpassed the U.S. Department of Energy Commercialization targets of 2017 for stability and activity under realistic fuel cell conditions, showing higher stability but lower activity than the octahedra (*16*). Such tests remain to be done for the octahedra to show if they can be used in applications such as fuel cells or air batteries. ■

REFERENCES

1. X. Huang *et al.*, *Science* **348**, 1230 (2015).
2. L. Zhang *et al.*, *Science* **349**, 412 (2015).
3. I. E. L. Stephens *et al.*, *Energy Environ. Sci.* **5**, 6744 (2012).
4. V. R. Stamenkovic *et al.*, *Science* **315**, 493 (2007).
5. H. A. Gasteiger, N. M. Marković, *Science* **324**, 48 (2009).
6. L. Gan *et al.*, *Science* **346**, 1502 (2014).
7. J. Wu *et al.*, *J. Am. Chem. Soc.* **132**, 4984 (2010).
8. J. Zhang *et al.*, *Nano Lett.* **10**, 638 (2010).
9. J. Wu, A. Gross, H. Yang, *Nano Lett.* **11**, 798 (2011).
10. C. Cui *et al.*, *Nano Lett.* **12**, 5885 (2012).
11. C. Cui *et al.*, *Nat. Mater.* **12**, 765 (2013).
12. S.-I. Choi *et al.*, *Nano Lett.* **13**, 3420 (2013).
13. C. Chen *et al.*, *Science* **343**, 1339 (2014).
14. X. Wang *et al.*, *Nat. Commun.* **6**, 10.1038/ncomms8594 (2015).
15. L. Gan *et al.*, *Nano Lett.* **13**, 1131 (2013).
16. B. H. Han *et al. Energy, Environ. Sci.* **8**, 258 (2015).

10.1126/science.aac7861

GENE REGULATION

Breakers and blockers—miRNAs at work

MicroRNAs mediate silencing through messenger RNA degradation and translation repression

By **Elisa Izaurralde**

MicroRNAs (miRNAs) are small, ~22-nucleotide-long noncoding RNAs. They silence the expression of messenger RNAs (mRNAs) containing complementary sequences (*1*). The human genome encodes ~1500 miRNAs, each with the potential to bind hundreds of different mRNAs (*1*). miRNAs regulate many biological processes, and the dysregulation of their expression is linked to various human diseases, including cancer (*1*). To exert their repressive function, miRNAs associate with the Argonaute family of proteins (AGOs) to form the core of miRNA-induced silencing complexes (miRISCs) (*1*) (see the figure). In animals, miRISCs silence mRNA expression at two levels, by preventing protein production (translation) and inducing mRNA degradation. Over the past decade, progress has been made in our understanding of the mechanism by which miRISCs induce mRNA degradation, but the question of how miRISCs repress translation remains elusive.

miRISCs were originally thought to repress protein synthesis without detectable changes in mRNA abundance. However, work from many laboratories has established that miRISCs degrade their mRNA targets, thereby reducing protein synthesis, at least in part, indirectly (*1*–*3*). Nevertheless, the possibility that a fraction of targets were regulated only at the translational level without changes in mRNA levels could not be ruled out, raising concerns that an unknown fraction of targets would be overlooked if only mRNA levels were monitored (*2*, *3*). Mechanistically, mRNA degradation was thought to represent a secondary effect of the inhibition of translation, with the primary effect of the miRISC being interference with protein synthesis.

These issues have been in part addressed with the advent of ribosome profiling, which maps the position of translating ribosomes on mRNAs at a global level (*2*, *3*). Ribosome profiling analyses combined with simultaneous detection of mRNA amounts did not yield evidence of a large number of targets that are regulated exclusively at the translational level. These studies revealed that mRNA degradation is the dominant effect of miRNA-mediated regulation at steady state, accounting for most (66 to 90%) of the repression observed in cultured mammalian cells (*2*, *3*).

The mechanism by which miRNAs degrade their mRNA targets occurs through a cellular pathway—the 5′-to-3′ mRNA decay pathway—which also degrades bulk mRNA (*1*). miRISCs recruit the cellular machinery involved in this pathway to the mRNA target, thereby accelerating its degradation. mRNA degradation is initiated by deadenylation, the removal of the polyadenylate tail at the 3′ end of the mRNA. Deadenylation is catalyzed by the consecutive action of two deadenylase complexes: the PAN2-PAN3 complex and the CCR4-NOT complex (see the figure). Following deadenylation, the cap structure that protects the mRNA 5′ end is removed by the decapping enzyme DCP2 in complex with additional cofactors. Decapping makes the mRNA 5′ end accessible to the major cytoplasmic exonuclease XRN1 that degrades the mRNA from the 5′ end (*1*, *4*–*6*).

The Argonaute proteins of the miRISC recruit the two deadenylase complexes to the mRNA. They do so indirectly, through their interaction with a protein of the GW182 family (*1*, *4*–*6*). GW182 proteins (also known as TNRC6 proteins in vertebrates) are conserved in animals. These proteins are mainly unstructured and contain multiple glycine (G) tryptophan (W) repeats. They use these repeats to bind to Argonaute proteins and subunits of the PAN2-PAN3 and the CCR4-NOT deadenylase complexes, thereby bridging their interaction (*4*–*6*).

Structures of human Argonaute-2 (AGO2) bound to miRNAs (*7*), as well as of AGO2 and subunits of the deadenylase complexes (PAN3 and NOT9) bound to tryptophan residues (*8*–*10*), have revealed how miRISCs recognize target mRNA, and subsequently how GW182 proteins bridge the interaction between Argonaute proteins and the

Department of Biochemistry, Max Planck Institute for Developmental Biology, Spemannstrasse 35, D-72076 Tübingen, Germany. E-mail: elisa.izaurralde@tuebingen.mpg.de

deadenylase complexes. Thus, we can now describe in molecular terms a chain of direct interactions leading all the way from miRNA target recognition to mRNA deadenylation, decapping, 5′-to-3′ mRNA degradation, and eventually translational repression (*7–10*). Additionally, these structural studies have definitively shown that miRISC actively recruits mRNA degradation factors and thus that mRNA destabilization is a primary effect of silencing.

"Pure" translational repression (that cannot be explained by mRNA degradation) is thought to account for 6 to 26% of the repression of each endogenous target in mammalian cells (*2*, *3*). However, the precise translation-repressive mechanism remains poorly understood.

Ribosomal profiling has been instrumental in simplifying our understanding of silencing by excluding models invoking inhibition of translation elongation, as well as models involving protein degradation. These and additional studies have implicated initiation and the eukaryotic translation initiation factor eIF4A as the target for miRISC inhibition (*2*, *3*, *11–13*). eIF4A has two paralogs involved in translation in vertebrates: eIF4A1 and eIF4A2 (*11–13*). eIF4A proteins are RNA helicases that unwind secondary structures within the mRNA 5′ untranslated regions (UTRs), allowing the small ribosomal subunit, in association with initiation factors, to scan the 5′ UTR in search of the AUG start codon. Thus, interfering with eIF4A function is likely to reduce or inhibit the initiation of protein synthesis.

However, there is debate regarding how this interference is achieved. In one model, miRISC recruits and locks eIF4A2 on the mRNA 5′ UTR, forming a "roadblock" for scanning ribosomes (*13*). A second model proposes that miRISC dislodges eIF4A1 and eIF4A2 from the silenced mRNA (*11*, *12*). Both models imply that miRNAs can only repress mRNAs that are translated via a

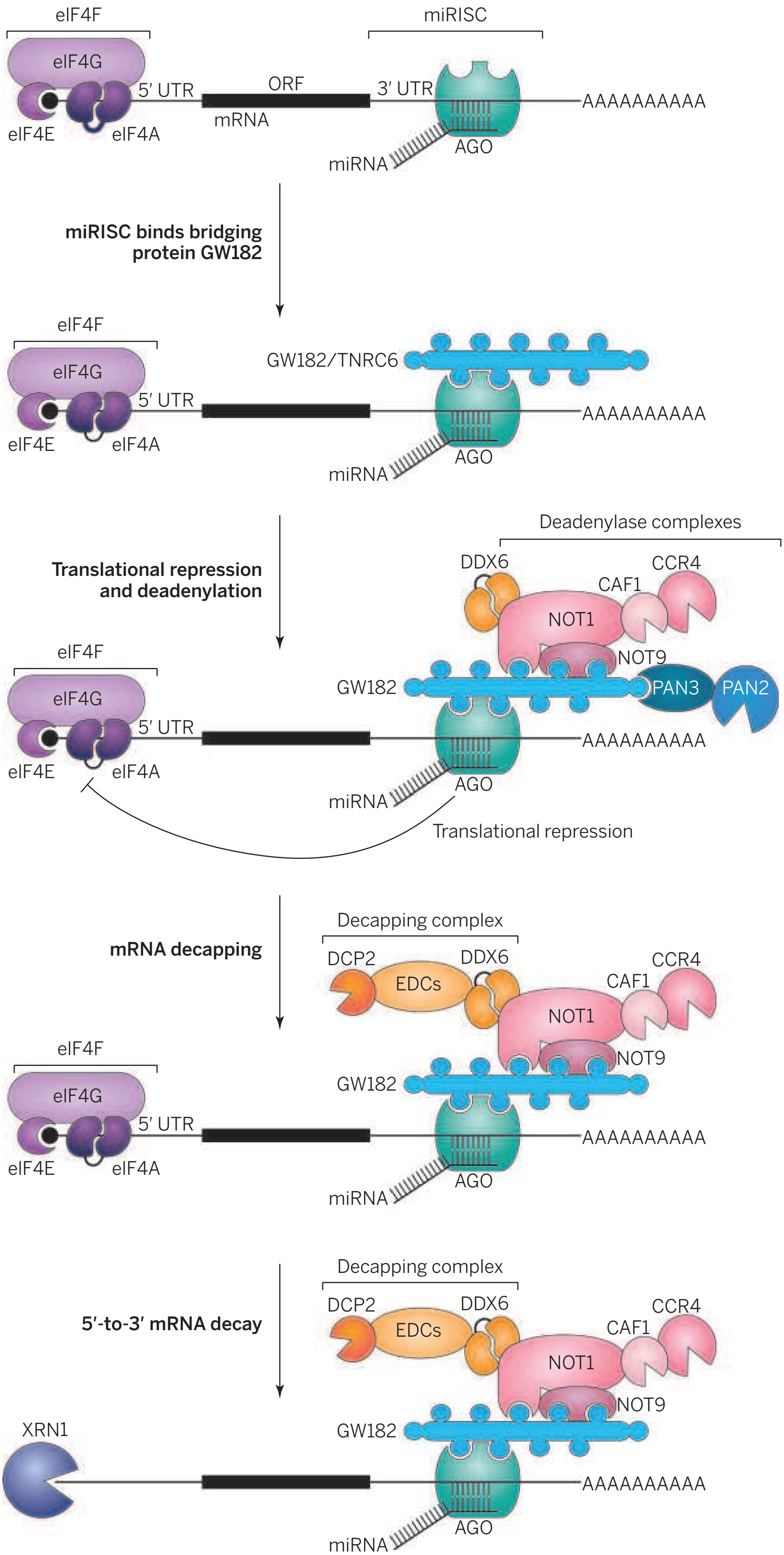

MiRNA-mediated silencing. Animal miRNAs bound to an Argonaute protein (AGO) recognize their mRNA targets by base-pairing to partially complementary binding sites. AGOs interact with GW182 proteins, which recruit deadenylase complexes. The decapping complex is recruited, at least in part, through interactions with the CCR4-NOT complex, which are mediated by the DDX6 protein. In addition, miRNAs repress translation, possibly through DDX6 and/or interference by miRISCs with the function of the initiation factor eIF4A. The decapping complex contains multiple components, which are shown as a single oval labeled EDCs (enhancers of decapping). The CCR4-NOT complex contains at least eight subunits, of which only four are shown. The cap structure is shown as a black dot. ORF: open reading frame; UTR: untranslated region; CAF1: chromatin assembly factor 1. Cyan circles in GW182 represent W-containing motifs.

scanning and eIF4A-dependent mechanism. Experiments to test this prediction have so far yielded conflicting results.

In the "roadblock" model, eIF4A2 has been proposed to be recruited to miRNA targets through an interaction with NOT1 (*13*). However, other studies have indicated that NOT1 interacts with DDX6 rather than eIF4A2 (*9*, *10*, *14*). Because DDX6 represses translation and its depletion inhibits silencing in human cells (*9*, *10*, *14*, *15*), its recruitment to miRNA targets could explain how translational repression by miRISC is achieved.

It is becoming increasingly clear that the CCR4-NOT complex is a conserved and central downstream effector of silencing that can elicit all of the effects that the miRISC has on its targets, namely translational repression, deadenylation, decapping, and mRNA decay (*4*, *5*, *9*, *10*). A possible contribution by additional silencing mechanisms, independent of the CCR4-NOT complex (*12*), remains an important topic for future work.

A complicating factor in the study of silencing mechanisms that has not yet been addressed is redundancy. Redundancy is manifested at two levels. The first level is due to gene-duplication events that generated four Argonaute and three GW182 paralogs in most vertebrates. Similarly, there are two paralogs for each of the two catalytic subunits of the CCR4-NOT complex, resulting in the assembly of at least four distinct complexes. Another level of redundancy is observed in the network of interactions between the factors involved. For example, deadenylase complexes interact both with each other, and CCR4-NOT interacts with decapping factors independently of GW182 and DDX6. Redundancy offers alternative ways to assemble silencing complexes, which might ultimately differ in their functional outcomes, potentially resulting in distinct molecular mechanisms, which might become dominant in a context-dependent manner. ■

REFERENCES

1. M. R. Fabian, N. Sonenberg, *Nat. Struct. Mol. Biol.* **19**, 586 (2012).
2. H. Guo, N. T. Ingolia, J. S. Weissman, D. P. Bartel, *Nature* **466**, 835 (2010).
3. S. W. Eichhorn *et al.*, *Mol. Cell* **56**, 104 (2014).
4. J. E. Braun, E. Huntzinger, M. Fauser, E. Izaurralde, *Mol. Cell* **44**, 120 (2011).
5. M. Chekulaeva *et al.*, *Nat. Struct. Mol. Biol.* **18**, 1218 (2011).
6. M. R. Fabian *et al.*, *Nat. Struct. Mol. Biol.* **18**, 1211 (2011).
7. N. T. Schirle, I. J. MacRae, *Science* **336**, 1037 (2012).
8. M. Christie, A. Boland, E. Huntzinger, O. Weichenrieder, E. Izaurralde, *Mol. Cell* **51**, 360 (2013).
9. Y. Chen *et al.*, *Mol. Cell* **54**, 737 (2014).
10. H. Mathys *et al.*, *Mol. Cell* **54**, 751 (2014).
11. A. Fukao *et al.*, *Mol. Cell* **56**, 79 (2014).
12. T. Fukaya, H.- Iwakawa, Y. Tomari, *Mol. Cell* **56**, 67 (2014).
13. H. A. Meijer *et al.*, *Science* **340**, 82 (2013).
14. C. Rouya *et al.*, *RNA* **20**, 1398 (2014).
15. C.-Y. Chu, T. M. Rana, *PLOS Biol.* **4**, e210 (2006).

10.1126/science.1260969

STRETCHABLE ELECTRONICS

Stretch, wrap, and relax to smartness

Carbon nanotubes wrapped around rubber cores create resilient conducting fibers

By **Tushar Ghosh**

For thousands of years, humankind has assembled polymeric fibers into textiles for protection against the environment and as an expression of cultural and social status (*1*). What began with fibers collected from nature (e.g., flax) is now made from a wide range of high-performance polymers that possess useful mechanical, thermal, and chemical properties. Despite these advances, electrically conducting fibers for the most part have remained elusive, with the exception of fibers based on inherently conducting polymers; to date, the electrical properties of conducting fibers deteriorate when repeatedly stretched and released. In a remarkable development, described on page 400 of this issue, Liu *et al.* (*2*) have made superelastic conducting fibers based on carbon nanotubes (CNTs) that can be stretched 1000% with almost no change in electrical conductivity, even after thousands of strain cycles.

Conducting electrical fibers are envisioned as a key component for flexible electronics for biomimetic devices, electronic textiles, and large-area conformable electronics with unusual form factors (e.g., for deploying soft sensors and actuators). Soft, flexible conducting materials will likely undergo relatively large strains during use and must not lose performance. Polymeric fibers are flexible, lightweight, and easy to process at low cost (think textiles) into structures that offer tremendous design flexibility in form as well as function and are therefore ideal building blocks for these applications. The most common strategy for making electrical conductive polymers is to mix conducting species into a soft polymer matrix that is usually an insulator. Conduction in these composites occurs through percolating networks of metallic or carbonaceous particles, in powder, fiber, or platelet form.

Of these, CNTs have attracted tremendous interest because of their remarkable mechanical, physical, thermal, and electrical properties (*3*). Although many polymer nanocomposites containing various forms of CNTs have been reported, in almost all cases, the extensibility is limited and conductivity is strain dependent. Fortunately, stretchable conductors can be created from otherwise inextensible and intrinsically rigid inorganic building blocks by using a buckling-induced, wavy surface architecture. Formation of buckled structures of metallic layers on the surface of a contracted underlying elastomeric substrate was first reported as a strategy to develop nearly strain-invariant conductance in polymers (*4*). Since then, buckling has been used to develop flexibility in a variety of materials and fabrication processes. Thin films of high-quality single-crystal silicon deposited on prestrained elastomeric substrates have been used to fabricate conductors with a wavelike geometry and high stretchability and compressibility (*5*). Composite materials undergoing mechanical or thermal strain can form a wavy buckling pattern on surfaces to create materials that are both stretchable and conductive (*6*).

> ***"Textiles are one of the obvious application areas of flexible electronics that offer tremendous opportunities."***

Stretchable conductors based on CNTs have been fabricated by dispersing single-walled CNTs in ionic liquids and mixing in a copolymer matrix (*7*) and by spraying an aqueous dispersion of CNTs onto acrylic films (*8*). The buckling-induced wavy surface architecture of CNT sheets has been produced both by deposition on a stretched substrate followed by release of stretch (*9*) and by deposition on unstretched substrate followed by application of stretch-release cycles (*10*). In both cases, the conductivity remained largely unchanged. More recently, formation of buckling-induced kink bands in electrodes

Fiber and Polymer Science Program, Textile Engineering, Chemistry, and Science Department, North Carolina State University, Raleigh, NC 27695, USA. E-mail: tghosh@ncsu.edu

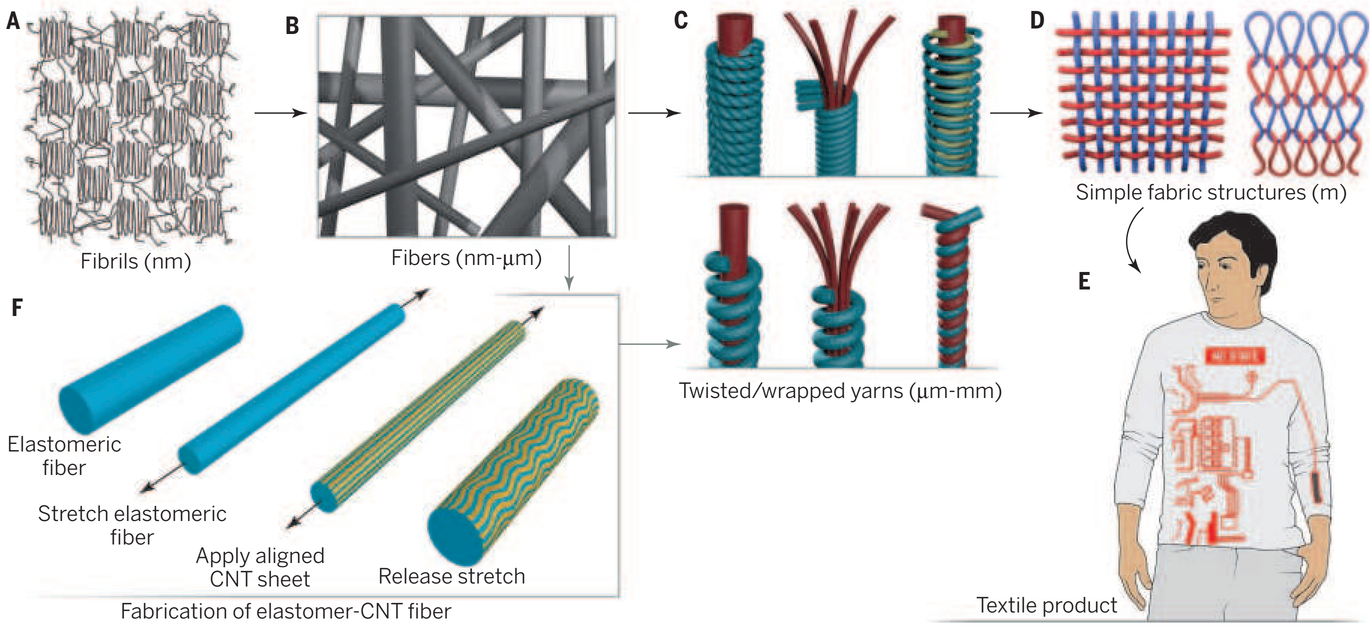

Hierarchical structure of textiles and potential opportunities for flexible electronics. The hierarchical structure of textiles with typical length scale shown in parentheses. (**A**) Fibrils are clusters of partially aligned polymer molecules organized in ordered (crystalline) and disordered (noncrystalline) regions. (**B**) Synthetic fibers of very high aspect ratio (length to diameter) are made from natural and synthetic polymers, with one or more polymer types, in many cross-sectional shapes. (**C**) Fibers are subsequently assembled into yarns through processes such as twisting or wrapping. (**D**) These yarns are processed into fabrics. In both yarn and fabric manufacturing, an enormous variety of structures are possible. Other routes of making textile products from polymers are not shown in the illustration for clarity. (**E**) Three-dimensional textile products are generally made from planar fabrics. Functional materials can be incorporated in textiles at any of the hierarchical levels. (**F**) Elastomer-CNT sheath core fibers made by Liu *et al*. (*2*) can be directly introduced into (C) yarns, (D) fabrics, or (E) products.

of forest-drawn oriented CNT sheets was observed after repeated actuation cycling of dielectric elastomer actuators (*11*).

Liu *et al.* used multiwall CNT sheets wound as sheath layers on a highly stretched rubbery fiber [a plasticized styrene-(ethylene-butylene)-styrene (SEBS) copolymer (*12*) fiber core] to fabricate a series of multilayer fibers. After the applied fabrication strain was relaxed, these fibers underwent interesting morphological changes because of hierarchical two-dimensional buckling of the CNT sheets and produced periodic structures as a function of strain.

The idea advanced by Liu *et al.* of incorporating precise and highly ordered layers of conducting materials in the fiber structure to enable sensing, actuation, and transmission is indeed attractive for the development of flexible electronics and, in particular, electronic textiles. The electrical conductivity of these fibers remains almost unchanged, even under very high levels of strain and over thousands of strain cycles of large amplitude. Furthermore, nonhysteretic, reversible, and linear capacitance changes of these fibers in coiled configuration were observed that has potential application as strain sensors. These fibers, when twisted, also work as torsional and/or tensile dielectric elastomer actuators (*12*) because of the electrostatic attraction between the CNT layers.

Textiles are one of the obvious application areas of flexible electronics that offer tremendous opportunities. Textiles are worn and also cover many of the surfaces around us. Unobtrusive integration of electronic capabilities without loss of the accompanying desirable attributes (e.g., texture and comfort) requires a fundamental understanding of the hierarchical nature of textile structures and their particular methods of assembly (see the figure).

Textiles are so common that we often are not aware of their distinctive properties: They can be both strong and flexible. These properties arise from the hierarchical structure of the fiber assembly through the complex interactions of the inherent fiber material properties and the characteristic fiber structure at multiple length scales derived from the distinctive methods of assembly (e.g., twisting and interlacing). Although electronic functionalities can be engineered into textiles at one or more of the hierarchical levels (i.e., molecules, fibers, yarns, or fabrics) involved in the contemporary manufacture of textiles, introduction of desired electrical characteristics into the fiber level constitutes the most effective and inconspicuous strategy.

Finally, most current efforts in the emerging area of flexible electronics seek to develop enabling technologies to produce, for example, devices and systems such as flexible displays, solar cells, physiological monitors, and electronic skin. In this regard, it is not hard to imagine a flexible, smart, and closed-loop system, with distributed sensors and actuators for use in conjunction with rehabilitation or haptic interface that is designed to be worn on a human body with no discomfort to the subject. Studies such as the one by Liu *et al.* offer a promising pathway to achieve such goals through the use of processes that are compatible with mainstream manufacture of textiles. ■

REFERENCES

1. E. J. W. Barber, *Prehistoric Textiles: The Development of Cloth in the Neolithic and Bronze Ages with Special Reference to the Aegean* (Princeton Univ. Press, Princeton, NJ, 1991).
2. Z. F. Liu *et al.*, *Science* **349**, 400 (2015).
3. R. H. Baughman, A. A. Zakhidov, W. A. de Heer, *Science* **297**, 787 (2002).
4. N. Bowden, S. Brittain, A. G. Evans, J. W. Hutchinson, G. M. Whitesides, *Nature* **393**, 146 (1998).
5. D.-Y. Khang, H. Jiang, Y. Huang, J. A. Rogers, *Science* **311**, 208 (2006).
6. D. C. Hyun *et al.*, *Adv. Mater.* **23**, 2946 (2011).
7. T. Sekitani *et al.*, *Science* **321**, 1468 (2008).
8. L. B. Hu, W. Yuan, P. Brochu, G. Gruner, Q. B. Pei, *Appl. Phys. Lett.* **94**, 161108 (2009).
9. F. Xu, X. Wang, Y. Zhu, Y. Zhu, *Adv. Funct. Mater.* **22**, 1279 (2012).
10. Y. Zhu, F. Xu, *Adv. Mater.* **24**, 1073 (2012).
11. E. Cakmak, X. Fang, O. Yildiz, P. D. Bradford, T. K. Ghosh, *Carbon* **89**, 113 (2015).
12. R. Shankar, T. K. Ghosh, R. J. Spontak, *Adv. Mater.* **19**, 2218 (2007).

10.1126/science.aac7417

SCIENCE AND GOVERNMENT

Yellow lights for emerging technologies

All-or-none regulatory systems are not adequate for revolutionary innovations

By **R. Alta Charo**

There is an infuriating, often confusing four-way stop intersection near my home. The city refuses to install traffic lights, because devices such as roundabouts, four-way stop signs, and flashing yellow lights, which require drivers to slow and scan before entering, can result in fewer accidents, as well as a faster and more even flow of traffic. There is a lesson to be learned here for regulation of new technologies. Clear, decisive rules are seductive. New drugs cannot be sold untold until proven safe. Food supplements are sold until proven unsafe. Although such clean demarcations can be reassuring, they do not work well for technologies whose applications cannot be presumed safe or unsafe.

Technology innovates faster than the regulatory system can adapt, whether with innovative modes of governance or interpretations of standard regulatory models (*1*).

POLICY

Emerging technologies, such as nanotechnology, synthetic biology, and gene editing are characterized by rapidly evolving scientific understanding of fundamental mechanisms; novel application possibilities; parallel development of measurement and evaluation tools; and public reactions that include excitement and concern. The uncertainties of emerging technologies can make it difficult or even impossible for regulators to apply traditional risk-benefit analyses, because they may have neither a definitive idea of what to look for nor a means to identify it. Yet waiting to satisfy these methodological and data needs could effectively block technology deployment, deny possible benefits, and possibly forestall developing data to resolve the uncertainties.

The White House issued a set of principles (*2*) for regulating emerging technologies: scientific integrity, public participation, benefits and costs, flexibility, risk assessment and risk management, coordination, and international cooperation. Perhaps the most interesting and important is "flexibility." The challenge of combining flexibility and public trust is that, in the absence of confidence in the regulatory system's independence, integrity, and ability to revisit earlier decisions, trust can morph into a demand for rigid protections against the unknown.

A prime example of this tension is the history of genetically engineered ("GE") foods. Food regulation comes in two basic flavors. There is a lengthy, onerous rule-making process for food additives that can take an average of 6 years in the United States (*3*), or even more in Europe (*4*), versus a streamlined, largely self-enforced process for foods that are "generally recognized as safe" ("GRAS") (*5*) that allows producers to market their products immediately and indefinitely with little U.S. Food and Drug Administration (FDA) involvement, unless the agency subsequently proves that the food is not safe for its intended use (*6*).

For GE foods, companies generally follow a voluntary consultation process with the FDA to confirm GRAS status, because the agency has found nothing in the biotechnology process inherently unsafe. But opposition to these foods and calls for more regulation are far from abating. An innovative process that legally required greater involvement by the FDA or the Department of Agriculture (USDA) before and after these foods were marketed might have helped to quell concerns without slowing innovation. Indeed, USDA recently initiated a stakeholder consultation process to consider whether and how to change the current system (*7*).

When another technology comes around, e.g., the use of nanotechnology to change the size (and potentially, some properties) of common ingredients, it may not be possible to categorically label it as GRAS or non-GRAS. The choice, again, is between stifling innovation with rule-making or losing public confidence owing to voluntary procedures based largely on industry-driven research.

A more cautious approach. We need to enhance our red-light, green-light regulatory system.

PHOTO: ZAYATS-AND-ZAYATS/THINKSTOCK

There are tools that might add flexibility, many already used in some area of regulation. Restricted approvals put limits on how a product can be purchased, such as requiring certain medical tests be performed before a drug may be prescribed. Conditional approvals impose penalties or approval withdrawal if manufacturers do not submit the follow-up information. Sunset clauses withdraw approval automatically when conditions are unmet, without the need for the agency to satisfy a burden of proof before a court or other arbiter. Marketing restrictions place limits on how a product can be advertised. One observer describes these various approaches as "experimental" noting that "[e]xperimenting with laws can be particularly useful to test new regulations on a small-scale basis, gather more facts on the response of the market to an innovative product, and improve regulation as more information becomes available" (*8*).

But innovative tools must be deployed properly. In 1972, the FDA developed an intermediate option when problems are detected in marketed foods. The agency would use a category of "interim" food additive for the time it would take to resolve the issues (*9*). The interim food additive status gave the FDA the power to impose limits on the food's marketing while the requested studies were completed. But this option has been used infrequently, and in some cases, the interim status has become an indefinite label. Overall, it has not resulted in more aggressive FDA oversight of foods marketed as GRAS (*10*).

The European Medicines Agency's efforts to implement a system of conditional drug approval that might get drugs out more quickly but with greater regulatory control does not have measured outcomes. The European Commission has created two pathways. The first works for drugs for which it is not possible to provide the European Medicines Agency with additional data, a category that might be interpreted to include drugs based on novel technologies. The second, called "conditional approvals" (CAs), allows drugs to enter the market with less than the usual level of safety and efficacy data, if they have a good risk-benefit ratio demonstrated in initial trials, and it is expected that more data will be obtainable once marketed.

In some ways, this resembles the proposals made in the United States to increase use

School of Law and School of Medicine & Public Health, University of Wisconsin–Madison, WI, USA. E-mail: alta.charo@wisc.edu

of biomarkers and surrogate end points, with postmarket demonstration of clinical end points to follow. But the European CA does this without losing tight control over the medication, because conditionally approved drugs lose their approval status and are removed automatically from the market if sponsors fail to meet their postmarket commitments for further trials (*11*). Early indications are that the system has not increased the frequency of problems with drugs approved under this process (*12*), although, in a similar Canadian system, the number of postmarket warnings and drug withdrawals is higher than that for drugs receiving standard (and lengthier) premarket review (*13*).

In the United States, withdrawal of a marketed drug takes positive action. Under conditional approval in the European Union, the mere failure either to submit postmarket data to support the initial release or to apply for a limited-time renewal of the conditional approval means that the drug can no longer be marketed. But this approach, which reduces time-to-market for innovative drugs while maintaining strong tools for public health protection, has not been extended to emerging technologies generally.

Analogously, in the conditional registration system for agricultural pesticides, new active ingredients are moved to market with the condition that the U.S. Environmental Protection Agency (EPA) receives additional data. It is limited to circumstances (similar to the interim food additive rule) in which the agency can demonstrate that the product does not pose a threat. It also is limited to situations in which a sponsor did not have enough time to meet agency requests for specific data and in which there is a significant public need for the new product. It is not, however, aimed at products based on emerging technologies for which there may be initial safety data but for which additional data on safety and benefits will be developing over the next few years (*14*).

Another example of the conditional approval approach comes from Japan, where recent amendments to their pharmaceutical law allow sponsors to seek short-term market approval for stem-cell therapy products, provided that early studies show promise. While on the market, these conditionally approved therapies are eligible for reimbursement (*15*). The effect is to put a lot of pressure on postmarket surveillance and responsive regulation (*16*). For particularly controversial technologies, such as embryonic stem cell therapy, early introduction poses a risk that any high-profile failure might increase political opposition or public skepticism, as happened in the field of gene therapy (*17*).

Another obstacle to developing and deploying a wider variety of restricted, conditional, and sunsetting regulatory actions is the need for new legislative authority under which new regulations might be issued. Although the 21st Century Cures Act (*18*) is being discussed in Congress, there is no evidence of a broader legislative agenda. Also, our tort system cannot act as a regulator, given that it depends on attention to industry-set or customary practice standards, which for emerging technologies will not yet have been formed.

The problem may sort itself out without explicit attention from lawmakers. When emerging technologies create uncertainties, a regulatory gap can emerge along with the technology. Into this void can flow professional self-regulation, as happened with recombinant DNA and human embryonic stem cell research. The scientists proceeded to devise and implement guidelines with such success that they eventually became the basis of government regulation and funding policy. In neither case was the emphasis on declaring technologies or applications inherently acceptable or not. Rather, guidelines took a provisionally precautionary approach toward the risk of environmental release or physical harm to humans, without putting a halt to the work entirely.

"Technology innovates faster than the regulatory system can adapt..."

The recent call for a temporary moratorium on clinical attempts to use CRISPR-Cas9 for human nuclear DNA germline editing may provide the same pause for reflection (*19*). Within months, the U.S. National Academies announced an initiative that would include both an international summit and a consensus study committee. But the central challenges remain: For a technology whose effects might reverberate for generations, is it possible to have enough information to satisfy risk-benefit analyses? Who has the moral authority to make the decision to proceed? To the extent that it is "the public," experience tells us that the venues are limited (e.g., testimony to presidential bioethics commissions or expert advisory committees) or risk being captured by ideological agendas. Other countries have been more comfortable including public opinion and morality-based arguments in their technical decisions, e.g., in the United Kingdom's regulation of regenerative medicine through a comprehensive licensing body. But such centralized control runs into political and even constitutional obstacles in the United States.

A more iterative process would incorporate a variety of tools, designed to enhance partnership between industry and regulators through an expanded range of consultation processes and postmarket reviews; enhance transparency of developing data, including data about failed trials and experiments; incorporate limitations on advertising and applications while research continues; put the burden of producing information to maintain approval on the sponsors; ease the burden on regulators who seek to add protections or withdraw problematic products; and continually reevaluate the real benefits and harms. It would also provide increased access to existing venues for public discussion and legislative action, as well as new opportunities at the state and local level for community education and discussion. This might include greater use of temporary moratoria that allow the public to catch up with new information and reflect on the implications of new technologies.

Iterative regulation, constant monitoring and reevaluation, wider consultation, and a broader array of conditions and restrictions may at times be confusing, but they also might forestall a regulatory "no" or prevent public outcry over a regulatory "yes," either of which can, in the end, slow innovation. One might say that what we need are more roundabouts, four-way stops, and yellow lights to supplement our red-light, green-light regulatory system. ■

REFERENCES

1. G. E. Marchant *et al*., Eds., *The Growing Gap Between Emerging Technologies and Legal-Ethical Oversight: The Pacing Problem* (Springer, New York, 2011).
2. Office of Science and Technology Policy *et al*., "Principles for regulation and oversight of emerging technologies" [memo]; http://1.usa.gov/1Rj9DqJ.
3. L. Noah, Appendix A, of *Enhancing the Regulatory Decision-Making Approval Process for Direct Food Ingredient Technologies* (National Academy Press, Washington, DC, 1999); http://bit.ly/Regul-Food.
4. D. Vogel, *Br. J. Polit. Sci.* **33**, 557 (2003).
5. Food Insight, The Rigorous Road to Food Ingredient Approval (2015); http://bit.ly/IFIC-Nutrition-Food.
6. USDA, Determining the Regulatory Status of a Food Ingredient; http://bit.ly/Reg_food.
7. USDA, "New Stakeholder Engagement on APHIS Biotechnology Regulation," docket no. APHIS-2015-0036.
8. S. Ranchordás, *Jurimetrics* **55**, 201 (2015).
9. Institute of Medicine, *Enhancing the Regulatory Decision-Making Approval Process for Direct Food Ingredient Technologies* (National Academy Press, Washington, DC, 1999).
10. M. Sanchez, *Food Law and Regulation for Non-Lawyers: A U.S. Perspective* (Springer International, Berlin, 2014).
11. R. A. Charo, *JAMA Intern. Med.* **173**, 1165 (2013).
12. W. P. C. Boon *et al*., *Clin. Pharmacol. Ther.* **88**, 848 (2010).
13. J. Lexchin, *Br. J. Pharmacol.* **79**, 8 (2015).
14. Government Accountability Office, "Pesticides: EPA should take steps to improve its oversight of conditional registrations" (GAO 13-145; GAO, Washington, DC, 2013).
15. K. Konomi *et al*., *Cell Stem Cell* **16**, 350 (2015).
16. D. Sipp, *Cell Stem Cell* **16**, 353 (2015).
17. J. Akst, *Scientist*, 1 June 2012; http://bit.ly/TargetingDNA (2012).
18. House Committee on Energy and Commerce, 21st Century Cures; http://energycommerce.house.gov/cures.
19. D. Baltimore *et al*., *Science* **348**, 36 (2015).

10.1126/science.aab3885

PUBLIC HEALTH

Toward an HIV vaccine: A scientific journey

Different strategies are coming together to provide insights for an effective HIV vaccine

By **Anthony S. Fauci**[1]*
and **Hilary D. Marston**[2]

POLICY

In the face of a global pandemic, the search for an effective vaccine against the human immunodeficiency virus (HIV) remains an urgent priority. From the first HIV vaccine trials in the 1980s to the present, a tension has existed between the desire to move quickly to clinical trials to stem the spread of the epidemic and the view that research into HIV pathogenesis and host immunity were necessary predicates to and informative of vaccine design. Those advocating the first strategy—an empirical (or inductive) approach—argued that in vitro and animal studies were poorly predictive of the human response to HIV infection and that the only way to gauge vaccine efficacy was to test candidates in humans. Those advocating the second strategy—a theoretical (or deductive) approach—hoped to establish an understanding of the immune response to natural infection and to find ways to recapitulate and enhance that response through vaccination. Today, these approaches are coalescing into concomitant paths toward a safe and effective HIV vaccine.

When HIV was identified in 1983 and proven to be the causative agent of AIDS in 1984, the field of vaccinology was experiencing dramatic successes. Traditional vaccine approaches using whole pathogens, either attenuated or killed, to induce immunity paid substantial dividends in reducing the global burden of polio, measles, mumps, and other important diseases. Smallpox was eradicated, by using a relative of *Variola major* to induce protection. New technologies, such as subunit vaccines were producing impressive efficacy against hepatitis B virus. Against this backdrop, a vaccine against a novel virus such as HIV seemed to be readily attainable; now, in retrospect, this is seen as a somewhat naïve perspective.

However, even in the 1980s, many virologists deemed a vaccine using inactivated whole virus unsafe because of the possibility that poorly inactivated HIV could integrate into the host genome or revert to a pathogenic wild-type phenotype (as had been seen with an inactivated polio vaccine) (*1*). Moreover, unlike smallpox and measles, HIV invariably produced a chronic, progressive illness that was not ultimately cleared by the host immune response. Thus, the host response to natural infection did not provide a clear blueprint on which to base vaccine design. Additional challenges emerged. For example, HIV superinfection is regularly observed, which demonstrates that constant in vivo immune stimulation by replicating autologous virus fails to protect against subsequent challenges with heterologous viruses. Furthermore, the propensity of HIV for mutation is quite high among human viruses (*2*).

The first U.S. government-sponsored phase I trial of an HIV vaccine, a gp160 subunit candidate, was launched in 1987. Many similar constructs entered safety trials over the next few years, with disappointing results. Although the investigational vaccines often yielded robust antibody titers, most of the antibodies failed to neutralize in vitro. Moreover, the neutralization that was seen was against laboratory-adapted virus, not primary isolates (*3*).

This inability to induce an adequate antibody response was perplexing. Furthermore, contemporaneous studies of passive infusion of HIV-specific immune globulin into nonhuman primates (NHPs) failed to protect against HIV or related viruses (*4*). Thus, broadly neutralizing antibodies were difficult to induce, and HIV-specific antibodies in general were apparently ineffective. Famed vaccinologist Maurice Hilleman voiced the frustration best, stating: "I don't know of anything like this. This is the first time in vaccine development that neutralizing antibodies don't seem to amount to much" (*5*).

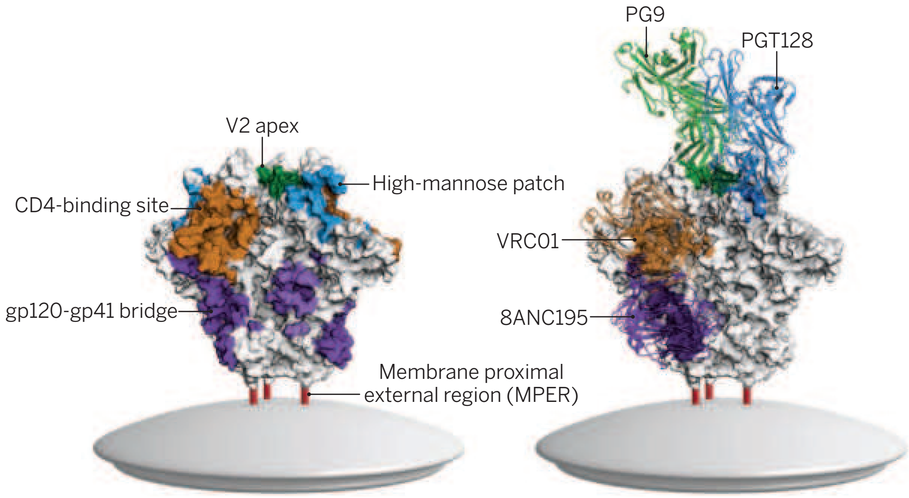

HIV trimer with neutralizing epitopes and selected bNAbs. Crystal structure of the HIV-1 trimer in its closed state, labeled with binding sites for broadly-neutralizing antibodies (left), and with antigen-binding fragments of selected bNAbs (right). Crystal structures of membrane-proximal external region (MPER) antibodies have not been determined in the trimer context, and therefore are not pictured.

Despite such challenges, the growing HIV pandemic created intense pressure to expedite vaccine development. Some prominent scientists advocated large-scale empiric trials (*6*). Advocates for basic research studies questioned the utility of clinical trials when fundamental questions remained unanswered. This debate came to a head in 1994, when a panel convened by the National Institute of Allergy and Infectious Diseases (NIAID) considered the merits of phase III trials for two vaccine candidates based on a recombinant HIV envelope protein platform (*6*). Citing limited immune responses in early-stage trials, concerns about recruitment for larger future studies, and cost, the panel recommended against government sponsorship of such trials. Nonetheless, trials of one candidate moved forward with industry support: VaxGen's AIDSVAX

SOURCES: REF. 20: ADAPTATION COURTESY OF J. STUCKEY, I.S. GEORGIEV AND P.D. KWONG/STRUCTURAL BIOLOGY SECTION, NIAID VACCINE RESEARCH CENTER, NATIONAL INSTITUTES OF HEALTH

[1]Anthony S. Fauci M.D. is the Director of the National Institute of Allergy and Infectious Diseases at the National Institutes of Health, Bethesda, MD 20892, USA. [2]Hilary D. Marston M.D., M.P.H. is a Medical Officer and Policy Advisor for Global Health at the National Institute of Allergy and Infectious Diseases at the National Institutes of Health, Bethesda, MD 20892, USA. *Corresponding author. E-mail: afauci@niaid.nih.gov

gp120. Unfortunately, two phase III studies that used the envelope from different clades of HIV in men who have sex with men and injection drug users, respectively, failed to demonstrate protection (*7*, *8*).

Given the disappointment associated with B cell–targeted vaccines (designed to induce antibodies), many HIV vaccinologists turned to the induction of T cell responses against HIV. These vaccines were not intended to prevent acquisition of virus; rather, they were designed to lower the viral set point (or the level of plasma virus at which HIV settles after acute infection in the absence of therapy), which would mitigate, somewhat, the deleterious effects of the virus. Given favorable immunogenicity in animal studies and early-stage human trials, adenovirus type 5–vectored (Ad5) candidates garnered interest. Unfortunately, two phase IIb trials (STEP and Phambili) testing a candidate that expressed HIV *gag, pol*, and *nef* were halted after interim Data and Safety Monitoring Board reviews revealed poor efficacy (*9*). In fact, the trials demonstrated evidence of increased risk of viral acquisition among vaccine recipients as compared with placebo. A scientific symposium reviewing those data concluded that vaccine-related immune activation might have led to increased susceptibility to infection (*10*).

Although certain investigators pursued Ad5 vectors, others proposed combining a pox virus–vectored gp120 *env* prime with a gp120 protein boost, two candidates that alone did not induce potentially protective immunity. The RV144 trial stirred controversy in the scientific field, once again pitting empirical approaches against theoretical approaches. In the end, advocates of empiricism pushed ahead and the trial proceeded. To the surprise of many, the trial demonstrated a 31% reduction in HIV acquisition (*11*). Investigators now seek to improve on RV144, hoping to increase the durability, potency, and breadth of responses. A range of trials under the auspices of the Pox-Protein Public-Private Partnership (P5) are examining the impact of alternate priming and dosing schedules, as well as various vectors and adjuvants (*12*). Several teams are also studying the immune responses of RV144 participants, looking for markers predictive of efficacy. In this regard, attention has centered on an immunoglobulin G response against the V_1V_2 loop of the HIV envelope, which appeared particularly prominent as a correlate of decreased HIV transmission risk in RV144 (*13*).

Concomitantly, those pursuing a theoretical approach made a series of discoveries related to broadly neutralizing antibodies (bNAbs). Investigators found that ~20% of infected individuals develop antibodies capable of neutralizing a wide range of viral isolates; however, development of this breadth of response typically occurred only with continuous viremia after 2 to 4 years of infection. The time lapse is largely explained by the evolutionary hurdles that bNAbs must surmount. Some are autoreactive and clonally deleted to prevent the development of autoimmunity; some have specialized structures, such as long complementarity-determining regions that are rare among germline B cells; and others require a high degree of somatic hypermutation (the process by which B cell receptors adapt to produce higher-affinity antibodies) (*14*). With careful study of existing cohorts, a range of bNAbs has been characterized (see the figure).

"...human in vivo studies have shown decreased levels of circulating virus after administration of bNAbs."

Although bNAbs provide an intriguing model for vaccine development, their efficacy in preventing infection is as yet unproven in humans. Passive transfer studies using bNAbs in NHPs, have demonstrated prevention of viral acquisition among uninfected animals (*15*) and suppression of viremia among infected animals (*16*, *17*). Ex vivo studies have shown marked suppression of expression of virus from HIV viral reservoirs by bNAbs (as measured by in vitro replication of reservoir virus in $CD4^+$ T cells obtained from infected individuals receiving antiretroviral therapy) (*18*). In addition, human in vivo studies have shown decreased levels of circulating virus after administration of bNAbs (*19*). Other approaches to the utilization of preformed bNAbs are increasing the half-life of the antibodies and vector-based delivery. Primary prevention studies in humans are imminent.

Although passive transfer studies are instructive, ultimately a pragmatic vaccine approach will likely require induction of bNAbs by active immunization. Several recent findings have advanced the field. First, the epitopes to which the bNAbs bind have been characterized in detail; in fact, the envelope trimer itself has been stabilized in a soluble form and might be a suitable immunogen (see the figure) (*20–24*). In addition, B cell lineages for bNAbs have been defined and the cellular evolutionary process necessary to create such antibodies has been characterized. Some of these lineages show minimal mutation, although these antibodies display modest breadth of neutralization. Combinations of modestly mutated antibodies, however, could offer an alternative means to achieve breadth. In addition, combinations of antibodies targeting different binding sites (neutralizing epitopes) could impede development of resistance.

Even with these approaches, however, B cells will likely require sequential stimulation by different immunogens in order to drive the B cell lineage to express broadly neutralizing antibodies (*25*).

Alternative approaches are also being pursued. One promising method uses live rhesus cytomegalovirus vectors encoding simian immunodeficiency virus (SIV) genes *gag*, *pol*, *rev*, *nef*, *tat*, and *env*. The strategy does not prevent initial infection but provides a powerful stimulation of SIV-specific $CD8^+$ T lymphocytes that control and eliminate virus in 50% of animals (*26*).

These bNAb and $CD8^+$ T cell–based approaches remain at early stages, as they move from theory toward regimen design. Simultaneously, research stemming from the RV144 trial could improve upon the modest efficacy already seen. Ultimately, the theoretical and empirical approaches will coalesce, converging upon the effective vaccine so critically needed to end HIV transmission worldwide. ■

REFERENCES AND NOTES

1. W. Dowdle, *Public Health Rep.* **101**, 232 (1986).
2. B. Korber *et al.*, *Br. Med. Bull.* **58**, 19 (2001).
3. R. Dolin *et al.*, NIAID AIDS Vaccine Clinical Trials Network, *Ann. Intern. Med.* **114**, 119 (1991).
4. A. M. Prince *et al.*, *Proc. Natl. Acad. Sci. U.S.A.* **85**, 6944 (1988).
5. G. Kolata, in *New York Times*, 16 February 1988.
6. H. Collins, in *The Philadelphia Inquirer*, 8 November 1994, p. A1.
7. P. Pitisuttithum *et al.*, Bangkok Vaccine Evaluation Group, *J. Infect. Dis.* **194**, 1661 (2006).
8. N. M. Flynn *et al.*, rgp120 HIV Vaccine Study Group, *J. Infect. Dis.* **191**, 654 (2005).
9. National Institutes of Health, Statement: Immunizations are discontinued in two HIV vaccine trials [press release] (2007); http://bit.ly/vaccines-discontinued.
10. A. S. Fauci., *Science* **344**, 49 (2014).
11. S. Rerks-Ngarm *et al.*, MOPH-TAVEG Investigators, *N. Engl. J. Med.* **361**, 2209 (2009).
12. U.S. Military Health Research Program, Pox-Protein Public-Private Partnership (2013); www.hivresearch.org/news.php?NewsID=270&GlobalID=11.
13. B. F. Haynes *et al.*, *N. Engl. J. Med.* **366**, 1275 (2012).
14. B. F. Haynes, G. Kelsoe, S. C. Harrison, T. B. Kepler, *Nat. Biotechnol.* **30**, 423 (2012).
15. M. Shingai *et al.*, *J. Exp. Med.* **211**, 2061 (2014).
16. D. H. Barouch *et al.*, *Nature* **503**, 224 (2013).
17. M. Shingai *et al.*, *Nature* **503**, 277 (2013).
18. T. W. Chun *et al.*, *Proc. Natl. Acad. Sci. U.S.A.* **111**, 13151 (2014).
19. M. Caskey *et al.*, *Nature* **522**, 487 (2015).
20. M. Pancera *et al.*, *Nature* **514**, 455 (2014).
21. J. P. Julien *et al.*, *Science* **342**, 1477 (2013).
22. D. Lyumkis *et al.*, *Science* **342**, 1484 (2013).
23. R. W. Sanders *et al.*, *PLOS Pathog.* **9**, e1003618 (2013).
24. R. W. Sanders *et al.*, *Science* **349**, 154 (2015).
25. P. Dosenovic *et al.*, *Cell* **161**, 1505 (2015).
26. S. G. Hansen *et al.*, *Nature* **502**, 100 (2013

10.1126/science.aac6300

BOOKS *et al.*


Discovered in 2007, "Lyuba" the woolly mammoth was preserved in the Arctic for over 40,000 years.

PHOTO: RIA NOVOSTI/SCIENCE SOURCE

ANCIENT DNA

Raising the dead

Confronting the technical challenges of reversing extinction

By **A. Rus Hoelzel**

Many know that *Star Trek* creator Gene Roddenberry's "beam me up" communicator predated the creation of the flip-top mobile phone by some 30 years. Fewer may appreciate the prescience of some of the ideas in Michael Crichton's *Jurassic Park*, such as the concept of combining ancient and modern genomes. However, the part about creating a park full of dinosaurs was not among those prescient ideas. Or as Beth Shapiro puts it in *How to Clone a Mammoth*, "What? No *Jurassic Park*?"

In the 1980s, the advent of the technique known as the polymerase chain reaction (PCR) created the potential for amplifying DNA from ancient samples, the first step toward de-extinction. DNA from the recently extinct marsupial wolf, *Thylacinus cynocephalus*, was amplified in 1989, followed by claimed amplifications from organisms preserved in amber and even stone fossils, dating back many millions of years. However, the sensitivity of PCR wasn't fully appreciated in the 1980s. We now know, for example, that you can amplify small traces of DNA collected in samples of seawater and use it to identify the fish that recently swam by. Consistent with this, ancient amplifications unfortunately turned out to be modern contamination, and it seems that DNA can't survive millions of years. This book is therefore about the potential resurrection of species lost more recently, such as the woolly mammoth, which went extinct ~4000 years ago.

How to Clone a Mammoth
The Science of De-Extinction
Beth Shapiro
Princeton University Press, 2015. 250 pp.

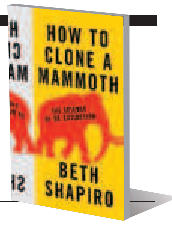

Shapiro is well placed to provide a book on the topic of de-extinction that is rich in anecdote and scientifically precise. She was among those early in this century who worked to determine the potential for ancient DNA amplification (and its limitations), eventually contributing to what is the oldest item verifiably amplified to date (a ~700,000-year-old horse). She has also seemed a consistent voice of reason in the divisive debate over the prospect of de-extinction.

Early on in the book, Shapiro considers which species would make good candidates for de-extinction and discusses the evolution of ideas about what approaches may be possible. Nearly extinct (or perhaps very recently extinct) species may have the best potential for reincarnation because of the availability of living eggs or cells. However, the prospect of finding intact cells from long-extinct species seems slight (even in permafrost).

Shapiro goes through a remarkably long list of potential problems with de-extinction—a cautionary note that it is better to protect endangered species now than to hope for resurrection later. The problems range from the low success rate of cloning (even with fresh, extant materials) to issues associated with the influence of captivity on a newly resurrected organism and the potential impact of its release into ecosystems that have "moved on." What is great about this book is that it is very thorough and cautious throughout. This is the prospect of de-extinction, warts and all.

In the end, though, there probably wouldn't actually be any mammoth warts. The closest prospect for the mammoth (though still not all that close) would be a "designer elephant" in which key genes are engineered to match mammoth sequences. One tricky aspect would be the need to make a reasonably large number of engineered individuals from separate genomes. This is especially true in cases like the elephant, in which the "host" species has a relatively large effective population size. In large, stable populations, recessive variants can be maintained (hitching a ride as heterozygotes). A new population based on one or a few clones would be vulnerable to reduced survival and fertility known as "inbreeding depression" as a result of the homozygous expression of these recessive, sometimes lethal, traits.

The book finishes with a chapter posing the question "Should we?" Here, Shapiro offers an even-handed and clear discussion of the pros and cons. For her, the rationale for pursuing de-extinction is ecosystem revival, a common theme among the scientists who support this work. The cynic in me worries about others motivated by captive display and profit, but hopefully, if de-extinction becomes a reality, such things could be regulated. I am, however, very interested in another prospect the author discusses, a sort of de-extinction "lite." Small endangered populations can lose diversity by chance through a phenomenon known as genetic drift. Once we can figure out which loci are important (still a ways to go for that), perhaps we could reintroduce variation to help endangered species avoid extinction in the first place.

I found this book to be an entertaining and deeply informative read that captures the complexity of both the science and the broader issues raised very well. The next time a film about rampaging Jurassic reptiles is on offer, you could instead settle in with this book and the beverage of your choice and learn about the true potential for species resurrection. Popcorn optional.

10.1126/science.aaa9849

The reviewer is at the School of Biological and Biomedical Sciences, Durham University, South Road, Durham DH1 3LE, UK. E-mail: a.r.hoelzel@durham.ac.uk

IMMUNOLOGY

The quest for a magic bullet

Widely used in science and medicine today, monoclonal antibodies got off to a rocky start

The Lock and Key of Medicine
Monoclonal Antibodies and the Transformation of Healthcare
Lara V. Marks
Yale University Press, 2015. 344 pp.

By **Sudhakaran Prabakaran**

On a cold January evening in 1975, postdoctoral fellow Georges Köhler brought his wife to the lab to keep him company as he checked on his latest experiment. Far from the uneventful evening he anticipated, what he observed that night would transform the world of drug development and disease treatment. "I looked down at the first two plates. I saw these halos.... It was the best result I could think of," he recalls. The halos were evidence that the cells in the petri dish were secreting highly specific antibodies. Dubbed "monoclonal antibodies," or Mabs, they would have a radical influence on both science and medicine in the years that followed.

In her book, *The Lock and Key of Medicine,* Lara Marks presents a compelling, well-researched account of the discovery of Mabs and the development of Mab-based treatments and therapies. The book also narrates the challenges faced by César Milstein (Köhler's postdoctoral adviser) and his collaborators, from patenting their findings to raising money for further testing and scaling up production. It is an excellent account of all the impediments the researchers faced in bringing Mabs from the bench to the market. Personal stories of the major players involved are skillfully interwoven with the narrative, bringing a human face to the drug discovery process.

In the early 1970s, Köhler and Milstein were studying the variable regions of antibodies—the proteins that recognize foreign molecules and tag them for destruction—with the hope of understanding how diverse populations of antibodies are generated by the mammalian immune system. In the course of their studies, they developed a technique that enabled the mass production of antibodies designed to recognize a specific antigen. The technique involved fusing a myeloma cell with an antibody-producing B cell taken from the spleen of an immunized mouse. The B cell provided the immunological specificity, whereas the myeloma lent immortality to the construct.

These hybrid cells, or hybridomas as they were later called, became a vehicle for thousands of other biomedical inventions. However, the initial reception to this breakthrough was lukewarm. When they tried to publish their results, the editors at *Nature* reportedly requested that the article be shortened and did not feature it prominently in the journal, and their patent application was rejected.

César Milstein (left), Georges Köhler (right), and Niels Jerne (not pictured) were awarded the Nobel Prize in 1984 for their work on monoclonal antibodies.

PHOTO: BORJE THURESSON/GETTY IMAGES

Milstein sent samples and protocols of his newly created antibody-secreting cell lines to other research institutions and even trained scientists to generate their own hybridomas. One such scientist who benefited from this goodwill was Hilary Koprowski, director of the Wistar Institute in Philadelphia. The first patents for monoclonal antibodies were granted to Koprowski and his colleagues in October 1979 (for Mabs targeting influenza antigens) and April 1980 (for Mabs targeting tumor antigens). The "Wistar patents" proved controversial in the scientific community, because the antibodies had been created using the cell lines originally supplied by Milstein.

In the years that followed, there was an explosion in Mab research. Some were generated to identify different types of white blood cells, and several proved to be important in investigating HIV/AIDS. The first medical application of this technology used Mabs to purify interferons, signaling proteins that are released by cells in response to the presence of pathogens.

Mabs were soon being used to identify blood group types, an application that radically improved the accuracy and cost of blood typing. This now-routine test has since saved millions of lives.

After these initial success stories, many clinicians and founders of biotech companies began to believe that Mabs were "magic bullets" for diagnosing and curing diseases. In 1979, Koprowski cofounded Centocor, one of the original companies that exploited Mabs to diagnose cancer, cardiovascular disorders, and liver problems. The fortunes of Centocor ebbed and flowed during the 1980s and 1990s. It was acquired by Johnson & Johnson in 1999 and is known today as Janssen Biotech. It is one of the few original companies still in existence today.

In 1995, edrecolomab (Panorex)—a Mab developed in mice—was licensed by German authorities as an adjuvant therapy for postoperative colorectal cancer. It was the first Mab-based cancer therapeutic to proceed to market. In 1997, rituximab (Rituxan), a chimeric (part human and part mouse) Mab, was authorized by the FDA to treat B cell lymphoma. It was later found to be beneficial in the treatment of rheumatoid arthritis as well.

By 2012, there were more than 30 Mab drugs on the market, generating more than \$50 billion in revenue (10 of which generated profits exceeding \$1 billion each). The number of Mab-based therapies (and their market share) will likely increase with time.

Marks has done great justice to the topic, although the book would have been strengthened by the inclusion of additional illustrations and a broader discussion of the impact of Mabs on basic science. This book is in many ways a tribute to Köhler and Milstein, which makes the timing of its publication (just over 40 years since that fateful January evening) all the more appropriate.

The reviewer is at Science Signaling, AAAS, Washington, DC 20005, USA. E-mail: sprabaka@aaas.org

10.1126/science.aac5603

LETTERS

Edited by **Jennifer Sills**

Precision medicine: Look to the mice

BY ALL ACCOUNTS, President Obama's Precision Medicine Initiative (PMI) promising molecular-guided diagnostics, therapeutics, and prevention strategies is eliciting enthusiasm and excitement among clinicians, translational researchers, and patients ("NIH plots million-person megastudy," J. Kaiser, In Depth, 20 February, p. 817). To make this hope reality, the PMI Working Group of the Advisory Committee to the Director (ACD) of the National Institutes of Health (NIH) is holding workshops with stakeholders to discuss and resolve critical issues and challenges before launching NIH's $200 million in funding initiatives later this year. Key to the PMI's success is how to gather, manage, and interpret for clinical benefit the unprecedented amounts of genomic, metabolomic, and other –omic data generated by the planned 1 million plus–person research cohort (*1*). There are many facets to this question, including: the advantages and disadvantages of holding patient data in federated and/or centralized databases; standardization of data generated by multiple testing regimens; deriving data both from electronic health records as well as metadata pertaining to environmental influences; ensuring access to and availability of patient data and information that is sufficiently deidentified to uphold privacy rights; curation and other data manipulation to ensure that data is organized and assembled into a format conducive to secondary and tertiary analyses; and sharing of data with national and international research groups.

Many of the issues regarding data management, accessibility, and interpretation first confronted the mouse research community in the Knockout Mouse Production and Phenotyping (KOMP2) project. KOMP2 was established as part of an international consortium [International Mouse Phenotyping Consortium (IMPC)] to provide a comprehensive description of function for each of the more than 21,000 protein coding genes in the mouse genome. Approaching 4 years into a planned 10-year NIH Common Fund timeline, KOMP2 and its global partners are using a common set of phenotyping tests covering 10 organ systems on sex-balanced cohorts of knockout mice (*2*). This process is similar to how the PMI will examine multiple cohorts of male and female patients according to an agreed-upon set of clinical assays across a broad spectrum of organ systems and disease phenotypes.

From a data management perspective, KOMP2 is now accomplishing in mice what the PMI seeks to accomplish in people. KOMP2 is successfully implementing collaborative solutions to address challenges with phenotyping data from globally distributed cohorts of mice. Biologists, software engineers, and research staff are working together to standardize data through harmonization of test protocols and identification of critical metadata. Access to results is facilitated by central curation of data, transparent statistical analysis, and real-time public posting of curated data from a central website (www.mousephenotype.org) (*3*). (Granted, the absence of privacy and informed consent concerns makes this process simpler for mice than for human studies.) Furthermore, our data meet guidelines for reproducibility of biomedical animal studies (*4*), and our statistical analysis platform is freely available for others to use (*5*).

In addition to data management, results from KOMP2 can provide substantial insight to inform the PMI's effort to define a new molecular taxonomy (*6*). Because we remain largely ignorant of the multiple functions of genes within the mammalian genome, revealing pleiotropy (one gene affecting multiple seemingly unrelated traits) will generate vital new information on genes and disease (*7*). Undoubtedly, many variants of unknown significance will be identified in the PMI 1 million–person cohort. As a majority of genes to be studied by KOMP2 have little or no functional data, our ongoing studies are enabling discoveries beyond what we already know (*8*), revealing essential new knowledge to guide interpretation of the PMI studies planned in humans. As we journey together into this brave new world of precision medicine, we encourage and welcome cooperation of the PMI with KOMP2/IMPC.

K. C. Kent Lloyd,[1]* Terry Meehan,[2] Arthur Beaudet,[3] Steve Murray,[4] Karen Svenson,[4] Colin McKerlie,[5] David West,[6] Iva Morse,[7] Helen Parkinson,[2] Steve Brown,[8] Ann-Marie Mallon,[8] Mark Moore[9]

[1]University of California, Davis, Davis, CA 95616, USA. [2]European Bioinformatics Institute, Hinxton, Cambridge, CB10 1SD, UK. [3]Baylor College of Medicine, Houston, TX 77030, USA. [4]The Jackson Laboratory, Bar Harbor, ME 04609, USA. [5]Toronto Centre for Phenogenomics, Toronto, ON, M5T 3H7, Canada. [6]Children's Hospital Oakland Research Institute, Oakland, CA 94609, USA. [7]Charles River Laboratories, Wilmington, MA 01887, USA. [8]Medical Research Council Harwell, Oxfordshire, OX11 0RD, UK. [9]International Mouse Phenotyping Consortium, Hinxton, Cambridge, CB10 1SD, UK.

*Corresponding author. E-mail: kclloyd@ucdavis.edu

REFERENCES

1. NIH Precision Medicine Initiative (www.nih.gov/precisionmedicine/workshop-20150528.htm).
2. S. D. Brown, M. W. Moore, *Mamm. Genome* **23**, 632 (2012).
3. G. Koscielny *et al.*, *Nucl. Acids Res. Database Issue* **42**, 802 (2014).
4. N. A. Karp *et al.*, *PLOS Biol*. **20**, 13 (2015).
5. N. V. Kurbatova *et al.*, *PLOS ONE* **10**, e0131274 (2015).
6. National Research Council, *Toward Precision Medicine* (National Academies Press, Washington, DC, 2011).
7. A. Oellrich *et al.*, *J. Biomed. Semantics* **5** (suppl. 1), S4 (2014).
8. A. M. Edwards *et al.*, *Nature* **470**, 163 (2011).

Sexism discussion misses the point

TIM HUNT'S RECENT comments on women in science were incredibly inappropriate (*1*). However, as the response has ballooned into a public discussion excoriating pervasive sexism and discrimination among male scientists (*2*), I find myself bewildered by this message.

Personally, the senior male mentors in my life have bent over backwards to advance not only my research and career, but also my mental health and my work-life balance. Although there are certainly men in the sciences who hold negative stereotypes of women, science is a generally socially progressive community. Even Hunt himself seems to have largely been a strong mentor and supporter of women in science (*3*). If he represents the tail end of the distribution for sexism in science, that is a happy reflection of where the mean lies.

By blaming poor male mentors, and focusing our communal attention on a few egregious comments, we are distracting ourselves from a real opportunity to call attention to much more substantial institutional and structural burdens to women

PHOTO: © 145/ANTHONY BRADSHAW/OCEAN/CORBIS

in science. It is an unfortunate biological reality that child-bearing age for women coincides nearly perfectly with the age when scientists' research productivity needs to be the highest. Yet most institutions have woeful basic childcare available, no support for urgent or extended childcare during work-related obligations, inadequate support for maternity needs, financial disincentives to PIs for hiring postdoctoral fellows with children needing insurance coverage or those who are likely to need maternity leave, no insurance coverage for fertility treatment for women who choose to delay reproduction for career reasons, and little way to account for delays in productivity due to time spent in childcare in the faculty hiring process.

This discussion also inadvertently sends a dangerous, and largely untrue, message to young female scientists that they are still likely to be viewed differently and as lesser than their male counterparts. This undermines the confidence of young women and risks becoming a self-fulfilling prophecy.

Although it is fun to attack outspoken sexist outbursts, we can't let this distract us from the more substantial problem at hand: addressing the shortcomings of our scientific institutions to address the many substantial, if mundane, barriers that still impede women from reaching full equality in science.

Hillary S. Young

Department of Ecology, Evolution, and Marine Biology, University of California, Santa Barbara, Santa Barbara, CA 93106, USA.
E-mail: hillary.young@lifesci.ucsb.edu

REFERENCES

1. D. Bilefsky, "Women respond to Nobel Laureate's 'trouble with girls,'" *New York Times* (11 June 2015); www.nytimes.com/2015/06/12/world/europe/tim-hunt-nobel-laureate-resigns-sexist-women-female-scientists.html.
2. S. C. Soper, "What it's like as a 'girl' in the lab," *New York Times* (18 June 2015); www.nytimes.com/2015/06/18/opinion/what-its-like-as-a-girl-in-the-lab.html.
3. A. Errico, "Judge by actions, not words," *Nature* (23 June 2015); www.nature.com/news/judge-by-actions-not-words-1.17823.

Chimpanzees deserve their freedom

SUSAN LARSON THINKS that keeping extraordinarily cognitively complex chimpanzees locked up for years with interaction with only one conspecific, stimulated by tearing magazines and playing with plastic airplanes, is all right ("The scientist behind the 'personhood' chimps," D. Grimm, In Depth, 12 June, p. 1187). That her prisoners are "collaborators" and "willing participants in the project" is a narrative she may need to believe, but we do not.

Larson mistakes our demand that chimpanzees be recognized as "persons" (i.e., an entity with the capacity for a legal right) eligible for habeas corpus relief for a demand they be treated as "people," when the Nonhuman Rights Project actually demands that they be treated as chimpanzees. She claims that she and her team "don't do anything with these chimpanzees that we haven't done on ourselves," when she hasn't locked herself in a cage with one conspecific for 6 years with newspapers to tear and plastic airplanes to manipulate.

Larson's is a voice from a faded era; because the U.S. Fish and Wildlife Service recently reclassified chimpanzees as "endangered" and the National Institutes of Health refuses to fund chimpanzee research, it may be the last such voice we will ever hear.

Steven M. Wise

President and Lead Counsel, Nonhuman Rights Project, Coral Springs, FL 33076, USA.
E-mail: swise@nonhumanrights.org

TECHNICAL COMMENT ABSTRACTS

Comment on "Expectations of brilliance underlie gender distributions across academic disciplines"

Donna K. Ginther and Shulamit Kahn

Leslie *et al.* (Reports, 16 January 2015, p. 262) concluded that "expectations of brilliance" explained the gender makeup of academic disciplines. We reestimated their models after adding measures of disaggregated Graduate Record Examination scores by field. Our results indicated that female representation among Ph.D. recipients is associated with the field's mathematical content and that faculty beliefs about innate ability were irrelevant.
Full text at http://dx.doi.org/10.1126/science.aaa9632

Response to Comment on "Expectations of brilliance underlie gender distributions across academic disciplines"

Andrei Cimpian and Sarah-Jane Leslie

Ginther and Kahn claim that academics' beliefs about the importance of brilliance do not predict gender gaps in Ph.D. attainment beyond mathematics and verbal test scores. However, Ginther and Kahn's analyses are problematic, exhibiting more than 100 times the recommended collinearity thresholds. Multiple analyses that avoid this problem suggest that academics' beliefs are in fact uniquely predictive of gender gaps across academia.
Full text at http://dx.doi.org/10.1126/science.aaa9892

Published by AAAS

TECHNICAL COMMENT

WOMEN IN SCIENCE

Comment on "Expectations of brilliance underlie gender distributions across academic disciplines"

Donna K. Ginther[1,2]* and Shulamit Kahn[3]

Leslie *et al*. (Reports, 16 January 2015, p. 262) concluded that "expectations of brilliance" explained the gender makeup of academic disciplines. We reestimated their models after adding measures of disaggregated Graduate Record Examination scores by field. Our results indicated that female representation among Ph.D. recipients is associated with the field's mathematical content and that faculty beliefs about innate ability were irrelevant.

We read Leslie *et al.*'s paper (*1*) with great interest, having completed a review on academic women in science, technology, engineering, and mathematics (STEM) disciplines with our colleagues Stephen Ceci and Wendy Williams (*2*). Leslie *et al.* showed that "women are underrepresented in fields whose practitioners believe that raw, innate talent is the main requirement for success" and argued that this is "because women are stereotyped as not possessing such talent." We reexamined this conclusion and found that their results were not supported by the data once disaggregated Graduate Record Examination (GRE) scores were included in the model. Female representation was associated with the field's math-intensive content—especially relative to the field's verbal content—and, controlling for this, faculty beliefs about innate ability were irrelevant.

This is not to say that we think beliefs about ability are unimportant—quite the opposite. We return to this after critiquing Leslie *et al.*'s empirical results.

Reading Leslie *et al.*, we were immediately struck by the similarity between its Fig. 1 (graphing fields by percentage female and ability beliefs) and figure 9 in our own work (*2*) (graphing percentage female and average GRE quantitative scores). Below, we replicated these figures for 28 of the 30 fields used in Leslie *et al.*, excluding two fields for which we could not match GRE scores. The correlation between the percentage of female Ph.D.s and GRE quantitative score was –0.79 ($P < 0.0001$), whereas the correlation with ability beliefs was a much smaller –0.58 ($P = 0.0012$) in these 28 fields.

We therefore performed our own regression analysis using Leslie *et al.*'s survey data merged with data on the 2011–2013 GRE scores (*3*). We included three GRE variables by field (identified as the person's desired area of study): the field's average quantitative GRE score, the field's average GRE verbal score, and the ratio of the quantitative to verbal scores. We add this ratio because research has shown (*4*, *5*) that math ability relative to verbal ability (what economists refer to as a comparative advantage in mathematics) is an important influence on a person's choice of major or occupational field.

Before we present our results, we note that Leslie *et al.* did compare the percentage female with the composite GRE scores—averaging standardized quantitative, verbal, and analytical writing scores—and found no significant correlation. However, we found that it is not overall ability, but mathematical ability, especially relative to verbal ability, that predicted female representation.

We identified GRE scores for 28 of the 30 fields addressed by Leslie *et al.*. They had only matched 18 (*6*). As examples, we classified molecular biology as "biological and biomedical sciences" and Spanish as "foreign languages and literatures." We could not match GRE scores for the fields of linguistics and music composition.

In the first column of Table 1, we replicated Leslie *et al.*'s final analysis (model 5) for all 30 fields (presenting standardized coefficients and t statistics, as they did). For comparison with our later results, in the second column, we reestimated this model using the 28 fields with GRE scores. In the third column, we introduced the separate GRE scores and the ratio of GRE quantitative and verbal scores. We observed that the GRE quantitative score was positively associated with women in these fields (11.98, $P = 0.08$), whereas the GRE verbal score (–6.92, $P = 0.07$) and the ratio GRE scores (–15.16, $P = 0.07$) were negatively associated with the percentage of female Ph.D.s. These coefficients were jointly significant ($P = 0.02$), and the adjusted R^2 increased from 0.494 in Leslie *et al.*'s model 5 to 0.645. Most notably, we found that adding these variables rendered the coefficient on field-specific ability beliefs insignificant and decreased the magnitude of its effect by two-thirds.

We were also concerned that the number of respondents per field in (*1*) differed widely, from 8 to 143. We therefore weighted both their model 5 and our version by the number of observations

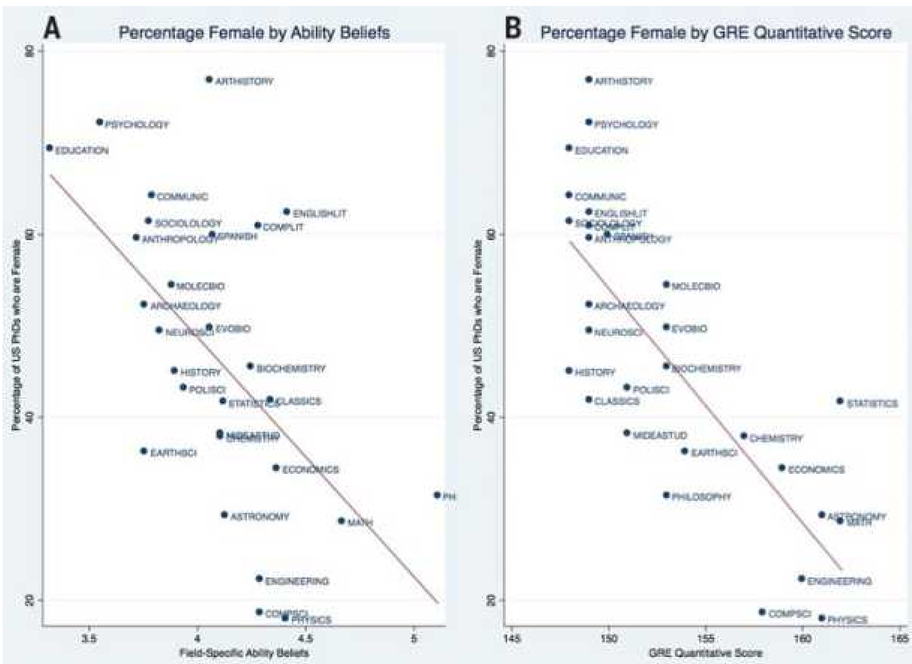

Fig. 1. Relationship between percentage female, ability beliefs, and quantitative scores. (**A**) Correlation between the percentage of U.S. Ph.D.s who are female and field-specific ability beliefs. (**B**) Correlation between the percentage of U.S. Ph.D.s who are female and GRE quantitative score. [Data from (*1*) and (*3*).]

[1]Department of Economics, Center for Science, Technology and Economic Policy, Institute for Policy and Social Research, University of Kansas, Lawrence, KS 66045, USA. [2]National Bureau of Economic Research, Cambridge, MA 02138, USA. [3]Questrom School of Business, Boston University, Boston, MA 02215, USA.
*Corresponding author. E-mail: dginther@ku.edu

Table 1. Estimates of the impact of field-specific beliefs and GRE scores on the percentage of U.S. Ph.D.s who are female. *T* statistics in brackets.

Variables	(1) Model 5	(2) 28 Fields	(3) Add GRE scores	(4) Weighted	(5) Weighted and GRE scores	(6) Drop ratio
STEM indicator	−0.28	−0.39	−0.04	−0.20	0.02	−0.12
	[−1.07]	[−1.41]	[−0.14]	[−0.83]	[0.10]	[−0.47]
Field-specific ability beliefs	−0.56**	−0.51**	−0.16	−0.55**	−0.03	−0.32
	[−3.44]	[−2.99]	[−0.80]	[−3.37]	[−0.13]	[−1.60]
On-campus hours worked	0.02	−0.01	−0.25	0.002	−0.04	−0.03
	[0.08]	[−0.04]	[−1.08]	[0.01]	[−0.20]	[−0.16]
Selectivity	0.24	0.11	0.07	0.24	0.16	0.12
	[1.55]	[0.62]	[0.49]	[1.58]	[1.11]	[0.75]
Systemizing versus empathizing	−0.06	−0.05	0.19	−0.12	−0.16	0.08
	[−0.24]	[−0.18]	[0.69]	[−0.51]	[−0.62]	[0.31]
GRE quantitative score			11.98		14.29*	−0.55*
			[1.83]		[2.39]	[−2.31]
GRE verbal score			−6.92		−7.39*	−0.04
			[−1.92]		[−2.49]	[−0.30]
Ratio: GRE quantitative/verbal			−15.16		−17.13*	
			[−1.93]		[−2.48]	
Observations	30	28	28	30	28	28
Adjusted *R*-squared	0.494	0.494	0.645	0.634	0.749	0.685
R-squared	0.582	0.588	0.750	0.697	0.823	0.766

***$P < 0.001$; **$P < 0.01$; *$P < 0.05$

in each field. This weighting changed their estimates very little (column 4). In our version (column 5), it made all GRE variables significant and reduced the coefficient on the field-specific ability beliefs to basically zero (–0.03, $P = 0.89$).

Finally, in column 6, we drop the GRE ratio as a test. This is a less accurate fit than column 5 ($F = 6.15$, $P = 0.02$). The coefficient on the quantitative GRE score is negative and significant (–0.55, $P = 0.03$). The coefficient on ability is not ($P = 0.13$).

We conclude that Leslie *et al.*'s work has not convincingly identified a robust association, let alone a causal relationship, running from beliefs about innate ability to the percentage of female Ph.D.s in a given field. While field-specific ability beliefs were negatively correlated with the percentage of female Ph.D.s in a field, this correlation is likely explained by women being less likely than men to study these math-intensive fields, combined with the fact that people in these fields are more likely to believe that ability is innate. As other evidence reviewed in (*2*) has shown, math ability relative to verbal ability is particularly important in decisions to enter math-intensive fields, consistent with the finding that the ratio of GRE quantitative to verbal ability was negatively associated with the percentage female (–17.13, $P = 0.02$) in our preferred specification (column 5). Table 2 contains data that we included and used in the preceding analysis.

Moreover, as our recent survey article (*2*) indicated, there is considerable evidence that it is not the stereotypical beliefs of college faculty that are the core reason that women do not enter math-intensive fields. Rather, it is the stereotypical beliefs of the teachers and parents of younger children that become part of the self-fulfilling belief systems of the children themselves from a very early age (*7*).

That said, we surely agree with the sentiment that all children, and girls in particular, should be taught that life—and math—is 99% perspiration. Numerous educational experiments have shown that if a person believes in their own ability to learn material, they will master that material (*8*, *9*). This is particularly crucial in STEM disciplines, where women continue to be underrepresented. If girls believe they can, they can.

REFERENCES AND NOTES

1. S. J. Leslie, A. Cimpian, M. Meyer, E. Freeland, *Science* **347**, 262–265 (2015).
2. S. J. Ceci, D. K. Ginther, S. Kahn, W. M. Williams, *Psychol. Sci. Public Interest* **15**, 75–141 (2014).
3. Educational Testing Service, GRE Guide to Use of Scores, 2013-2014; www.ets.org/s/gre/pdf/gre_guide.pdf.
4. M. T. Wang, J. S. Eccles, S. Kenny, *Psychol. Sci.* **24**, 770–775 (2013).
5. D. Lubinski, C. P. Benbow, *Perspect. Psychol. Sci.* **1**, 316–345 (2006).
6. Although their text says that they matched 19 fields, their supplementary materials show GRE composite scores for 18.
7. V. Lavy, E. Sand, National Bureau of Economic Research Working Paper #20909 (2015).
8. C. J. Good, J. Aronson, M. Inzlicht, *J. Appl. Dev. Psychol.* **24**, 645–662 (2003).
9. C. Bagès, D. Martinot, *Br. J. Soc. Psychol.* **50**, 536–543 (2011).

ACKNOWLEDGMENTS

We acknowledge financial support from NIH grant 1R01AG36820-01.

20 February 2015; accepted 29 May 2015
10.1126/science.aaa9632

Table 2. Variables added to the analysis. We added the following variables: s_e, indicator for STEM used by (*1*).; stem, NSF's definition of STEM disciplines; greverbal, average GRE verbal score by field; grewriting, average GRE writing score by field; ratio, ratio of GRE quantitative score/GRE verbal score by field; number, number of survey respondents by field in (*1*); inours, fields with nonmissing GRE scores.

Discipline	gremath	stem	s_e	greverbal	grewriting	ratio	number	inours
ANTHROPOLOGY	149	1	0	156	4.1	0.955128	69	1
ARCHEOLOGY	149	1	0	156	4.1	0.955128	30	1
ARTHISTORY	149	0	0	156	4.1	0.955128	29	1
ASTRONOMY	161	1	1	156	3.9	1.032051	35	1
BIOCHEMISTRY	153	1	1	153	3.9	1	29	1
CHEMISTRY	157	1	1	153	3.8	1.026144	83	1
CLASSICS	149	0	0	157	4.2	0.949045	24	1
COMMUNIC	148	1	0	151	3.8	0.980132	43	1
COMPLIT	149	0	0	157	4.2	0.949045	43	1
COMPSCI	158	1	1	148	3.3	1.067568	47	1
EARTHSCI	154	1	1	154	3.9	1	54	1
ECONOMICS	159	1	0	154	3.9	1.032467	85	1
EDUCATION	148	0	0	151	3.8	0.980132	58	1
ENGINEERING	160	1	1	150	3.5	1.066667	103	1
ENGLISHLIT	149	0	0	157	4.2	0.949045	66	1
EVOBIO	153	1	1	153	3.9	1	27	1
HISTORY	148	0	0	156	4.1	0.948718	101	1
LINGUISTICS		1	0				39	0
MATH	162	1	1	154	3.8	1.051948	133	1
MIDEASTUD	151	0	0	156	4.2	0.967949	8	1
MOLECBIO	153	1	1	153	3.9	1	60	1
MUSICTH		0	0				28	0
NEUROSCI	149	1	1	150	3.7	0.993333	42	1
PHILOSOPHY	153	0	0	160	4.4	0.95625	58	1
PHYSICS	161	1	1	156	3.9	1.032051	104	1
POLISCI	151	1	0	156	4.2	0.967949	112	1
PSYCHOLOGY	149	1	0	152	3.9	0.980263	143	1
SOCIOLOLOGY	148	1	0	152	3.9	0.973684	117	1
SPANISH	150	0	0	155	4	0.967742	22	1
STATISTICS	162	1	1	154	3.8	1.051948	28	1

TECHNICAL RESPONSE

WOMEN IN SCIENCE

Response to Comment on "Expectations of brilliance underlie gender distributions across academic disciplines"

Andrei Cimpian[1]* **and Sarah-Jane Leslie**[2]*

Ginther and Kahn claim that academics' beliefs about the importance of brilliance do not predict gender gaps in Ph.D. attainment beyond mathematics and verbal test scores. However, Ginther and Kahn's analyses are problematic, exhibiting more than 100 times the recommended collinearity thresholds. Multiple analyses that avoid this problem suggest that academics' beliefs are in fact uniquely predictive of gender gaps across academia.

In a nationwide study of academics in 30 disciplines, we found that the distribution of gender gaps in Ph.D. attainment is predicted by the extent to which practitioners of a given discipline believe that success requires raw, unteachable aptitude (*1*). These field-specific ability beliefs combine with cultural stereotypes linking men, but not women, with such inherent brilliance, thereby decreasing women's participation. Ginther and Kahn claim that these field-specific ability beliefs are irrelevant to female representation at the Ph.D. level (*2*). According to Ginther and Kahn, what instead accounts for the pattern of gender gaps is the extent to which fields emphasize mathematics-intensive content matter. Ginther and Kahn base this conclusion on regression analyses in which Graduate Record Examination (GRE) scores predict female representation but ability beliefs do not.

Ginther and Kahn's preferred regression models (namely, 3 and 5) are problematic because they include three variables that are highly redundant with one another: the quantitative GRE score, the verbal GRE score, and their ratio. A more appropriate modeling strategy would be, for example, to include just one of the GRE scores and their ratio, as other researchers have done (*3*). Models with multiple variables that are highly correlated encounter a problem known as multicollinearity, which inflates standard errors and leads to unreliable results (*4*–*6*). A typical means of quantifying multicollinearity is to calculate a variance inflation factor (VIF), which is the ratio between a predictor's actual variance in a model and its variance, assuming that it was uncorrelated with the other predictors in the model. The statistics literature typically places an upper bound of 10 on the recommended VIFs (*5*, *6*); caution is recommended in interpreting models with VIFs above this threshold. By comparison, Ginther and Kahn's models 3 and 5 have average VIFs of more than 1100—more than 110 times the conventional threshold. Moreover, the VIFs for the variables of most interest to Ginther and Kahn (namely, the quantitative GRE scores and the ratio of quantitative to verbal scores) have VIFs ranging from 3258 to 5046. As a sign of the problems caused by this extreme form of collinearity, note the unusual values for the standardized regression coefficients of these variables in Ginther and Kahn's models 3 and 5. For instance, the quantitative:verbal GRE ratio has a standardized coefficient of –17.13 in their model 5. Taken at face value, this coefficient suggests that an increase of 1 standard deviation in the quantitative:verbal ratio would be accompanied by a decrease of 17.13 standard deviations in a field's percentage of female Ph.D.'s (which, to provide an intuitive metric, is equivalent to a decrease that is more than 17 times the difference in female Ph.D.'s between history and mathematics). Such implausible estimates are not uncommon in highly collinear models (*5*, *6*).

Contrary to Ginther and Kahn's claims, we found evidence that academics' ability beliefs predict female representation in a wide range of models that include disaggregated GRE scores, as well as measures of a field's relative emphasis on mathematics versus verbal ability, and that also have acceptable VIFs. We include 22 such models in Table 1. The top half of the table displays unweighted models, and the bottom half displays weighted models (in keeping with Ginther and Kahn's models 4 to 6). As analytic weights, we used the inverse of the variance of the field-specific ability beliefs, which was calculated from the raw, individual-level data. These inverse-variance analytic weights allow fields whose ability beliefs are estimated more precisely (that is, with lower variance) to carry more weight in the regression models (*7*). In contrast, Ginther and Kahn used as their analytic weights the number of respondents within each field, which here does not track the precision with which ability beliefs were measured at the field level: There was no correlation between the number of respondents within a field and the variance of the ability belief estimate for that field, $r(28) = -0.01$, $P = 0.929$. There is thus no reason to penalize (i.e., downweight) fields that are small but whose ability beliefs were nevertheless measured with as much precision as those of larger fields. Within each half of Table 1, the models are sorted in increasing order of average VIF; thus, as one moves down the table, the models become more collinear. All of the models in Table 1 include as predictors the ability beliefs of each field's practitioners and the three competing variables tested in (*1*) (namely, on-campus hours worked, selectivity, and systemizing versus empathizing; these coefficients are not displayed in the table). In addition, the models include various permutations of the following GRE-based variables: the quantitative score, the verbal score, the analytical writing score, the quantitative:verbal ratio score, and the quantitative–verbal difference score. Adjusting for quantitative GRE scores provides a conservative test of our hypothesis, as academics and nonacademics alike believe that success in mathematics depends largely on raw ability (*1*, *8*). Thus, young men and women's quantitative GRE scores may already reflect the influence of mathematics-specific ability beliefs, so adjusting for these scores in our analyses may underestimate the true impact of ability beliefs on gender gaps in representation.

The results displayed in Table 1 make it clear that academics' ability beliefs are a significant predictor of female representation above and beyond whether a discipline (i) requires mathematical ability (as indicated by the quantitative GRE score) and (ii) privileges this ability relative to verbal ability (as indicated by the quantitative: verbal ratio or the quantitative–verbal difference) (see, e.g., models 7, 8, 9, 20, and 21). More generally, academics' beliefs are a statistically reliable predictor of gender gaps in all 22 models with acceptable average VIFs. Additional models in which we weighted the observations by the inverse of the standard error of the field-specific ability beliefs, rather than the inverse of their variance, revealed the same results [$Ps \leq 0.063$ for ability beliefs in parallel versions of models 13 to 23 (not shown)]. Academics' ability beliefs were also a significant predictor of gender gaps when we used the National Science Foundation's definition of science, technology, engineering, and mathematics (STEM) disciplines, as supplied by Ginther and Kahn [$Ps \leq 0.029$ for parallel versions of models 1 to 11 and 13 to 23 (not shown)]. It is only in models whose average VIFs are greater than 1000 (models 12 and 24 in Table 1, which parallel Ginther and Kahn's models 3 and 5) that ability beliefs no longer predict female representation.

In light of these analyses, the claims we made in Leslie, Cimpian *et al.* (*1*) remain valid as originally stated: Fields whose practitioners idolize brilliance and genius have fewer women.

[1]Department of Psychology, University of Illinois, Champaign, IL 61821, USA. [2]Department of Philosophy, Princeton University, Princeton, NJ 08544, USA.
*Corresponding author. E-mail: acimpian@illinois.edu (A.C.); sjleslie@princeton.edu (S.-J.L.)

Table 1. Multiple regression models predicting women's Ph.D. representation. The table displays standardized coefficients (and *P* values) from models predicting female representation at the Ph.D. level (*10*) on the basis of field-specific ability beliefs; the three control variables in (*1*) (on-campus hours worked, selectivity, and systemizing versus empathizing; coefficients not shown); a STEM indicator variable; and various combinations of quantitative, verbal, and analytical writing GRE scores. Dashes indicate that a predictor was not included in the model. All models included the 28 disciplines for which GRE scores were available, as supplied in (*2*). The *P* values were calculated using standard errors that were robust to heteroskedasticity (*9*). We used the inverse of the variance of the field-specific ability beliefs as analytic weights.

Weighting?	Model no.	Average VIF*	Field-specific ability beliefs	Quantitative GRE	Verbal GRE	Analytical writing GRE	Quantitative/ verbal GRE ratio	Quantitative/ verbal GRE difference
No	1	3.38	−0.53 (*P* = .001)	—	—	—	−0.49 (*P* = .011)	—
No	2	3.38	−0.53 (*P* = .001)	—	—	—	—	−0.49 (*P* = .014)
No	3	3.52	−0.37 (*P* = .015)	−0.63 (*P* = .004)	—	—	—	—
No	4	3.53	−0.38 (*P* = .037)	−0.63 (*P* = .004)	+0.01 (*P* = .935)	—	—	—
No	5	3.95	−0.38 (*P* = .037)	—	−0.33 (*P* = .092)	—	—	−0.76 (*P* = .004)
No	6	3.96	−0.37 (*P* = .043)	—	−0.34 (*P* = .076)	—	−0.77 (*P* = .003)	—
No	7	5.59	−0.39 (*P* = .031)	−0.58 (*P* = .104)	—	—	−0.06 (*P* = .870)	—
No	8	5.67	−0.38 (*P* = .037)	−0.61 (*P* = .092)	[Dropped out][†]	—	—	−0.03 (*P* = .935)
No	9	5.67	−0.38 (*P* = .037)	−0.61 (*P* = .092)	—	—	—	−0.03 (*P* = .935)
No	10	9.26	−0.39 (*P* = .030)	−0.48 (*P* = .231)	−0.39 (*P* = .533)	+0.48 (*P* = .545)	—	—
No	11	25.27	−0.39 (*P* = .030)	−1.20 (*P* = .160)	[Dropped out][†]	+0.48 (*P* = .545)	—	+0.87 (*P* = .533)
No	12[‡]	1120.82	−0.17 (*P* = .329)	+11.90 (*P* = .024)	−6.88 (*P* = .018)	—	−15.06 (*P* = .017)	—
Yes	13	3.46	−0.56 (*P* = .001)	—	—	—	−0.47 (*P* = .014)	—
Yes	14	3.47	−0.57 (*P* = .001)	—	—	—	—	−0.46 (*P* = .017)
Yes	15	3.58	−0.40 (*P* = .012)	−0.60 (*P* = .004)	—	—	—	—
Yes	16	3.66	−0.40 (*P* = .036)	−0.60 (*P* = .005)	+0.01 (*P* = .999)	—	—	—
Yes	17	4.13	−0.40 (*P* = .036)	[Dropped out][†]	−0.35 (*P* = .084)	—	—	−0.73 (*P* = .005)
Yes	18	4.13	−0.40 (*P* = .036)	—	−0.35 (*P* = .084)	—	—	−0.73 (*P* = .005)
Yes	19	4.15	−0.38 (*P* = .042)	—	−0.36 (*P* = .070)	—	−0.75 (*P* = .004)	—
Yes	20	5.77	−0.41 (*P* = .030)	−0.58 (*P* = .094)	—	—	−0.03 (*P* = .936)	—
Yes	21	5.86	−0.40 (*P* = .036)	−0.60 (*P* = .084)	—	—	—	−0.01 (*P* = .999)
Yes	22	9.71	−0.41 (*P* = .034)	[Dropped out][†]	−0.59 (*P* = .234)	+0.36 (*P* = .668)	—	−0.60 (*P* = .214)
Yes	23	10.13	−0.41 (*P* = .034)	−0.50 (*P* = .214)	−0.31 (*P* = .652)	+0.36 (*P* = .668)	—	—
Yes	24[§]	1205.87	−0.16 (*P* = .403)	+11.55 (*P* = .027)	−7.15 (*P* = .020)	—	−14.81 (*P* = .019)	—

*VIF, Variance inflation factor. The models are sorted in increasing order of the average VIF of their predictors (where higher VIFs indicate higher collinearity in the model). †The variable dropped out of the model because of collinearity. ‡Parallel to Ginther and Kahn's model 3. The results are not an exact match because we used more than two-decimal precision for the variables from (*1*) and robust standard errors. §Parallel to Ginther and Kahn's model 5. The results are not an exact match because we used more than two-decimal precision for the variables from (*1*) and robust standard errors, and weighted the observations by the inverse of the variance of a field's ability beliefs (rather than its sample size).

REFERENCES AND NOTES

1. S. J. Leslie, A. Cimpian, M. Meyer, E. Freeland, *Science* **347**, 262–265 (2015).
2. D. K. Ginther, S. Kahn, *Science* **349**, 391 (2015).
3. C. Riegle-Crumb, B. King, E. Grodsky, C. Muller, *Am. Educ. Res. J.* **49**, 1048–1073 (2012).
4. J. Fox, *Applied Regression Analysis, Linear Models, and Related Methods* (SAGE, Thousand Oaks, CA, 1997).
5. S. Chatterjee, A. S. Hadi, B. Price, *Regression Analysis by Example* (Wiley, New York, ed. 3, 2000).
6. M. H. Kutner, C. J. Nachtsheim, J. Neter, *Applied Linear Regression Models* (McGraw-Hill, New York, ed. 4, 2004).
7. J. M. Wooldridge, *Introductory Econometrics: A Modern Approach* (Cengage, Mason, OH, ed. 5, 2012).
8. M. Meyer, A. Cimpian, S. J. Leslie, *Front. Psychol.* **6**, 235 (2015).
9. H. White, *Econometrica* **48**, 817–830 (1980).
10. National Science Foundation, Survey of Earned Doctorates (2011); www.nsf.gov/statistics/srvydoctorates.

ACKNOWLEDGMENTS

We thank J. Robinson-Cimpian, D. Miller, M. Johnston, and the members of the Cognitive Development Laboratory at the University of Illinois for helpful comments. This work was supported by University of Illinois research funds to A.C. and NSF grant BCS-1226942 to S.-J.L.

17 March 2015; accepted 29 May 2015
10.1126/science.aaa9892

RESEARCH

Beyond origami: A way to fold thick materials

Chen et al., *p. 396*

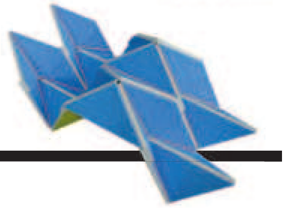

IN *SCIENCE* JOURNALS

Edited by **Stella Hurtley**

Xanthomonas oryzae disease lesions on rice plants

PLANT PATHOGENS

Rice is on the lookout for bugs

Xanthomonas oryzae (Xoo) is a serious bacterial pathogen that severely limits rice yields in Africa and Asia. Rice defends itself against Xoo and other bacterial pathogens by expressing a particular cell-surface immune receptor protein. Pruitt *et al.* identified a Xoo protein that is the target of the rice immune evasion machinery. Xoo lacking this protein can attack rice unimpeded. This insight could help crop scientists help rice win the rice-Xoo arms race. — BJP

Sci. Adv. 10.1126/ sciadv.1500245 (2015).

STRETCHY ELECTRONICS

Composite stretchable conducting wires

Think how useful a stretchable electronic "skin" could be. For example you could place it over an aircraft fuselage or a body to create a network of sensors, processors, energy stores, or artificial muscles. But it is difficult to make electronic interconnects and strain sensors that can stretch over such surfaces. Liu *et al*. created superelastic conducting fibers by depositing carbon nanotube sheets onto a prestretched rubber core (see the Perspective by Ghosh). The nanotubes buckled on relaxation of the core, but continued to coat it fully and could stretch enormously, with relatively little change in resistance. — MSL

Science, this issue p. 400; see also p. 382

NEURODEVELOPMENT

Keeping synaptic plasticity plastic

Neuronal synapses in the brain adjust according to shifting demands as we experience the world. This synaptic plasticity forms the basis for critical periods in the visual and somatosensory systems. Greenhill *et al*. have now found, in mice, a critical period for the development of plasticity itself. At the core is a protein that in its mutant form is associated with schizophrenia. Disrupting this protein's function temporarily during early development caused a failure in brain plasticity in adult mice. — PJH

Science, this issue p. 424

AUTOIMMUNE DISEASE

Trafficking from bedside to bench

Typically in translational research, a discovery in cell or molecular biology is later exploited to improve patient care. Occasionally, information flows in the opposite direction. Lo *et al*. found that patients with an autoimmune disorder caused by deficiency of a protein called LRBA responded dramatically to the drug abatacept (see the Perspective by Sansom). Abatacept contains a segment of a potent inhibitory immune receptor, CTLA4. Experiments prompted by this observation revealed the relationship between the two proteins: LRBA controls the intracellular trafficking and degradation of CTLA4. This information may further improve patient care, because other clinically approved drugs have the desired mechanism of action with potentially fewer side effects. — PAK

Science, this issue p. 436; see also p. 377

NANOCATALYSTS

Etching platinum nanocage catalysts

Although platinum is an excellent catalyst for the oxygen reduction

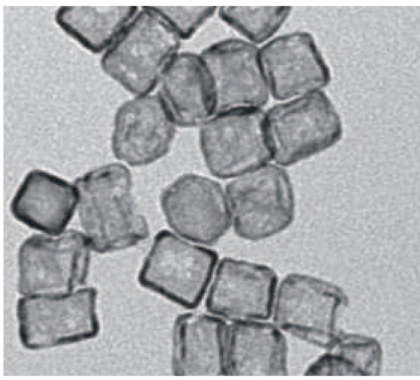

PHOTOS: (TOP TO BOTTOM) CHEN *ET AL*.; NIGEL CATTLIN/SCIENCE SOURCE; XIA LABORATORY

reaction that occurs in fuel cells, its scarcity continues to drive efforts to improve its utilization. Zhang *et al*. made nanocages of platinum by coating palladium nanocrystals with only a few layers of platinum and then etching away the palladium core (see the Perspective by Strasser). Platinum nanocages made using nanoscale octahedra and cubes of palladium displayed different catalytic activity for the oxygen reduction reaction. — PDS

Science, this issue p. 412; see also p. 379

QUANTUM INFORMATION

Making hybrid quantum information systems

Different physical implementations of qubits—quantum bits—each have their pros and cons. An appealing idea is to combine them into hybrid architectures, taking advantage of their respective strengths. Tabuchi *et al*. placed a ferromagnetic sphere and a superconducting qubit in a cavity and used an electromagnetic mode of the cavity as the mediator between the two. They achieved strong coupling between a collective magnetic mode of the sphere and the qubit. Viennot *et al*. coupled a single spin in a double quantum dot to photons in a cavity. Both approaches hold promise for future applications. — JS

Science, this issue pp. 405 and 408

EVOLUTION

Snakes' four-legged missing link

It may surprise you to learn that snakes, like us, are tetrapods derived from an ancient four-legged ancestor. Martill *et al*. describe a fossil from the Brazilian Cretaceous period that contains a snakelike species that is elongate and serpentine, with both hind- and forelimbs (see the Perspective by Evans). This species appears to have been a burrower and shows clearly the early transitional stages from a lizardlike body plan to the smooth legless snakes we know today. — SNV

Science, this issue p. 416; see also p. 374

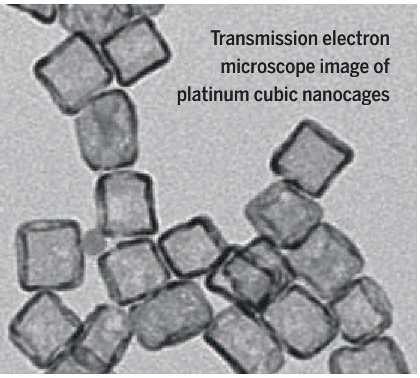

Transmission electron microscope image of platinum cubic nanocages

ILLUSTRATION: V. ALTOUNIAN/*SCIENCE*

METABOLISM

Counteracting the effects of a bad diet

Obesity is a risk factor for metabolic disorders. These include insulin resistance, which can lead to type 2 diabetes, and hepatic steatosis, in which fat accumulates in the liver. By inhibiting β-adrenergic signaling, the kinase GRK2 decreases adipose tissue function. GRK2 also decreases insulin sensitivity. Vila-Bedmar *et al.* genetically ablated GRK2 in adult mice after they had become obese and developed insulin resistance by eating a high-fat diet. GRK2 deletion prevented these mice from gaining more weight and from developing hepatic steatosis on the high-fat diet. It also improved their sensitivity to insulin. — WW

Sci. Signal. **8**, ra73 (2015).

DEEP BIOSPHERE

A deep sleep in coal beds

Deep below the ocean floor, microorganisms from forest soils continue to thrive. Inagaki *et al*. analyzed the microbial communities in several drill cores off the coast of Japan, some sampling more than 2 km below the seafloor (see the Perspective by Huber). Although cell counts decreased with depth, deep coal beds harbored active communities of methanogenic bacteria. These communities were more similar to those found in forest soils than in other deep marine sediments. — NW

Science, this issue p. 420; see also p. 376

IN OTHER JOURNALS

Edited by **Kristen Mueller** *and* **Jesse Smith**

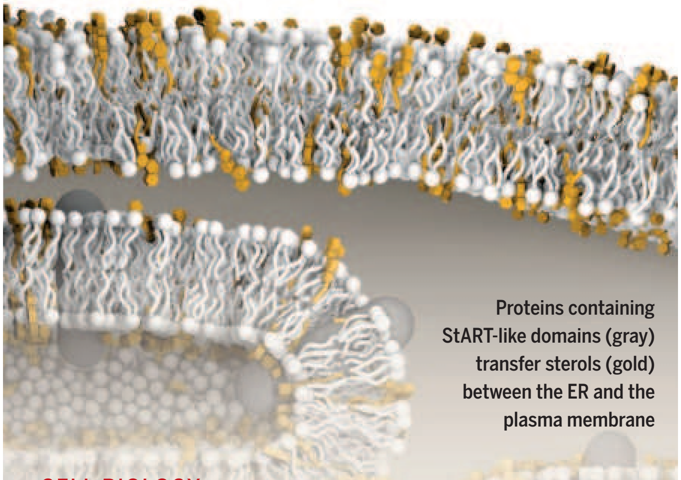

Proteins containing StART-like domains (gray) transfer sterols (gold) between the ER and the plasma membrane

CELL BIOLOGY

Making a StART on sterol transport

Different organelles and membranes within cells contain different sets of lipids. Sterols are key components of cellular membranes, and their trafficking within cells is poorly understood. Sterols must traffic between the endoplasmic reticulum (ER) and the cell surface, but do so via a nonvesicular route. Gatta *et al.* examined this fundamental process in yeast. They found a class of proteins involved in the transfer of sterols between the ER and the plasma membrane (PM) that contained so-called StART-like (for steroidogenic acute regulatory transfer) domains. These ER membrane proteins localized at specific ER-PM contact sites and bound sterols. Efficient PM-to-ER sterol transport required not only StART-like domain–containing proteins themselves, but also their proper localization at the contact sites. — SMH

eLife **4** e07253 (2015).

PSYCHOLOGY

Learning while listening to a foreign language

Speech not only conveys information in the form of the words uttered, but it also provides auditory cues that identify the speaker. Orena *et al*. now show that knowledge of the language spoken helped listeners to identify a speaker. The authors compared English-monolingual Montréal residents who could not understand spoken French or speak French themselves, to a similar set of residents of Connecticut, who were not regularly exposed to French. Montréal residents were better than the Connecticut residents at identifying the French-speaker voices, demonstrating that mere exposure improves language skills. — GJC

Cognition **143**, 36 (2015).

GENETIC ENGINEERING

SLIDE-ing to promote biosecurity

One hurdle facing the widespread use of genetically engineered organisms, such as probiotics or anticancer agents, is controlling their ability to reproduce. Lopez and Anderson developed one technique to do this, called "SLIDE" (synthetic auxotroph based on a ligand-dependent essential gene). Organisms that express SLIDE can only grow when supplied with a particular

Kangaroos and other marsupials favor using their left forelimbs over their right

EVOLUTION

Lefties find marsupial friends

As most lefties know, we live in a right-handed world. Scientists have long thought that such handedness is largely unique to humans; however, Giljov *et al*. now report that marsupials show handedness, too. Surprisingly, these wallabies and kangaroos preferred to predominantly use their left forelimbs, rather than their right. Unlike in humans, handedness in marsupials did not correlate with gender, and more bipedal than quadrupedal marsupial species exhibited handedness. Handedness did not associate with phylogenetic relationships between marsupial species, suggesting that ecological adaptations may have driven such preferences. Thus, yet another characteristic thought to be unique to humans falls by the wayside, or rather, to the wallabies. — PJH

Curr. Biol. 10.1016/j.cub.2015.05.043 (2015).

compound. Working with the bacterium *Escherichia coli*, the authors mutated genes essential for *E. coli*'s viability, so that the hydrophobic cores of the encoded proteins could be filled by a nontoxic, bioavailable complementing compound. The technology was easy and cheap, and bacteria engineered to express multiple SLIDE alleles showed limited escape. — BJ

ACS Synth. Biol. 10.1021/acssynbio.5b00085 (2015).

EDUCATION

Academic effort hindered by peer pressure

Allowing promising adolescents to keep their academic efforts private could prevent them from reducing their efforts in order to fit in with lower-performing classmates. Bursztyn and Jensen describe a natural experiment showing that effort among the highest performers on a computerized remedial tutoring system diminished after the system began to identify top performers for all users to see. Their field experiment offered free training for a college admissions test to students who took both honors and non-honors classes. If the offer was made during a non-honors class, enrollment was lower if students were told that their decision would be shared with the class, rather than kept private. There was no difference between public and private when offers were made during an honors class. — BW

Quart. J. Econ. 10.1093/qje/qjv021 (2015).

ORGANIC CHEMISTRY

Boron juggling makes two bonds in a row

Suzuki coupling is a widely used chemical reaction to make carbon-carbon bonds. Essentially, the technique relies on a boron substituent to activate one of the carbon centers. If two different compounds in the mix had C-B bonds, you might expect little control over which one reacted when. Seath *et al.* now show that by juggling the other groups bound to the boron, they can selectively activate two different C-B linkages sequentially. A timely swapping of methylaminodiacetic acid with pinacol enables selective and efficient coupling of three components in a single reaction mixture. — JSY

Angew. Chem. Int. Ed. 10.1002/anie.201504297 (2015).

CHEMISTRY

Printing potent patchy particles

Functionalized colloidal particles offer a versatile platform for building catalysts and sensors or for use as atomic analogs for studying packing and crystallization. However, selective asymmetric functionalization is still a challenge. Tigges *et al.* formed a monolayer of polystyrene particles with a surface layer of aldehyde groups. Then, using microcontact printing, they selectively modified the top of the particles by applying polymer inks containing poly(aminoethyl(meth)acrylate) homopolymers or copolymers that covalently link to the surface on amination. The polymer patches served as platforms for further functionalizing, using click-type reactions or copper-catalyzed cycloadditions, or through the inclusion of biotin in the inks for biorecognition reactions. — MSL

Small 10.1002/smll.201501071 (2015).

PHOTO: ANDREY GILJOV/NATIONAL GEOGRAPHIC SOCIETY

ALSO IN *SCIENCE* JOURNALS

Edited by **Stella Hurtley**

HUMAN MICROBIOTA

Microbial bioactive molecules

Human cells are outnumbered by the microbial cells of our commensals by an order of magnitude. All of these organisms are metabolically active and secrete multiple bioactive molecules. Genomics has unveiled a remarkable array of biosynthetic gene clusters in the human microbiota, which encode diverse metabolites. Donia *et al*. review how molecules ranging from lantibiotics and microcins to indoxyl sulfate and immune-modulatory oligosaccharides and lipids could affect the health and physiology of the whole organism, depending on the composition of an individual's microbial community. — CA

Science, this issue p. 395

APPLIED ORIGAMI

Expanding origami to thicker materials

A vast array of origami patterns can be applied to the folding of any material of near-zero thickness, such as paper. However, the folding of thick materials requires adding material and offsets. Chen *et al*. develop a general model in which the standard spherical linkages (creases) are replaced with rigid panels connected via offset folds, so that the folding motion of both near-zero–thickness and thick objects is the same. Furthermore, the hinges are constrained to move in only one direction, which is important for applications such as unfolding solar panels in space or large engineering structures, where you want the folding to occur automatically. — MSL

Science, this issue p. 396

INTRACELLULAR TRANSPORT

Membrane contact sites promote lipid exchange

Most membrane lipids are manufactured in the endoplasmic reticulum (ER). Different organelles and the plasma membrane (PM) have distinct phospholipid compositions. Chung *et al*., working in mammalian cells, and Moser von Filseck *et al*., working in yeast, both describe how a family of proteins is important in maintaining the balance of lipids within the cell. These special proteins accumulate at and tether contact sites between the ER and the PM and promote the exchange of specific phospholipids, which helps to maintain the PM's distinct identity. — SMH

Science, this issue pp. 428 and 432

HUMAN IMMUNOLOGY

The downside of diversity

The adaptive immune system exemplifies the benefits of diversity, allowing for individual responses to specific pathogens. Natural killer (NK) cells are also diverse at the single-cell level, but the contribution of this diversity to NK cell–mediated immunity has been unclear. Strauss-Albee *et al.* found that unlike adaptive immune cells, human NK cell diversity is lower at birth than in adults. Moreover, the diversification that results from antiviral responses decreases the flexibility of future responses. Indeed, high NK cell diversity was associated with increased risk of HIV-1 acquisition in African women. — ACC

Sci. Transl. Med. **7**, 297ra115 (2015).

REVIEW SUMMARY

HUMAN MICROBIOTA

Small molecules from the human microbiota

Mohamed S. Donia* and Michael A. Fischbach*

BACKGROUND: Two developments in distinct fields are converging to create interest in discovering small molecules from the human microbiome. First, the use of genomics to guide natural product discovery has led to the unexpected discovery of numerous biosynthetic gene clusters in genomes of the human microbiota. Second, the microbiome research community is moving from a focus on "who's there?" to "what are they doing?" with an accompanying emphasis on understanding microbiota-host interactions at the level of molecular mechanism. This merger has sparked a concerted hunt for the mediators of microbe-host and microbe-microbe interactions, including microbiota-derived small molecules.

ADVANCES: Numerous small molecules are known that are produced by the human microbiota. The microbiota-derived ribosomally synthesized, posttranslationally modified peptides (RiPPs) include widely distributed lantibiotics and microcins; these molecules have narrow-spectrum activity and are presumptive mediators of interactions among closely related species. Another notable RiPP is *Escherichia coli* heat-stable enterotoxin, a guanylate cyclase 2C agonist from which the recently approved gastrointestinal motility drug linaclotide was derived. Fewer amino acid metabolites are synthesized by the microbiota, but they are produced at very high levels that vary widely among individuals (e.g., indoxyl sulfate at 10 to 200 mg/day). Gut bacterial species convert common dietary amino acids into distinct end products, such as tryptophan to indoxyl sulfate, indole propionic acid, and tryptamine—indicating that humans with the same diet but different gut colonists can have widely varying gut metabolic profiles. Microbially produced oligosaccharides differ from other natural products because they are cell-associated (i.e., nondiffusible) and because many more biosynthetic loci exist for them than for other small molecule classes. Well-characterized examples, such as *Bacteroides* polysaccharide A, show that oligosaccharides may not simply play a structural role or mediate adhesion; rather, they can be involved in highly specific ligand-receptor interactions that result in immune modulation. Similarly, the (glyco)lipids α-galactosylceramide and mycolic acid can play roles in immune signaling. The most prominent microbiota-derived terpenoids are microbial conversion products of the cholic acid and chenodeoxycholic acid in host bile. These secondary bile acids can reach high concentration (mM) in the gut and vary widely in composition among individuals. Several canonical virulence factors from pathogens are derived from nonribosomal peptides (NRPs) and polyketides (PKs), but less is known about NRPs and PKs from the commensal microbiota. A recent computational effort has identified ~14,000 biosynthetic gene clusters in sequenced genomes from the human microbiota, 3118 of which were present in one or more of the 752 metagenomic sequence samples from the NIH Human Microbiome Project. Nearly all of the gene clusters that were present in >10% of the samples from the body site of origin are uncharacterized, highlighting the potential for identifying the molecules they encode and studying their biological activities.

OUTLOOK: There are two central challenges facing the field. The first is to distinguish, from among thousands of microbiota-derived molecules, which ones drive a key phenotype at physiologically relevant concentrations. Second, which experimental systems are appropriate for testing the activity of an individual molecule from a complex milieu? Meeting these challenges will require developing new computational and experimental technologies, including a capacity to identify biosynthetic genes and predict the structure and target of their biological activity, and systems in which germ-free mice are colonized by mock communities that differ only by the presence or absence of a biosynthetic gene cluster. ■

ON OUR WEB SITE

Read the full article at http://dx.doi.org/10.1126/science.1254766

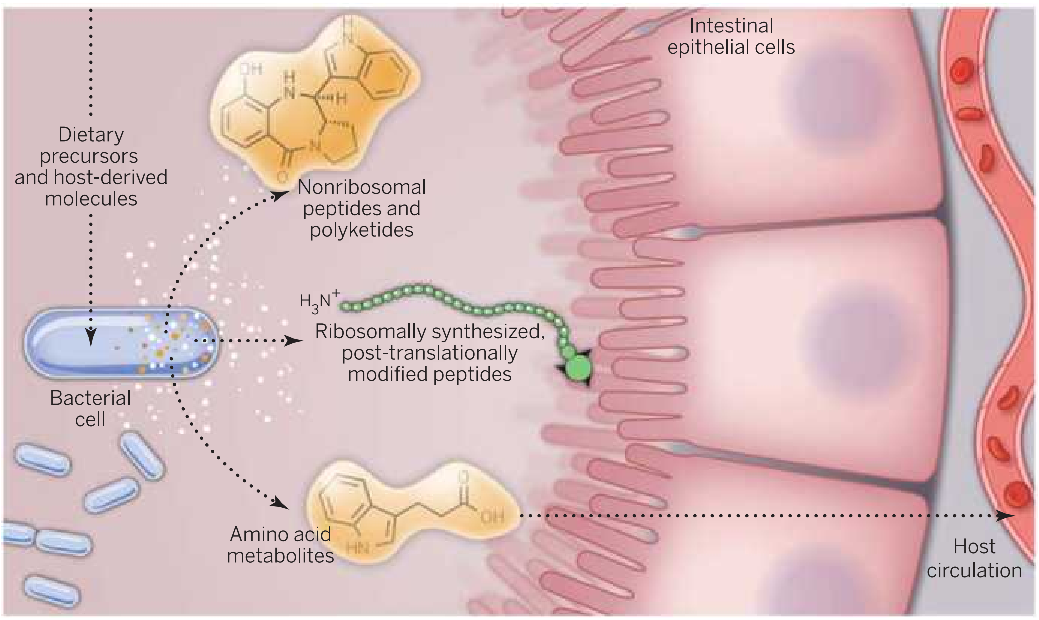

Small-molecule–mediated microbe-host and microbe-microbe interactions. Commensal organisms of the human microbiota produce many diverse small molecules with an equally diverse array of targets that can exacerbate or modulate immune responses and other physiological functions in the host. Several act as antibacterials to remove competing organisms, but many other products have unknown targets and effects on commensals and the host.

CREDIT: K. SUTLIFF/*SCIENCE*

The list of author affiliations is available in the full article online.
*Corresponding author. E-mail: donia@princeton.edu (M.S.D.); fischbach@fischbachgroup.org (M.A.F.).
Cite this paper as M. S. Donia, M. A. Fischbach, *Science* 349, 1254766 (2015). DOI: 10.1126/science.1254766

REVIEW

HUMAN MICROBIOTA

Small molecules from the human microbiota

Mohamed S. Donia[1]* and Michael A. Fischbach[2]*

Developments in the use of genomics to guide natural product discovery and a recent emphasis on understanding the molecular mechanisms of microbiota-host interactions have converged on the discovery of small molecules from the human microbiome. Here, we review what is known about small molecules produced by the human microbiota. Numerous molecules representing each of the major metabolite classes have been found that have a variety of biological activities, including immune modulation and antibiosis. We discuss technologies that will affect how microbiota-derived molecules are discovered in the future and consider the challenges inherent in finding specific molecules that are critical for driving microbe-host and microbe-microbe interactions and understanding their biological relevance.

Symbiotic relationships—including mutualism, commensalism, and parasitism—are ubiquitous in nature (*1*). Some of the best-known symbioses are between microorganisms and multicellular hosts; in these interkingdom relationships, the fitness of the microbe-host system (the holobiont) often relies on a diverse set of molecular interactions between the symbiotic partners (*2*, *3*). Examples include food digestion, nitrogen and carbon fixation, oxidation and reduction of inorganic molecules, and the synthesis of essential amino acids and cofactors (*2*, *4*–*6*). In light of the critical role of a molecular dialog in maintaining a productive mutualism, the community of researchers studying the symbiosis between humans and their microbiota has begun moving from a focus on "who's there?" to "what are they doing?" The accompanying emphasis on molecular mechanism has sparked a concerted hunt for the mediators of microbe-host interactions, including microbiota-derived small molecules.

It is now possible to identify biosynthetic genes in bacterial genome sequences and, in some cases, predict the chemical structure of their small-molecule products. This genome mining has led to the discovery of a growing number of molecules, and recently developed algorithms (*7*–*9*) have not only automated biosynthetic gene cluster identification but also have led to the unexpected discovery of numerous biosynthetic gene clusters in genomes of the human microbiota (*10*). In addition, a wealth of natural products has been discovered from bacterial and fungal symbionts of insects, nematodes, sponges and ascidians, and plants (*11*–*15*). The many known examples of microbe-host mutualisms in which the microbe synthesizes a metabolite important for the ecology of the pair raise an intriguing question: To what extent are mammals, including humans, a part of this paradigm?

We review what is known about small molecules from the human microbiota, examining in depth the diverse chemistries and biological functions of these molecules. Although our focus is predominantly on commensal bacterial species, we include a few notable examples of small molecules from bacterial pathogens. We also discuss recent insights into the metabolic potential of the human microbiota from computational analyses and conclude by considering approaches used to identify and discover the function of microbial molecules within a complex milieu. We have excluded some prominent microbiota-derived metabolite classes, including short-chain fatty acids (SCFAs) and trimethylamine-*N*-oxide, because their role in microbe-host interactions in the gut has been explored recently by Lee and Hase (*16*).

A wide range of small molecules has been isolated from human-associated bacteria (Fig. 1). These molecules cover the entire spectrum of chemical classes discovered so far from terrestrial and aquatic bacterial species and include well-characterized mediators of microbe-host and microbe-microbe interactions. Exploring their chemistry and function provides an entry point for understanding the effects of the microbiota on human health and disease.

Ribosomally synthesized, posttranslationally modified peptides (RiPPs)

Most human-associated bacteria live in complex communities and compete with other species for resources. Several natural products are secreted by bacteria to mediate these competitive and social interactions, including ribosomally synthesized, posttranslationally modified peptides (RiPP). Diverse RiPPs are produced by many organisms in the microbiota (*10*); they are often toxic for a limited set of species closely related to the producer, and likely to determine niche colonization. RiPPs are divided into numerous subclasses (*17*), five of which include members that have been isolated from human-associated bacteria, including lantibiotics, bacteriocins, microcins, thiazole/oxazole-modified microcins (TOMMs), and thiopeptides.

Lantibiotics and bacteriocins

Lantibiotics and bacteriocins are the most commonly isolated RiPPs from the human microbiota, and dozens have been found to date. Lantibiotics are short peptides of <40 amino acids with chemical cross-links formed posttranslationally between the terminal thiol of a cysteine residue and a dehydrated serine or threonine. The resulting "lanthionine" contains a thioether bond, which is typically more redox-stable than a disulfide. In contrast, bacteriocins are longer peptides that are usually unmodified. Microbiota-derived lantibiotics are predominantly produced by the Firmicutes and are usually active against a narrow spectrum of Gram-positive bacteria that are closely related to the producing strain.

Some microbiota-derived lantibiotics are synthesized by commensals (*18*), including the salivaricins from oral resident *Streptococcus salivarius* (*19*–*22*), a cocktail of five lantibiotics from the skin commensal *Staphylococcus epidermidis* (*23-27*), and ruminococcin A from the gut commensals *Ruminococcus gnavus* and *Clostridium nexile* (Table 1) (*28*, *29*). Each of these molecules inhibits the growth of pathogens that are closely related to the producer. Lantibiotics have also been isolated from human pathogens: Staphylococcin Au-26 (also known as Bsa) from *Staphylococcus aureus* (*30*, *31*), SA-FF22 from *Streptoccous pyogenes* (*32*, *33*), and the two-component lantibiotic cytolysin from *Enterococcus faecalis* (*34*) exert antibacterial activity against a range of common human commensals. Hence, lantibiotics are used by commensals and pathogens to compete and establish resilient colonization.

Microcins and TOMMs

Microcins are prototypical narrow-spectrum antibacterials displaying a wide range of unusual posttranslational modifications, including conversion of cysteine and serine residues to thiazoles and oxazoles (microcin B17), addition of adenosine monophosphate (microcin C7) or a siderophore to the C terminus (microcin E492; Fig. 2), and internal amide cross-linking to form a lassolike topology (microcin J25) (*35*–*38*). Because they derive exclusively from enterobacteria and have potent antibacterial activity against close relatives of the producer (*35*), the role of microcins in the Gram-negative microbiota is analogous to that of lantibiotics in the Gram-positive microbiota. Most microcins have been isolated from *Escherichia coli* strains and are widely distributed in both commensal and pathogenic enterobacteria (*35*, *39*–*41*).

[1]Department of Molecular Biology, Princeton University, Princeton, NJ 08544, USA. [2]Department of Bioengineering and Therapeutic Sciences and the California Institute for Quantitative Biosciences, University of California, San Francisco, San Francisco, CA 94158, USA.
*Corresponding author. E-mail: donia@princeton.edu (M.S.D.); fischbach@fischbachgroup.org (M.A.F.)

TOMMs are similar to microcin B17 in their biosynthesis and posttranslational modifications but encompass a larger family of natural products generated by both Gram-positive and Gram-negative bacteria (*17*, *42*). The best-studied example is streptolysin S from the human pathogen *S. pyogenes* (*43*). Despite intensive efforts for almost a century, the precise chemical structure and mechanism of action of streptolysin S have not been fully determined (*43*). However, streptolysin S contains multiple oxazole and thiazole residues that are required for its hemolytic activity (*44*, *45*). Related biosynthetic gene clusters from other human pathogens and commensals have been characterized (*43*), including listeriolysin S from *Listeria monocytogenes* (*46*) and clostridiolysin S from *Clostridium botulinum* and *Clostridium sporogenes* (*47*).

Heat-stable enterotoxin

Although most RiPPs from the human microbiota are thought to mediate microbe-microbe interactions, heat-stable enterotoxin is a RiPP produced by strains of *E. coli* associated with diarrheal disease and has a well-characterized host target. It is a 14–amino acid peptide stabilized by three internal disulfide bonds (*48*) and mimics the effect of the host peptide hormones guanylin and uroguanylin by agonizing guanylate cyclase 2C, a transmembrane protein expressed in intestinal epithelial cells with an extracellular ligand binding domain and a cytoplasmic catalytic domain (*49*). Guanylate cyclase 2C generates cyclic guanosine monophosphate to stimulate electrolyte secretion into the gut lumen. A single–amino acid variant of heat-stable enterotoxin, linaclotide, was approved by the Food and Drug Administration in 2012 for the treatment of constipation-associated with irritable bowel syndrome (Fig. 1) (*50*). The enzyme that introduces disulfide cross-links posttranslationally into heat-stable enterotoxin is not encoded in the toxin biosynthetic gene cluster, raising the question of whether the endogenous disulfide bond formation system is in fact operating in this system and whether other small peptides from enterobacteria undergo similar posttranslational processing. Importantly, a modified heat-stable enterotoxin peptide can survive the

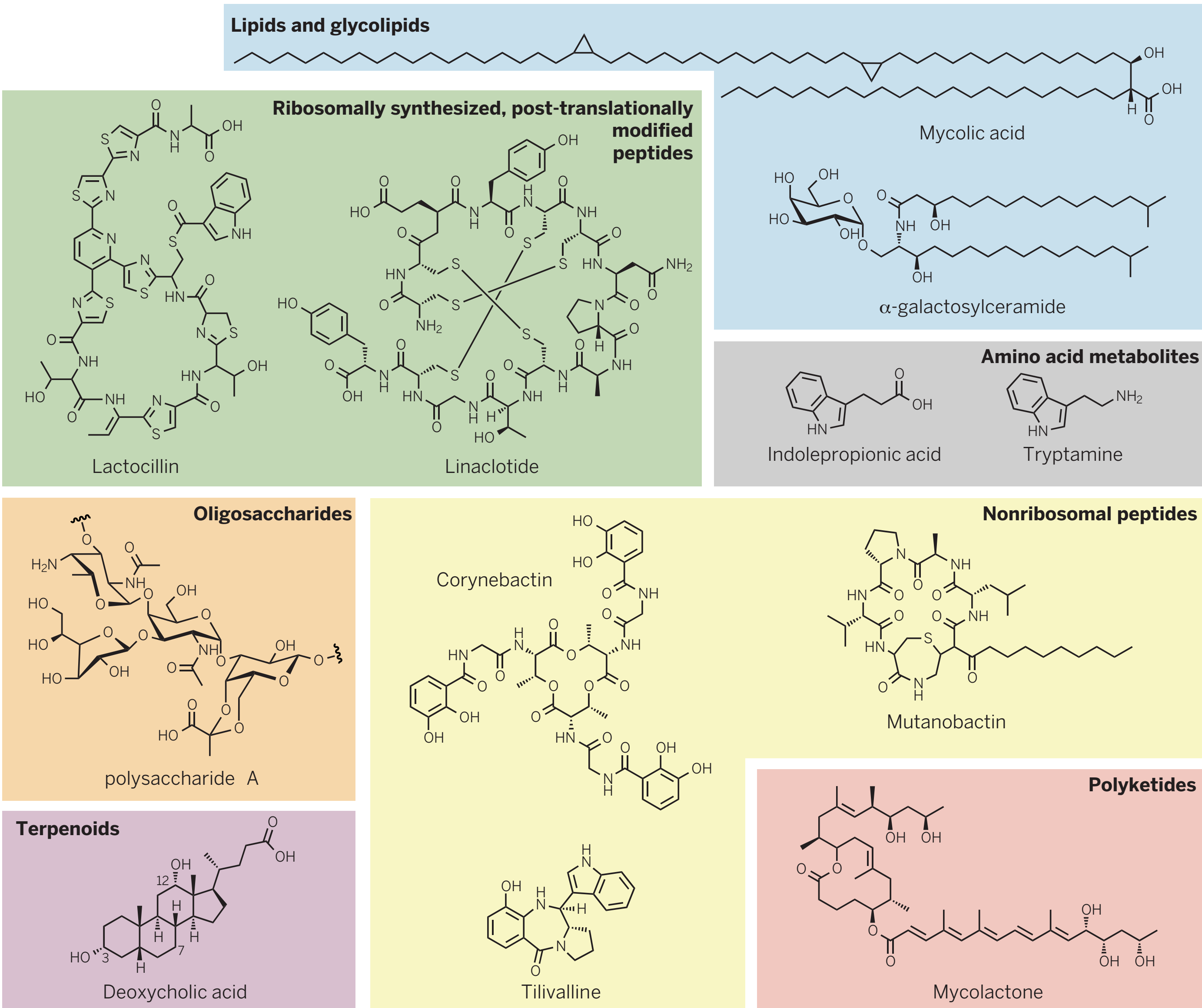

Fig. 1. Structurally diverse small molecules from the human microbiota. The diversity of chemical classes produced by the human microbiota rivals that of microorganisms from any ecological niche. Representative molecules are shown for each of the major molecular classes discussed: the RiPPs lactocillin and linaclotide; the amino acid metabolites indolepropionic acid and tryptamine; the oligosaccharide polysaccharide A; the lipids/glycolipids mycolic acid and α-galactosylceramide; the terpenoid deoxycholic acid, in which carbons 3, 7, and 12 of the bile acid scaffold are labeled; the NRPs corynebactin, tilivalline, and mutanobactin; and the PK mycolactone.

proteolytic milieu of the gut lumen and target a host receptor expressed in intestinal epithelial cells, delivering a potent biological activity without absorption into host circulation.

Products of amino acid metabolism

Gut bacteria living in an anaerobic environment require either an electron acceptor to drive fermentation or an anaerobic electron transport chain (51). Commonly among bacteria amino acids are used as electron acceptors, resulting in the production by the gut microbiota of high levels—sometimes exceeding 100 mg/day—of reductive amino acid metabolites, such as phenylpropionic acid and phenylacetic acid—molecules that are not found in most other habitats. Importantly, the amounts of these metabolites produced can vary widely among individuals, and, unlike RiPPs, they are generally permeable and accumulate systemically in the host (52). For example, humans with comparable levels of dietary tryptophan but distinct gut bacterial communities can have markedly different profiles of gut metabolites. One prominent tryptophan metabolite, indole,

Table 1. Selected small molecules from the human microbiota. A representative set of compounds are shown that cover the chemical classes discussed in the review. Asterisks indicate bacterial pathogens that are not normally present in human-associated communities.

Class	Compound	Producer (example)	Phylum	Host site	Known/predicted activity
RiPP (thiopeptide)	lactocillin	*L. gasseri*	Firmicutes	vagina	antibiotic
RiPP (lantibiotic)	epidermin	*S. epidermidis*	Firmicutes	skin	antibiotic
RiPP (lantibiotic)	salivaricin A2 and B	*S. salivarius*	Firmicutes	mouth	antibiotic
RiPP (lantibiotic)	cytolysin	*E. faecalis**	Firmicutes	gut	antibiotic, cytotoxic
RiPP (lantibiotic)	ruminococcin A	*R. gnavus*	Firmicutes	gut	antibiotic
RiPP (lantibiotic)	staphylococcin Au-26 (Bsa)	*S. aureus*	Firmicutes	skin	antibiotic
RiPP (lantibiotic)	SA-FF22	*S. pyogenes*	Firmicutes	oral/skin	antibiotic
RiPP (bacteriocin)	ruminococcin C	*R. gnavus*	Firmicutes	gut	antibiotic
RiPP (microcin)	microcin C7/C51	*E. coli*	Proteobacteria	gut	antibiotic
RiPP (microcin)	microcin B17	*E. coli*	Proteobacteria	gut	antibiotic
RiPP (microcin)	microcin J25	*E. coli*	Proteobacteria	gut	antibiotic
RiPP (microcin)	microcin H47	*E. coli*	Proteobacteria	gut	antibiotic
RiPP (TOMM)	streptolysin S	*S. pyogenes*	Firmicutes	oral/skin	cytotoxic
RiPP (TOMM)	clostridiolysin S	*C. sporogenes*	Firmicutes	gut	unknown
RiPP (TOMM)	listeriolysin S	*L. monocytogenes*	Firmicutes	gut	unknown
RiPP	heat-stable enterotoxin	*E. coli*	Proteobacteria	gut	GI motility (guanylate cyclase 2C)
Amino acid metabolite	indolepropionic acid	*C. sporogenes*	Firmicutes	gut	immunomodulatory
Amino acid metabolite	indole	unknown	unknown	gut	converted to indoxyl sulfate
Amino acid metabolite	skatole	*Clostridium* spp.	Firmicutes	gut	unknown
Amino acid metabolite	tryptamine	*R. gnavus*	Firmicutes	gut	neurotransmitter
Amino acid metabolite	phenyllactic acid	*Bifidobacterium* spp.	Actinobacteria	gut	unknown
Amino acid metabolite	phenethylamine	*Lactobacillus* spp.	Firmicutes	gut	neurotransmitter
Amino acid metabolite	δ-aminovaleric acid	*Clostridium* spp.	Firmicutes	gut	unknown
Amino acid metabolite	GABA	unknown	unknown	gut	unknown
Amino acid metabolite	α-aminobutyric acid	unknown	unknown	gut	unknown
Amino acid metabolite	3-aminoisobutyric acid	*Clostridium* spp.	Firmicutes	gut	unknown
Amino acid metabolite	*p*-cresol	*Clostridium* spp.	Firmicutes	gut	unknown
Acid (short-chain)	propionic acid	*Bacteroides* spp.	Bacteroidetes	gut	immunomodulatory (GPR43)
Oligosaccharide	polysaccharide A	*B. fragilis*	Bacteroidetes	gut	immunomodulatory (TLR2)
Oligosaccharide	capsular polysaccharide	*Streptococcus pneumoniae*	Firmicutes	airways	immunomodulatory
Glycolipid	α-galactosylceramide	*B. fragilis*	Bacteroidetes	gut	immunomodulatory (CD1d)
Glycolipid	corynomycolic acid	*Corynebacterium* spp.	Actinobacteria	skin	unknown
Glycolipid	mycolic acid	*Mycobacterium* spp.	Actinobacteria	airways	immunomodulatory (CD1b)
Glycopeptide	muramyl di- and tripeptides	*Fusobacterium nucleatum*	Fusobacteria	oral	immunomodulatory (NOD1, NOD2)
Terpenoid	staphyloxanthin	*S. aureus*	Firmicutes	skin	unknown (antioxidant?)
Terpenoid	bile acids (e.g., deoxycholic acid)	*Clostridium* spp.	Firmicutes	gut	metabomodulatory [TGR5, farnesoid X receptor (FXR), VDR]
NRP	phevalin	*S. aureus*	Firmicutes	skin	unknown (virulence inducer?)
NRP	cereulide	*B. cereus**	Firmicutes	gut	cytotoxic, immunomodulatory
NRP	yersiniabactin	*Yersinia pestis**	Proteobacteria	bloodstream	siderophore
NRP	corynebactin	*Corynebacterium* spp.	Actinobacteria	skin	siderophore
NRP	tilivalline	*K. oxytoca**	Proteobacteria	gut	cytotoxic
NRP-PK	zwittermicin	*B. cereus**	Firmicutes	gut	antimicrobial
NRP-PK	mutanobactin	*S. mutans*	Firmicutes	mouth	unknown
NRP-PK	colibactin	*E. coli*	Proteobacteria	gut	cytotoxic
PK	mycolactone	*M. ulcerans**	Actinobacteria	skin	immunomodulatory
Porphyrin	coproporphyrin III	*Propionibacterium acnes*	Actinobacteria	skin	unknown
Citrate amide	staphyloferrin B	*S. aureus*	Firmicutes	skin	siderophore

is derived from tryptophan by as-yet-unidentified enzyme(s) that are presumably homologs of tryptophanases seen in other bacterial species. In its unmodified form, indole serves as a signaling agent in bacterial communities (*53*). In addition, following absorption through the intestinal epithelium, indole is 3-hydroxylated and *O*-sulfated in the liver to become indoxyl sulfate, a well-known uremic toxin that is known from germ-free rodent studies to be derived entirely from the gut microbiota (*54*). Indoxyl sulfate occurs at a wide range of concentrations in human urine (10 to 200 mg/day), likely reflecting differences among individuals in diet and in the level of indole-producing bacterial species in the gut community (*55*). A second reductive tryptophan metabolite, indolepropionic acid (Fig. 2), is found in mouse serum if *C. sporogenes* is present in the gut (*52*). Although the function of this molecule is unknown, several producers have been identified including *Clostridium sporogenes*. A third tryptophan metabolite, the decarboxylation product tryptamine, which can act as a biogenic amine neurotransmitter, is synthesized by a variety of gut bacteria (*56*) and has been linked to signaling in the enteric nervous system (*57*), one of several findings that has revealed a role for the microbiota in the gut-brain axis (*58*–*61*). Thus, tryptophan can be diverted to end products with distinct biological activities depending on the composition of the gut community.

The metabolic products of aliphatic amino acids are equally prominent but less well characterized. Notable examples include δ-aminovaleric acid, which derives from arginine, proline, and ornithine, and acts as an electron source for secondary fermenters (*62*), and α-aminobutyric acid, which derives from threonine or methionine. Notably, the neurotransmitter γ-aminobutyric acid (GABA), the decarboxylation product of glutamate, is both produced and consumed by various species of gut bacteria (*62*), although its potential role in microbe-host signaling remains unexplored. Many of the less-common SCFAs, including isobutyric, valeric, 2- and 3-methylbutyric, caproic, and isocapropic acids, are also the products of reductive amino acid metabolism, but it is not known whether their signaling properties differ from those of the better known SCFAs (*62*).

Oligosaccharides

Oligosaccharides provide some of the best-characterized examples of how small molecules from the human microbiota can mediate microbe-host interactions. Diffusible oligosaccharides are well known in the natural products community (*63*, *64*), but the best-studied oligosaccharides from the human microbiota are cell-associated. Capsular polysaccharides from *Bacteroides* and *Streptococcus* are not simply structural or nonspecifically adhesive; they can have highly specific ligand-receptor interactions that result in immune modulation, similarly to glycolipids (see below).

Species of *Bacteroides*, the most abundant bacterial genus in the human gut, produce an array of capsular polysaccharides, the best characterized of which is polysaccharide A from *Bacteroides fragilis*. Polysaccharide A is an oligomer in which the tetrasaccharide repeating unit consists of four derivatives of galactose: galactofuranose, *N*-acetylgalactosamine (GalNAc), 4,6-pyruvoylgalactose, and 4-amino-6-deoxy-GalNAc. Although the biosynthesis of polysaccharide A has just begun to be explored (*65*, *66*), its biological activity has been investigated in detail. Polysaccharide A signals to the host's innate immune system through the Toll-like receptor 2 (TLR2), which then leads to the induction of regulatory T cells to produce the tolerogenic cytokine interleukin-10 (IL-10).

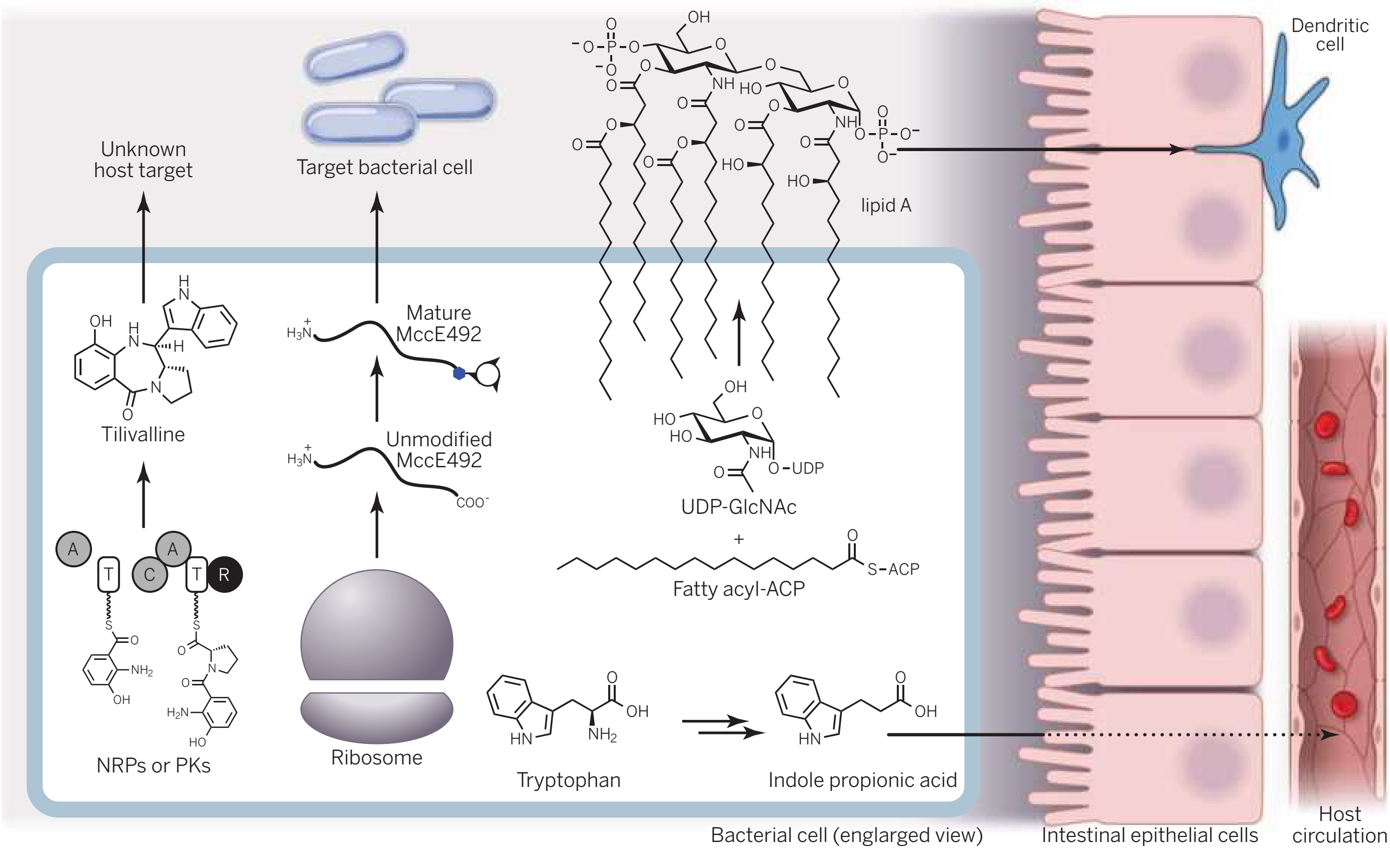

Fig. 2. Small-molecule–mediated microbe-host and microbe-microbe interactions. The microbiota produces a range of small molecules from various classes with distinct targets. Four examples are shown: the NRP tilivalline, whose host target is unknown; the ribosomally synthesized and posttranslationally modified peptide microcin E492 (MccE492), a narrow spectrum antibacterial; lipid A, the glycolipid core of LPS, which targets TLR4 in host immune cells; and indole propionic acid, a reductive metabolite of tryptophan that enters host circulation but whose biological activity is poorly understood. These metabolites are each produced by different species of the microbiota but are shown here in a single cell for schematic purposes. The following are abbreviations for domains in the NRPS that produces tilivalline: A, adenylation domain; T, thiolation domain; C, condensation domain; R, terminal reductase domain. ACP, acyl carrier protein; UDP-GlcNAc, uridine 5′-diphosphate *N*-acetylglucosamine.

This signaling event restricts the activity of T helper 17 (T_H17) cells and not only promotes *B. fragilis* colonization but also suppresses *Helicobacter hepaticus*–induced colitis (*67*, *68*). Remarkably little is known about the structures and biological activities of the tens to hundreds of other *Bacteroides* capsular polysaccharides, although they are likely to be the most abundant small molecules in the human gut (*10*).

Cell-associated oligosaccharides can also play a defensive role, as is the case with the richly diverse capsular polysaccharides elaborated by species of *Streptococcus*, including a family of capsular polysaccharides from group B *Streptococcus*, a pathogen (*69*). Although the repeating unit varies in size, composition, and connectivity among group B *Streptococcus* serotypes, a common chemical feature is a terminal sialic acid, which blocks phagocytosis by inhibiting the deposition of the complement component C3b (*69*).

An area of great therapeutic promise is the identification of microbially derived ligands in the microbiota for host receptors. In addition to recent studies on the role of SCFAs and G protein–coupled receptor 43 (GPR43) in regulatory T cell function (*70*), glycolipids and saccharides are significant candidate ligands. One example is muramyl dipeptide, a glycopeptide fragment of the repeating unit of peptidoglycan, that is a ligand for nucleotide-binding oligomerization domain–containing protein 2 (NOD2) and forms the scaffold for the immune-stimulatory osteosarcoma drug mifamurtide (*71*, *72*). Additionally, the large numbers of uncharacterized oligosaccharide biosynthetic loci in the human microbiome are particularly interesting in light of the C-type lectin receptors in the dectin/langerin/DC-SIGN (dendritic cell–specific C-type lectin) family, which are known to bind oligosaccharides and modulate immune-cell function, but for which few convincing ligands have been discovered (*73*).

Glycolipids and terpenoids

Perhaps the best-known microbiota-derived molecule is lipopolysaccharide (LPS), a glycolipid that is a major component of the outer membrane of Gram-negative bacteria (Fig. 2). LPS is the ligand for the innate immune receptor TLR4 and has been reviewed extensively elsewhere (*74*); here, we focus on two other families of bacterial glycolipids with similar immunomodulatory activities: the *Bacteroides* glycosphingolipid α-galactosylceramide and the mycolic acids of *Mycobacterium* and *Corynebacterium*.

Glycolipids

α-Galactosylceramide is a glycosphingolipid that was originally discovered nearly two decades ago as a natural product from a sponge and was later found to be a potent ligand for CD1d-restricted natural killer T (NKT) cells (*75*). Even though >1000 papers have been published on synthetic derivatives of this sphingolipid and the identification and stimulation of NKT cells, the source of the "native" ligand for CD1d has remained a mystery (*76*). Recently, *B. fragilis*, a common gut commensal, was discovered to produce α-galactosylceramide (*77*). Colonization of germ-free mice as neonates by wild-type *B. fragilis* suppresses NKT cells in the gut and blocks oxazolone-induced colitis (*78*). These findings suggest that the "native" ligand for the highly conserved mammalian receptor CD1d might originate in the microbiota rather than the host. This may be true for other "orphan" receptors expressed by immune and epithelial cells.

Mycolic acids are distinctive components of the cell wall of *Mycobacterium* (mostly pathogens) and *Corynebacterium* (both pathogens and skin and oral commensals). They consist of an all-carbon backbone with two lipid tails, one of which can be 40 to 60 carbons long in *Mycobacterium*, and occur both as free carboxylic acids and as esters of cell-wall polysaccharides. In addition to being important structural components of the capsule (*79*), glucose monomycolate serves as a ligand for CD1b-restricted T cells, eliciting a specific immune response against infection (*80*–*83*). Another glycolipid derivative of mycolic acid, trehalose-6,6-dimycolate, is a potent immune elicitor that binds to the C-type lectin Mincle to induce macrophage activation and a T cell response characteristic of vaccination (*84*). Mycolic acid has many chemical modifications, including methylation and cyclopropanation, both of which appear to shield it from immune detection: The MmaA4-catalyzed methylation of mycolic acid in *Mycobacterium tuberculosis* blocks IL-12 production and prevents detection and elimination by macrophages (*85*), and an *M. tuberculosis* mutant that is deficient in mycolic acid cyclopropanation is attenuated and hyperinflammatory in a mouse model of infection (*86*).

Terpenoids

The major microbiota-derived terpenoids are not synthesized de novo by the microbiota; they are secondary bile acids derived from the host's primary bile acids cholic acid (CA) and chenodeoxycholic acid (CDCA) (Fig. 1). CA and CDCA are biosynthesized in the human liver, conjugated to taurine or glycine, and then excreted in bile; although 90% of the bile acid pool is absorbed in the terminal ileum, the remaining 10% enters the large intestine (*87*). Here, the bile acid pool reaches concentrations of ~1 mM and varies widely in composition among healthy humans. Numerous biochemical transformations of CA and CDCA are performed by gut bacteria, including deconjugation from taurine and glycine; oxidation and subsequent epimerization of the hydroxyl groups at C_3, C_7, and C_{12}; dehydration and reduction of the hydroxyl group at C_7; and esterification with ethanol at the C_{24} carboxylate. Among these, dehydroxylation at C_7 has been characterized most extensively (*87*–*89*).

Several species of Firmicutes (e.g., *Clostridium scindens* and *Clostridium hylemonae*) dehydroxylate CA and CDCA at the C_7 position to form deoxycholic acid (DCA) and lithocholic acid (LCA), respectively. The high flux of this biochemical transformation results in DCA and LCA making up nearly two-thirds of the fecal bile acid pool (*87*). Both DCA and LCA are toxic to human cells and have been implicated in hepatoxicity and colon cancer (*90*). 7-Dehydroxylation is carried out in part by the eight-gene *bai* operon. This gene cluster is thought to perform eight successive chemical transformations in a pathway for which the early oxidative steps have been characterized biochemically, but the later, reductive steps remain speculative (*89*). Little is known about the biosynthetic genes for other secondary bile acids, although there is preliminary evidence that some bile acid pathways might involve transformations by more than one gut bacterial species.

The carotenoids are terpenoids, exemplified by staphyloxanthin, the golden-colored pigment for which *S. aureus* is named. Staphyloxanthin is composed of a glucose residue that is esterified with both a fatty acid (12-methyltetradecanoate) at the C6″ position and a carotenoid (4,4′-diaponeurosporen-4-oate) at the C1‴ position (*91*). The core structure of staphyloxanthin is assembled by two biosynthetic enzymes: a glycosyltransferase, which esterifies the C1″ position of glucose, and an acyltransferase, which esterifies its C6″ position. The unusual 4,4′-diaponeurosporen-4-oate originates from dehydrosqualene by further dehydrogenation and oxidation steps (*92*, *93*). The conjugated double bonds of staphyloxanthin's carotenoid tail serve as a "sponge" for oxygen radicals, protecting *S. aureus* against killing by hydrogen peroxide, superoxide, and hydroxyl radical, which are produced by host neutrophils and macrophages (*94*, *95*).

Polyketides and nonribosomal peptides

Although polyketides (PKs) and nonribosomal peptides (NRPs) are among the largest classes of natural products in soil and aquatic bacteria, relatively few are known from human-associated bacteria. Two recently discovered examples come from the common pathobionts *S. aureus* and *Streptococcus mutans* (Table 1 and Fig. 1). A conserved NRP gene cluster in *S. aureus* encodes a family of pyrazinones, which are derivatives of the ubiquitous diketopiperazines (*96*, *97*). Although the role of the pyrazinones in regulating the expression of *S. aureus* virulence factors remains unclear (*96*, *98*), they are unlikely to function exclusively in the context of pathogenesis because they are also produced by the skin commensal *S. epidermidis* (*97*). Isolates of *S. mutans*, the leading cause of dental caries, harbor a genomic island encoding hybrid PK synthase (PKS)/NRP synthetase (NRPS) pathways (*99*). The product of one of these pathways, mutanobactin, contains an unusual 1,4-thiazepan-5-one ring, which originates from the cyclization of a cysteine and a glycine residue. The biological activity of the mutanobactins has not been fully determined but may involve modulating growth and biofilm formation by the fungal pathogen *Candida albicans* (*100*–*102*).

Four pathogen-derived NRPs and PKs cause disease: cereulide, mycolactone, colibactin, and tilivalline. Cereulide, a dodecadepsipeptide toxin, is responsible for the emetic effects of the food-poisoning pathogen *Bacillus cereus* (*103*, *104*). The ester bonds in cereulide's alternating ester/amide backbone enable the molecule to have

high affinity for potassium ions, which results in uncoupling of oxidative phosphorylation and causes mitochondrial toxicity (105, 106).

Mycolactones are PK toxins produced by the causative agent of Buruli ulcer, *Mycobacterium ulcerans* (107, 108). These molecules, which cause the necrosis, ulceration, and immune suppression associated with this disease, are encoded by a >100-kb type I PKS biosynthetic gene cluster that includes two genes >40 kb. Interestingly, a heterogeneous suite of mycolactone derivatives is produced by different strains of *M. ulcerans*, which may explain the variation observed in the virulence of the strains and their biogeography (107, 109–112).

Colibactin is produced by a subset of enterobacteria, including strains of *E. coli* B2, *Enterobacter aerogenes*, *Klebsiella pneumoniae*, and *Citrobacter koseri* (113, 114). Exposure of mammalian cells to colibactin-producing *E. coli* and *K. pneumoniae* induces DNA damage in vitro and in vivo. Surprisingly, the colibactin gene cluster occurs in one of the most commonly used probiotic *E. coli* strains (*E. coli* Nissle 1917 or EcN) (114–118). Considerable efforts have been made to study the biosynthesis of colibactin (119–121), and its chemical structure has recently been characterized, revealing a unique spirocyclopropane "warhead" that cross-links DNA (122). It is not yet clear what role colibactin plays in the ecology of the interaction between *E. coli* and the host and how the genotoxic activity of colibactin benefits its producer.

Tilivalline is an NRP toxin produced by colitogenic strains of the pathobiont *Klebsiella oxytoca* (Fig. 2) (123). Importantly, tilivalline is essential for the inflammatory pathology characteristic of antibiotic-associated hemorrhagic colitis and induces apoptosis in cultured human epithelial cells. Although the discovery of tilivalline sheds light on one mechanism of antibiotic-induced colitis, there are likely to be alternative mechanisms, because *K. oxytoca* is present in, at most, 10% of the healthy human population (124).

Much is known about the biosynthesis of NRP-derived and NRP-independent siderophores in a broad range of human pathogens and their role in iron acquisition as an essential component of bacterial pathogenesis, both of which have been reviewed extensively elsewhere (125–127). In contrast, very little is known about the mechanisms by which commensals acquire iron, and, to our knowledge, no iron acquisition system has ever been shown to be required for colonization by a commensal.

Outlook

We have used ClusterFinder (7) to identify biosynthetic gene clusters in the human microbiome as a way to assess the metabolic potential of the human microbiota (10). Of >14,000 putative small-molecule biosynthetic gene clusters identified in human-associated bacterial genomes, 3118 were present in one or more of the 752 whole-genome shotgun metagenomic sequence samples from the NIH Human Microbiome Project (HMP). Although each of the major natural product classes is produced by the human microbiota, oligosaccharide and RiPP gene clusters predominate, underscoring the need to improve analytical chemical techniques to purify and assay these molecules. Nearly all of the gene clusters that were present in over 10% of the subjects in the study are uncharacterized.

There are two central challenges facing the field: First, from the wealth of microbiota-derived molecules, which ones are the functionally "important" ones? Second, what experimental systems are appropriate for testing the activity of an individual molecule from a complex milieu?

Identifying significant microbiota-derived molecules

Human-associated microbial communities can consist of hundreds of abundant bacterial species and perhaps thousands of molecules at physiologically relevant concentrations. Figuring out which of these molecules drive a phenotype and how they act requires new computational and experimental approaches.

Initial mapping of metagenomic sequence data onto KEGG (Kyoto Encyclopedia of Genes and Genomes) or COG (Clusters of Orthologous Groups database) gene categories provides a way of seeing coarse changes, for example, a shift from oligosaccharide toward amino acid catabolism in a community. Resolution is not yet high enough to make reliable predictions about specific biosynthetic pathways or products. Methods that predict the gene content of a sample from 16*S* data can predict pathways that are present or absent in every member of an operational taxonomic unit (128) but have limited utility for biosynthetic pathways, which are highly variable even among closely related strains of a bacterial species (129, 130).

Methods are needed that take genomic and metagenomic sequence data as an input and use it to predict, at high resolution, pathways for specific molecules. Multiple algorithms will likely be needed: some for identifying clustered biosynthetic pathways, characteristic of a conventional secondary metabolite, and others for predicting unclustered pathways more commonly found in primary metabolism. The dearth of knowledge about primary metabolic pathways in anaerobes from the gut community is a critical gap in current knowledge, and addressing this problem will be a major achievement.

Nicholson, Holmes, and colleagues have pioneered the use of metabolomics to profile microbiota-derived metabolites in a variety of sample types and disease models, developing powerful and widely applicable analytical pipelines (131, 132) (Fig. 3A). By using similar approaches, a range of microbiota-derived molecules have been connected to specific bacterial species through the metabolomic profiling of various artificial and disease-associated communities from mice (52, 59, 133, 134). Although metabolomic profiling is capable of measuring hundreds to thousands of known metabolites in a single run, applying untargeted metabolomics to discovering molecules of interest is laborious and generally requires purification and structural characterization of milligram quantities of compound.

Although bioassay-guided fractionation is immensely powerful, it is painstaking and difficult to scale, so it is better suited for unusually important phenotypes of interest, including the search for ligands for orphan, sensing molecules GPCRs expressed in the gut (Fig. 3B). A derivative of this approach in which microbes, not molecules, are "fractionated" was recently used to identify a cocktail of 17 gut bacterial strains that induce regulatory T cells and attenuate colitis. This activity was further correlated with SCFAs produced by this anti-inflammatory cocktail of bacteria (135, 136).

An alternative to bioassay-guided fractionation is the candidate molecule approach (Fig. 3C). We used this method for the discovery of the potent thiopeptide antibiotic, lactocillin, from *Lactobacillus gasseri*, a prominent member of the vaginal community (10, 137). We performed a systematic analysis of all biosynthetic gene clusters for small molecules in genomes of human-associated bacteria and identified 13 previously unknown thiopeptide gene clusters, four of which are present in >20% of HMP samples. Thiopeptides are a class of antibiotics with potent activity against Gram-positive bacteria that bind to a site on the 50*S* subunit of the bacterial ribosome. One member of this class, LFF571, is currently in a phase II clinical trial (138). Lactocillin has been purified, structurally characterized, and shown to have low-to-mid nanomolar antibiotic activity against vaginal pathogens but not against vaginal commensals.

Another class of molecules ideally suited to the candidate molecule approach is the secondary bile acids. Bile acids, and the sterol scaffold more generally, are rich in biological activity, and there are numerous host receptors for these molecules (87). The levels of secondary bile acids vary widely among individuals, although the bile acid pool in the gut lumen is held at high micromolar to low millimolar concentrations. Although dozens of secondary bile acids are known, very few have been assigned a biological activity or have known biosynthetic genes, making this a promising area for detailed experimental investigation.

Studying individual molecules from a pool

The discoveries of highest impact will come not from simply cataloging new microbiota-derived molecules, but from studying the biological activities of individual molecules in a complex molecular milieu. With the exception of fecal metabolite profiling, few microbiota-derived molecules have been detected in host-derived samples. More sensitive analytical techniques, such as nanospray desorption electrospray ionization mass spectrometry, are needed to verify the production of a molecule in the skin, oral, and vaginal communities. An alternative approach—the detection of RNA transcripts for a particular bacterial gene cluster in metatranscriptomic data—has been used to profile the expression of the cluster in native samples. This approach is consistent

with, but not proof of, small molecule production in the "natural" habitat of the microbiome (10).

Although preliminary studies on the biological effects of target molecules have been carried out for three microbiota-derived RiPPs (139–143), their biological relevance has not yet been tested experimentally. Colonization studies in germ-free mice have the advantage of simplicity, but there are drawbacks. For example, molecules derived from a monocolonist can be produced at super-physiological levels, leading to a false signal. In addition, the activity of some molecules, such as immune modulators, may require the activity of co-stimulatory signals from other bacterial species. Last, the biological relevance of certain molecules, like antibacterials, may only be observed when other members of the microbiota are present. Faith *et al.* have overcome some of these challenges in studies on regulatory T cells in the gut, by using small subsets of gut bacterial strains to colonize mice (Fig. 3D) (144).

Similar experimental systems have recently been developed for the skin. Conventional mice can be colonized by individual skin commensals, and the T cell response can be tracked over long periods (145). By contrast, few experimental systems are available for interrogating the role of small-molecule–mediated interactions in the community structure (146) and dynamics (137) of oral and vaginal communities.

Many molecules of interest are produced by bacterial species that are difficult to manipulate genetically, such as the anaerobic Firmicutes (*Clostridium* and its relatives). Two technologies would be transformative for their study: gene knock-out in the native host (147) and synthetic-biology-based approaches to express biosynthetic gene clusters in a more genetically tractable host (148).

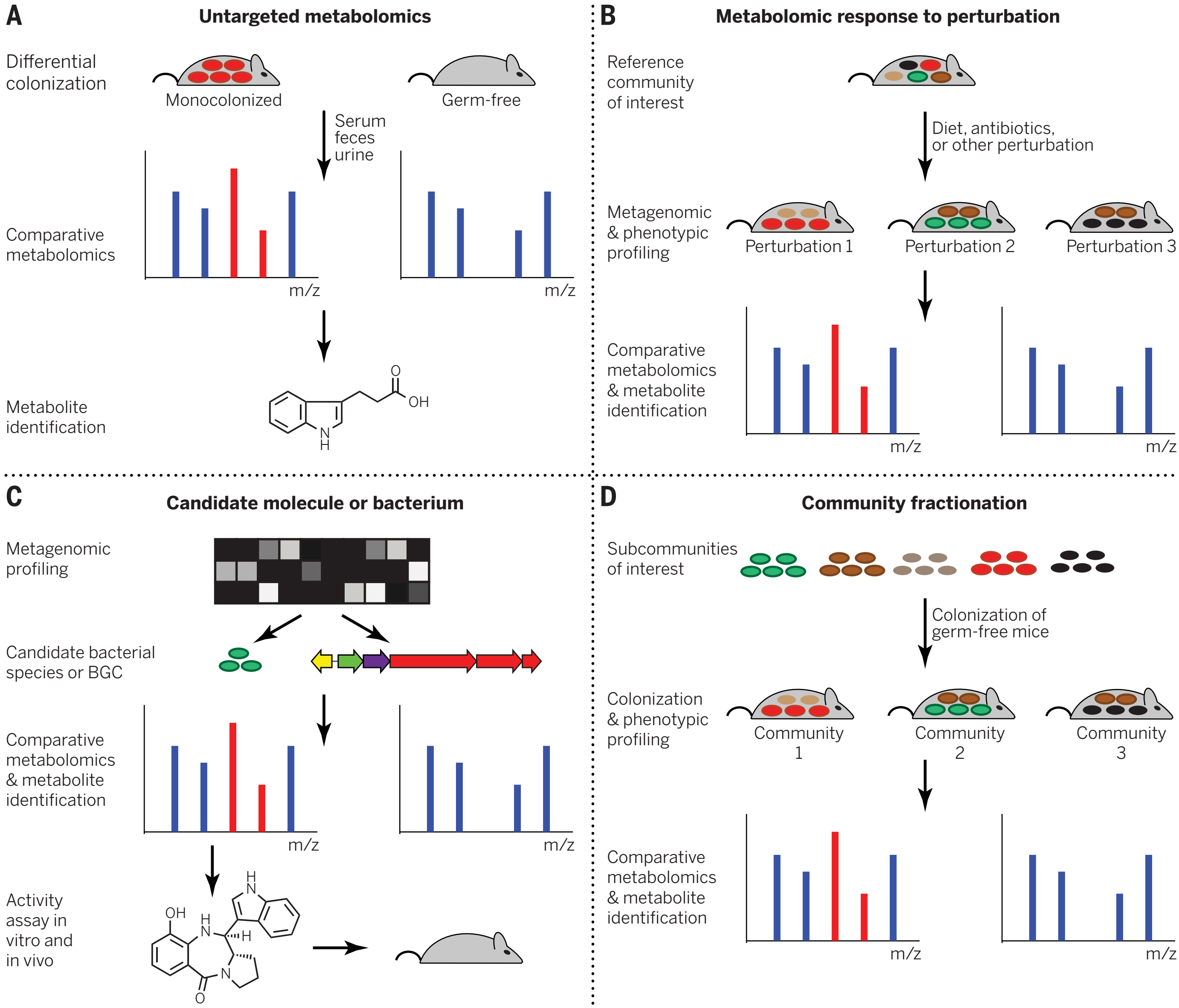

Fig. 3. Approaches to discovering small molecules from the microbiota. (**A**) Samples from germ-free and colonized mice can be analyzed by untargeted metabolomics to identify molecules that are present in a microbiota-dependent fashion. (**B**) A mouse harboring a reference gut community can be subjected to antibiotic treatment, a dietary shift, or another perturbation. Comparative metabolomics can be used to identify microbiota-derived molecules whose abundance changes as a consequence of the perturbation. (**C**) Candidate biosynthetic gene clusters (BGCs) or bacterial species can be selected by metagenomic profiling, for example, for gene clusters or species that are widely distributed or differ in abundance between cases and controls. Comparative metabolomics can then be used to identify molecules produced by a gene cluster or bacterial species of interest. (**D**) Subsets of bacteria from a fractionated complex community or designed synthetic communities can be used to colonize mice in order to identify specific bacterial species whose presence correlates with the production of a molecule of interest. *m/z*, mass-charge ratio.

Conclusion

Much is known about which bacterial species are most abundant in human-associated communities and how they vary among individuals. Yet comparatively little is known about the most abundant bacterially derived or modified small molecules in the gut, despite the fact that these molecules are present at high micromolar concentration, their levels can vary greatly among individuals, and the human host is chronically exposed to them for decades with unknown consequences. Certain low-abundance molecules with potent biological activities may also be significant to host physiology. Against this backdrop, it seems likely that in the near future the suite of microbiota-derived molecules in an individual's gut community will not be left to chance. Pharmaceutical companies go to great lengths to get a single molecule into the human gut at comparable concentrations. Discovering the most abundant, widely (or variably) distributed, and biologically active molecules produced by the microbiota—and connecting them to the genes that encode them—are critical first steps in understanding which molecules have desired effects and which are deleterious, what receptors they target, and how therapeutic communities of microorganisms can be designed in which the production and nonproduction of molecules can be genetically specified.

REFERENCES AND NOTES

1. L. Margulis, R. Fester, *Symbiosis as a Source of Evolutionary Innovation: Speciation and Morphogenesis* (MIT Press, Cambridge, MA, 1991).
2. G. E. Oldroyd, J. D. Murray, P. S. Poole, J. A. Downie, The rules of engagement in the legume-rhizobial symbiosis. *Annu. Rev. Genet.* **45**, 119–144 (2011). doi: 10.1146/annurev-genet-110410-132549; pmid: 21838550
3. N. A. Moran, J. P. McCutcheon, A. Nakabachi, Genomics and evolution of heritable bacterial symbionts. *Annu. Rev. Genet.* **42**, 165–190 (2008). doi: 10.1146/annurev.genet.41.110306.130119; pmid: 18983256
4. A. El Kaoutari, F. Armougom, J. I. Gordon, D. Raoult, B. Henrissat, The abundance and variety of carbohydrate-active enzymes in the human gut microbiota. *Nat. Rev. Microbiol.* **11**, 497–504 (2013). doi: 10.1038/nrmicro3050; pmid: 23748339
5. J. P. McCutcheon, N. A. Moran, Parallel genomic evolution and metabolic interdependence in an ancient symbiosis. *Proc. Natl. Acad. Sci. U.S.A.* **104**, 19392–19397 (2007). doi: 10.1073/pnas.0708855104; pmid: 18048332
6. T. Woyke *et al*., Symbiosis insights through metagenomic analysis of a microbial consortium. *Nature* **443**, 950–955 (2006). doi: 10.1038/nature05192; pmid: 16980956
7. P. Cimermancic *et al*., Insights into secondary metabolism from a global analysis of prokaryotic biosynthetic gene clusters. *Cell* **158**, 412–421 (2014). doi: 10.1016/j.cell.2014.06.034; pmid: 25036635
8. K. Blin *et al*., antiSMASH 2.0—a versatile platform for genome mining of secondary metabolite producers. *Nucleic Acids Res.* **41**, W204– W212 (2013). doi: 10.1093/nar/gkt449; pmid: 23737449
9. M. H. Medema *et al*., antiSMASH: Rapid identification, annotation and analysis of secondary metabolite biosynthesis gene clusters in bacterial and fungal genome sequences. *Nucleic Acids Res.* **39** (suppl.), W339–W346 (2011). doi: 10.1093/nar/gkr466; pmid: 21672958
10. M. S. Donia *et al*., A systematic analysis of biosynthetic gene clusters in the human microbiome reveals a common family of antibiotics. *Cell* **158**, 1402–1414 (2014). doi: 10.1016/j.cell.2014.08.032; pmid: 25215495
11. S. R. Long, Genes and signals in the rhizobium-legume symbiosis. *Plant Physiol.* **125**, 69–72 (2001). doi: 10.1104/pp.125.1.69; pmid: 11154299
12. Y. Zhang, C. Ruyter-Spira, H. J. Bouwmeester, Engineering the plant rhizosphere. *Curr. Opin. Biotechnol.* **32**, 136–142 (2015). doi: 10.1016/j.copbio.2014.12.006; pmid: 25555138
13. J. Piel, Metabolites from symbiotic bacteria. *Nat. Prod. Rep.* **26**, 338–362 (2009). doi: 10.1039/B703499G; pmid: 19240945
14. A. O. Brachmann, H. B. Bode, Identification and bioanalysis of natural products from insect symbionts and pathogens. *Adv. Biochem. Eng. Biotechnol.* **135**, 123–155 (2013). doi: 10.1007/10_2013_192; pmid: 23657492
15. J. M. Crawford, J. Clardy, Bacterial symbionts and natural products. *Chem. Commun.* **47**, 7559–7566 (2011). doi: 10.1039/c1cc11574j; pmid: 21594283
16. W. J. Lee, K. Hase, Gut microbiota-generated metabolites in animal health and disease. *Nat. Chem. Biol.* **10**, 416–424 (2014). doi: 10.1038/nchembio.1535; pmid: 24838170
17. P. G. Arnison *et al*., Ribosomally synthesized and post-translationally modified peptide natural products: Overview and recommendations for a universal nomenclature. *Nat. Prod. Rep.* **30**, 108–160 (2013). doi: 10.1039/C2NP20085F; pmid: 23165928
18. A. J. van Heel, M. Montalban-Lopez, O. P. Kuipers, Evaluating the feasibility of lantibiotics as an alternative therapy against bacterial infections in humans. *Expert Opin. Drug Metab. Toxicol.* **7**, 675–680 (2011). doi: 10.1517/17425255.2011.573478; pmid: 21521092
19. A. Barbour, K. Philip, S. Muniandy, Enhanced production, purification, characterization and mechanism of action of salivaricin 9 lantibiotic produced by *Streptococcus salivarius* NU10. *PLOS ONE* **8**, e77751 (2013). doi: 10.1371/journal.pone.0077751; pmid: 24147072
20. K. F. Ross, C. W. Ronson, J. R. Tagg, Isolation and characterization of the lantibiotic salivaricin A and its structural gene salA from *Streptococcus salivarius* 20P3. *Appl. Environ. Microbiol.* **59**, 2014–2021 (1993). pmid: 8357242
21. P. A. Wescombe *et al*., Salivaricin G32, a homolog of the prototype *Streptococcus pyogenes* nisin-like lantibiotic SA-FF22, produced by the commensal species *Streptococcus salivarius*. *Int. J. Microbiol.* **2012**, 738503 (2012). doi: 10.1155/2012/738503; pmid: 22567013
22. P. A. Wescombe *et al*., Production of the lantibiotic salivaricin A and its variants by oral streptococci and use of a specific induction assay to detect their presence in human saliva. *Appl. Environ. Microbiol.* **72**, 1459–1466 (2006). doi: 10.1128/AEM.72.2.1459-1466.2006; pmid: 16461700
23. J. S. Nascimento *et al*., Bacteriocins as alternative agents for control of multiresistant staphylococcal strains. *Lett. Appl. Microbiol.* **42**, 215–221 (2006). doi: 10.1111/j.1472-765X.2005.01832.x; pmid: 16478507
24. M. B. Ekkelenkamp *et al*., Isolation and structural characterization of epilancin 15X, a novel lantibiotic from a clinical strain of *Staphylococcus epidermidis*. *FEBS Lett.* **579**, 1917–1922 (2005). doi: 10.1016/j.febslet.2005.01.083; pmid: 15792796
25. C. Heidrich *et al*., Isolation, characterization, and heterologous expression of the novel lantibiotic epicidin 280 and analysis of its biosynthetic gene cluster. *Appl. Environ. Microbiol.* **64**, 3140–3146 (1998). pmid: 9726851
26. H. G. Sahl, H. Brandis, Production, purification and chemical properties of an antistaphylococcal agent produced by *Staphylococcus epidermidis*. *J. Gen. Microbiol.* **127**, 377–384 (1981). pmid: 7343644
27. J. E. Velásquez, X. Zhang, W. A. van der Donk, Biosynthesis of the antimicrobial peptide epilancin 15X and its N-terminal lactate. *Chem. Biol.* **18**, 857–867 (2011). doi: 10.1016/j.chembiol.2011.05.007; pmid: 21802007
28. J. Dabard *et al*., Ruminococcin A, a new lantibiotic produced by a *Ruminococcus gnavus* strain isolated from human feces. *Appl. Environ. Microbiol.* **67**, 4111–4118 (2001). doi: 10.1128/AEM.67.9.4111-4118.2001; pmid: 11526013
29. F. Marcille *et al*., Distribution of genes encoding the trypsin-dependent lantibiotic ruminococcin A among bacteria isolated from human fecal microbiota. *Appl. Environ. Microbiol.* **68**, 3424–3431 (2002). doi: 10.1128/AEM.68.7.3424-3431.2002; pmid: 12089024
30. J. C. Scott, H. G. Sahl, A. Carne, J. R. Tagg, Lantibiotic-mediated anti-lactobacillus activity of a vaginal *Staphylococcus aureus* isolate. *FEMS Microbiol. Lett.* **72**, 97–102 (1992). doi: 10.1111/j.1574-6968.1992.tb05047.x; pmid: 1612423
31. K. M. Daly *et al*., Production of the Bsa lantibiotic by community-acquired *Staphylococcus aureus* strains. *J. Bacteriol.* **192**, 1131–1142 (2010). doi: 10.1128/JB.01375-09; pmid: 20023032
32. R. W. Jack *et al*., Elucidation of the structure of SA-FF22, a lanthionine-containing antibacterial peptide produced by *Streptococcus pyogenes* strain FF22. *Eur. J. Biochem.* **220**, 455–462 (1994). doi: 10.1111/j.1432-1033.1994.tb18643.x; pmid: 8125103
33. J. R. Tagg, L. W. Wannamaker, Streptococcin A-FF22: Nisin-like antibiotic substance produced by a group A streptococcus. *Antimicrob. Agents Chemother.* **14**, 31–39 (1978). doi: 10.1128/AAC.14.1.31; pmid: 28692
34. P. S. Coburn, M. S. Gilmore, The *Enterococcus faecalis* cytolysin: A novel toxin active against eukaryotic and prokaryotic cells. *Cell. Microbiol.* **5**, 661–669 (2003). doi: 10.1046/j.1462-5822.2003.00310.x; pmid: 12969372
35. S. Duquesne, D. Destoumieux-Garzón, J. Peduzzi, S. Rebuffat, Microcins, gene-encoded antibacterial peptides from enterobacteria. *Nat. Prod. Rep.* **24**, 708–734 (2007). doi: 10.1039/b516237h; pmid: 17653356
36. Y. M. Li, J. C. Milne, L. L. Madison, R. Kolter, C. T. Walsh, From peptide precursors to oxazole and thiazole-containing peptide antibiotics: Microcin B17 synthase. *Science* **274**, 1188–1193 (1996). doi: 10.1126/science.274.5290.1188; pmid: 8895467
37. R. F. Roush, E. M. Nolan, F. Löhr, C. T. Walsh, Maturation of an *Escherichia coli* ribosomal peptide antibiotic by ATP-consuming N-P bond formation in microcin C7. *J. Am. Chem. Soc.* **130**, 3603–3609 (2008). doi: 10.1021/ja7101949; pmid: 18290647
38. E. M. Nolan, M. A. Fischbach, A. Koglin, C. T. Walsh, Biosynthetic tailoring of microcin E492m: Post-translational modification affords an antibacterial siderophore-peptide conjugate. *J. Am. Chem. Soc.* **129**, 14336–14347 (2007). doi: 10.1021/ja074650f; pmid: 17973380
39. L. Micenková *et al*., Bacteriocin-encoding genes and ExPEC virulence determinants are associated in human fecal *Escherichia coli* strains. *BMC Microbiol.* **14**, 109 (2014). doi: 10.1186/1471-2180-14-109; pmid: 24774171
40. D. Šmajs *et al*., Bacteriocin synthesis in uropathogenic and commensal *Escherichia coli*: Colicin E1 is a potential virulence factor. *BMC Microbiol.* **10**, 288 (2010). doi: 10.1186/1471-2180-10-288; pmid: 21078157
41. A. Zschüttig *et al*., Identification and characterization of microcin S, a new antibacterial peptide produced by probiotic *Escherichia coli* G3/10. *PLOS ONE* **7**, e33351 (2012). doi: 10.1371/journal.pone.0033351; pmid: 22479389
42. J. O. Melby, N. J. Nard, D. A. Mitchell, Thiazole/oxazole-modified microcins: Complex natural products from ribosomal templates. *Curr. Opin. Chem. Biol.* **15**, 369–378 (2011). doi: 10.1016/j.cbpa.2011.02.027; pmid: 21429787
43. E. M. Molloy, P. D. Cotter, C. Hill, D. A. Mitchell, R. P. Ross, Streptolysin S-like virulence factors: The continuing sagA. *Nat. Rev. Microbiol.* **9**, 670–681 (2011). doi: 10.1038/nrmicro2624; pmid: 21822292
44. S. W. Lee *et al*., Discovery of a widely distributed toxin biosynthetic gene cluster. *Proc. Natl. Acad. Sci. U.S.A.* **105**, 5879–5884 (2008). doi: 10.1073/pnas.0801338105; pmid: 18375757
45. D. A. Mitchell *et al*., Structural and functional dissection of the heterocyclic peptide cytotoxin streptolysin S. *J. Biol. Chem.* **284**, 13004–13012 (2009). doi: 10.1074/jbc.M900802200; pmid: 19286651
46. P. D. Cotter *et al*., Listeriolysin S, a novel peptide haemolysin associated with a subset of lineage I *Listeria monocytogenes*. *PLOS Pathog.* **4**, e1000144 (2008). doi: 10.1371/journal.ppat.1000144; pmid: 18787690
47. D. J. Gonzalez *et al*., Clostridiolysin S, a post-translationally modified biotoxin from *Clostridium botulinum*. *J. Biol. Chem.* **285**, 28220–28228 (2010). doi: 10.1074/jbc.M110.118554; pmid: 20581111
48. H. Ozaki *et al*., Molecular structure of the toxin domain of heat-stable enterotoxin produced by a pathogenic strain of *Escherichia coli*. A putative binding site for a binding protein on rat intestinal epithelial cell membranes. *J. Biol. Chem.* **266**, 5934–5941 (1991). pmid: 2005130
49. S. Schulz, C. K. Green, P. S. Yuen, D. L. Garbers, Guanylyl cyclase is a heat-stable enterotoxin receptor. *Cell* **63**, 941–948 (1990). doi: 10.1016/0092-8674(90)90497-3; pmid: 1701694
50. V. McWilliams, G. Whiteside, K. McKeage, Linaclotide: First global approval. *Drugs* **72**, 2167–2175 (2012). doi: 10.2165/11470590-000000000-00000; pmid: 23083112
51. M. A. Fischbach, J. L. Sonnenburg, Eating for two: How metabolism establishes interspecies interactions in the gut. *Cell Host Microbe* **10**, 336–347 (2011). doi: 10.1016/j.chom.2011.10.002; pmid: 22018234

52. W. R. Wikoff *et al*., Metabolomics analysis reveals large effects of gut microflora on mammalian blood metabolites. *Proc. Natl. Acad. Sci. U.S.A.* **106**, 3698–3703 (2009). doi: 10.1073/pnas.0812874106; pmid: 19234110
53. J. H. Lee, J. Lee, Indole as an intercellular signal in microbial communities. *FEMS Microbiol. Rev.* **34**, 426–444 (2010). doi: 10.1111/j.1574-6976.2009.00204.x; pmid: 20070374
54. P. A. Aronov *et al*., Colonic contribution to uremic solutes. *J. Am. Soc. Nephrol.* **22**, 1769–1776 (2011). doi: 10.1681/ASN.2010121220; pmid: 21784895
55. K. P. Patel, F. J. Luo, N. S. Plummer, T. H. Hostetter, T. W. Meyer, The production of p-cresol sulfate and indoxyl sulfate in vegetarians versus omnivores. *Clin. J. Am. Soc. Nephrol.* **7**, 982–988 (2012). doi: 10.2215/CJN.12491211; pmid: 22490877
56. B. B. Williams *et al*., Discovery and characterization of gut microbiota decarboxylases that can produce the neurotransmitter trytamine. *Cell Host Microbe* **16**, 495–503 (2014). doi: 10.1016/j.chom.2014.09.001; pmid: 25263219
57. M. Takaki, G. M. Mawe, J. M. Barasch, M. D. Gershon, M. D. Gershon, Physiological responses of guinea-pig myenteric neurons secondary to the release of endogenous serotonin by tryptamine. *Neuroscience* **16**, 223–240 (1985). doi: 10.1016/0306-4522(85)90059-4; pmid: 2940472
58. J. M. Yano *et al*., Indigenous bacteria from the gut microbiota regulate host serotonin biosynthesis. *Cell* **161**, 264–276 (2015). doi: 10.1016/j.cell.2015.02.047; pmid: 25860609
59. E. Y. Hsiao *et al*., Microbiota modulate behavioral and physiological abnormalities associated with neurodevelopmental disorders. *Cell* **155**, 1451–1463 (2013). doi: 10.1016/j.cell.2013.11.024; pmid: 24315484
60. E. A. Mayer, K. Tillisch, A. Gupta, Gut/brain axis and the microbiota. *J. Clin. Invest.* **125**, 926–938 (2015). doi: 10.1172/JCI76304; pmid: 25689247
61. A. Burokas, R. D. Moloney, T. G. Dinan, J. F. Cryan, Microbiota regulation of the Mammalian gut-brain axis. *Adv. Appl. Microbiol.* **91**, 1–62 (2015). doi: 10.1016/bs.aambs.2015.02.001; pmid: 25911232
62. H. A. Barker, Amino acid degradation by anaerobic bacteria. *Annu. Rev. Biochem.* **50**, 23–40 (1981). doi: 10.1146/annurev.bi.50.070181.000323; pmid: 6791576
63. P. M. Flatt, T. Mahmud, Biosynthesis of aminocyclitol-aminoglycoside antibiotics and related compounds. *Nat. Prod. Rep.* **24**, 358–392 (2007). doi: 10.1039/B603816F; pmid: 17390001
64. E. K. McCranie, B. O. Bachmann, Bioactive oligosaccharide natural products. *Nat. Prod. Rep.* **31**, 1026–1042 (2014). doi: 10.1039/C3NP70128J; pmid: 24883430
65. A. Z. Mostafavi, J. M. Troutman, Biosynthetic assembly of the *Bacteroides fragilis* capsular polysaccharide A precursor bactoprenyl diphosphate-linked acetamido-4-amino-6-deoxygalactopyranose. *Biochemistry* **52**, 1939–1949 (2013). doi: 10.1021/bi400126w; pmid: 23458065
66. J. M. Troutman, S. Sharma, K. M. Erickson, C. D. Martinez, Functional identification of a galactosyltransferase critical to *Bacteroides fragilis* Capsular Polysaccharide A biosynthesis. *Carbohydr. Res.* **395**, 19–28 (2014). doi: 10.1016/j.carres.2014.06.003; pmid: 24997288
67. S. K. Mazmanian, J. L. Round, D. L. Kasper, A microbial symbiosis factor prevents intestinal inflammatory disease. *Nature* **453**, 620–625 (2008). doi: 10.1038/nature07008; pmid: 18509436
68. J. L. Round *et al*., The Toll-like receptor 2 pathway establishes colonization by a commensal of the human microbiota. *Science* **332**, 974–977 (2011). doi: 10.1126/science.1206095; pmid: 21512004
69. M. J. Cieslewicz *et al*., Structural and genetic diversity of group B streptococcus capsular polysaccharides. *Infect. Immun.* **73**, 3096–3103 (2005). doi: 10.1128/IAI.73.5.3096-3103.2005; pmid: 15845517
70. P. M. Smith *et al*., The microbial metabolites, short-chain fatty acids, regulate colonic Treg cell homeostasis. *Science* **341**, 569–573 (2013). doi: 10.1126/science.1241165; pmid: 23828891
71. S. E. Girardin *et al*., Nod1 detects a unique muropeptide from gram-negative bacterial peptidoglycan. *Science* **300**, 1584–1587 (2003). doi: 10.1126/science.1084677; pmid: 12791997
72. S. E. Girardin *et al*., Nod2 is a general sensor of peptidoglycan through muramyl dipeptide (MDP) detection. *J. Biol. Chem.* **278**, 8869–8872 (2003). doi: 10.1074/jbc.C200651200; pmid: 12527755
73. T. B. Geijtenbeek, S. I. Gringhuis, Signalling through C-type lectin receptors: Shaping immune responses. *Nat. Rev. Immunol.* **9**, 465–479 (2009). doi: 10.1038/nri2569; pmid: 19521399
74. C. Whitfield, M. S. Trent, Biosynthesis and export of bacterial lipopolysaccharides. *Annu. Rev. Biochem.* **83**, 99–128 (2014). doi: 10.1146/annurev-biochem-060713-035600; pmid: 24580642
75. K. Akimoto, T. Natori, M. Morita, Synthesis and stereochemistry of agelasphin-9b. *Tetrahedron Lett.* **34**, 5593–5596 (1993). doi: 10.1016/S0040-4039(00)73890-1
76. A. Bendelac, P. B. Savage, L. Teyton, The biology of NKT cells. *Annu. Rev. Immunol.* **25**, 297–336 (2007). doi: 10.1146/annurev.immunol.25.022106.141711; pmid: 17150027
77. L. C. Wieland Brown *et al*., Production of α-galactosylceramide by a prominent member of the human gut microbiota. *PLOS Biol.* **11**, e1001610 (2013). doi: 10.1371/journal.pbio.1001610; pmid: 23874157
78. D. An *et al*., Sphingolipids from a symbiotic microbe regulate homeostasis of host intestinal natural killer T cells. *Cell* **156**, 123–133 (2014). doi: 10.1016/j.cell.2013.11.042; pmid: 24439373
79. H. Marrakchi, M. A. Lanéelle, M. Daffé, Mycolic acids: Structures, biosynthesis, and beyond. *Chem. Biol.* **21**, 67–85 (2014). doi: 10.1016/j.chembiol.2013.11.011; pmid: 24374164
80. E. Layre *et al*., Mycolic acids constitute a scaffold for mycobacterial lipid antigens stimulating CD1-restricted T cells. *Chem. Biol.* **16**, 82–92 (2009). doi: 10.1016/j.chembiol.2008.11.008; pmid: 19171308
81. D. B. Moody *et al*., Lipid length controls antigen entry into endosomal and nonendosomal pathways for CD1b presentation. *Nat. Immunol.* **3**, 435–442 (2002). pmid: 11938350
82. D. B. Moody *et al*., Structural requirements for glycolipid antigen recognition by CD1b-restricted T cells. *Science* **278**, 283–286 (1997). doi: 10.1126/science.278.5336.283; pmid: 9323206
83. I. Van Rhijn *et al*., A conserved human T cell population targets mycobacterial antigens presented by CD1b. *Nat. Immunol.* **14**, 706–713 (2013). doi: 10.1038/ni.2630; pmid: 23727893
84. E. Ishikawa *et al*., Direct recognition of the mycobacterial glycolipid, trehalose dimycolate, by C-type lectin Mincle. *J. Exp. Med.* **206**, 2879–2888 (2009). doi: 10.1084/jem.20091750; pmid: 20008526
85. D. N. Dao *et al*., Mycolic acid modification by the mmaA4 gene of *M. tuberculosis* modulates IL-12 production. *PLOS Pathog.* **4**, e1000081 (2008). doi: 10.1371/journal.ppat.1000081; pmid: 18535659
86. D. Barkan, D. Hedhli, H. G. Yan, K. Huygen, M. S. Glickman, Mycobacterium tuberculosis lacking all mycolic acid cyclopropanation is viable but highly attenuated and hyperinflammatory in mice. *Infect. Immun.* **80**, 1958–1968 (2012). doi: 10.1128/IAI.00021-12; pmid: 22431648
87. J. M. Ridlon, D. J. Kang, P. B. Hylemon, Bile salt biotransformations by human intestinal bacteria. *J. Lipid Res.* **47**, 241–259 (2006). doi: 10.1194/jlr.R500013-JLR200; pmid: 16299351
88. P. Gérard, Metabolism of cholesterol and bile acids by the gut microbiota. *Pathogens* **3**, 14–24 (2013). doi: 10.3390/pathogens3010014; pmid: 25437605
89. J. M. Ridlon, D. J. Kang, P. B. Hylemon, Isolation and characterization of a bile acid inducible 7alpha-dehydroxylating operon in *Clostridium hylemonae* TN271. *Anaerobe* **16**, 137–146 (2010). doi: 10.1016/j.anaerobe.2009.05.004; pmid: 19464381
90. W. S. Garrett, Cancer and the microbiota. *Science* **348**, 80–86 (2015). doi: 10.1126/science.aaa4972; pmid: 25838377
91. J. H. Marshall, G. J. Wilmoth, Pigments of *Staphylococcus aureus*, a series of triterpenoid carotenoids. *J. Bacteriol.* **147**, 900–913 (1981). pmid: 7275936
92. A. Pelz *et al*., Structure and biosynthesis of staphyloxanthin from *Staphylococcus aureus*. *J. Biol. Chem.* **280**, 32493–32498 (2005). doi: 10.1074/jbc.M505070200; pmid: 16020541
93. B. Wieland *et al*., Genetic and biochemical analyses of the biosynthesis of the yellow carotenoid 4,4′-diaponeurosporene of *Staphylococcus aureus*. *J. Bacteriol.* **176**, 7719–7726 (1994). pmid: 8002598
94. A. Clauditz, A. Resch, K. P. Wieland, A. Peschel, F. Götz, Staphyloxanthin plays a role in the fitness of *Staphylococcus aureus* and its ability to cope with oxidative stress. *Infect. Immun.* **74**, 4950–4953 (2006). doi: 10.1128/IAI.00204-06; pmid: 16861688
95. A. C. Olivier, S. Lemaire, F. Van Bambeke, P. M. Tulkens, E. Oldfield, Role of rsbU and staphyloxanthin in phagocytosis and intracellular growth of *Staphylococcus aureus* in human macrophages and endothelial cells. *J. Infect. Dis.* **200**, 1367–1370 (2009). doi: 10.1086/606012; pmid: 19817587
96. M. A. Wyatt *et al*., *Staphylococcus aureus* nonribosomal peptide secondary metabolites regulate virulence. *Science* **329**, 294–296 (2010). doi: 10.1126/science.1188888; pmid: 20522739
97. M. Zimmermann, M. A. Fischbach, A family of pyrazinone natural products from a conserved nonribosomal peptide synthetase in *Staphylococcus aureus*. *Chem. Biol.* **17**, 925–930 (2010). doi: 10.1016/j.chembiol.2010.08.006; pmid: 20851341
98. F. Sun *et al*., Aureusimines in *Staphylococcus aureus* are not involved in virulence. *PLOS ONE* **5**, e15703 (2010). doi: 10.1371/journal.pone.0015703; pmid: 21209955
99. C. Wu *et al*., Genomic island TnSmu2 of *Streptococcus mutans* harbors a nonribosomal peptide synthetase-polyketide synthase gene cluster responsible for the biosynthesis of pigments involved in oxygen and H2O2 tolerance. *Appl. Environ. Microbiol.* **76**, 5815–5826 (2010). doi: 10.1128/AEM.03079-09; pmid: 20639370
100. P. M. Joyner *et al*., Mutanobactin A from the human oral pathogen *Streptococcus mutans* is a cross-kingdom regulator of the yeast-mycelium transition. *Org. Biomol. Chem.* **8**, 5486–5489 (2010). doi: 10.1039/c0ob00579g; pmid: 20852771
101. H. Sztajer *et al*., Cross-feeding and interkingdom communication in dual-species biofilms of *Streptococcus mutans* and *Candida albicans*. *ISME J.* **8**, 2256–2271 (2014). doi: 10.1038/ismej.2014.73; pmid: 24824668
102. X. Wang, L. Du, J. You, J. B. King, R. H. Cichewicz, Fungal biofilm inhibitors from a human oral microbiome-derived bacterium. *Org. Biomol. Chem.* **10**, 2044–2050 (2012). doi: 10.1039/c2ob06856g; pmid: 22281750
103. N. Agata, M. Ohta, M. Mori, M. Isobe, A novel dodecadepsipeptide, cereulide, is an emetic toxin of *Bacillus cereus*. *FEMS Microbiol. Lett.* **129**, 17–20 (1995). pmid: 7781985
104. S. Suwan *et al*., Structure of cereulide, a cyclic dodecadepsipeptide toxin from B*acillus cereus* and studies on NMR characteristics of its alkali metal complexes including a conformational structure of the K+ complex. *J. Chem. Soc. Perkin Trans. 1* **1995**, 765–775 (1995). doi: 10.1039/p19950000765
105. M. Ehling-Schulz *et al*., Cereulide synthetase gene cluster from emetic *Bacillus cereus*: Structure and location on a mega virulence plasmid related to *Bacillus anthracis* toxin plasmid pXO1. *BMC Microbiol.* **6**, 20 (2006). doi: 10.1186/1471-2180-6-20; pmid: 16512902
106. V. V. Teplova, R. Mikkola, A. A. Tonshin, N. E. Saris, M. S. Salkinoja-Salonen, The higher toxicity of cereulide relative to valinomycin is due to its higher affinity for potassium at physiological plasma concentration. *Toxicol. Appl. Pharmacol.* **210**, 39–46 (2006). doi: 10.1016/j.taap.2005.06.012; pmid: 16039680
107. Y. Kishi, Chemistry of mycolactones, the causative toxins of Buruli ulcer. *Proc. Natl. Acad. Sci. U.S.A.* **108**, 6703–6708 (2011). doi: 10.1073/pnas.1015252108; pmid: 21383136
108. F. S. Sarfo *et al*., Kinetics of mycolactone in human subcutaneous tissue during antibiotic therapy for *Mycobacterium ulcerans* disease. *BMC Infect. Dis.* **14**, 202 (2014). doi: 10.1186/1471-2334-14-202; pmid: 24731247
109. A. Mve-Obiang, R. E. Lee, F. Portaels, P. L. C. Small, Heterogeneity of mycolactones produced by clinical isolates of *Mycobacterium ulcerans*: Implications for virulence. *Infect. Immun.* **71**, 774–783 (2003). doi: 10.1128/IAI.71.2.774-783.2003; pmid: 12540557
110. A. C. Chany, C. Tresse, V. Casarotto, N. Blanchard, History, biology and chemistry of *Mycobacterium ulcerans* infections (Buruli ulcer disease). *Nat. Prod. Rep.* **30**, 1527–1567 (2013). doi: 10.1039/c3np70068b; pmid: 24178858
111. H. Hong, C. Demangel, S. J. Pidot, P. F. Leadlay, T. Stinear, Mycolactones: Immunosuppressive and cytotoxic polyketides produced by aquatic mycobacteria. *Nat. Prod. Rep.* **25**, 447–454 (2008). doi: 10.1039/b803101k; pmid: 18497894
112. E. Marion *et al*., Mycobacterial toxin induces analgesia in buruli ulcer by targeting the angiotensin pathways. *Cell* **157**, 1565–1576 (2014). doi: 10.1016/j.cell.2014.04.040; pmid: 24949969
113. J. Putze *et al*., Genetic structure and distribution of the colibactin genomic island among members of the family Enterobacteriaceae. *Infect. Immun.* **77**, 4696–4703 (2009). doi: 10.1128/IAI.00522-09; pmid: 19720753

114. J. P. Nougayrède *et al*., Escherichia coli induces DNA double-strand breaks in eukaryotic cells. *Science* **313**, 848–851 (2006). doi: 10.1126/science.1127059; pmid: 16902142
115. G. Cuevas-Ramos *et al*., *Escherichia coli* induces DNA damage in vivo and triggers genomic instability in mammalian cells. *Proc. Natl. Acad. Sci. U.S.A.* **107**, 11537–11542 (2010). doi: 10.1073/pnas.1001261107; pmid: 20534522
116. A. Cougnoux *et al*., Bacterial genotoxin colibactin promotes colon tumour growth by inducing a senescence-associated secretory phenotype. *Gut* **63**, 1932–1942 (2014). doi: 10.1136/gutjnl-2013-305257; pmid: 24658599
117. T. Secher, A. Samba-Louaka, E. Oswald, J. P. Nougayrède, *Escherichia coli* producing colibactin triggers premature and transmissible senescence in mammalian cells. *PLOS ONE* **8**, e77157 (2013). doi: 10.1371/journal.pone.0077157; pmid: 24116215
118. Y. C. Lai *et al*., Genotoxic *Klebsiella pneumoniae* in Taiwan. *PLOS ONE* **9**, e96292 (2014). doi: 10.1371/journal.pone.0096292; pmid: 24852749
119. X. Bian *et al*., In vivo evidence for a prodrug activation mechanism during colibactin maturation. *ChemBioChem* **14**, 1194–1197 (2013). doi: 10.1002/cbic.201300208; pmid: 23744512
120. M. I. Vizcaino, P. Engel, E. Trautman, J. M. Crawford, Comparative metabolomics and structural characterizations illuminate colibactin pathway-dependent small molecules. *J. Am. Chem. Soc.* **136**, 9244–9247 (2014). doi: 10.1021/ja503450q; pmid: 24932672
121. C. A. Brotherton, E. P. Balskus, A prodrug resistance mechanism is involved in colibactin biosynthesis and cytotoxicity. *J. Am. Chem. Soc.* **135**, 3359–3362 (2013). doi: 10.1021/ja312154m; pmid: 23406518
122. M. I. Vizcaino, J. M. Crawford, The colibactin warhead crosslinks DNA. *Nat. Chem.* **7**, 411–417 (2015). doi: 10.1038/nchem.2221; pmid: 25901819
123. G. Schneditz *et al*., Enterotoxicity of a nonribosomal peptide causes antibiotic-associated colitis. *Proc. Natl. Acad. Sci. U.S.A.* **111**, 13181–13186 (2014). doi: 10.1073/pnas.1403274111; pmid: 25157164
124. C. Högenauer *et al*., *Klebsiella oxytoca* as a causative organism of antibiotic-associated hemorrhagic colitis. *N. Engl. J. Med.* **355**, 2418–2426 (2006). doi: 10.1056/NEJMoa054765; pmid: 17151365
125. G. L. Challis, A widely distributed bacterial pathway for siderophore biosynthesis independent of nonribosomal peptide synthetases. *ChemBioChem* **6**, 601–611 (2005). doi: 10.1002/cbic.200400283; pmid: 15719346
126. J. H. Crosa, C. T. Walsh, Genetics and assembly line enzymology of siderophore biosynthesis in bacteria. *Microbiol. Mol. Biol. Rev.* **66**, 223–249 (2002). doi: 10.1128/MMBR.66.2.223-249.2002; pmid: 12040125
127. M. A. Fischbach, H. Lin, D. R. Liu, C. T. Walsh, How pathogenic bacteria evade mammalian sabotage in the battle for iron. *Nat. Chem. Biol.* **2**, 132–138 (2006). doi: 10.1038/nchembio771; pmid: 16485005
128. M. G. Langille *et al*., Predictive functional profiling of microbial communities using 16S rRNA marker gene sequences. *Nat. Biotechnol.* **31**, 814–821 (2013). doi: 10.1038/nbt.2676; pmid: 23975157
129. M. S. Donia *et al*., Complex microbiome underlying secondary and primary metabolism in the tunicate-Prochloron symbiosis. *Proc. Natl. Acad. Sci. U.S.A.* **108**, E1423–E1432 (2011). doi: 10.1073/pnas.1111712108; pmid: 22123943
130. N. Ziemert *et al*., Diversity and evolution of secondary metabolism in the marine actinomycete genus *Salinispora*. *Proc. Natl. Acad. Sci. U.S.A.* **111**, E1130–E1139 (2014). doi: 10.1073/pnas.1324161111; pmid: 24616526
131. E. Holmes *et al*., Therapeutic modulation of microbiota-host metabolic interactions. *Sci. Transl. Med.* **4**, 137rv6 (2012). doi: 10.1126/scitranslmed.3004244; pmid: 22674556
132. J. K. Nicholson *et al*., Host-gut microbiota metabolic interactions. *Science* **336**, 1262–1267 (2012). doi: 10.1126/science.1223813; pmid: 22674330
133. S. Yoshimoto *et al*., Obesity-induced gut microbial metabolite promotes liver cancer through senescence secretome. *Nature* **499**, 97–101 (2013). doi: 10.1038/nature12347; pmid: 23803760
134. A. Marcobal *et al*., A metabolomic view of how the human gut microbiota impacts the host metabolome using humanized and gnotobiotic mice. *ISME J.* **7**, 1933–1943 (2013). doi: 10.1038/ismej.2013.89; pmid: 23739052
135. K. Atarashi *et al*., Induction of colonic regulatory T cells by indigenous *Clostridium* species. *Science* **331**, 337–341 (2011). doi: 10.1126/science.1198469; pmid: 21205640
136. K. Atarashi *et al*., Treg induction by a rationally selected mixture of *Clostridia* strains from the human microbiota. *Nature* **500**, 232–236 (2013). doi: 10.1038/nature12331; pmid: 23842501
137. P. Gajer *et al*., Temporal dynamics of the human vaginal microbiota. *Sci. Transl. Med.* **4**, 132ra52 (2012). doi: 10.1126/scitranslmed.3003605; pmid: 22553250
138. M. J. LaMarche *et al*., Discovery of LFF571: An investigational agent for *Clostridium difficile* infection. *J. Med. Chem.* **55**, 2376–2387 (2012). doi: 10.1021/jm201685h; pmid: 22315981
139. E. H. Crost *et al*., Ruminococcin C, a new anti-*Clostridium perfringens* bacteriocin produced in the gut by the commensal bacterium *Ruminococcus gnavus* E1. *Biochimie* **93**, 1487–1494 (2011). doi: 10.1016/j.biochi.2011.05.001; pmid: 21586310
140. A. Pujol *et al*., Characterization and distribution of the gene cluster encoding RumC, an anti-*Clostridium perfringens* bacteriocin produced in the gut. *FEMS Microbiol. Ecol.* **78**, 405–415 (2011). doi: 10.1111/j.1574-6941.2011.01176.x; pmid: 22092178
141. F. Ramare *et al*., Trypsin-dependent production of an antibacterial substance by a human *Peptostreptococcus* strain in gnotobiotic rats and in vitro. *Appl. Environ. Microbiol.* **59**, 2876–2883 (1993). pmid: 8215361
142. L. Cursino *et al*., Exoproducts of the *Escherichia coli* strain H22 inhibiting some enteric pathogens both in vitro and in vivo. *J. Appl. Microbiol.* **100**, 821–829 (2006). doi: 10.1111/j.1365-2672.2006.02834.x; pmid: 16553738
143. R. E. Wooley, P. S. Gibbs, E. B. Shotts Jr.., Inhibition of *Salmonella typhimurium* in the chicken intestinal tract by a transformed avirulent avian *Escherichia coli*. *Avian Dis.* **43**, 245–250 (1999). doi: 10.2307/1592614; pmid: 10396637
144. J. J. Faith, P. P. Ahern, V. K. Ridaura, J. Cheng, J. I. Gordon, Identifying gut microbe-host phenotype relationships using combinatorial communities in gnotobiotic mice. *Sci. Transl. Med.* **6**, 220ra11 (2014). doi: 10.1126/scitranslmed.3008051; pmid: 24452263
145. S. Naik *et al*., Commensal-dendritic-cell interaction specifies a unique protective skin immune signature. *Nature* **520**, 104–108 (2015). doi: 10.1038/nature14052; pmid: 25539086
146. P. E. Kolenbrander, R. J. Palmer Jr., S. Periasamy, N. S. Jakubovics, Oral multispecies biofilm development and the key role of cell-cell distance. *Nat. Rev. Microbiol.* **8**, 471–480 (2010). doi: 10.1038/nrmicro2381; pmid: 20514044
147. P. D. Hsu, E. S. Lander, F. Zhang, Development and applications of CRISPR-Cas9 for genome engineering. *Cell* **157**, 1262–1278 (2014). doi: 10.1016/j.cell.2014.05.010; pmid: 24906146
148. K. Temme, D. Zhao, C. A. Voigt, Refactoring the nitrogen fixation gene cluster from *Klebsiella oxytoca*. *Proc. Natl. Acad. Sci. U.S.A.* **109**, 7085–7090 (2012). doi: 10.1073/pnas.1120788109; pmid: 22509035

ACKNOWLEDGMENTS

We thank members of the Fischbach and Donia groups for helpful discussions. Work in the authors' laboratories is supported by Princeton University (M.S.D.); a Medical Research Program Grant from the W.M. Keck Foundation (M.A.F.); a Fellowship for Science and Engineering from the David and Lucile Packard Foundation (M.A.F.); an Investigators in the Pathogenesis of Infectious Disease award from the Burroughs Wellcome Foundation (M.A.F.); Defense Advanced Research Projects Agency award HR0011-12-C-0067 (M.A.F.); the Program for Breakthrough Biomedical Research (M.A.F.); and NIH grants OD007290, AI101018, GM081879, and DK101674 (M.A.F.). M.A.F. is on the scientific advisory boards of NGM Biopharmaceuticals and Warp Drive Bio.

10.1126/science.1254766

REPORTS

APPLIED ORIGAMI

Origami of thick panels

Yan Chen,[1] Rui Peng,[1] Zhong You[2]*

Origami patterns, including the rigid origami patterns in which flat inflexible sheets are joined by creases, are primarily created for zero-thickness sheets. In order to apply them to fold structures such as roofs, solar panels, and space mirrors, for which thickness cannot be disregarded, various methods have been suggested. However, they generally involve adding materials to or offsetting panels away from the idealized sheet without altering the kinematic model used to simulate folding. We develop a comprehensive kinematic synthesis for rigid origami of thick panels that differs from the existing kinematic model but is capable of reproducing motions identical to that of zero-thickness origami. The approach, proven to be effective for typical origami, can be readily applied to fold real engineering structures.

Origami is the art of folding essentially two-dimensional materials such as paper into three-dimensional objects. It has recently gained popularity among scientists and engineers because the technique can be used to create shape-changing structures. Rigid origami is a subset of origami that considers rigid objects connected by hinges. This type of origami has probably the greatest application potential in engineering structures (*1*, *2*)—ranging from solar panels (*3*), space mirrors, and aircraft wings, to robots (*4*)—because most materials used in these applications are relatively rigid. To date, all kinematic modeling of rigid origami treats the paper as having zero thickness. At each vertex where creases, or fold lines, meet, the origami is considered as a spherical linkage, where creases act as revolute joints (*R*) and the paper bounded by the creases act as links. A rigid origami pattern is therefore a combination of many such linkages. For panels of nonzero thickness, various techniques have been suggested to use the same kinematic model, which include adding tapered materials to the plane of zero-thickness (*5*) or offsetting panels away from the planes defined by the adjacent creases (*6*). The tapered material technique has been used to fold a thick panel based on the Miura-ori, whereas the offset one has been used for folding a square-twist origami pattern. However, these methods often result in surfaces that are either not entirely flat or with voids to allow folding. Two exceptions to this are the technique introduced by Hoberman to fold the symmetric Miura-ori (*7*), and the technique by De Temmerman for the diamond origami pattern (*8*). Not all of the fold lines meet at a point in either of these methods, and thus, the vertices no longer exist. This indicates that their folding cannot be simply treated as the motion of spherical linkage assemblies. This has led us to question what a rigorous equivalent kinematic model of this type of origami should be, and whether the model can be generalized and applied so as to create origami for thick materials.

Rigid origami patterns, designed universally for a zero-thickness sheet, are made from creases intersecting at vertices. However, these patterns cannot be directly applied to a panel of nonzero thickness, given that all of the fold lines cannot be placed on the same face of the panel because the subpanels would collide during folding. For this reason, some fold lines must be placed on the top face whereas others must be placed on the bottom face of a panel, forming an assembly in which the fold lines are neither concurrent nor intersecting at a vertex. As a result, the kinematic model of the spherical linkage around each vertex used for a zero-thickness sheet has now been replaced by a loop of rigid bodies (panels) connected by a set of revolute joints (fold lines) that are placed a distance apart because of the thickness. Its foldability depends on two conditions: (i) Each loop of connected rigid bodies must be a mechanical linkage, and (ii) the assembly of these linkages retains mobility so that it can be folded.

Most practically used patterns—such as the Miura-ori, square-twist, diamond, and waterbomb patterns—have four, five, or six creases intersecting at a vertex, and thus, the corresponding closed kinematic chains for thick panels, when foldable, are spatial 4*R*, 5*R*, and 6*R* linkages. These linkages belong to a specific family of spatial linkages often referred to as the overconstrained linkages because the Kutzbach criterion yields a mobility value of less than one (*9*). The existence of mobility is due to specific geometries that the linkages possess. In this work, we first found the kinematically equivalent spatial linkages to the single-vertex origami patterns made from four, five, and six creases, respectively, and then extended this to multiple vertex patterns by ensuring that the motion of the assembly of these linkages matches that of the zero-thickness pattern. Using this approach, origami patterns can still be designed based on a zero-thickness rigid sheet, and these patterns can consequently be synthesized for a thick rigid panel. We assume that thick panels are rigid with nonzero thickness and that fold lines, equivalent to creases in zero-thickness paper and revolute joints in linkages, can only be placed on the faces of a thick panel, and no fold lines along the depth of the panels are permitted.

A partially folded single-vertex four-crease origami pattern of a zero-thickness rigid sheet is shown in Fig. 1A. This pattern is the basic element in many well-known origami forms, such as the Miura-ori and the square-twist pattern. Four creases divide the sheet into four portions, with sector angles α_{12}, α_{23}, α_{34}, and α_{41}, respectively, and the sum of these angles equals 2π. To be flat foldable—the folded origami can be pressed flat eventually—$\alpha_{12} + \alpha_{34} = \alpha_{23} + \alpha_{41} = \pi$ must be satisfied (*10*).

The kinematic motion of this origami can be modeled as a spherical 4*R* linkage. It has a single degree of freedom, and the relationship among four dihedral angles φ_1, φ_2, φ_3, and φ_4 can be obtained analytically (*11*)

$$\frac{\tan\frac{\varphi_2}{2}}{\tan\frac{\varphi_1}{2}} = -\frac{\sin\frac{\alpha_{12}-\alpha_{23}}{2}}{\sin\frac{\alpha_{12}+\alpha_{23}}{2}},\ \varphi_1 = \varphi_3 \text{ and } \varphi_2 = \varphi_4 \quad (1)$$

Now consider its thick-panel counterpart (Fig. 1B), in which the panel is partitioned by the same set of sector angles into four subpanels. Place one fold line on the top face of subpanels, three on bottom faces. a_{12}, a_{23}, a_{34}, and a_{41} are distances between adjacent fold lines, respectively, which effectively represent the thicknesses of the subpanels.

Kinematically, this assembly is no longer a spherical linkage. It must be a spatial 4*R* linkage if it is capable of motion. The only spatial 4*R* linkage is the Bennett linkage, a century-old mechanism in which the axes of revolute joints neither meet nor are parallel (*12*). The existence of mobility is due to the special geometry conditions (*13*), which are

$$\alpha_{12} + \alpha_{34} = \alpha_{23} + \alpha_{41} = \pi \quad (2)$$

$$a_{12} = a_{34}, a_{23} = a_{41} \quad (3)$$

and

$$\frac{a_{12}}{a_{23}} = \frac{\sin\alpha_{12}}{\sin\alpha_{23}} \quad (4)$$

Equation 2 matches the flat foldable condition for a zero-thickness sheet, whereas Eqs. 3 and 4 are conditions governing the placement of fold lines. The Bennett linkage has a single degree of freedom. We can prove that the relationships among the dihedral angles are identical to those in Eq. 1, except that φ_1, φ_2, φ_3, and φ_4 are replaced by φ_1^{Be}, φ_2^{Be}, φ_3^{Be}, and φ_4^{Be}, respectively. Its motion is therefore identical to that of the spherical 4*R* linkage throughout the entire folding process (fig. S4). The spherical 4*R* linkage and this Bennett linkage are kinematically equivalent as a result. The folding process of a zero-thickness rigid origami and its thick-panel counterpart is

[1]School of Mechanical Engineering, Tianjin University, 92 Weijin Road, Nankai District, Tianjin 300072, China.
[2]Department of Engineering Science, University of Oxford, Parks Road, Oxford OX1 3PJ, UK.
*Corresponding author. E-mail: zhong.you@eng.ox.ac.uk

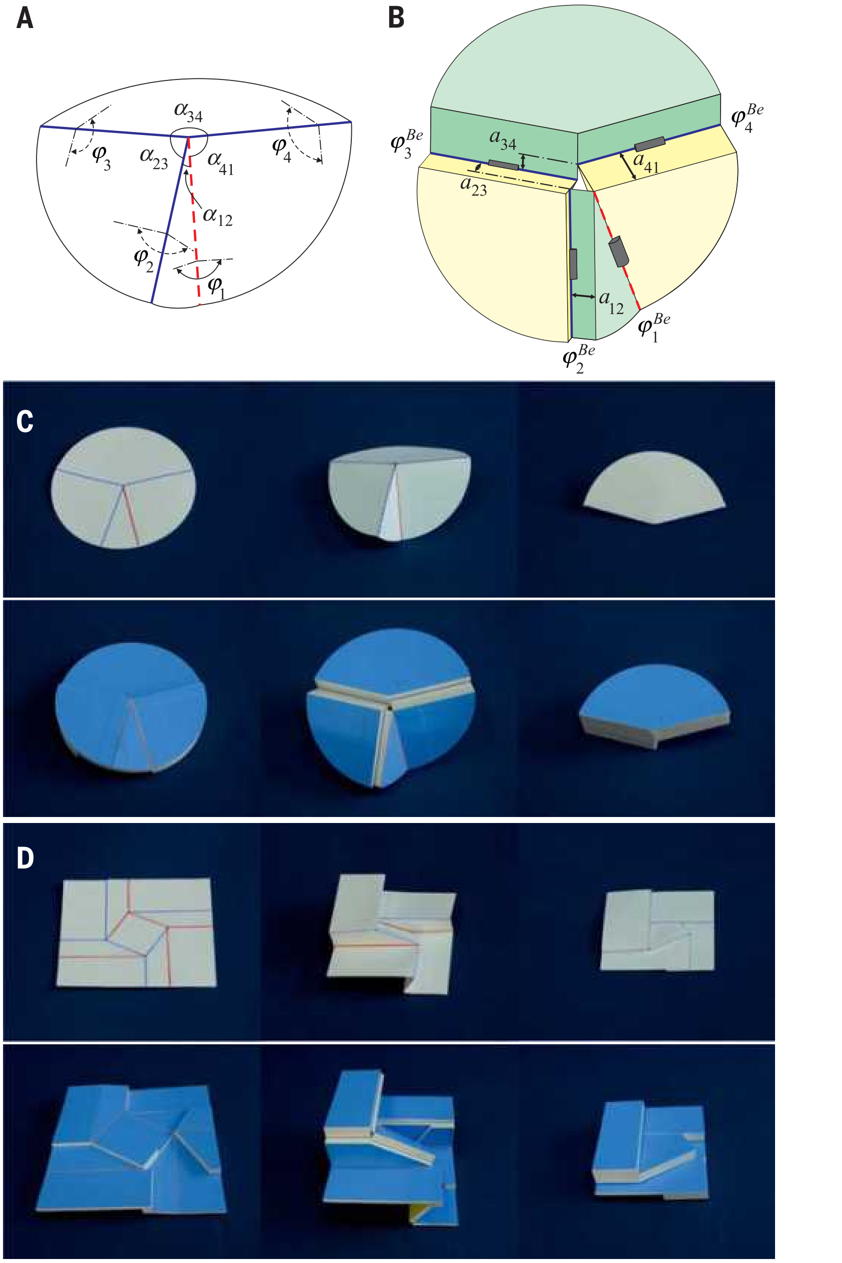

Fig. 1. Four-crease single- and multiple-vertex origami. (**A**) A partially folded single-vertex four-crease rigid origami for a zero-thickness sheet. Blue solid and red dash lines represent mountain and valley creases, respectively. αs and φs are sector and dihedral angles, respectively. (**B**) The thick-panel counterpart with the sector angles identical to those in (A), but the fold lines no longer meet at a point (vertex). *a*s are distances between adjacent fold lines, and φ^{Be}s are dihedral angles. (**C**) Folding sequence of a model made of zero-thickness sheet and its thick-panel counterpart. The sector angles for both models are $\pi/6$, $\pi/2$, $5\pi/6$, and $\pi/2$. (**D**) Folding sequence of a zero-thickness square-twist origami and its thick-panel counterpart based on the Bennett linkage. The pattern consists of four identical four-crease vertices arranged in rotational symmetry. The sector angles for each vertex are the same as those for the single-vertex model in (C).

demonstrated in Fig. 1C and movie S1. Both have four fold lines, with the same sector angles.

The four-crease thick-panel origami can be readily applied to find the thick-panel equivalence of multiple-vertex rigid origami. For example, the square-twist pattern with rotational symmetry: First, the Bennett linkage can be applied to each vertex of the pattern, preserving the sector angle of each subpanel. We then merge the fold lines that are shared by two adjacent Bennett linkages. This is possible because there is rotational symmetry in the square-twist pattern, leading to the exact same amount of rotation for the combined fold lines. The folding process of a zero-thickness rigid panel and its thick counterpart by using the square-twist pattern are shown in Fig. 1D, fig. S4, and movie S1.

Similarly, we can also create a folding scheme of a thick panel using the Miura-ori, as done by Hoberman (*7*). However, Hoberman only reported the symmetrical case in which $\alpha_{12} = \alpha_{23}$ and $\alpha_{34} = \alpha_{41}$, which is a special case of Eq. 2.

The Bennett linkage requires sector angles to satisfy Eq. 2 that equates to the condition for flat foldability. Because the Bennett linkage is the only known spatial 4*R* linkage, it can be concluded that for the four-crease rigid origami, only flat foldable patterns can have thick-panel equivalents.

The method for devising folding of four-crease patterns can be extended to the single-vertex five-crease rigid origami case. Many single-vertex five-crease origami patterns for a zero-thickness sheet exist, and here, we consider a particular one that has been used to make boxes (Fig. 2A). In this pattern, the creases divide the sheet into five pieces, with sector angles αs in which $\alpha_{51} = \alpha_{12}$, $\alpha_{23} = \alpha_{45} = \frac{\pi}{2}$, and $\alpha_{34} = \pi - 2\alpha_{12}$. It can be modeled as a spherical 5*R* linkage. In general, this linkage has two degrees of freedom, but we restrict its motion by preserving symmetry—that is, during folding, by letting the dihedral angles satisfy

$$\varphi_5 = \varphi_2 \text{ and } \varphi_4 = \varphi_3 \qquad (5)$$

We then consider its nonzero thickness counterpart (Fig. 2B), in which the thick panel is apportioned by exactly the same set of sector angles. The fold lines are then placed either on top or bottom of the panel surfaces, and the distances between a pair of neighboring fold lines are *a*s. It has become a spatial 5*R* linkage.

There are a number of 5*R* overconstrained linkages. The arrangement of the sector angles makes it possible to be a Myard linkage (*14*) because it has the same angle conditions as those for this particular linkage. In addition, the Myard linkage requires

$$a_{12} = a_{51}, a_{23} = a_{45}, \text{ and } a_{34} = 0 \qquad (6)$$

and

$$\frac{a_{12}}{a_{23}} = \frac{\sin\alpha_{12}}{\sin\alpha_{23}} \qquad (7)$$

The thick-panel assembly will have one degree of freedom if the arrangement of fold lines satisfies Eqs. 6 and 7 because it is now a Myard linkage. Furthermore, the proof in the supplementary text shows that the motion of this linkage is identical to that of the spherical 5*R* linkage when Eq. 5 is imposed. This folding scheme has been used to fold a box (Fig. 2C and movie S1).

The Myard linkage has only one degree of freedom, whereas a spherical 5*R* linkage commonly has two. It is possible to find a kinematic match only if one of the degrees of freedom of the latter is frozen, which is achieved in the above example by imposing symmetry. The same strategy is used for the six-crease example discussed next.

One of the typical six-crease origami patterns is the diamond pattern. The zero-thickness pattern (Fig. 3A) has sector angles $\alpha_{12} = \alpha_{34} = \alpha_{45} = \alpha_{61}$ and $\alpha_{23} = \alpha_{56} = \pi - 2\alpha_{12}$. This spherical linkage has three degrees of freedom in general. However, if

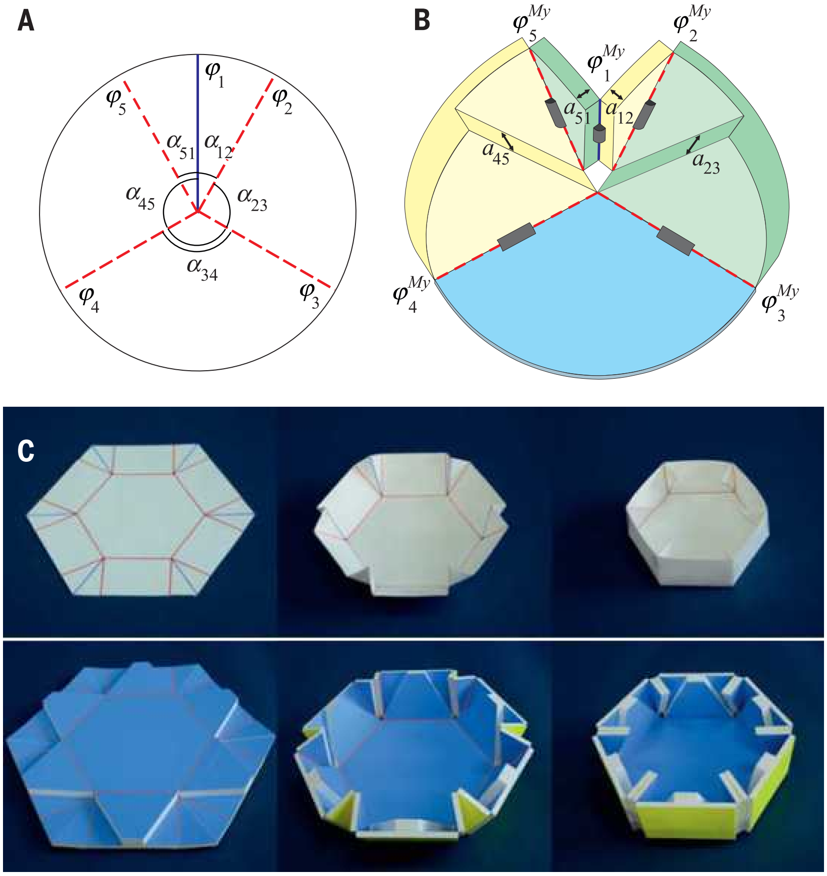

Fig. 2. Five-crease single- and multiple-vertex origami. (**A**) A single-vertex five-crease rigid origami pattern for a zero-thickness sheet. (**B**) The thick-panel counterpart with sector angles identical to those in (A), but the fold lines no longer meet at a point (vertex). (**C**) Folding sequence of a zero-thickness rigid origami with five-crease vertices and its thick-panel counterpart based on the Myard linkage. The pattern has six five-crease vertices arranged in rotational symmetry. The sector angles at each vertex are π/6, π/2, 2π/3, π/2, and π/6.

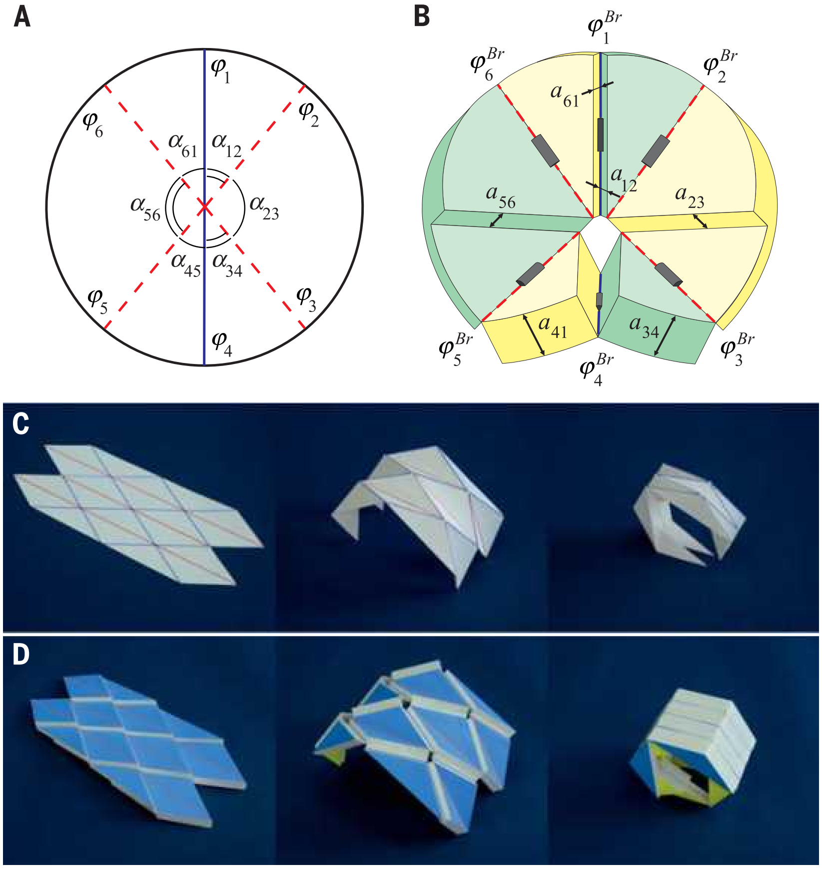

Fig. 3. The diamond origami pattern. (**A**) A single-vertex six-crease diamond pattern for a zero-thickness sheet. (**B**) The thick-panel counterpart with sector angles identical to those in (A), but the fold lines no longer meet at a point (vertex). (**C**) Folding sequence of a zero-thickness origami model of the diamond pattern and its thick-panel counterpart based on the plane-symmetric Bricard linkage. All the vertices are identical. The sector angles around each vertex are π/6, 2π/3, π/6, π/6, 2π/3, and π/6.

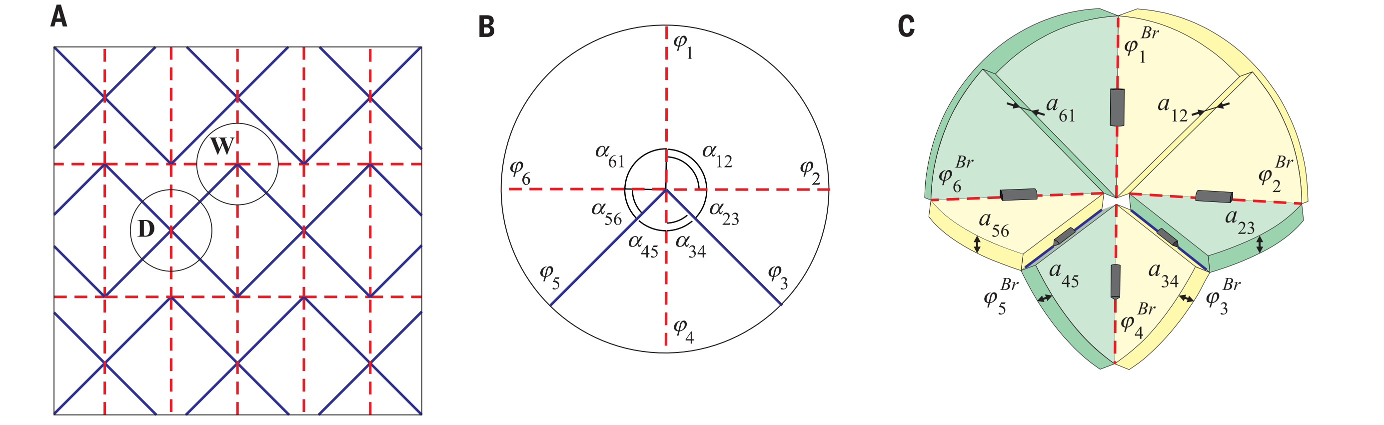

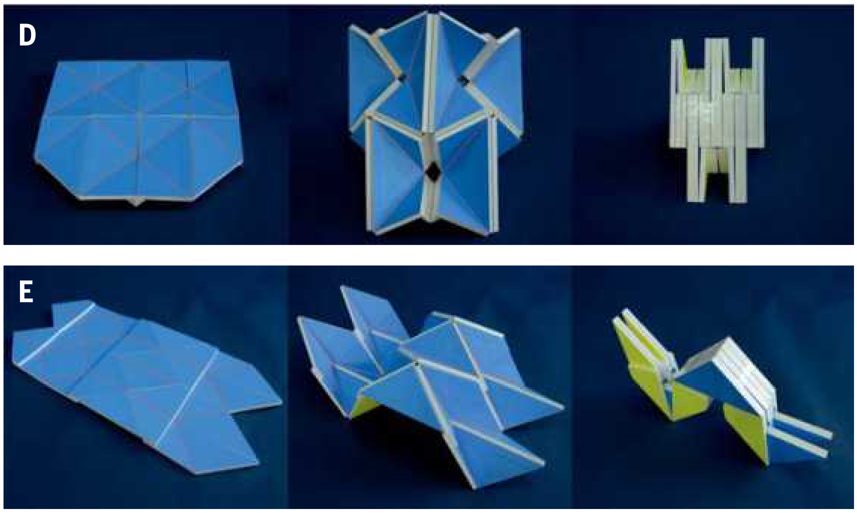

Fig. 4. Origami using the waterbomb pattern for zero- and nonzero-thickness panels and thick-panel origami of a pattern with a mixture of vertices with four and six creases. (**A**) The traditional waterbomb pattern for zero-thickness sheet. Two types of vertices are marked as **D** and **W**. (**B**) Origami pattern around vertex **W**. (**C**) Its thick-panel counterpart. (**D**) Folding sequence of the thick-panel waterbomb pattern. Around type **D** vertex, the sector angles are $\pi/4$, $\pi/2$, $\pi/4$, $\pi/4$, $\pi/2$, and $\pi/4$, whereas they are $\pi/2$, $\pi/4$, $\pi/4$, $\pi/4$, $\pi/4$, and $\pi/2$ around type **W** vertex. (**E**) Folding sequence of a thick-panel origami derived from an origami pattern with a mixture of both four- and six-crease vertices. It contains both the Bennett and Bricard linkages.

we confine its motions to the symmetric case by letting

$$\varphi_1 = \varphi_4 \text{ and } \varphi_2 = \varphi_3 = \varphi_5 = \varphi_6 \tag{8}$$

it reduces to a linkage with a single degree of freedom.

The corresponding thick-panel pattern is given in Fig. 3B, in which all sector angles are identical to those of the zero-thickness pattern. The distances between axes of fold lines are marked in the diagram.

The *6R* assembly of Fig. 3B reassembles the plane-symmetric Bricard linkage (*15*) with line- and plane-symmetric behavior. The geometrical conditions of the Bricard linkage for the distances between neighboring axes of the rotational joints are

$$a_{12} = a_{61}, a_{23} = a_{56}, \text{and } a_{34} = a_{45} \tag{9}$$

In addition, to achieve compact folding, there must be

$$a_{12} + a_{23} = a_{34}, \tag{10}$$

which is obvious by considering the completely packaged configuration.

The kinematic motion of this Bricard linkage again matches that of the spherical *6R* linkage of the zero-thickness model (fig. S8). This enables us to make a thick-panel origami arch using the diamond pattern. The folding sequences of both zero- and nonzero-thickness models are shown in Fig. 3C and movie S1. This agrees with results reported by De Temmerman (*8*), but a complete mathematic proof is presented here.

Another typical six-crease origami pattern is the traditional waterbomb pattern (*16*), whose zero-thickness origami pattern is shown in Fig. 4A. Unlike the diamond pattern, there are two types of vertices, marked as **D** and **W**. **D** is a special case of the diamond pattern for which Eqs. 9 and 10 can be used to syntheses thick panel origami. **W**, specific to the waterbomb pattern, is enlarged in Fig. 4B, in which the sector angles are

$$\alpha_{12} = \alpha_{61} = \frac{\pi}{2} \text{ and}$$

$$\alpha_{23} = \alpha_{34} = \alpha_{45} = \alpha_{56} = \frac{\pi}{4} \tag{11}$$

For **W**, we can show that the corresponding Bricard linkage is a plane-symmetric one in which the thicknesses of subpanels must satisfy

$$a_{23} = a_{56}, a_{34} = a_{45} = \mu a_{23}, \text{and}$$

$$a_{12} = a_{61} = (1 + \mu) a_{23} \tag{12}$$

in order to achieve compact folding. μ is a constant. When $\mu = 1$, the motion of this Bricard linkage is kinematically equivalent to that of the spherical linkage at **W**, as shown in Fig. 4C.

Considering the common folds appearing in both Bricard linkages as we did with the square-twist pattern described previously, the waterbomb pattern for the thick panel can be obtained. The folding sequence of nonzero thickness model is shown in Fig. 4D and movie S1.

If $\mu \neq 1$, the motion of the corresponding Bricard linkage differs from that of the spherical linkage at **W**, although both are flat foldable and can expand flat, which is demonstrated by the relationship between φ_1 (φ_1^{Br}) and φ_2 (φ_2^{Br}) in fig. S14. This indicates that the thick-panel origami can be devised by the mechanism theory alone without referring to its parent rigid origami pattern.

We have developed a comprehensive kinematic model for rigid origami of panels with nonzero thickness. This is done by identifying a spatial linkage model that is kinematically equivalent to the rigid origami of a zero-thickness sheet. In other words, the motion of the spatial linkage mimics that of the spherical linkage commonly used to model rigid origami. To achieve this, we identified a spatial linkage that has the angular conditions for arrangement of fold lines identical to that of the spherical linkage and then proved analytically that their motions are precisely alike.

The thick-panel counterparts to four-, five-, and six-crease vertex origami patterns are overconstrained spatial linkages. The number of such linkages is rather limited (17). It is relatively straightforward for four-crease origami patterns because only one spatial 4*R* linkage exists. However, five- and six-crease single-vertex patterns commonly comprise two or three degrees of freedom, whereas their corresponding spatial overconstrained linkages have only one mobility degree of freedom. In these cases, equivalence can only be accomplished through reducing the degrees of freedom of the former by symmetry or other means. This may be beneficial for practical applications because the folding of thick panels can be more easily controlled owing to their single degree of freedom. Moreover, the synthesis can also be used for origami patterns consisting of a mixture of vertices with various creases. The folding sequence of a thick-panel origami based on a pattern with both four- and six-crease vertices is shown in Fig. 4E and movie S1.

REFERENCES AND NOTES

1. Z. You, *Science* **345**, 623–624 (2014).
2. I. Hagiwara, in *System Simulation and Scientific Computing*, T. Xiao, L. Zhang, S. Ma, Eds. (Springer, Berlin, 2012), pp. 259–268.
3. K. Miura, "Method of packaging and deployment of large membrane in space," 31st Congress of International Astronautical Federation, New York, Paper A 31 (1980), pp. 1–10.
4. S. Felton, M. Tolley, E. Demaine, D. Rus, R. Wood, *Science* **345**, 644–646 (2014).
5. T. Tachi, in *Origami*[5], P. Wang-Iverson, R. J. Lang, M. Yim, Eds. (AK Peters, Natick, MA, 2011), pp. 253–264.
6. B. J. Edmondson *et al*., "An offset panel technique for thick rigidily foldable origami," presented in ASME 2014 International Design Engineering Technical Conferences, Buffalo, NY, 17 to 21 August 2014.
7. C. S. Hoberman, U.S. Patent No. 4,780,344 (1988).
8. I. A. N. De Temmerman, M. Mollaert, T. Van Mele, L. De Laet, *Int. J. Space Structures* **22**, 161–168 (2007).
9. J. Phillips, *Freedom of Machinery*, vol. II (Cambridge Univ. Press, Cambridge, 1990).
10. T. Hull, *Congr. Numer.* **100**, 215–224 (1994).
11. C. H. Chiang, *Kinematics of Spherical Mechanisms* (Krieger Publishing, Malabar, FL, 2000).
12. G. T. Bennett, *Engineering* **76**, 777–778 (1903).
13. J. S. Beggs, *Advanced Mechanism* (Macmillan Company, New York, 1966).
14. F. E. Myard, *Soc. Math. France* **59**, 183–210 (1931).
15. R. Bricard, Leçons de cinématique, *Tome II Cinématique Appliquée* (Gauthier-Villars, Paris, 1927), pp. 7–12.
16. S. Randlett, *The Art of Origami: Paper Folding, Traditional and Modern* (Faber and Faber, London, 1963)
17. Z. You, Y. Chen, *Motion Structures* (Spon Press, Oxford, UK, 2012).

ACKNOWLEDGMENTS

This research was funded by the Royal Academy of Engineering (1314RECI061). Y.C. acknowledges the support of the National Natural Science Foundation of China (Projects 51290293 and 51422506), and Z.Y. acknowledges the support of the Air Force Office of Scientific Research (R&D Project 134028). The authors also thank H. Feng for verifying one of the diagrams.

SUPPLEMENTARY MATERIALS

www.sciencemag.org/content/349/6246/396/suppl/DC1
Materials and Methods
Supplementary Text
Figs. S1 to S14
Movie S1

6 April 2015; accepted 26 June 2015
10.1126/science.aab2870

STRETCHY ELECTRONICS

Hierarchically buckled sheath-core fibers for superelastic electronics, sensors, and muscles

Z. F. Liu,[1,2,3] S. Fang,[1,3*] F. A. Moura,[1,4] J. N. Ding,[2,10] N. Jiang,[1,3] J. Di,[1] M. Zhang,[5] X. Lepró,[1] D. S. Galvão,[4] C. S. Haines,[1] N. Y. Yuan,[2,3] S. G. Yin,[3,6] D. W. Lee,[3] R. Wang,[2,3] H. Y. Wang,[3,6] W. Lv,[2,3] C. Dong,[2,3] R. C. Zhang,[3,6] M. J. Chen,[2,3] Q. Yin,[2,3] Y. T. Chong,[3] R. Zhang,[7,8] X. Wang,[8] M. D. Lima,[1] R. Ovalle-Robles,[9] D. Qian,[8] H. Lu,[8] R. H. Baughman[1,3*]

Superelastic conducting fibers with improved properties and functionalities are needed for diverse applications. Here we report the fabrication of highly stretchable (up to 1320%) sheath-core conducting fibers created by wrapping carbon nanotube sheets oriented in the fiber direction on stretched rubber fiber cores. The resulting structure exhibited distinct short- and long-period sheath buckling that occurred reversibly out of phase in the axial and belt directions, enabling a resistance change of less than 5% for a 1000% stretch. By including other rubber and carbon nanotube sheath layers, we demonstrated strain sensors generating an 860% capacitance change and electrically powered torsional muscles operating reversibly by a coupled tension-to-torsion actuation mechanism. Using theory, we quantitatively explain the complementary effects of an increase in muscle length and a large positive Poisson's ratio on torsional actuation and electronic properties.

Highly elastic electrical conductors are needed for stretchable electronic circuits, pacemaker leads, light-emitting displays, batteries, supercapacitors, and strain sensors (*1*). For such purposes, conducting elastomers have been fabricated by incorporating conducting particles in rubber (*2*–*5*) or by attaching sheets of conducting nanofibers (*6*–*9*), graphene sheets (*10*, *11*), or coiled or serpentine conductors to a rubber sheet or fiber (*12*–*17*). Although reversible strains exceeding 500% have been demonstrated, the quality factor (*Q*, the percent strain divided by the percent resistance change) has been below three for such large strains (*17*–*20*). Elastomeric conductors with very low quality factors are useful as strain sensors, but the other applications noted above would benefit from the realization of very high quality factors. The availability of conducting fibers that can be stretched to great extents without significantly changing conductivity could enable the deployment of superelastic fibers as artificial muscles, electronic interconnects, supercapacitors, or light-emitting elements.

We replaced the frequently used laminate of a carbon nanotube (CNT) sheet wrapped on a stretched rubber sheet with a multilayer CNT sheath wrapped on a rubber fiber core (*21*, *22*). We enabled additional functions by including other rubber and CNT sheath layers. The conducting sheaths were derived from highly oriented multiwalled CNT aerogel sheets, which were drawn from CNT forests (*21*). Three basic configurations were deployed: NTS_m@fiber, rubber@NTS_m@fiber, and NTS_n@rubber@NTS_m@fiber. NTS_m@fiber denotes m carbon nanotube sheet (NTS) layers deposited on top of a rubber fiber core, rubber@NTS_m@fiber is a rubber-coated NTS_m@fiber, and NTS_n@rubber@NTS_m@fiber indicates an NTS_n sheath (where n is the number of NTS layers) on a rubber@NTS_m@fiber core.

The rubber fiber core was highly stretched (typically to 1400% strain) during the wrapping of NTS layers, and the CNT orientation was parallel to the rubber fiber direction (Fig. 1A). For the preparation of rubber@NTS_m@fibers, the outermost rubber coating was applied while the rubber core was fully stretched, whereas for the preparation of NTS_n@rubber@NTS_m@fibers, the thicker rubber layer used as a dielectric was deposited on an NTS_m@fiber that was not stretched (*22*). The parallel orientations of CNT fibers and the rubber core, the substantial strain applied during sheath wrapping, and the use of a large m resulted in the observed hierarchical two-dimensional buckling and corresponding

[1]Alan G. MacDiarmid NanoTech Institute, University of Texas at Dallas, Richardson, TX 75080, USA. [2]Jiangsu Collaborative Innovation Center of Photovoltaic Science and Engineering, Changzhou University, Changzhou 213164, China. [3]Jiangnan Graphene Research Institute, Changzhou 213149, China. [4]Applied Physics Department, State University of Campinas, Campinas, SP 13081-970, Brazil. [5]High-Performance Materials Institute, Florida State University, Tallahassee, FL 32310, USA. [6]Institute of Materials Physics, Tianjin University of Technology, Tianjin 300384, China. [7]School of Astronautics, Northwestern Polytechnical University, Xi'an 710072, China. [8]Department of Mechanical Engineering, University of Texas at Dallas, Richardson, TX 75080, USA. [9]Lintec of America, Nano-Science and Technology Center, Richardson, TX 75081, USA. [10]Micro/Nano Science and Technology Center, Jiangsu University, Zhenjiang 212013, China.
***Corresponding author. E-mail: sfang@utdallas.edu (S.F.); ray.baughman@utdallas.edu (R.H.B.)**

high performance. The rubber core and rubber layers separating nanotube sheets were a styrene-(ethylene-butylene)-styrene (SEBS) copolymer containing a plasticizer (Marcol 82, Exxon Mobil) (*22*). The diameter of the nonstrained rubber fiber was typically 2 mm, which decreased to 0.52 mm at 1400% strain (*22*).

Because the rubber fiber core must increase in diameter (and circumference) as it relaxes from the maximum fiber stretch, we observed that the realizable elastic deformation range decreased with increasing m for the NTS_m@fibers. Even though the CNT sheets were highly anisotropic, with a lower modulus in the belt direction of the CNT sheath, this low modulus and the bending modulus of the nanofibers were sufficient to limit the elastic range for the sheath-core fiber when m was large. The elastic range dramatically decreased when the nanotube orientation had a nonzero bias angle with respect to the fiber axis (fig. S4B).

We observed periodic hierarchical buckling in two dimensions for NTS_m@fibers when m was larger than 10 and the fabrication strain, ε_{fab} (i.e., the strain applied to the rubber fiber core during the wrapping of CNT sheaths), was large (typically 1400%). The scanning electron microscope (SEM) images (Fig. 1, C and D) show an elongation (100%) for which short and long buckling periods were simultaneously observed in the fiber axial direction (at ~8 and ~35 μm, respectively) and the fiber belt direction (at ~8.5 and ~51 μm, respectively). Unless otherwise indicated (for instance, with the term "fabrication strain"), mentioned strains are associated with the relaxed state of the sheath-core structure, rather than with the relaxed state of the sheath-free core. Also, characterizations of structure and properties refer to conducting elastomer fibers that have been conditioned by applying about five stretch-release cycles to the maximum strain that does not plastically stretch the NTSs in the sheet alignment direction. This conditioning was needed because the two-dimensionally buckled structure appeared during the first cycle and thereafter evolved slightly over the next few cycles, as indicated by a permanent increase of about 10% or less in the resistance of the strain-released state.

The reversible buckling in the fiber axial and belt directions was out of phase, as illustrated by the SEM images of an NTS_{92}@fiber (fig. S12), which can be reversibly elongated by 1000%. Long-period buckling along the fiber axis was seen at 0% strain (where short-period axial buckles exist but are squeezed together); at 200% strain, the axial short-period buckles were pulled apart. The long-period axial buckles disappeared at 400% strain and the short-period axial buckles disappeared near 1000% strain. There was no buckling in the belt direction at 0% strain, and long-period buckling in the belt direction appeared between 200 and 400% strain, becoming more pronounced at higher strains. During strain release (from 1000% strain), these out-of-phase buckling processes in the axial and belt directions reversed without noticeable hysteresis.

Although the emergence of these different types of buckling and their corresponding periods for NTS_m@fibers depended on m and the fabrication strain, the out-of-phase behavior for axial and belt buckling and the order in which short- and long-period axial buckling occurred were general phenomena for our sheath-core elastomeric fibers. As the fabrication strain or m decreased, the long-period buckling in the axial and belt directions disappeared, and subsequently all out-of-plane buckling disappeared (figs. S9 and S13). For about five NTS layers and a 1200% fabrication strain, only short-period axial buckles were observed. Long-period axial buckling appeared when m and the fabrication strain were large. Using a single sheet layer for the sheath resulted in only in-plane buckling for fabrication strains up to the maximum investigated, 1400% (fig. S8).

The explanation for this out-of-phase behavior in the axial and belt directions lies in the out-of-phase relationship between rubber fiber elongations in these directions, which resulted from the large positive Poisson's ratio of the rubber. Consequently, the relaxation of tensile strain from the fabrication strain quasi-plastically elongated the CNT sheath in the belt direction during the first contraction, causing periodic necking (Fig. 1D). Subsequent stretching of the rubber fiber caused the elongated sheath to buckle in the belt direction at the necking locations. During subsequent stretch-release cycles, this dependence of structure on strain was reversibly retained.

The dependence of $R(\varepsilon)/L_{max}$ on tensile strain (ε) for sheath-core NTS_m@fibers is shown in Fig. 2A, where $R(\varepsilon)$ is the resistance of a fiber with a maximum stretched length (L_{max}) of L_{fab}, and L_{fab} is the stretched length (corresponding to the fabrication strain) used for sheath wrapping. Reflecting the constraint on fiber belt expansion provided by the NTS_m sheath during fiber contraction, the length of the unloaded sheath-core fiber (L_{min}) was longer than the starting sheath-free rubber fiber. Hence, the available strain range (ε_{max}) was smaller than the fabrication strain and decreased with increasing m (Fig. 2B, inset).

The strain dependence of $[R(\varepsilon) - R_0]/R_0$, where R_0 is $R(0)$, is shown in Fig. 2B. Although applying an m of 1 resulted in reversible performance up to a very high strain (1320%), the maximum percent resistance change over this strain range, $\Delta R_{max}/R_0 = [R(\varepsilon_{max}) - R_0]/R_0$, decreased with increasing m (from 53% for $m = 1$ to 18% for $m = 200$) (Fig. 2B, inset). The corresponding values of R_0/L_{max} decreased monotonically from 2.1 kiloohm/cm for $m = 1$ to 26.1 ohm/cm for $m = 200$.

The increased $\Delta R_{max}/R_0$ for low m values is explained by the effect of sheath thickness on the period of axial short-period buckling. For low m values, the period of short-range buckling decreased with decreasing strain until adjacent buckles came into contact laterally. This contact provided a new transport path for the electric current, which was orthogonal to the local CNT orientation (which largely followed the buckles). Hence, when m was low, this pathway resulted in decreased fiber resistance relative to higher strain states where buckles were not in contact.

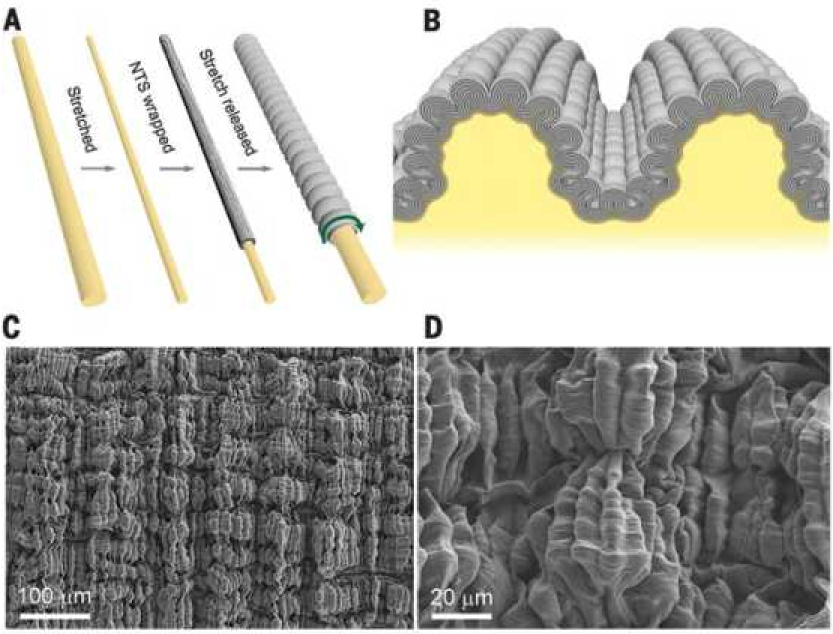

Fig. 1. Two-dimensional, hierarchically buckled sheath-core fibers. (**A**) Steps in the fabrication of an NTS_m@fiber. The circular arrow indicates the belt direction. (**B**) Illustration of the structure of a longitudinal section of an NTS_m sheath, showing two-dimensional hierarchical buckling. The fiber direction is horizontal. The yellow color in (A) and (B) represents SEBS rubber; the gray shells are NTS layers. (**C** and **D**) Low- and high-resolution SEM images showing long- and short-period buckles for an NTS_{180}@fiber at 100% applied strain. The fiber direction, which is the direction of the applied strain, is horizontal and the belt direction is vertical. The fabrication strain was 1400%.

To validate this hypothesis, a resistor network model was developed that agreed with the measured data (Fig. 2A), despite the limited experimental information on structural evolution during buckle contact (*22*). Correlation of transport data and SEM images as a function of strain (figs. S3A and S12) indicates that the strain below which $R(\varepsilon)$ deviates from $R(\varepsilon_{fab})$ corresponds to the strain at which buckles come into contact.

The measured increase in conductance caused by buckles coming into contact, which occurred abruptly at small strains, was appreciable (37% for the sheath-core fiber with m = 19, which contracted by 1200%). Despite the fact that the ratio of sheet conductivity in the nanotube direction to that in the orthogonal direction is about 10 to 20 for densified as-drawn sheets and 50 to 70 for nondensified sheets (*21*), this sizeable effect arose because the contacting area of buckle sidewalls was large compared with the cross-sectional area of the conducting pathway before the buckles came into contact. The conductivity ratios derived theoretically from $R(\varepsilon)$ for the sheath-core fibers (29 for m = 19 to 58 for m = 200) are consistent with the electrical anisotropy of the CNT sheets (*22*).

To avoid resistance changes resulting from buckle contact at low strains, we overcoated a fully stretched NTS$_m$@fiber conductor with a layer of SEBS ~6 μm thick, thereby reducing the resistance change to 4.5% for the application of 1000% strain to a rubber@NTS$_{50}$@fiber (Fig. 2A). For comparison, an NTS$_{50}$@fiber provided a 28% change in resistance over the same strain range.

The elastic range for reversible performance of a straight conducting fiber that we have demonstrated is much higher than previously realized for noncoiled elastomeric conducting fibers and continuous conducting coatings on elastomeric sheets and fibers (Fig. 2C). The Q that we demonstrated for a noncoiled sheath-core fiber was 75 times the value previously obtained for any of the above types of elastomeric conductors with a strain range above 450%. For NTS$_m$@fiber conductors (Fig. 2C), Q monotonically increased from 25 to 50 as the number of NTS layers increased from 1 to 100; Q then remained essentially constant for up to 200 NTS layers. Adding a thin outer layer of rubber to an NTS$_{100}$@fiber to prohibit inter-buckle electrical contact during contraction increased Q from 50 to 421 (corresponding to a 2.15% resistance change for a 905% elongation).

We can further increase the strain range of nearly strain-invariant electrical conductance by coiling a nonstretched rubber@NTS$_m$@fiber on a rigid mandrel of similar diameter. The resistance of a coiled rubber@NTS$_{19}$@fiber reversibly changed by only 5.01% when stretched up to 3000% strain, providing a Q of 598 (Fig. 3A). In this experiment, the mandrel (which was 1/29th the length of the stretched elastomeric conductor) was retained inside the coiled rubber@NTS$_m$@fiber to prevent the conducting fiber from relaxing to an inner coil diameter smaller than that of the mandrel fiber. Without this constraint, the strain range and Q value (2470% and 526, respectively) slightly decreased, but highly reversible behavior was still realized (Fig. 3A and fig. S6D).

This near invariance of conductance during extreme elongations was complemented by highly reversible retention of nearly constant conductance over thousands of high strain cycles, extremely small changes in conductance during small radius coiling, and no degradation in conductance during fiber twisting, which is important for electrically driven torsional actuation.

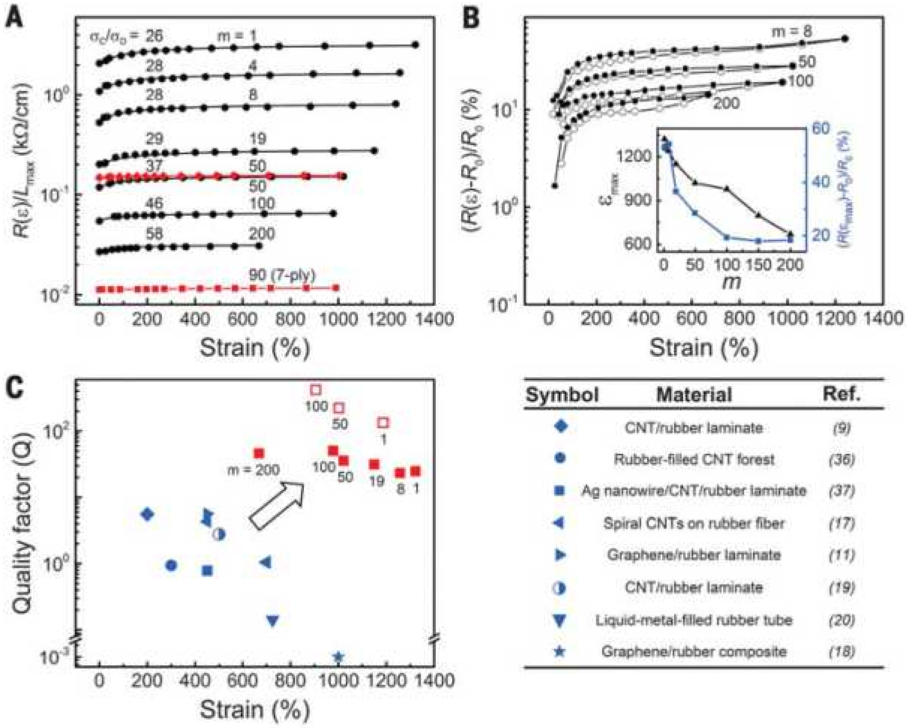

Fig. 2. The strain dependence of electrical properties for sheath-core fibers. (**A**) Measured data points and predicted curves for the dependence of resistance on strain for NTS$_m$@fibers (black circles), rubber@NTS$_{50}$@fibers (red diamonds), and seven-ply rubber@NTS$_{90}$@fibers (red squares). σ_C and σ_D are conductivities in the axial direction and in the inter-buckle contact region, respectively. (**B**) Resistance change versus strain for NTS$_m$@fibers under increasing strain (open circles) and decreasing strain (solid circles). The inset shows the dependence of the available strain range and the maximum percent resistance change on m. (**C**) Comparison of Q and the maximum reversible tensile strain for the sheath-core fibers in our study and previous elastomeric conductors with a strain range ≥200%. Red squares (open for rubber@NTS$_m$@fibers, solid for NTS$_m$@fibers) represent our results; blue symbols represent results previously published in the literature, which are described in the table on the right. The arrow indicates the direction of property changes (improvements) compared with previous results.

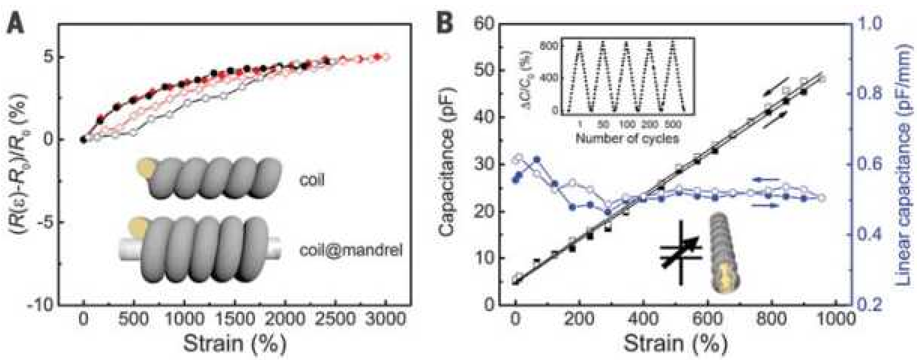

Fig. 3. Electromechanical response of coiled sheath-core fibers. (**A**) Resistance change versus strain for coiled rubber@NTS$_{19}$@fibers made by mandrel-free coiling (black circles) and by coiling a fiber on a rigid mandrel of similar diameter (red diamonds). (**B**) The strain dependence of capacitance and linear capacitance (per instantaneous length) of NTS$_4$@rubber@NTS$_3$@fibers. The upper inset shows the capacitance change during selected cycles to 950% strain. The lower inset illustrates the fiber's structure and uses the symbol for a variable capacitor to indicate the fiber's tunable capacitance. In (A) and (B), open and solid symbols indicate increasing and decreasing strains, respectively.

For example, the resistance change over a 500% strain range varied little during 2000 cycles for rubber@NTS_{15}@fibers (from 0.22 to 0.36%) (fig. S6A). Similarly, completely coiling a 1.5-mm-diameter rubber@NTS_{200}@fiber around a 0.5-mm-diameter mandrel decreased resistance by only 0.7% (fig. S6C). Finally, inserting 37 turns/cm of twist into a 1.7-mm-diameter rubber@NTS_{50}@fiber at a constant load (37.1 kPa, normalized to the original diameter) caused a 0.76% decrease in resistance (fig. S6B), probably because of increased inter-nanotube electronic connectivity produced by twist-induced NTS densification. A tightly knotted rubber@NTS_{116}@fiber underwent a <3% resistance change when elongated to 600% strain (fig. S3C). Additionally, the resistance of a 1.7-mm-diameter rubber@NTS_{92}@fiber changed less than 2.8% when it was cyclically bent to a radius of 2 mm for 200,000 cycles (fig. S6E).

The large strain range (and the small dependence of fiber resistance on strain) of the NTS_m@fiber encouraged our fabrication of the NTS_n@rubber@NTS_m@fiber for use as a fiber capacitor, tensile strain sensor, and artificial muscle that combines torsional and tensile actuation. Because the choice of small n and m values enabled especially large strain ranges where electronic properties were reversible, we used n = 10 and m = 20 for these studies unless otherwise indicated.

Relevant for its application as a capacitive strain sensor, a 950% stretch of an NTS_4@rubber@NTS_3@fiber provided a 860% increase in capacitance (C), and this capacitance change was largely nonhysteretic and reversible (Fig. 3B). This percent of capacitance change was substantially higher than that obtained for an elastomeric fiber dielectric capacitor [230% for a maximum 300% strain, using carbon black–elastomer composite as electrodes (*23*)] and for an electrochemical fiber supercapacitor [7.5% for a maximum strain of 400%, using NTS electrodes wrapped helically around a rubber core (*17*)].

Capacitance measurements for the stretched fiber provide a convenient means to determine strain, and our results show that both high linearity and high sensitivity can be obtained over an immense strain range (Fig. 3B). In agreement with the theoretical prediction that $\Delta C/C_0 = \Delta L/L_0$ (*22*), the data show that the change in capacitance is linearly proportional to the change in length and that the proportionality constant (0.91) is close to unity. This end-to-end capacitance could be used to control muscle stroke for artificial muscles.

Artificial muscles based on the electrostatic attraction between electrodes of dielectric rubber capacitors are well known and commercially exploited (*24*–*28*). High-stroke torsional fiber muscles have been made by inserting twist into sheath-core NTS_n@rubber@NTS_m@fibers while maintaining a constant fiber length (*22*). The amount of inserted twist was far below the amount needed to provide coiling (*22*). The twisted fiber geometry in our fabrication provides torsional actuators with a torsional stroke per muscle length up to 104 times the value previously demonstrated for electrically driven, nonthermal, nonelectrochemical muscle fibers (*29*, *30*). It avoids the Carnot efficiency limit of thermally powered artificial muscles and the use of liquids or vapors for electrochemically or absorption-powered muscles (*31*–*33*).

The first actuator that we fabricated comprised a twist-inserted dielectric muscle that was mechanically in series with a nonactuating rubber fiber, which served as a torsional return spring (Fig. 4A, inset). Our theoretical analysis shows that to maximize torsional stroke, the torsional return spring should serve as a reservoir of twist at constant torque (*22*). Therefore, it should have low torsional stiffness, so that the inserted twist is large compared to the torsional stroke. This muscle operated isobarically (i.e., under a constant applied tensile load), such that it provided both tensile and torsional actuation. The applied load during isobaric actuation prohibited coiling. The maximum applied electric field was between 10.3 and 11.7 million volts (MV)/m.

One might expect that the torsional stroke for a noncoiled NTS_n@rubber@NTS_m@fiber would linearly increase with inserted twist. This is not the case because of the nonlinear elastic behavior of the rubber at high strains, which is apparent in the measured tensile stress-strain curve (fig. S5B) and the dependence of torsional stiffness on the stretch ratio (fig. S11). For an intermediate degree of twist insertion, the torsional stiffness of the rubber is low, which enables the torque of torsional actuation to act as an enhanced torsional stroke. Torsional stroke for isobaric actuation was maximized for a 0.9-mm-diameter NTS_{10}@rubber@NTS_{20}@fiber by inserting 3.20 turns/cm of twist (Fig. 4B).

The dependencies of maximum equilibrium rotation angle, rotation speed, and tensile stroke on the applied field and inserted twist for an isobarically operated NTS_{10}@rubber@NTS_{20}@fiber muscle are shown in Fig. 4, A and B. The torsional stroke reached a maximum value of 21.8°/cm for this 0.9-mm-diameter muscle. When applying a square-wave voltage pulse (fig. S14), tensile and torsional strokes simultaneously reached peak values for a 2-mm-diameter fiber of this type (4.1% and 7.8°/cm, respectively); they then simultaneously decayed to steady-state tensile and torsional strokes of 2.9% and 6.1°/cm, respectively (fig. S14).

Theory can be used to quantitatively explain these results for the low-twist region and to show that the drive mechanism for torsional actuation is fundamentally different from that for previously fabricated torsional muscles (*22*). For earlier electrochemically or thermally driven hybrid

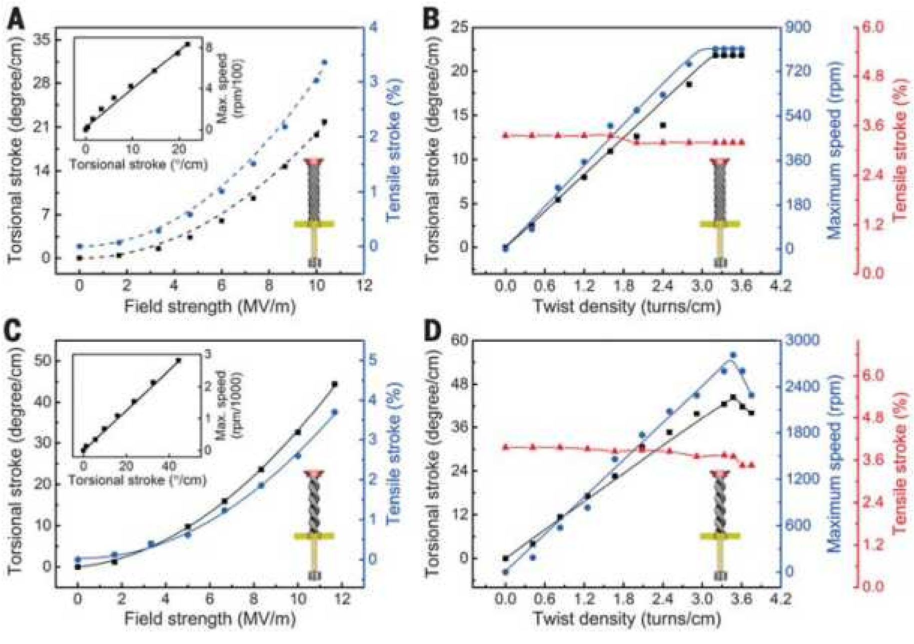

Fig. 4. Maximum equilibrium muscle strokes and maximum rotation speeds obtained using a single voltage step for single-ply and two-ply NTS_{10}@rubber@NTS_{20}@fibers. (**A**) Theoretical (dashed curves) and experimental data points showing the dependence of the rotation angle and tensile stroke on the electric field for an isobarically operated single-ply muscle, plied using 3.20 turns/cm of twist. The inset shows the relationship between the maximum rotation speed and the torsional stroke. (**B**) The dependence of the rotation angle, rotation speed, and tensile stroke on the inserted twist for the single-ply muscle in (A), operated isobarically at a field of 10.3 MV/m. (**C**) The dependence of the rotation angle and tensile stroke on the electric field for an isobarically operated two-ply muscle, plied using 3.47 turns/cm of twist. The inset shows the relationship between the maximum rotation speed and the torsional stroke. (**D**) The dependence of the rotation angle, rotation speed, and tensile stroke on the inserted twist for the two-ply muscle in (B), operated isobarically at a field of 11.7 MV/m. The fabrication strain for the single- and two-ply muscles was 900%. The applied stress was 15.6 kPa for the single-ply muscle and 10.0 kPa for the two-ply muscle.

nanofiber muscles, the volume change of guest material in the twisted nanofiber yarns has driven both tensile and torsional actuation (*32*). On the other hand, tensile actuation of coiled, thermally driven polymer fiber muscles has been shown experimentally and theoretically to be driven by torsional rotation of the twisted fiber (*31*).

Similar to planar dielectric muscles, the electrostatic attraction between cylindrical capacitor electrodes in the twisted rubber muscle generates a stress that reduces the thickness of the rubber dielectric in the muscle (*25*). Because the rubber in the muscle core and surrounding capacitor has a Poisson's ratio of ~0.5, the muscle increases in length to conserve volume. The resulting reduced torsional stiffness of the actuating segment causes a transfer of twist to the actuating segment, such that the paddle rotates to maintain torque balance. Consequently, torsional actuation arises from two complementary effects on torsional stiffness: the increase in muscle length and the decrease of muscle diameter caused by the large positive Poisson's ratio.

Using a neo-Hookean hyperelastic model shows that the coupling of tensile to torsional actuation is realized through an equivalent axial force, which effectively reduces the torsional stiffness of the muscle fiber and causes it to uptwist. Theory and experiment show that torsional actuation is quadratic with the electric field and linear with the initial inserted twist (*22*). Because the same torsional actuation energy is responsible for the maximum kinetic energy of the paddle, the maximum torsional stroke is proportional to maximum rotation speed, as we observed experimentally (Fig. 4A, inset). Theory accurately predicts the measured field dependence of torsional and tensile stroke (Fig. 4A). A more sophisticated nonlinear model (*22*), which considers the nonlinear stress-strain relationship of rubber, explains the observed plateau in torsional stroke when the inserted twist is high (Fig. 4B).

Other configurations were explored as alternatives to the isobaric single-ply torsional muscle described above. An isometric (constant length), single-ply, dual-segment torsional muscle provided a slightly smaller equilibrium torsional stroke than did the isobaric (constant load) configuration shown in Fig. 4, because tensile stroke (which drives torsional actuation) was partially absorbed by the contraction of the torsional return spring. Instead of inserting twist in a single-ply NTS_n@rubber@NTS_m@fiber, we made a torsional muscle by plying together (with 3.47 turns/cm of twist) two 0.9-mm-diameter, nontwisted NTS_{10}@rubber@NTS_{20}@fibers. When this two-ply muscle was operated isobarically in the muscle–return-spring configuration used for the single-ply muscles, an unusually large torsional stroke was observed (44.4°/cm) with a tensile stroke of 3.7% (Fig. 4, C and D). The torsional actuation of the two-ply muscle is shown in movie S1.

Similar to thermally driven torsional muscles, theory predicts that the product of muscle diameter and stroke is scale-invariant for dielectric torsional muscles (*22*). Hence, torsional stroke per muscle length for a given electric field can be dramatically increased (while the voltage is decreased) by proportionally decreasing core and sheath thicknesses, as long as the bias angle α is kept constant, where $\tan\alpha = \pi D T_w$ (D is the muscle diameter; T_w is the inserted twist in turns per muscle length). This inverse dependence of torsional stroke on muscle diameter must be considered when comparing the torsional strokes of muscles with different diameters. Electrothermally or electrochemically driven fiber-based muscles with smaller diameters provide much higher torsional strokes per muscle length (*32*, *34*). Nevertheless, when this length-normalized torsional stroke is scaled by multiplying by the fiber diameter, the dielectric fiber torsional muscles that are advantageously liquid-free and unlimited in Carnot efficiency provide length- and diameter-corrected torsional strokes of 1.50° for single-ply muscles and 4.71° for the two-ply muscle. These values are comparable to those measured for the highest performing electrically driven torsional muscles [0.71° for electrothermally driven wax-filled CNT yarn muscles (*32*), 4.30° for electrothermally driven nylon muscles (*31*), and 2.16° for electrochemically driven CNT muscles (*34*)].

Various potential applications for the sheath-core conducting fibers are suggested by our results. The capacitance-based torsional actuation could be exploited for rotating optical elements, such as mirrors, in optical circuits. For applications in which increased electrical conductance or capacitance is needed (*9*, *15*), we have shown that a fundamentally unlimited number of individual small-diameter NTS_m@fibers or NTS_n@rubber@NTS_m@fibers can be plied together (using a small plying angle) or interconnected by infiltrated rubber (applied in the zero-stress state) without a loss of per-fiber performance (*22*). Additionally, we can increase the conductivity of an fiber stretched to 870% by a factor of 13 (realizing a conductivity of 360 S/m) by reducing the diameter of the rubber core from 2 mm to 150 μm while maintaining constant sheath thickness (fig. S15). The elastomeric fibers of our design might be deployable for such applications as pacemaker leads (movie S2) (*35*). Other possibilities include cables that are extendable up to 31 times their initial length without significant resistance change, which could be applied for morphing structures in space, robotic arms or exoskeletons capable of extreme reach, or interconnects for highly elastic electronic circuits.

REFERENCES AND NOTES

1. J. A. Rogers, T. Someya, Y. Huang, *Science* **327**, 1603–1607 (2010).
2. T. Sekitani *et al*., *Nat. Mater.* **8**, 494–499 (2009).
3. Y. Kim *et al*., *Nature* **500**, 59–63 (2013).
4. M. Park *et al*., *Nat. Nanotechnol.* **7**, 803–809 (2012).
5. K.-Y. Chun *et al*., *Nat. Nanotechnol.* **5**, 853–857 (2010).
6. T. Chen, R. Hao, H. Peng, L. Dai, *Angew. Chem. Int. Ed.* **54**, 618 (2015).
7. J. Liang, L. Li, X. Niu, Z. Yu, Q. Pei, *Nat. Photonics* **7**, 817–824 (2013).
8. Y. Zhu, F. Xu, *Adv. Mater.* **24**, 1073–1077 (2012).
9. T. Yamada *et al*., *Nat. Nanotechnol.* **6**, 296–301 (2011).
10. T. Chen, Y. Xue, A. K. Roy, L. Dai, *ACS Nano* **8**, 1039–1046 (2014).
11. J. Zang *et al*., *Nat. Mater.* **12**, 321–325 (2013).
12. C. Wang, W. Zheng, Z. Yue, C. O. Too, G. G. Wallace, *Adv. Mater.* **23**, 3580–3584 (2011).
13. N. Bowden, S. Brittain, A. G. Evans, J. W. Hutchinson, G. M. Whitesides, *Nature* **393**, 146–149 (1998).
14. M. S. White *et al*., *Nat. Photonics* **7**, 811–816 (2013).
15. L. Cai *et al*., *Sci. Rep.* **3**, 3048 (2013).
16. D.-Y. Khang, H. Jiang, Y. Huang, J. A. Rogers, *Science* **311**, 208–212 (2006).
17. Z. Zhang *et al*., *Adv. Mater.* **27**, 356–362 (2015).
18. C. S. Boland *et al*., *ACS Nano* **8**, 8819–8830 (2014).
19. U.-H. Shin *et al*., *Carbon* **80**, 396–404 (2014).
20. S. Zhu *et al*., *Adv. Funct. Mater.* **23**, 2308–2314 (2013).
21. M. Zhang *et al*., *Science* **309**, 1215–1219 (2005).
22. Materials and methods are available as supplementary materials on *Science* Online.
23. G. Kofod, H. Stoyanov, R. Gerhard, *Appl. Phys. A Mater. Sci. Process.* **102**, 577–581 (2011).
24. Q. M. Zhang, V. Bharti, X. Zhao, *Science* **280**, 2101–2104 (1998).
25. R. Pelrine, R. Kornbluh, Q. Pei, J. Joseph, *Science* **287**, 836–839 (2000).
26. F. Carpi, S. Bauer, D. De Rossi, *Science* **330**, 1759–1761 (2010).
27. R. Shankar, T. K. Ghosh, R. J. Spontak, *Soft Matter* **3**, 1116 (2007).
28. P. Brochu, Q. Pei, *Macromol. Rapid Commun.* **31**, 10–36 (2010).
29. C. L. Pan, Z. H. Feng, Y. T. Ma, Y. B. Liu, *Appl. Phys. Lett.* **92**, 012923 (2008).
30. J. Kim, B. Kang, *Smart Mater. Struct.* **10**, 750–757 (2001).
31. C. S. Haines *et al*., *Science* **343**, 868–872 (2014).
32. M. D. Lima *et al*., *Science* **338**, 928–932 (2012).
33. H. Cheng *et al*., *Adv. Mater.* **26**, 2909–2913 (2014).
34. J. Foroughi *et al*., *Science* **334**, 494–497 (2011).
35. J. S. Hanker, B. L. Giammara, *Science* **242**, 885–892 (1988).
36. M. K. Shin *et al*., *Adv. Mater.* **22**, 2663–2667 (2010).
37. P. Lee *et al*., *Adv. Funct. Mater.* **24**, 5671–5678 (2014).

ACKNOWLEDGMENTS

We thank A. Ruhparwar, S. F. Cogan, and X. Li for discussions of pacemaker applications; X. Zhang, B. Lin, X. Zhou, Y. Hou, and F. Jia for sample preparations; H. Luo for mechanical properties characterizations; A. Needleman for discussions on periodic necking and buckling; T. Xu, L. Tong, H. Zhang, and Y. Du for discussions on modeling and measurement techniques; and D. Wang for drawings. Support in the United States was from Air Force Office of Scientific Research grants FA9550-12-1-0211, FA9550-15-1-0089, and FA9550-14-1-0227; Robert A. Welch Foundation grant AT-0029; U.S. Army grants W91CRB-14-C-0019 and W91CRB-13-C-0037; Department of Defense grant W81XWH-14-1-0228; NIH grant 1R01DC011585-01; NSF grants CMMI-1031829, CMMI-1120382, CMMI-1335204, and ECCS-1307997; Office of Naval Research Multidisciplinary University Research Initiative grant NOOD14-11-1-0691; and the Louis A. Beecherl Jr. Chair. Support in China was from the Priority Academic Program Development of Jiangsu Higher Education Institutions on Renewable Energy Materials Science and Engineering, Jiangsu Key Laboratory for Photovoltaic Engineering Science, Jiangsu Specially-Appointed Professor Program Sujiaoshi-2012-34, National Natural Science Foundation of China grant 31200637, Jiangsu Basic Research Program grant BK2012148, Science and Technology Support Program of Changzhou grants CC20140016 and CZ20140013, Chinese Ministry of Science and Technology grant 2013AA014201, and State Scholarship Fund grant 201406290125. Brazilian support was from Coordenação de Aperfeiçoamento de Pessoal de Nível Superior Scholarship 12264/13-0 and Fundação de Amparo à Pesquisa do Estado de São Paulo-Centros de Pesquisa, Inovação e Difusão grant 2013/08293-7. A provisional patent application has been filed.

SUPPLEMENTARY MATERIALS

www.sciencemag.org/content/349/6246/400/suppl/DC1
Materials and Methods
Supplementary Text
Figs. S1 to S15
References (*38–43*)
Movies S1 and S2

27 January 2015; accepted 8 June 2015
10.1126/science.aaa7952

QUANTUM INFORMATION

Coherent coupling between a ferromagnetic magnon and a superconducting qubit

Yutaka Tabuchi,[1]* Seiichiro Ishino,[1] Atsushi Noguchi,[1] Toyofumi Ishikawa,[1] Rekishu Yamazaki,[1] Koji Usami,[1] Yasunobu Nakamura[1,2]

Rigidity of an ordered phase in condensed matter results in collective excitation modes spatially extending to macroscopic dimensions. A magnon is a quantum of such collective excitation modes in ordered spin systems. Here, we demonstrate the coherent coupling between a single-magnon excitation in a millimeter-sized ferromagnetic sphere and a superconducting qubit, with the interaction mediated by the virtual photon excitation in a microwave cavity. We obtain the coupling strength far exceeding the damping rates, thus bringing the hybrid system into the strong coupling regime. Furthermore, we use a parametric drive to realize a tunable magnon-qubit coupling scheme. Our approach provides a versatile tool for quantum control and measurement of the magnon excitations and may lead to advances in quantum information processing.

Low-dissipative magnon dynamics in ferromagnetic insulators have been extensively studied in the contexts of ferromagnetic resonance (*1*, *2*), Bose-Einstein condensation (*3*), and spintronics (*4*, *5*). Moreover, the coupling of magnons and microwave photons in a resonator has been investigated (*6*–*9*) with the aim of realizing hybrid quantum systems for quantum memories and transducers. However, coherent manipulation of a magnon at the single-quantum level has remained elusive because of the lack of anharmonicity in the system.

Single-electron spins, being a natural and genuine two-level system, play crucial roles in numerous applications in quantum information processing. However, they have intrinsic drawbacks, such as a small magnetic moment equal to μ_B (the Bohr magneton) and the limited spatial extension of the electron wave function, making coherent coupling with an electromagnetic field rather weak. To circumvent these problems, paramagnetic spin ensembles such as atoms (*10*), nitrogen vacancy centers (*11*, *12*), and rare-earth ions in a crystal (*13*, *14*) have been studied. Generally, the coupling strength is enhanced by the square root of the number of the spins involved. At the same time, a collective spin excitation mode, which matches the input electromagnetic-field mode, is spanned among the spatially and spectrally extended spin ensemble. However, with an increased spin density needed for a stronger coupling, the spin-spin interactions within the ensemble drastically degrade the coherence of the system, leading to a trade-off.

Here we take a different approach by introducing, counterintuitively, a strong exchange interaction between neighboring spins to make them fully ordered in the ferromagnetic state. Even though they typically have a spin density several orders of magnitude higher than those of paramagnetic spin crystals mentioned above, the strong exchange and dipolar interactions among the spins dominate their dynamics, leading to narrow-linewidth magnetostatic modes. The simplest mode, called the Kittel mode, has uniform spin precessions in the whole volume.

In this Report, we demonstrate a hybrid quantum system that combines two heterogeneous collective-excitation modes: i.e., the Kittel mode in a ferromagnetic crystal and a superconducting qubit. In the latter system, the nonlinearity of Josephson junctions plays a crucial role for the realization of the qubit: i.e., an effective two-level system. The progress in the past decade has made these qubits and their integrated circuits one of the most advanced technologies for quantum information processing (*15*–*17*). In the setups of circuit quantum electrodynamics, a qubit as an artificial atom is coupled strongly to a microwave resonator (*18*) or a waveguide (*19*). These setups allow precise control and readout of the qubit states, as well as synthesis and characterization of arbitrary quantum states in the microwave modes (*20*); these techniques can readily be applied to quantum engineering with magnon excitations. The anharmonicity contributed by the superconducting qubit is the critical element.

In our experimental setup (Fig. 1), a transmon-type superconducting qubit and a single-crystalline yttrium iron garnet (YIG) sphere are mounted in a microwave cavity. The qubit with a 0.7-mm-long dipole antenna has a resonant frequency $\omega_q/2\pi$ of 8.136 GHz. It strongly couples to the electric fields of the cavity modes; e.g., the coupling strength $g_q/2\pi$ between the qubit and the TE_{102} (transverse electric) mode at $\omega_{102}/2\pi =$ 8.488 GHz is 121 MHz (*21*). The YIG sphere with a diameter of 0.5 mm is glued to an aluminum oxide rod and mounted near the antinode of the magnetic field of the TE_{102} mode. We also apply a local static field $B_{\mathrm{static}} \sim 0.29$ T, which makes the YIG sphere a single-domain ferromagnet (fig. S1). The sphere now has an enormous magnetic dipole moment $N\mu_B$, which couples strongly to the magnetic field of the cavity mode. The large enhancement factor $N = 1.4 \times 10^{18}$ is the number of the net electron spins in the sphere; we take advantage of the high spin density compared to that of previously studied paramagnetic systems. We perform a series of spectroscopic measurements in a dilution refrigerator at T = 10 mK. All the data are taken in the quantum regime, where very few thermally excited photons and magnons exist. The average probe-photon number in the cavity is also kept below one. To characterize the coupling between the magnon and the photon, we perform spectroscopy with the qubit frequency far detuned. Figure 1B shows the normal-mode splitting between the TE_{102} mode and the Kittel mode in the YIG sphere. The pronounced anticrossing indicates the strong coupling between the two systems (*7*). We obtain the coupling strength, $g_m/2\pi$ = 21.0 MHz, and the linewidths of the TE_{102} and Kittel modes, $\kappa_{102}/2\pi$ = 2.5 MHz and $\gamma_m/2\pi$ = 1.4 MHz, from the fit. The additional splitting seen in the upper branch originates from another magnetostatic mode, which is detuned from the Kittel mode.

Whereas the qubit and the magnon electrically and magnetically couple to the cavity mode, respectively, they have a negligibly small direct interaction in between. Therefore, we first establish a static coupling scheme between the magnon and the qubit by using the presence of the cavity mode (Fig. 2A) (*22*). We tune the qubit and the magnon frequencies, ω_q and ω_{FMR}, while both are far detuned from the cavity frequency $\omega_c(\equiv\omega_{102})$. When $\omega_q \simeq \omega_{\mathrm{FMR}}$, coherent exchange of the qubit excitation and a magnon is mediated by the virtual-photon excitation in the cavity mode. The interaction is described by a Jaynes-Cummings-type Hamiltonian, which is written as

$$H_{\mathrm{qm,s}}/\hbar = g_{\mathrm{qm,s}}\,\hat{\sigma}^{+}\hat{c} + g^{*}_{\mathrm{qm,s}}\hat{\sigma}^{-}\hat{c}^{\dagger} \qquad (1)$$

where $g_{\mathrm{qm,s}} = g_q g_m/\Delta$ is the effective qubit-magnon coupling strength, and $\hat{\sigma}^{-}[=(\hat{\sigma}^{+})^{\dagger}]$ and $\hat{c}$ are annihilation operators of the qubit excitation and the magnon, respectively. The detuning Δ is the difference between the bare frequencies of the qubit and the cavity mode (*21*). The first and the second excited states of the hybridized system are bonding and antibonding states between the qubit and the magnon excitation.

To demonstrate the qubit-magnon coupling, we perform qubit excitation spectroscopy by using the qubit readout through the cavity TE_{103} mode. Despite the large detuning, the TE_{103} mode at $\omega_{103}/2\pi = 10.461$ GHz is subject to a dispersive frequency shift: The change in the cavity reflection coefficient, $\mathrm{Re}(\Delta r)$, at ω_{103} reflects the qubit state. Figure 2B shows $\mathrm{Re}(\Delta r)$ as a function of the excitation microwave frequency and the static

[1]Research Center for Advanced Science and Technology (RCAST), The University of Tokyo, Meguro-ku, Tokyo 153-8904, Japan. [2]Center for Emergent Matter Science (CEMS), RIKEN, Wako, Saitama 351-0198, Japan.
*Corresponding author. E-mail: tabuchi@qc.rcast.u-tokyo.ac.jp

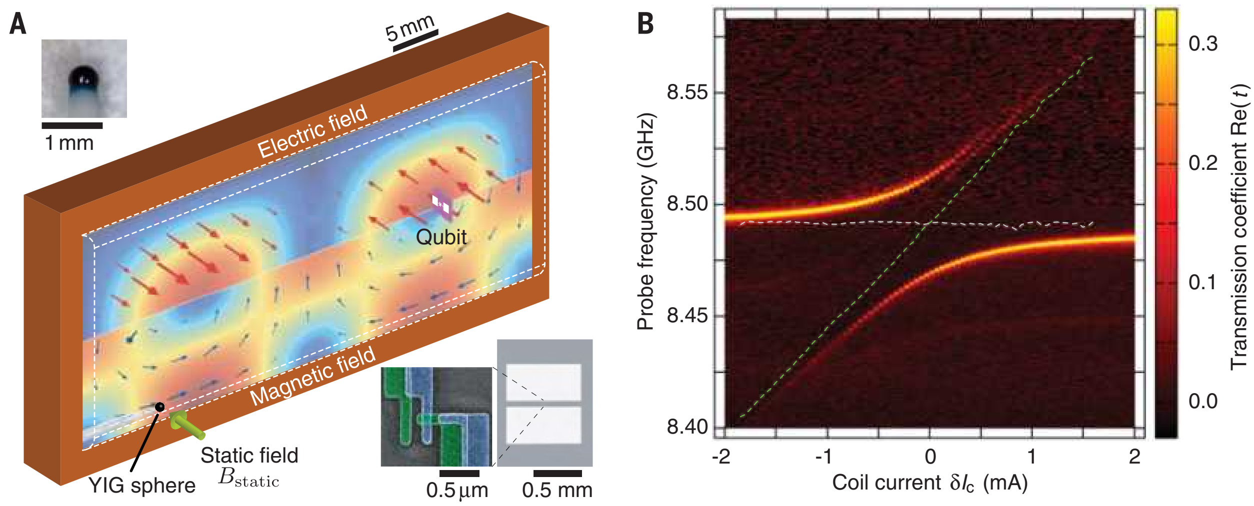

Fig. 1. Qubit-magnon hybrid quantum system in a microwave cavity. (**A**) Simulated microwave field distribution of the TE_{102} (transverse electric) mode in the cavity. The upper half of the sketch displays the electric field lines (red arrows); the electric field couples to a transmon-type superconducting qubit (right insets: optical image of the qubit's antenna pads and false-color scanning-electron micrograph of the Josephson junction bridging them). The lower half of the sketch shows the magnetic field (blue arrows), which couples to the spins in a single-crystalline sphere of yttrium iron garnet (YIG; photo in the left inset). A static magnetic field B_{static} is applied locally to the sphere (see fig. S1). (**B**) Magnon-photon normal-mode splitting. Amplitude of the microwave transmission coefficient, Re(t), is measured through the TE_{102} mode as a function of the probe frequency and the static magnetic field. The field is represented by the relative coil current δI_c, which is defined to be zero at the anticrossing. The dashed lines show the TE_{102}-mode (white) and Kittel-mode (green) frequencies obtained from fitting.

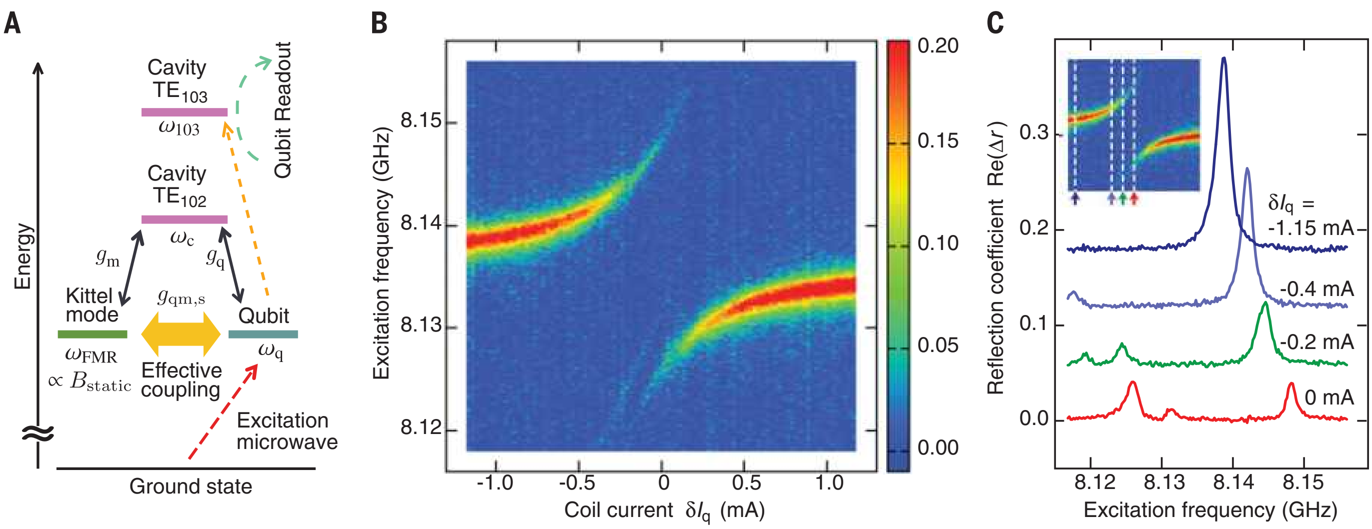

Fig. 2. Magnon-vacuum–induced Rabi splitting of the superconducting qubit. (**A**) Cavity-mediated coupling scheme. The energy diagram illustrates the frequencies of the cavity TE_{102} and TE_{103} modes, ω_c ($\equiv\omega_{102}$) and ω_{103}; the Kittel-mode frequency ω_{FMR}; and the qubit frequency ω_q. The qubit couples to the electric field of the TE_{102} mode with a coupling strength g_q, whereas the Kittel mode in the YIG sphere magnetically couples to the same mode with a coupling strength g_m. When $\omega_q \simeq \omega_{FMR}$, a qubit excitation is transformed to a Kittel-mode magnon and vice versa via the virtual-photon excitation in the TE_{102} mode. The qubit also couples to the TE_{103} mode weakly, which results in the dispersive frequency shift of the cavity mode depending on the states of the qubit. (**B**) Magnon-vacuum–induced Rabi splitting. Change in the cavity reflection coefficient Δr at ω_{103} is measured as a function of the qubit excitation frequency and the static magnetic field represented by the relative coil current δI_q, which is defined to be zero at the anticrossing. An additional splitting around 8.125 GHz is attributed to another magnetostatic mode (*21*). (**C**) Cross sections of (B) at various static magnetic fields. For clarity, the individual curves are offset vertically by 0.06 each from bottom to top.

magnetic field. The anticrossing is a manifestation of the magnon-vacuum–induced Rabi splitting, which indicates coherent coupling between the qubit and the Kittel mode. From the size of the splitting, the effective coupling strength $g_{qm,s}/2\pi$ = 10.0 MHz is obtained. The coupling strength far exceeds the linewidths of the qubit and the magnon, $\gamma_q/2\pi = 1.2$ MHz and $\gamma_m/2\pi = 1.3$ MHz, respectively. The value is also in a good agreement with the calculated value of 11.8 MHz based on the lowest-order approximation (*21*).

For dynamical control of the magnon quantum state, fast on-off switching of the interaction with the qubit would be useful. In the static coupling scheme, however, it is technically challenging to sweep the magnetic field in a time scale faster than that of the coupling strength. To obtain a dynamically tunable coupling between the qubit and the Kittel mode, we adopt a parametrically induced interaction that has

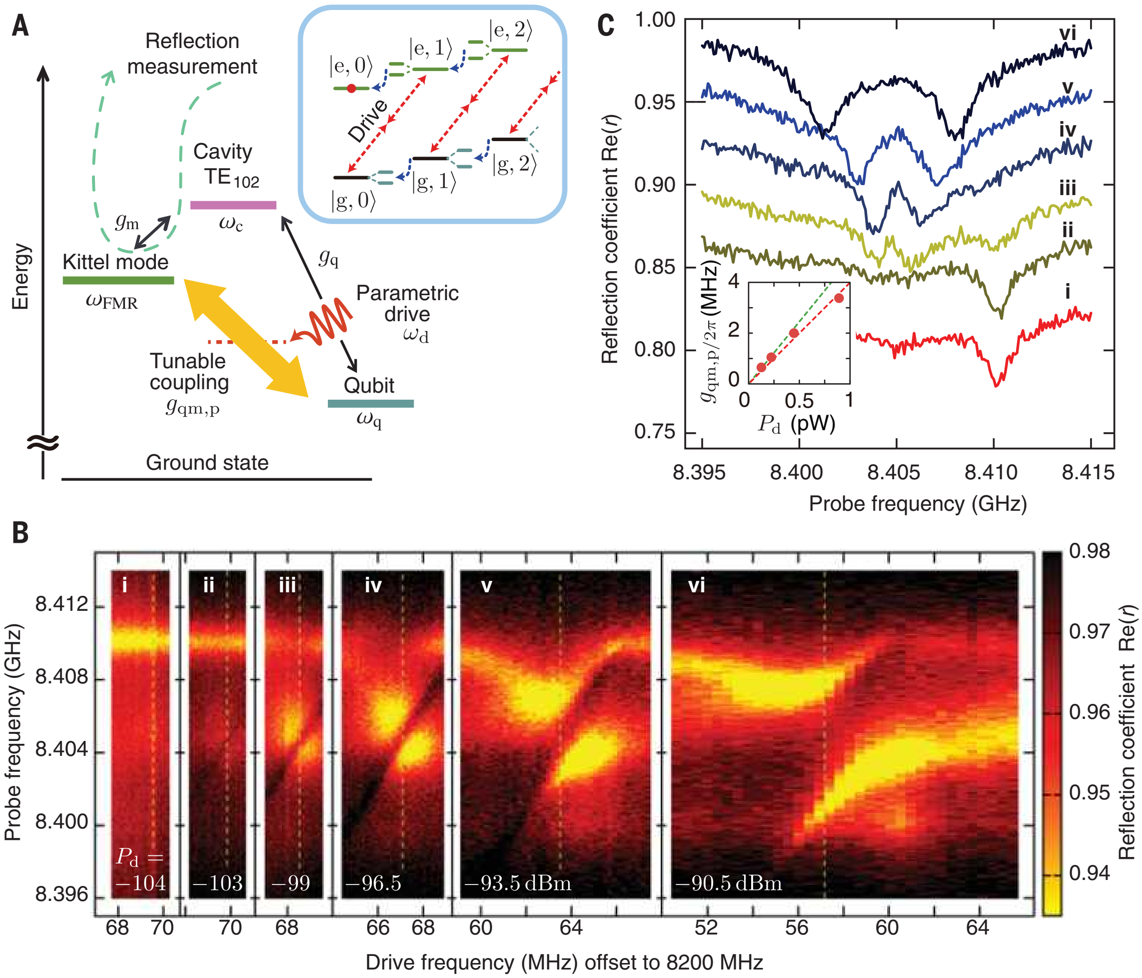

Fig. 3. Tunable coupling between a superconducting qubit and the Kittel mode. (**A**) Parametrically induced coupling scheme. The coupling between the qubit and the Kittel mode detuned from each other is parametrically induced by a drive microwave at the frequency $\omega_d = (\omega_{FMR} + \omega_q)/2$. The inset shows energy levels labeled with the qubit state (g or e) and the magnon number ($n_m = 0, 1, \ldots$). The parametric drive (red dashed arrows) induces the two-photon transitions, e.g., $|g,0\rangle \Leftrightarrow |e,1\rangle$, resulting in the Rabi splitting. The blue arrows depict the Kittel-mode decay, and the red circle at $|e,0\rangle$ illustrates the dominant steady-state population at higher drive powers. (**B**) Kittel-mode spectra for various drive powers P_d indicating tunable coupling with the qubit. (**C**) Cross sections of (B) at the drive frequencies corresponding to $(\omega_{FMR} + \omega_q)/2$ [yellow dashed lines in (B)]. Note that the frequency depends on P_d through the Stark shift of the qubit. For clarity, the individual curves i to v are offset vertically by −0.03 from each other from top to bottom. Inset: Coupling strength $g_{qm,p}$ as a function of the drive power P_d. Also plotted are the linear fit (red dashed line) and the theoretical expectation (green dashed line) (*21*).

been proposed and demonstrated in superconducting circuits (*23*–*25*) (Fig. 3A). To suppress the static coupling, a large detuning of 274 MHz between the qubit and the Kittel mode ($\omega_{FMR}/2\pi = 8.410$ GHz) is chosen. Next, we introduce a microwave drive at a frequency equal to the average of the qubit and the Kittel-mode frequencies—i.e., $\omega_d = (\omega_{FMR} + \omega_q)/2$—to induce the parametric coupling. This is basically a third-order nonlinear process; the system absorbs two drive photons and excites the qubit and a magnon simultaneously. The substantial third-order nonlinearity stems from the anharmonicity of the qubit, as well as the large coupling strengths g_q and g_m. The interaction Hamiltonian for the parametrically induced coupling is written as

$$H_{qm,p}/\hbar = g_{qm,p}\,\hat{\sigma}^{+}\hat{c}^{\dagger} + g^{*}_{qm,p}\hat{\sigma}^{-}\hat{c} \qquad (2)$$

where the effective coupling strength $g_{qm,p}$ is proportional to the drive microwave power P_d (*21*).

To understand how the continuous-wave spectroscopy reveals the parametrically induced coupling, we consider the inset of Fig. 3A, which illustrates the energy levels of the driven hybrid system in the bases of the qubit states $\{|g\rangle, |e\rangle\}$ and the Kittel-mode magnon-number states $\{|n_m\rangle = |0\rangle, |1\rangle, |2\rangle, \ldots\}$. The two-photon drive induces the Rabi splitting $2g_{qm,p}\sqrt{n_m+1}$ between the states $|g, n_m\rangle$ and $|e, n_m+1\rangle$. With a probe microwave at frequencies near ω_{FMR}, the change of the magnon excitation spectrum in the driven system is monitored. The color intensity plots in Fig. 3B show the reflection coefficient as a function of the probe frequency and the parametric drive frequency for several drive powers. When the drive frequency hits the two-photon resonance condition (yellow dashed lines), the dip in the spectrum splits into two. As the drive power increases, the anticrossing feature grows in the spectra, and an abrupt shift of the magnon frequency occurs (ii → iii). The shift from 8.410 to 8.405 GHz is identified as a qubit-state–dependent shift, corresponding to the transition $|g,0\rangle \leftrightarrow |g,1\rangle$ for small P_d (i, ii) and $|e,0\rangle \leftrightarrow |e,1\rangle$ for large P_d (iii to vi). This is caused by the population transfer from $|g,0\rangle$ to $|e,0\rangle$ at large P_d, as well as the residual static coupling between the qubit and the Kittel mode (*21*). The anticrossing observed in the $|e,0\rangle \leftrightarrow |e,1\rangle$ transition manifests parametrically induced coupling between the qubit and the magnon. As seen in the cross sections presented in Fig. 3C, the spacing between the dips, corresponding to $2g_{qm,p}/2\pi$, increases linearly with the drive power. This indicates the capability of dynamically tunable coupling between the qubit and the Kittel mode via tailoring the parametric drive. The maximum coupling $g_{qm,p}/2\pi$ obtained is 3.4 MHz, which exceeds the decoherence rates of the qubit and the magnon and ensures coherent coupling between them. Importantly, the linewidths of the dips are consistent with the expected value $(\gamma_q + \gamma_m)/2$

and do not show any notable broadening in the presence of the microwave drive.

Magnons in a macroscopic-scale ferromagnetic crystal are now ready to be controlled in a quantum manner, enabling the investigation of the ultimate limit of spintronics and magnonics at the single-quantum level. It would be of particular interest to consider an analogy with recent advances in optoelectromechanics (*26*): Phonons in nanomechanical devices, yet another example of spatially extended collective excitations in solids, coherently interact both with microwave and optical degrees of freedom and thus are studied as a candidate for realizing quantum transducers between two spectrally distant frequency domains (*27–29*). Given the demonstrated strong coupling to microwave and the anticipated magneto-optical coupling, magnons in ferromagnetic insulators may provide an alternative route toward that goal.

REFERENCES AND NOTES

1. M. Sparks, *Ferromagnetic-Relaxation Theory* (McGraw-Hill, New York, 1964).
2. A. G. Gurevich, G. A. Melkov, *Magnetization Oscillations and Waves* (CRC Press, Boca Raton, FL, 2010).
3. S. O. Demokritov *et al.*, *Nature* **443**, 430–433 (2006).
4. K. Uchida *et al.*, *Nature* **455**, 778–781 (2008).
5. Y. Kajiwara *et al.*, *Nature* **464**, 262–266 (2010).
6. H. Huebl *et al.*, *Phys. Rev. Lett.* **111**, 127003 (2013).
7. Y. Tabuchi *et al.*, *Phys. Rev. Lett.* **113**, 083603 (2014).
8. X. Zhang, C.-L. Zou, L. Jiang, H. X. Tang, *Phys. Rev. Lett.* **113**, 156401 (2014).
9. M. Goryachev *et al.*, *Phys. Rev. Appl.* **2**, 054002 (2014).
10. K. Hammerer, A. S. Sørensen, E. S. Polzik, *Rev. Mod. Phys.* **82**, 1041–1093 (2010).
11. X. Zhu *et al.*, *Nature* **478**, 221–224 (2011).
12. Y. Kubo *et al.*, *Phys. Rev. Lett.* **107**, 220501 (2011).
13. J. J. Longdell, E. Fraval, M. J. Sellars, N. B. Manson, *Phys. Rev. Lett.* **95**, 063601 (2005).
14. S. Probst *et al.*, *Phys. Rev. Lett.* **110**, 157001 (2013).
15. M. H. Devoret, R. J. Schoelkopf, *Science* **339**, 1169–1174 (2013).
16. R. Barends *et al.*, *Nature* **508**, 500–503 (2014).
17. N. G. Dickson *et al.*, *Nat. Commun.* **4**, 1903 (2013).
18. A. Wallraff *et al.*, *Nature* **431**, 162–167 (2004).
19. O. Astafiev *et al.*, *Science* **327**, 840–843 (2010).
20. M. Hofheinz *et al.*, *Nature* **459**, 546–549 (2009).
21. Materials and methods are available as supplementary materials on *Science* Online.
22. A. Imamoğlu, *Phys. Rev. Lett.* **102**, 083602 (2009).
23. P. J. Leek *et al.*, *Phys. Rev. B* **79**, 180511 (2009).
24. E. Zakka-Bajjani *et al.*, *Nat. Phys.* **7**, 599–603 (2011).
25. E. Flurin, N. Roch, J. D. Pillet, F. Mallet, B. Huard, *Phys. Rev. Lett.* **114**, 090503 (2015).
26. M. Aspelmeyer, T. J. Kippenberg, F. Marquardt, *Rev. Mod. Phys.* **86**, 1391–1452 (2014).
27. J. Bochmann, A. Vainsencher, D. D. Awschalom, A. N. Cleland, *Nat. Phys.* **9**, 712–716 (2013).
28. T. Bagci *et al.*, *Nature* **507**, 81–85 (2014).
29. R. W. Andrews *et al.*, *Nat. Phys.* **10**, 321–326 (2014).

ACKNOWLEDGMENTS

We acknowledge P.-M. Billangeon for fabricating the transmon qubit. This work was partly supported by the Project for Developing Innovation System of the Ministry of Education, Culture, Sports, Science and Technology, Japan Society for the Promotion of Science KAKENHI (grant no. 26600071, 26220601), the Murata Science Foundation, Research Foundation for Opto-Science and Technology, and National Institute of Information and Communications Technology (NICT).

SUPPLEMENTARY MATERIALS

www.sciencemag.org/content/349/6246/405/suppl/DC1
Materials and Methods
Figs. S1 to S4
References (*30*, *31*)

25 November 2014; accepted 26 May 2015
Published online 9 July 2015;
10.1126/science.aaa3693

QUANTUM INFORMATION

Coherent coupling of a single spin to microwave cavity photons

J. J. Viennot,* M. C. Dartiailh, A. Cottet, T. Kontos*

Electron spins and photons are complementary quantum-mechanical objects that can be used to carry, manipulate, and transform quantum information. To combine these resources, it is desirable to achieve the coherent coupling of a single spin to photons stored in a superconducting resonator. Using a circuit design based on a nanoscale spin valve, we coherently hybridize the individual spin and charge states of a double quantum dot while preserving spin coherence. This scheme allows us to achieve spin-photon coupling up to the megahertz range at the single-spin level. The cooperativity is found to reach 2.3, and the spin coherence time is about 60 nanoseconds. We thereby demonstrate a mesoscopic device suitable for nondestructive spin readout and distant spin coupling.

The methods of cavity quantum electrodynamics hold promise for an efficient use of the spin degree of freedom in the context of quantum computation and simulation (*1*). Realizing a coherent coupling between a single spin and cavity photons could enable quantum nondemolition readout of a single spin, quantum spin manipulation, and facilitate the coupling of distant spins (*1–4*). It could also be used in hybrid architectures in which single spins are coupled to superconducting quantum bits (*5*), or to simulate one-dimensional spin chains (*6*).

The natural coupling of a spin to the magnetic part of the electromagnetic field is weak (*7*). To enhance it, one needs a large spin ensemble, typically of about 10^{12} spins (*8–13*), but these ensembles lose the intrinsic nonlinearity of a single spin 1/2. Alternatively, several theoretical proposals have been put forward to electrically couple single spins to superconducting resonators in a mesoscopic circuit (*14–17*), building on the exquisite accuracy with which superconducting circuits can be used to couple superconducting qubits and photons and manipulate them (*18*). One such approach is to engineer an artificial spin-photon interaction by using ferromagnetic reservoirs (*15*). Notably, the spin-photon coupling is also raising experimental efforts in the optical domain (*19–23*), but the circuit approach presents the important advantage of scalability.

Recent experiments have demonstrated the coupling of double quantum dot charge states to coplanar waveguide resonators, with a coupling strength $g_{\text{charge}} \approx 2\pi \times 10$ to 50 MHz (*24–28*). In (*29*), the spin blockade readout technique in quantum dots (*30*) was combined with charge sensing with a microwave resonator (*31*). In contrast to this spin-blockade scheme, here we use the ferromagnetic proximity effect in a coherent conductor to engineer a spin-photon coupling.

Laboratoire Pierre Aigrain, Ecole Normale Supérieure–PSL Research University, CNRS, Université Pierre et Marie Curie–Sorbonne Universités, Université Paris Diderot–Sorbonne Paris Cité, 24 rue Lhomond, 75231 Paris Cedex 05, France.
*Corresponding author. E-mail: viennot@jila.colorado.edu (J.J.V.); kontos@lpa.ens.fr (T.K.)

Our scheme relies on the use of a noncollinear spin-valve geometry, which realizes an artificial spin-orbit interaction (*15*). Specifically, we contact two noncollinear ferromagnets on a carbon nanotube double quantum dot.

Our device is shown in Fig. 1, A to C. Our resonator is similar to that used in a previous experiment (*27*), with a coupling scheme adapted from (*24*). It is a Nb resonator with a quality factor $Q \approx 6200$ to 11800, depending on the external magnetic field (see fig. S6). We use a previously developed technique of stamping to preserve the Q factor of the resonator and use nanotubes grown by chemical vapor deposition (*32*). The imprints of the stamps used to transfer the nanotubes are visible in Fig. 1A. We use PdNi as a ferromagnetic alloy. It forms good contacts with carbon nanotubes (*33*, *34*), and its magnetization direction is simply controlled by the geometry of the electrodes (*35*). We set an angle (45° at zero magnetic field) between the magnetizations of the electrodes.

Ferromagnets deposited on carbon nanotubes induce effective magnetic fields (*33*, *36*). In our setup, each dot is contacted to one ferromagnet, creating a local effective magnetic field and therefore a Zeeman splitting with a quantization axis given by the ferromagnet magnetization direction. When an electron is moved from one dot to the other, its equilibrium spin orientation rotates (Fig. 1D). As a consequence, we obtain an artificial spin-orbit coupling, engineered extrinsically. The localization of an electron wave function depends on the interdot energy detuning ε (*31*). This parameter is controlled experimentally with DC voltages applied with local top gates. Notably, because this control parameter is governed by electric fields, it is also actuated by the AC electric field associated with the photons in the resonator (*24–29*). A single electron spin is thus coupled to the photons of the resonator via the natural coupling of the double dots' charge orbitals to the resonator electric field (Fig. 1D). To tune the transition frequency of the spin states and bring them in resonance with the cavity frequency, we also apply an external magnetic field B_{ext}. The different contributions of real

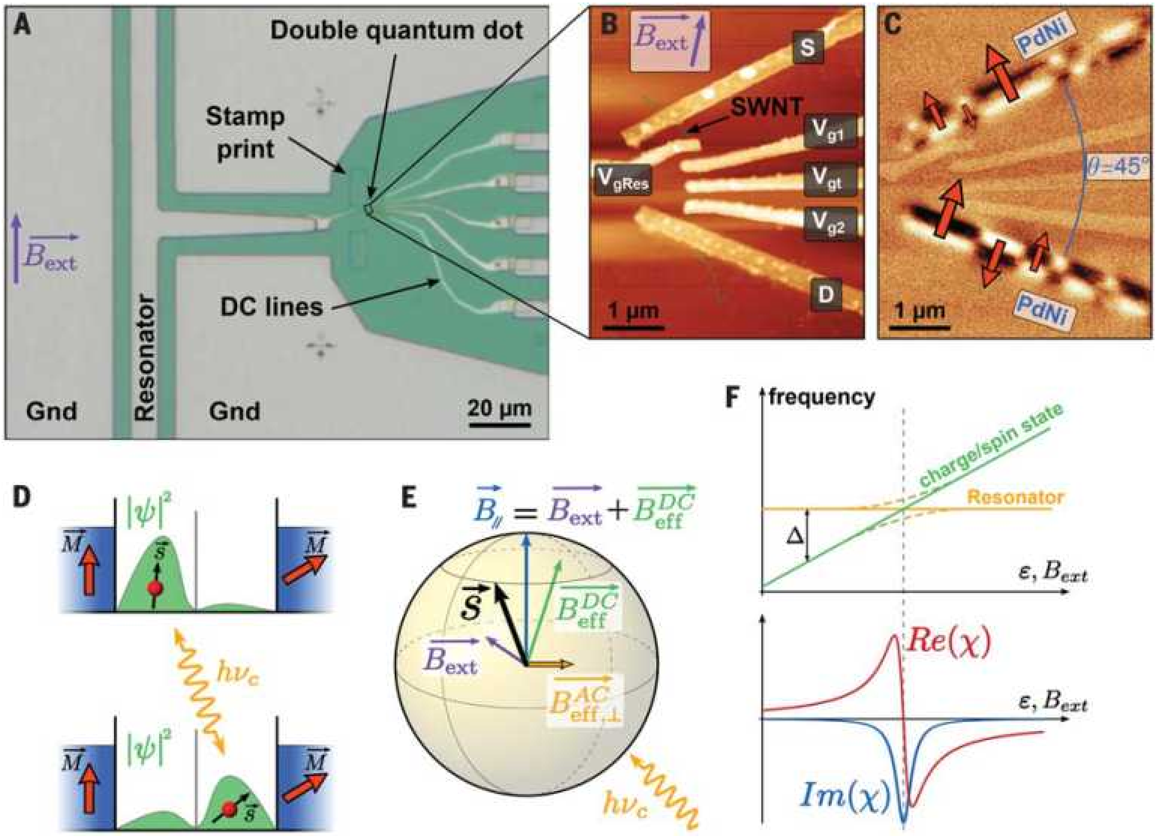

Fig. 1. Experimental setup. (**A**) Optical micrograph of the essential part of the device. The resonator central conductor is surrounded by ground planes that are open in a small region, in order to place a carbon nanotube and the necessary DC lines to form a double quantum dot. (**B**) Atomic force micrograph of the nanotube with four top gates used to bring DC electrical potentials, as well as couple to the resonator via V_{gRes}. As shown in the magnetic force micrograph (**C**), source S and drain D electrodes are made out of a ferromagnetic alloy (PdNi). Black and white colors correspond to north and south poles of ferromagnetic domains. (**D**) General principle of our coupling mechanism. The proximity of the noncollinear ferromagnets induces a different equilibrium spin orientation if an electron is localized in the left or in the right dot. Photons are coupled to transitions changing the localization of the wave function Ψ and hence coupled to transitions changing the spin orientation. (**E**) Bloch sphere of the electron spin showing the different magnetic field contributions. (**F**) When a transition crosses—or anticrosses—the resonator frequency, the associated susceptibility exhibits a resonance that is directly observable in the phase and amplitude of the resonator transmission.

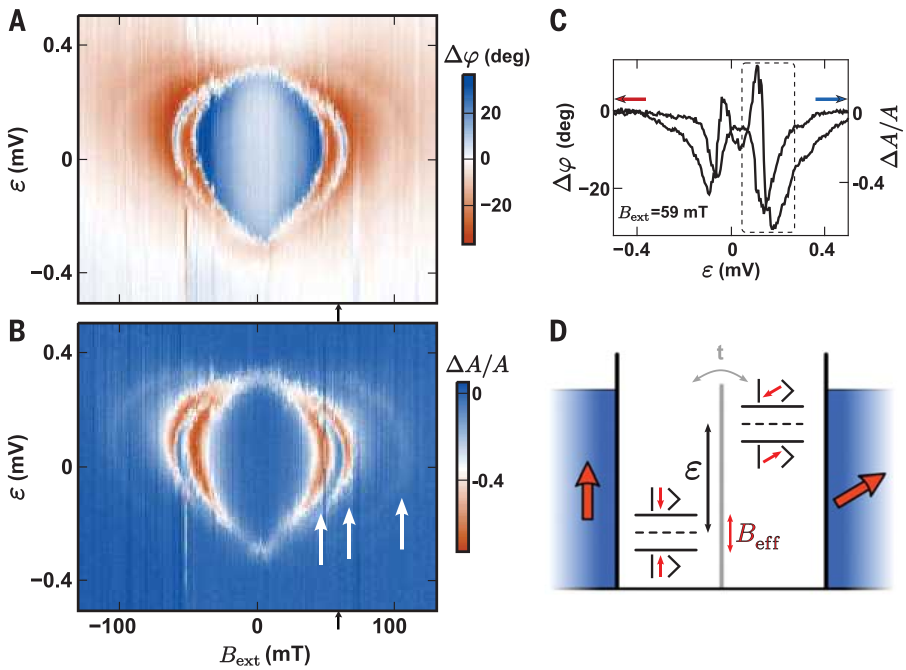

Fig. 2. Electric and magnetic dependence of the quantum dot transitions. (**A** and **B**) Measured phase and amplitude signals as a function of external magnetic field and interdot gate detuning ε, at a microwave power $P \approx -116$ dBm (about 40 photons in the cavity). We identify three transitions (indicated by white arrows). The temperature is 40 mK. (**C**) Phase and amplitude versus ε at B_{ext} = 59 mT [indicated by black arrows in (A) and (B)], showing resonances similar to that in Fig. 1F within the dashed region. (**D**) Charge states (black dashed levels) are spin-split owing to the effective fields B_{eff}. The four states (red levels) coherently hybridize via the interdot tunnel coupling t.

and effective magnetic fields are depicted in Fig. 1E. The longitudinal component $B_\parallel$ is given by the sum of the external magnetic field and the DC part of the effective fields, which depends on ε. This controls the Larmor frequency of the spin. When the electric field of the cavity actuates a charge modulation between the two dots, an AC effective magnetic field appears, with a transverse component $B^{AC}_{eff,\perp}$ oscillating at the resonator frequency. This yields the two noncollinear magnetic fields necessary for transverse coupling to the spin: a DC longitudinal component, and a transverse AC component that can be oscillating at the Larmor frequency. Although the hybridization of the spin with the charge orbitals is the mechanism responsible for coupling to the electric field of the resonator, in principle this hybridization can be weak enough to preserve spin coherence (*15*). Moreover, the sensitivity to charge noise depends on the dispersion relation of the hybridized spin-charge transitions, and therefore it can have a behavior different from that of the spin-photon coupling strength. By sweeping ε, the resonant lines in Fig. 2, A and B, go through a "sweet spot" where the double quantum dot (DQD) transition frequencies are minimum and therefore insensitive to charge noise at first order. The existence of this sweet spot contributes to the high cooperativity found for the spin transitions.

We measure the amplitude A and phase φ of the cavity transmission at resonance, at 40 mK. We tune the gate voltages of the device to form a DQD (see fig. S1). Transitions in the DQD yield phase and amplitude shifts Δφ and $\Delta A/A$ of the resonator transmission. The intrinsic dependence of the superconducting cavity on the external magnetic field is taken into account in all measurements. For every change in B_{ext}, the reference phase and amplitude are measured first, to obtain the correct Δφ and $\Delta A/A$ (*37*). A given transition between two DQD states $|i\rangle$ and $|j\rangle$ is characterized by a susceptibility to a microwave excitation $\chi_{ij} = \frac{g_{ij}}{-i\Gamma_{ij}/2+\Delta_{ij}}$, where g_{ij} is the coupling strength, Γ_{ij} is the decoherence rate, and Δ_{ij} is the frequency detuning (*37*). In practice, when such a transition is brought into resonance with the cavity mode, it shifts the mode frequency f_c by $\mathrm{Re}(\chi_{ij})$ and changes the mode linewidth κ by $\mathrm{Im}(\chi_{ij})$. The general form χ_{ij} is plotted in Fig. 1F. This signal is encoded in Δφ and $\Delta A/A$, which, to first order in χ_{ij}, are respectively given by $\mathrm{Re}(\chi_{ij})$ and $\mathrm{Im}(\chi_{ij})$. In the presence of multiple transitions, the phase and amplitude shifts are given by the sum of all the susceptibilities associated with transitions starting from a populated energy level (*8*, *24*).

Figure 2, A and B, shows, respectively, the phase and amplitude shifts as functions of interdot gate detuning ε and external magnetic field B_{ext}. Sign changes are observed in Δϕ, together with dips in $\Delta A/A$, indicating DQD transition frequencies crossing the cavity frequency. Figure 2C shows a line cut at B_{ext} = 59 mT. The variation of the phase and amplitude in the dashed area of Fig. 2C resembles that in Fig. 1F.

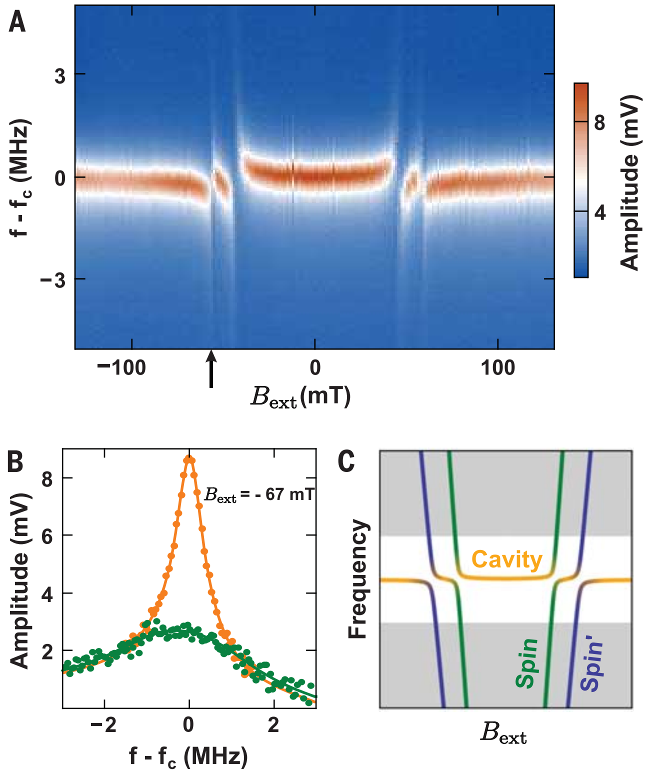

Fig. 3. Spin-cavity hybridization. (**A**) Measured transmission spectrum of the cavity as a function of B_{ext}, centered around the resonant frequency f_c, at small detuning ε ≈ 50 μV. The temperature is 40 mK. (**B**) Resonator transmission at B_{ext} = −67 mT (indicated by the black arrow) with spin transition detuned (ε > 1 mV, orange curve) and resonant (ε ≈ 50 μV, green curve), measured at microwave power P ≈ −119 dBm (about 20 photons in the cavity). Circles are data and solid line is theory [explained in (*37*)]. (**C**) Sketch of the spin transitions (Spin and Spin′) dispersing with B_{ext} and hybridizing with the resonator mode (Cavity). Our measurements focus on the white stripe around the cavity frequency.

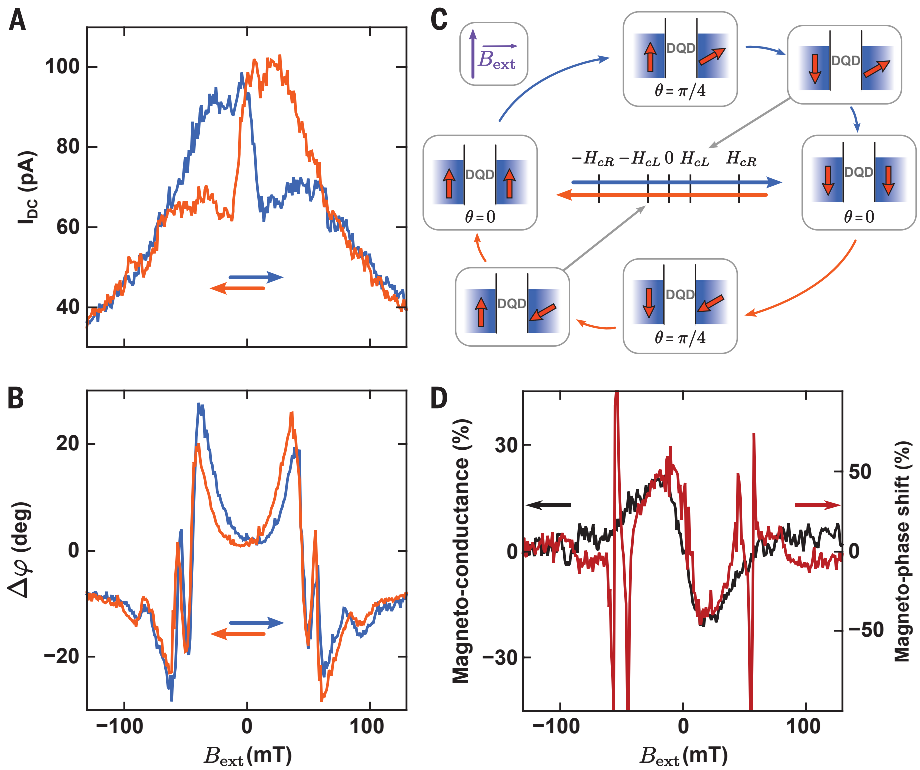

Fig. 4. Magnetic hysteresis. (**A** and **B**) Measured DC current and microwave phase shift for increasing (blue) and decreasing (orange) external magnetic field. See (*37*) for the details of the phase measurement. The temperature is 40 mK. (**C**) Schematics of the ferromagnets magnetization evolution with B_{ext}. H_{cL} and H_{cR} are the coercive fields of the ferromagnets. (**D**) Percentage of hysteresis for the DC current (magneto-conductance) and the phase signal (*37*).

Figure 2, A and B, therefore demonstrate that three transitions of the DQD are coupled to the cavity and disperse as functions of both ε and B_{ext} . This dependence on both gate voltage and magnetic field strongly suggests transitions involving changes in both charge and spin states (Fig. 2D). Charge states in the dots, separated by the energy ε, are Zeeman split by the effective fields induced by the ferromagnets. The tunnel coupling between the two dots coherently hybridizes their orbitals to form the analog of bonding and antibonding states (*27*, *31*). In addition, the noncollinear quantization axis of the two dots couples the spin populations. The four states of Fig. 2D thus coherently hybridize into four quantum states having both charge and spin components.

When a transition is resonant with the cavity (i.e., around Δ_{ij} = 0), the phase and amplitude contrasts are directly linked to the cooperativity:

$$C_{ij} = \frac{4{g_{ij}}^2}{\kappa\Gamma_{ij}}$$

The cavity linewidth κ varies slowly and by less than a factor of 2 in our magnetic field range ($2\pi \times 0.61$ MHz <κ < $2\pi \times 1$ MHz; see fig. S6). Nevertheless, we observe a higher phase and amplitude contrast at higher fields and smaller interdot detuning ε (see Fig. 2, A and B). This indicates that transitions become more coherent, or more coherently coupled to the cavity in this region.

To perform a more quantitative analysis, we measure the resonator transmission spectrum as a function of the magnetic field at small interdot detuning ε of about 50 μV (Fig. 3A). For the sake of clarity, the frequency traces are all centered around the bare cavity frequency f_c, which itself shows jumps with changes in B_{ext} (see fig. S2 for the data in absolute frequency). At ±50 mT, two DQD transitions become resonant with the cavity and cause strong distortions on the transmission spectrum. This confirms the high cooperativity between spin-hybridized transitions and the resonator. Figure 3B shows profiles of the resonator transmission at –67 mT, for a strongly detuned (ε > 1 mV, orange curve) and a resonant transition (ε ≈ 50 μV, green curve). We observe a pronounced change in the amplitude and width of the transmission. Fitting these data (*37*), we extract the bare cavity parameters and estimate the coupling strength $g_{spin} \approx 2\pi \times 1.3$ MHz for this transition, with a decoherence rate $\Gamma^*_{2,spin}/2 \approx 2\pi \times 2.5$ MHz, corresponding to a cooperativity $C \approx 2.3$ (*37*). We compare this to the much larger charge decoherence rate $\Gamma^*_{2,charge}/2 \approx 2\pi \times 0.45$ to 3 GHz measured previously in similar conditions on a carbon nanotube (*27*) and arising from charge noise. For the neighboring transition at –43 mT, we find that $C \approx 3.3$, which suggests that this transition is also dominantly a spin transition. Figure 3C shows a sketch of the spectrum obtained from a Hamiltonian generalized from (*15*) [see (*37*)]. In this sketch, we omit the third (faint) resonance visible in Fig. 2, A and B, because of its weaker coherence. The calculated spectrum in (*37*) is in agreement with Fig. 3A. We are also able to reproduce the three resonances in Fig. 2, A and B (fig. S5). In our model, the two strongest resonances correspond dominantly to spin transitions, as expected. The third faint resonance corresponds to a transition that is less coherently coupled (*37*).

The final piece of evidence that the hybridized spin states arise from the extrinsic artificial spin-orbit interaction is provided by operating our device as a spin valve. To achieve that, we swept the magnetic field fast enough for the ferromagnetic electrodes to switch hysteretically. Figure 4A shows a conventional DC current measurement as a function of the magnetic field and the magnetic field sweeping direction, done on a cotunneling line (such as shown in fig. S1). We observe the characteristic hysteretic behavior of a quantum dot spin valve, which can be explained by the magnetization reversal sequence of Fig. 4C. This typically results in a magneto-conductance such as the one shown in Fig. 4D. Importantly, the electrodes' magnetizations are noncollinear, and one of them is not aligned with the magnetic field. The magnetization configuration is therefore noncollinear up to high enough $B_{ext,}$, preserving the amplitude of spin-flipping matrix elements in the spin-photon Hamiltonian for transitions Spin and Spin′ (*15*). Figure 4B shows the phase shift close to ε = 0 for the same type of measurement as in Fig. 4A. The main part of the signal simply corresponds to the profile of Fig. 2A taken at small ε, showing the three transitions. Notably, the phase is hysteretic, revealing a hysteresis in the total susceptibility χ. We have ensured that this is not caused by spurious hysteresis of the cavity by measuring systematically all the cavity parameters along the hysteresis path (fig. S6). In Fig. 4D, we plot the hysteretic part of the phase shift (*37*). Sharp variations correspond to fields where the spin transition is resonant with the cavity. At these points, a small hysteresis in the transition frequency, therefore in the detuning Δ_{ij}, yields a strong hysteresis in the susceptibility. Outside of these areas, we observe a smooth variation similar to the behavior of the magneto-conductance. Both magneto-conductance and magneto–phase shift thus vary on the same scale of the magnetic field. This is further evidence that the spectrum is genuinely affected by the ferromagnets.

Along with a single spin-photon coupling strength $g_{spin} \approx 2\pi \times 1.3$ MHz, we can give a lower bound for the spin decoherence time in carbon nanotubes $T_2^* > 60$ ns ($T_2^* = 2/\Gamma_2^*$). This is already almost one order of magnitude larger than the previous measurements in nanotubes (*38*), but we believe that it could be improved further by optimizing the spin-charge hybridization. The cooperativity and decoherence rates given above indicate that our system is at the strong coupling threshold. Owing to the general principle used here, this method could be applied to many host materials for spin quantum bits. These results open an avenue for single spin–based circuit quantum electrodynamics experiments.

REFERENCES AND NOTES

1. A. Imamoglu *et al*., *Phys. Rev. Lett.* **83**, 4204–4207 (1999).
2. D. Loss, D. P. DiVincenzo, *Phys. Rev. A* **57**, 120–126 (1998).
3. G. Burkard, A. Imamoglu, *Phys. Rev. B* **74**, 041307 (2006).
4. J. M. Raimond, M. Brune, S. Haroche, *Rev. Mod. Phys.* **73**, 565–582 (2001).
5. D. D. Awschalom, L. C. Bassett, A. S. Dzurak, E. L. Hu, J. R. Petta, *Science* **339**, 1174–1179 (2013).
6. I. Buluta, F. Nori, *Science* **326**, 108–111 (2009).
7. G. Tosi, F. A. Mohiyaddin, H. Huebl, A. Morello, *AIP Advances* **4**, 087122 (2014).
8. D. I. Schuster *et al*., *Phys. Rev. Lett.* **105**, 140501 (2010).
9. Y. Kubo *et al*., *Phys. Rev. Lett.* **105**, 140502 (2010).
10. H. Huebl *et al*., *Phys. Rev. Lett.* **111**, 127003 (2013).
11. Y. Tabuchi *et al*., *Phys. Rev. Lett.* **113**, 083603 (2014).
12. X. Zhu *et al*., *Nature* **478**, 221–224 (2011).
13. Y. Kubo *et al*., *Phys. Rev. Lett.* **107**, 220501 (2011).
14. M. Trif, V. N. Golovach, D. Loss, *Phys. Rev. B* **77**, 045434 (2008).
15. A. Cottet, T. Kontos, *Phys. Rev. Lett.* **105**, 160502 (2010).
16. P.-Q. Jin, M. Marthaler, A. Shnirman, G. Schön, *Phys. Rev. Lett.* **108**, 190506 (2012).
17. X. Hu, Y.- Liu, F. Nori, *Phys. Rev. B* **86**, 035314 (2012).
18. A. Wallraff *et al*., *Nature* **431**, 162–167 (2004).
19. W. B. Gao, P. Fallahi, E. Togan, J. Miguel-Sanchez, A. Imamoglu, *Nature* **491**, 426–430 (2012).
20. A. Faraon, C. Santori, Z. Huang, V. M. Acosta, R. G. Beausoleil, *Phys. Rev. Lett.* **109**, 033604 (2012).
21. E. Togan *et al*., *Nature* **466**, 730–734 (2010).
22. B. B. Buckley, G. D. Fuchs, L. C. Bassett, D. D. Awschalom, *Science* **330**, 1212–1215 (2010).
23. C. Arnold *et al*., *Nat. Commun.* **6**, 6236 (2015).
24. T. Frey *et al*., *Phys. Rev. Lett.* **108**, 046807 (2012).
25. H. Toida, T. Nakajima, S. Komiyama, *Phys. Rev. Lett.* **110**, 066802 (2013).
26. A. Wallraff, A. Stockklauser, T. Ihn, J. R. Petta, A. Blais, *Phys. Rev. Lett.* **111**, 249701 (2013).
27. J. J. Viennot, M. R. Delbecq, M. C. Dartiailh, A. Cottet, T. Kontos, *Phys. Rev. B* **89**, 165404 (2014).
28. G.-W. Deng *et al*., Circuit QED with a graphene double quantum dot and a reflection-line resonator (2013); http://arxiv.org/abs/1310.6118.
29. K. D. Petersson *et al*., *Nature* **490**, 380–383 (2012).
30. K. Ono, D. G. Austing, Y. Tokura, S. Tarucha, *Science* **297**, 1313–1317 (2002).
31. R. Hanson, L. P. Kouwenhoven, J. R. Petta, S. Tarucha, L. M. K. Vandersypen, *Rev. Mod. Phys.* **79**, 1217–1265 (2007).
32. J. J. Viennot, J. Palomo, T. Kontos, *Appl. Phys. Lett.* **104**, 113108 (2014).
33. S. Sahoo *et al*., *Nat. Phys.* **1**, 99–102 (2005).
34. C. Feuillet-Palma *et al*., *Phys. Rev. B* **81**, 115414 (2010).
35. J.-Y. Chauleau *et al*., *Phys. Rev. B* **84**, 094416 (2011).
36. J. R. Hauptmann, J. Paaske, P. E. Lindelof, *Nat. Phys.* **4**, 373–376 (2008).
37. Supplementary materials are available on *Science* Online.
38. E. A. Laird, F. Pei, L. P. Kouwenhoven, *Nat. Nanotechnol.* **8**, 565–568 (2013).

ACKNOWLEDGMENTS

We acknowledge fruitful discussions with the Quantronics group, J. M. Raimond, B. Huard, A. Thiaville, L. Bretheau, E. Flurin, L. E. Bruhat, and M. P. Desjardins and acknowledge the technical support of M. Rosticher and J. Palomo. We gratefully acknowledge P. Senellart and L. Lanco for discussions and for communicating results to us prior to publication. The work was financed by the European Union project SE2ND and the European Research Council Starting Grant CirQys. The data described in the paper are presented in this report and supplementary materials.

SUPPLEMENTARY MATERIALS

www.sciencemag.org/content/349/6246/408/suppl/DC1
Materials and Methods
Figs. S1 to S6

26 November 2014; accepted 29 June 2015
10.1126/science.aaa3786

NANOCATALYSTS

Platinum-based nanocages with subnanometer-thick walls and well-defined, controllable facets

Lei Zhang,[1,2] Luke T. Roling,[3] Xue Wang,[1,2] Madeline Vara,[4] Miaofang Chi,[5] Jingyue Liu,[6] Sang-Il Choi,[1] Jinho Park,[4] Jeffrey A. Herron,[3] Zhaoxiong Xie,[2] Manos Mavrikakis,[3] Younan Xia[1,4,7]*

A cost-effective catalyst should have a high dispersion of the active atoms, together with a controllable surface structure for the optimization of activity, selectivity, or both. We fabricated nanocages by depositing a few atomic layers of platinum (Pt) as conformal shells on palladium (Pd) nanocrystals with well-defined facets and then etching away the Pd templates. Density functional theory calculations suggest that the etching is initiated via a mechanism that involves the formation of vacancies through the removal of Pd atoms incorporated into the outermost layer during the deposition of Pt. With the use of Pd nanoscale cubes and octahedra as templates, we obtained Pt cubic and octahedral nanocages enclosed by {100} and {111} facets, respectively, which exhibited distinctive catalytic activities toward oxygen reduction.

One strategy to increase the utilization efficiency (UE) of platinum group metals (PGMs) is to increase the proportion of atoms exposed on the surface (the dispersion) by reducing particle size. For example, the UE of platinum (Pt) atoms can be increased from 9.5 to 26% by reducing the edge length of a Pt cube from 11.7 to 3.9 nm. Despite the extensive use of this strategy, it has been difficult to optimize the specific activity of such small nanocrystals (NCs) by engineering their surface structure through facet-controlled synthesis (*1*). Such NCs also tend to sinter (form larger particles), detach from the support, or both during operation (*2*). An alternative strategy is to use nanoframes—open nanostructures comprising multiple ridges as thin as a few nanometers (*3–5*). Each ridge of a nanoframe can be considered as a linear aggregate of NCs. Essentially, all the PGMs can be prepared as nanoframes by using methods that involve the selective removal of a sacrificial component: for example, the more reactive metal in alloyed NCs or the NC serving as a template for the site-selected deposition of the PGM. In a notable example, Pt_3Ni nanoframes with extraordinary mass activity of 5.7 amperes per milligram of Pt ($A\ mg^{-1}_{Pt}$) toward the oxygen reduction reaction (ORR) have been developed (*5*), but this method still faces challenges in selecting the exposed crystal facet with which to control their catalytic activity and selectivity.

A different strategy for increasing the UE of a PGM is to assemble the metal atoms into nanosheets (*6–8*). For such a system consisting of four atomic layers, the UE could in principle reach 50%, but the use of PGM nanosheets as catalysts encounters several drawbacks: (i) the top and bottom surfaces of a sheet must be capped by ligands; (ii) the metal atoms can only assume a hexagonal lattice, corresponding to one type of facet only; and (iii) it is challenging to deposit and expose individual nanosheets on a catalytic support. An alternative to this strategy is to deposit the PGM conformally as subnanometer-thick shells of only a few atomic layers on the surfaces of NC templates made of another metal. In addition to the electrochemical approach explored by a number of groups (*9–11*), we recently developed a solution-phase method for the deposition of Pt on facet-controlled palladium (Pd) NCs to generate $Pd@Pt_{nL}$ core-shell structures (where n is the number of Pt atomic layers), in which the Pt shells could be controlled at 1 to 6 atomic layers in thickness (*12–14*). The $Pd@Pt_{nL}$ NCs showed great improvement in terms of both mass activity and durability toward ORR relative to a commercial Pt/carbon (C) catalyst.

The interiors of these core-shell structures, however, are still occupied by another PGM (Pd, in this case), which will contribute to a large portion of the materials cost associated with such a catalyst. A logical solution is to selectively remove the Pd template after Pt deposition, generating a nanocage made of Pt only. When conducted appropriately, the facets present on the surface of a template can be well preserved during the Pt coating and Pd etching processes

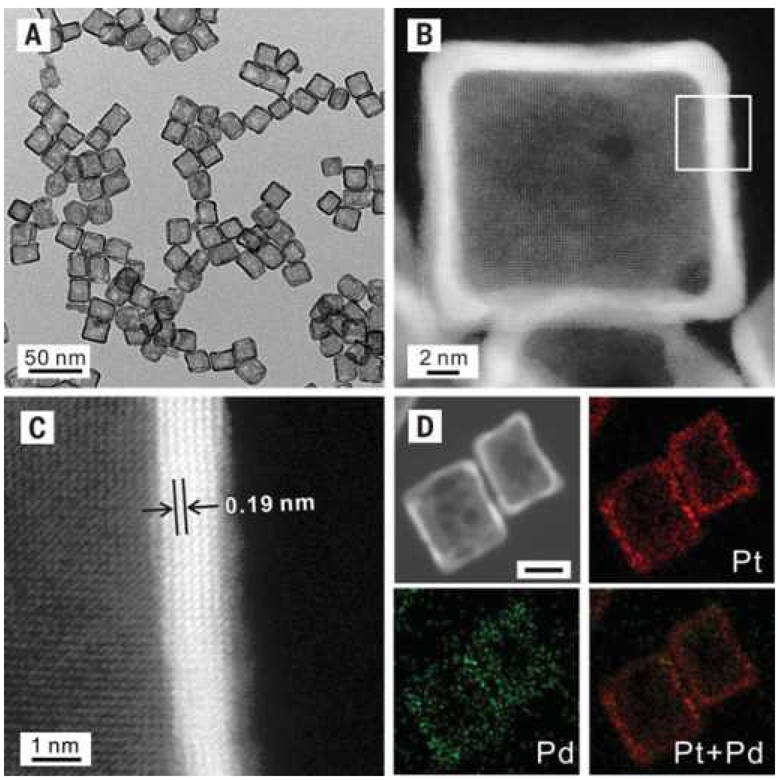

Fig. 1. Structural and compositional analyses of Pt cubic nanocages. (**A**) TEM image of a typical sample. (**B**) HAADF-STEM image of an individual nanocage. (**C**) High-resolution HAADF-STEM image taken from the region boxed in (B), showing a wall thickness of six atomic layers. (**D**) EDS elemental mapping of Pt and Pd for two nanocages. Scale bar, 10 nm.

[1]Wallace H. Coulter Department of Biomedical Engineering, Georgia Institute of Technology and Emory University, Atlanta, GA 30332, USA. [2]State Key Laboratory of Physical Chemistry of Solid Surfaces, Collaborative Innovation Center of Chemistry for Energy Materials, and Department of Chemistry, Xiamen University, Xiamen, Fujian 361005, P. R. China. [3]Department of Chemical and Biological Engineering, University of Wisconsin–Madison, Madison, WI 53706, USA. [4]School of Chemistry and Biochemistry, Georgia Institute of Technology, Atlanta, GA 30332, USA. [5]Center for Nanophase Materials Sciences, Oak Ridge National Laboratory, Oak Ridge, TN 37831, USA. [6]Department of Physics, Arizona State University, Tempe, AZ 85287, USA. [7]School of Chemical and Biomolecular Engineering, Georgia Institute of Technology, Atlanta, GA 30332, USA.
*Corresponding author. E-mail: younan.xia@bme.gatech.edu

so as to engineer the activity and/or selectivity of the catalyst. We demonstrate this concept by coating the surfaces of Pd nanoscale cubes and octahedra with four atomic layers of Pt, followed by selective removal of the Pd templates. Density functional theory (DFT) calculations suggest that the etching is initiated via a mechanism that involves the formation of surface vacancies by etching away Pd atoms incorporated into the Pt shells from intermixing and/or co-reduction (*15*). We could obtain Pt nanocages with walls as thin as three atomic layers (0.7 nm thick), with their surfaces terminated in {100} or {111} facets. The nanocages show distinctive specific activities toward ORR depending on the exposed facet, whereas the activity and durability are both enhanced relative to a commercial Pt/C catalyst.

We first synthesized Pd cubes with an average edge length of 18.2 nm (fig. S1, A and B) (*16*, *17*). Four atomic layers of Pt were then deposited on the surface of each Pd cube as a conformal shell (fig. S1C) by introducing a Pt(IV) precursor at 200°C (*12*). The use of a slow injection rate and a relatively high temperature resulted in the formation of core-shell cubes with atomically flat surfaces (*18*). When subjected to etching, the Pd templates could be selectively removed to leave behind Pt cubic nanocages with ultrathin walls covered by {100} facets.

A transmission electron microscopy (TEM) image of Pt cubic nanocages derived from Pd@Pt_{4L} cubes by using a standard procedure is shown in Fig. 1A (*17*). The nanocages had an average edge length of 20.2 nm (fig. S1D), together with small holes on the surfaces. The high-angle annular dark-field scanning TEM (HAADF-STEM) image (Fig. 1B) taken from one of the nanocages revealed a periodic lattice extending across the entire surface, suggesting that the single-crystal structure of the Pd template was transferred to the Pt shell. The uniform contrast across the side face indicates that essentially all the Pd atoms in the core had been removed, except for those alloyed with Pt atoms in the walls. The atomic-resolution HAADF-STEM image (Fig. 1C) recorded from the region boxed in Fig. 1B indicates a wall thickness of ~1 nm, corresponding to six atomic layers along the [100] direction. The lattice spacing of 0.19 nm can be assigned to the (200) planes of face-centered cubic (fcc) Pt.

Although only four atomic layers of Pt were initially deposited on the surface of each Pd template, the wall thickness increased to six atomic

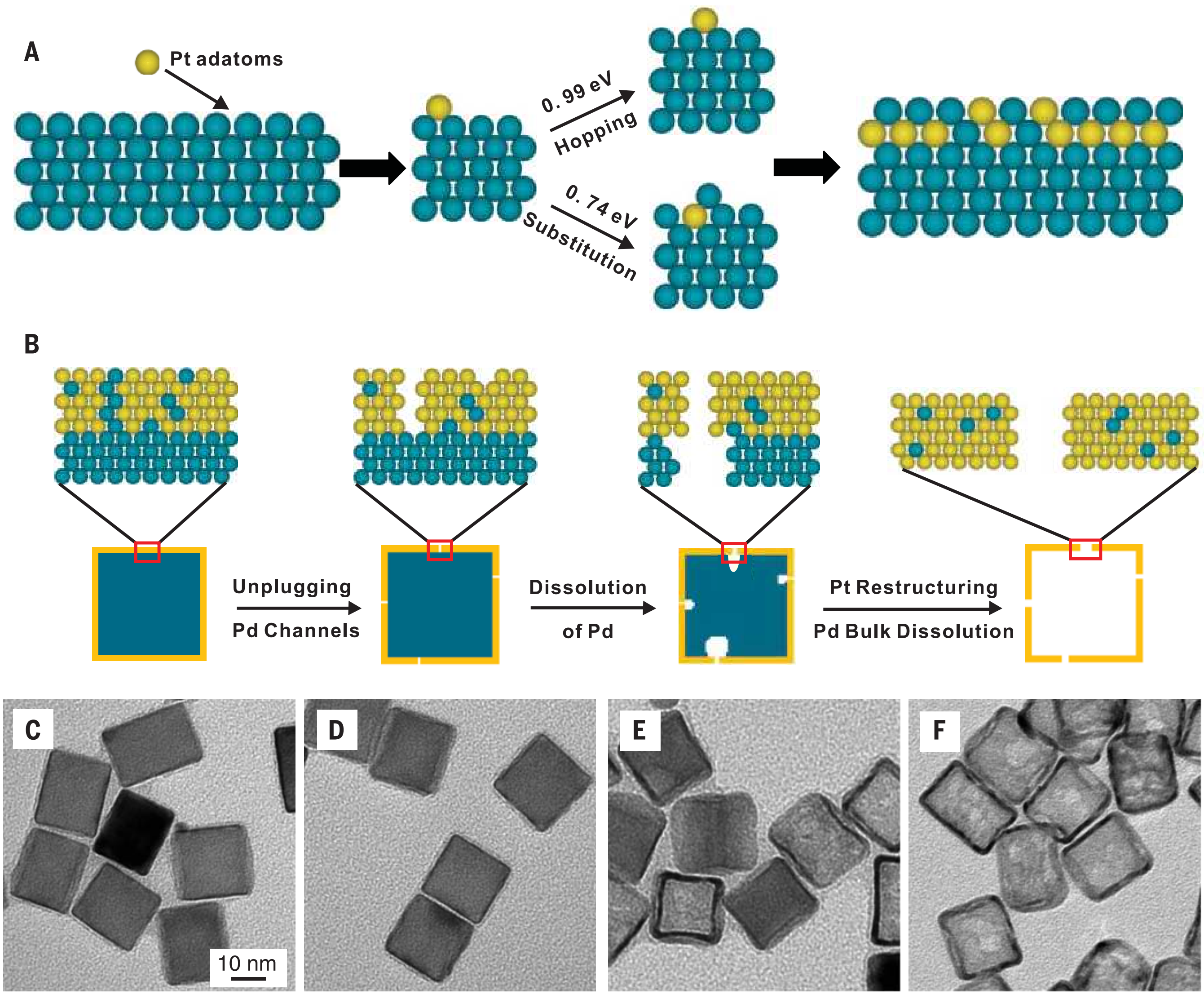

Fig. 2. Mechanistic details involved in the deposition and etching processes, and TEM images of the products obtained after etching for different periods of time. (**A**) Pt atoms deposited on the Pd surface may diffuse ("hop") across the surface or substitute into the surface (DFT-calculated activation barriers are shown), leading to a mixed outer-layer composition. (**B**) Schematic of the major steps involved in the continuous dissolution of Pd atoms from a Pd@Pt_{4L} cube to generate a Pt cubic nanocage. (**C** to **F**) TEM images of Pd@Pt_{4L} cubes after Pd etching for (C) 0, (D) 10, (E) 30, and (F) 180 min. Scale bar, 10 nm, applies to (C) to (F).

layers because of the following factors: the interdiffusion and alloying between Pt and Pd, and thus a small amount of Pd remains in the walls; the inclusion of small holes in the side faces; and the migration of atoms from side faces to ridges, making the walls appear thicker under TEM. Elemental mapping based on energy-dispersive x-ray spectroscopy (EDS) confirmed that the nanocages were composed of a Pt-Pd alloy (Fig. 1D). Inductively coupled plasma mass spectrometry (ICP-MS) analysis gave Pt mass percentages of 93.6 and 33.9% for the nanocages and core-shell cubes, respectively.

We hypothesize that the etching is initiated by oxidizing the Pd atoms in the outmost layer of the Pt shell to generate vacancies, followed by diffusion of Pd atoms from underlying layers to generate more vacancies (*15*). This process is similar to the mechanism proposed by Heggen *et al.* for the electrochemical dealloying of Co-Pt core-shell nanoparticles (*19*), but in our case, we were able to completely remove the Pd cores because of the involvement of ultrathin Pt shells and the persistence of pores in the shells. Previous work by Erlebacher *et al.* emphasized the role of mobile, low-coordinated metal atoms in a dealloying process because movement and clustering of these species continually exposed less noble atoms for dissolution (*20*). These observations may explain the restructuring of our atomic-width vacancies to larger pores, allowing more bulk-like dissolution of Pd from the core. In contrast, our system consists of ultrathin, smooth Pt surfaces with a relatively low Pd concentration. The amount of low-coordinated Pt should therefore be low, and surface restructuring is limited to areas near the atom-wide channels formed in the initial stage. We performed DFT calculations to evaluate the diffusion barrier of a Pd atom though the Pt shell using a fully relaxed Pt(100) membrane of four atomic layers as a model system (*17*). We examined a number of processes (such as one-to-one atom exchange, as well as three-body and four-body rotations), and concluded that (i) diffusion of Pd and Pt atoms through Pt, at 100°C, must be vacancy-mediated, and (ii) the lowest diffusion barrier is for Pd through Pt (0.88 eV). Previous experimental studies of Pd-Pt interdiffusion also found that Pd had a higher diffusion rate in Pt than in Pd (*21*).

Because diffusion must occur at vacancies in our model, we also considered the mechanism by which the vacancies arise. We believe that Pt-Pd intermixing occurs during the deposition of Pt (Fig. 2A), rather than after the formation of perfect Pt overlayers. The deposition was conducted at a relatively high temperature so as to give Pt atoms an opportunity to spread across the Pd surface and thus grow in a layer-by-layer fashion (*18*). Using DFT, we obtained an energy barrier of 0.99 eV for the diffusion of Pt adatoms across a Pd(100) surface (a "hopping" mechanism). However, a Pt adatom can instead substitute into the Pd surface, pushing the Pd atom to a nearby hollow surface site with a barrier of just 0.74 eV (a "substitution" mechanism); this process is exothermic by 0.38 eV. As a consequence of these two mechanisms, some Pd atoms will be incorporated into the Pt shell as each Pt overlayer is formed. The activation energy barrier for Pt substitution increases as the Pt coverage increases, so not all of the Pd atoms will be substituted by Pt atoms when each additional layer of Pt is deposited. Alternatively, Pd atoms can be incorporated into the Pt shell through a co-reduction mechanism. Because the synthesis was conducted in air at 200°C, a trace amount of Pd atoms on the templates could be oxidized and released into the reaction solution as Pd(II) ions before the introduction of Pt(IV) precursor. Subsequently, the Pd(II) and Pt(IV) ions would be co-reduced and deposited onto the templates to generate Pt shells doped with Pd atoms. Before the introduction of Pt(IV) precursor, however, the concentration of Pd(II) ions in the reaction solution was too low to be detected with ICP-MS.

A plausible mechanism involved in the formation of a Pt cubic nanocage from a Pd@Pt_{nL} cube is illustrated in Fig. 2B. During Pt deposition, some Pd atoms are incorporated into the Pt overlayers through intermixing and/or co-reduction. Upon contact with the etchant, the Pd atoms in the outermost layer are oxidized so as to generate surface vacancies. The underlying Pd atoms then diffuse to these vacancies and are continuously etched away, leaving behind atom-wide channels. In the early stage of etching, the diffusion of Pd through these channels leads to a Kirkendall effect because Pd diffuses outward faster than Pt diffuses inward, creating a void in the Pd template. Over time, the channels will grow in size (and also reconstruct) to allow direct corrosion of Pd from the core. TEM images of the initial Pd@Pt_{4L} cubes and the same batch of sample after etching with a standard procedure for 10 min are shown in Fig. 2, C and D, respectively. There were essentially no changes to the shape, morphology, or structure of the core-shell cubes. According to ICP-MS analysis, the Pd mass percentage of this sample was 63.5%, which only dropped slightly from the initial value of 66.1%. The data suggest that the initial etching only involved "unplugging" of the existing Pd atoms on the outermost layer of the Pt shell. In a control experiment, we noticed that the Pd etching could be initiated at a much faster rate and at a lower temperature by cotitrating Pd(II) and Pt(IV) precursors at a molar ratio of 1:99 during the deposition of Pt (fig. S2). Our results also indicate that the etching rate could be manipulated by varying the molar ratio of Pd(II) to Pt(IV) precursors.

Once initiated, the surface layers begin to undergo reconstruction facilitated by the high etching temperature, enlarging the channels to 1 to 3 nm wide for direct corrosion of Pd. As shown in Fig. 2E, most of the Pd@Pt_{4L} cubes had

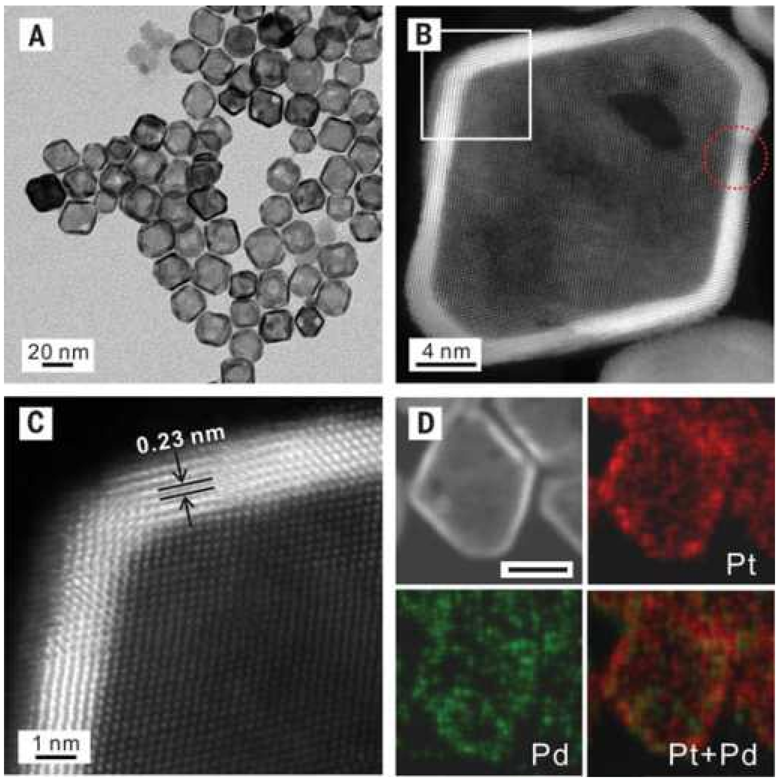

Fig. 3. Structural and compositional analyses of Pt octahedral nanocages. (**A**) TEM image of a typical sample. (**B**) HAADF-STEM image of an individual nanocage. The red circle marks a hole responsible for the dissolution of Pd from the core. (**C**) High-resolution HAADF-STEM image taken from the region boxed in (B), showing a wall thickness of seven atomic layers. (**D**) EDS mapping of Pt and Pd. Scale bar, 10 nm.

evolved into hollow structures after etching for 30 min. At the same time, the Pd mass percentage quickly dropped to 21.9%. Further etching led to Pt cubic nanocages characterized by a completely hollow interior and porous walls. Shown in Fig. 2F is a TEM image of the product obtained after etching for 3 hours and the Pd mass percentage had dropped to 6.4%. At this point, the removal of Pd was essentially completed because the Pd mass percentage did not show any change when the etching time was prolonged to 4 hours. We noted that Pt nanocages derived from $Pd@Pt_{2\text{-}3L}$ cubes (fig. S3A) tended to collapse when the standard procedure was used for etching but could be largely preserved under milder etching conditions (fig. S3, B to D).

The arrangement of atoms on the surface can affect both catalytic activity and selectivity; for example, Pt(111) is more active toward ORR than is Pt(100) (*22*). Thus, we extended Pt deposition and Pd etching procedures to the preparation of Pt octahedral nanocages enclosed by {111} facets (Fig. 3A). We prepared $Pd@Pt_{4\text{-}5L}$ octahedra from Pd octahedra of 19.4 nm in edge length (fig. S4) (*16*, *20*) and then etched away the Pd templates using more etchant relative to the standard procedure. The HAADF-STEM image in Fig. 3B shows a lattice spacing of 0.23 nm that can be assigned to the {111} planes of fcc Pt. The atomic-resolution HAADF-STEM image in Fig. 3C indicates the presence of seven atomic layers of Pt in the shell. The inclusion of Pd in the walls was confirmed with EDS (Fig. 3D). According to our ICP-MS analysis, the Pd mass percentage of the octahedral nanocages was only 9.1%, indicating the completion of template removal. By switching to $Pd@Pt_{2\text{-}3L}$ octahedra, we were able to obtain Pt octahedral nanocages with a wall thickness of only three atomic layers [or 0.7 nm along the [111] direction (fig. S5)] using a standard procedure.

We used ORR as a model reaction to demonstrate the ability to engineer the catalytic activity of such Pt nanocages by manipulating the type of facet exposed on the surface. We benchmarked their catalytic performance against a commercial Pt/C catalyst (table S1 and fig. S6). We used cyclic voltammetry (CV) to measure the electrochemically active surface area (ECSA) of each catalyst. The specific ECSAs of cubic and octahedral nanocages were measured as 46.8 and 38.2 square meters per gram of Pt ($m^2\ g^{-1}{}_{Pt}$), respectively, which are comparable with the value of 44.2 $m^2\ g^{-1}{}_{Pt}$ reported for Pt_3Ni nanoframes (*5*). Although the surfaces of the nanocages are covered by small holes (~20% of the total surface area), their ECSAs were still similar to those of the corresponding $Pd@Pt_{nL}$ NCs—39.7 and 38.0 $m^2\ g^{-1}{}_{Pt}$, respectively—for the cubic and octahedral systems (*12*, *13*) because of the contribution from the inner surface. The specific ECSAs of the nanocages were also on par with that of the Pt/C catalyst (56.8 $m^2\ g^{-1}{}_{Pt}$), even though their sizes differ more than sevenfold (20 versus 2.8 nm).

We then evaluated the electrocatalytic performance of the different catalysts toward ORR (fig. S6, B to D). As displayed in Fig. 4A, the octahedral nanocages had mass activity of 0.75 A $mg^{-1}{}_{Pt}$ at 0.9 volts versus reversible hydrogen electrode (V_{RHE}), which was five times greater than the Pt/C reference (0.14 A $mg^{-1}{}_{Pt}$). The results demonstrate that the transformation from $Pd@Pt_{nL}$ NCs into Pt nanocages could greatly improve the catalytic performance toward ORR in terms of Pt mass and materials cost. This catalytic system, however, needs to be optimized before it can compete with the more active (but more complex) system based on Pt-Ni alloys (*5*, *23*–*28*). As shown in Fig. 4B, the octahedral nanocages exhibited the highest specific activity, with a value of 1.98 mA cm^{-2} at 0.9 V_{RHE}, which was almost eight times greater than that of the Pt/C (0.25 mA cm^{-2}). The almost twofold difference in specific activity between the octahedral and cubic nanocages clearly demonstrates the feasibility to control the catalytic activity of such nanocages through facet engineering. We used DFT to analyze the ORR-specific activities of the nanocages by calculating the energetics of OH

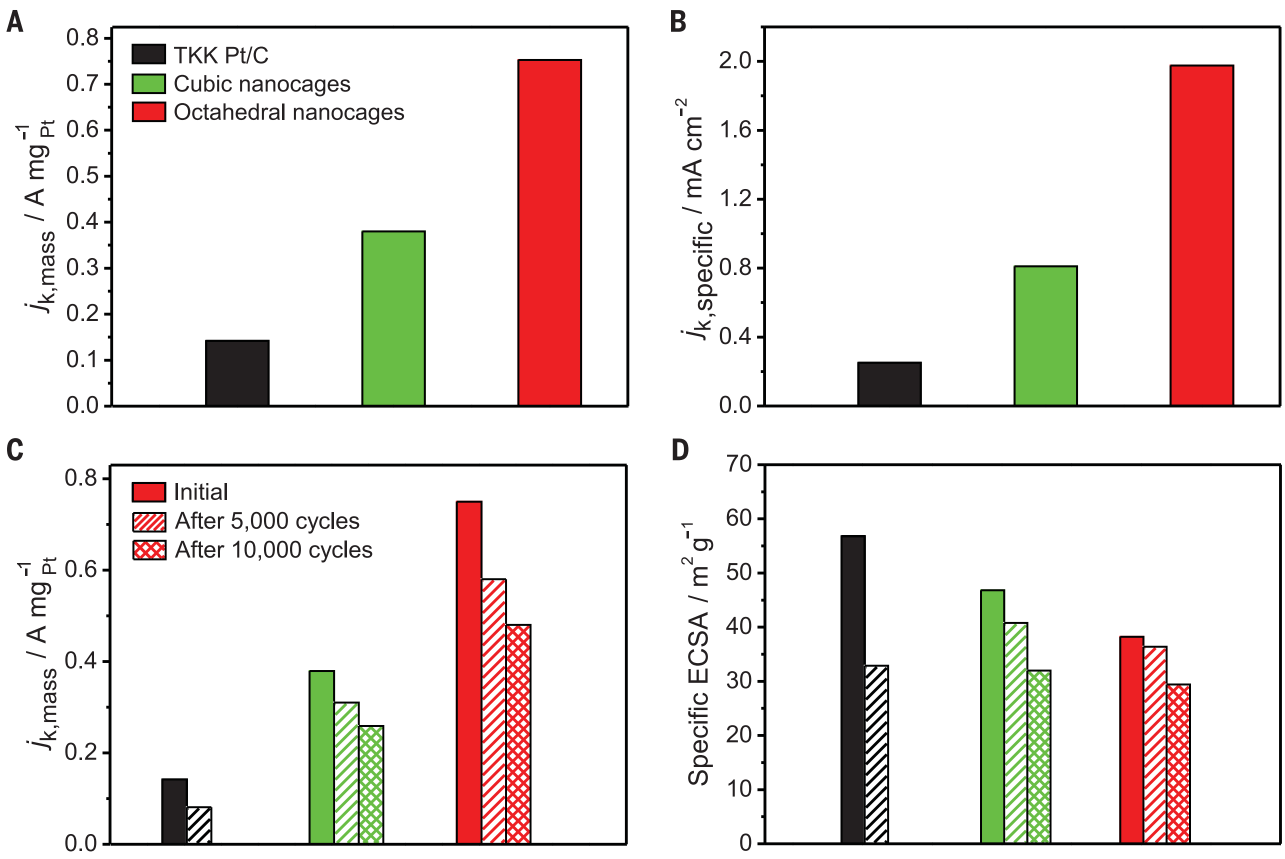

Fig. 4. Electrocatalytic properties of Pt nanocages relative to a commercial Pt/C catalyst. (**A**) Mass and (**B**) specific activities of the catalysts at 0.9 V_{RHE}. (**C**) Mass activities (at 0.9 V_{RHE}) and (**D**) specific ECSAs of the catalysts before and after accelerated durability test. The color scheme applies to all panels.

removal, which has been shown to be the rate-determining step on similar surfaces (*12–14*, *17*). Relative to their core-shell precursors, the nanocage models showed substantially enhanced activity, which is attributed to the shortening of Pt-Pt interatomic distances (table S2).

We evaluated the long-term stability of the catalysts through an accelerated durability test (Fig. 4, C and D). The Pt octahedral nanocages showed the best performance, with the ORR mass activity only reduced by 36% after 10,000 cycles, still showing 3.4-fold enhancement relative to the pristine Pt/C. The ECSAs of the cubic and octahedral nanocages only dropped by 13 and 6% after 5000 cycles and by 32 and 23% after 10,000 cycles, respectively. During the durability test, the holes in the walls of the nanocages were slightly enlarged (fig. S7). These results demonstrate that the excellent durability associated with the core-shell catalysts was not affected by the selective removal of Pd cores.

REFERENCES AND NOTES

1. J. Chen, B. Lim, E. P. Lee, Y. Xia, *Nano Today* **4**, 81–95 (2009).
2. F. A. de Bruijn, V. A. T. Dam, G. J. M. Janssen, *Fuel Cells (Weinh.)* **8**, 3–22 (2008).
3. X. Lu *et al*., *Nano Lett.* **7**, 1764–1769 (2007).
4. S. Xie *et al*., *Angew. Chem. Int. Ed. Engl.* **51**, 10266–10270 (2012).
5. C. Chen *et al*., *Science* **343**, 1339–1343 (2014).
6. A. Funatsu *et al*., *Chem. Commun. (Camb.)* **50**, 8503–8506 (2014).
7. H. Li *et al*., *Angew. Chem. Int. Ed. Engl.* **52**, 8368–8372 (2013).
8. H. Duan *et al*., *Nat. Commun.* **5**, 3093 (2014).
9. R. R. Adzic *et al*., *Top. Catal.* **46**, 249–262 (2007).
10. K. Sasaki *et al*., *Nat. Commun.* **3**, 1115 (2012).
11. M. Shao *et al*., *Chem. Commun. (Camb.)* **49**, 9030–9032 (2013).
12. S. Xie *et al*., *Nano Lett.* **14**, 3570–3576 (2014).
13. J. Park *et al*., *ACS Nano* **9**, 2635–2647 (2015).
14. X. Wang *et al*., *Nat. Commun.* **6**, 7594 (2015).
15. Y. Yin *et al*., *Science* **304**, 711–714 (2004).
16. M. Jin *et al*., *Nano Res.* **4**, 83–91 (2011).
17. Materials and methods are available as supplementary materials on *Science* Online.
18. X. Xia *et al*., *Proc. Natl. Acad. Sci. U.S.A.* **110**, 6669–6673 (2013).
19. M. Heggen, M. Oezaslan, L. Houben, P. Strasser, *J. Phys. Chem. C* **116**, 19073–19083 (2012).
20. J. Erlebacher, M. J. Aziz, A. Karma, N. Dimitrov, K. Sieradzki, *Nature* **410**, 450–453 (2001).
21. V. A. Baheti, R. Ravi, A. Paul, *J. Mater. Sci. Mater. Electron.* **24**, 2833–2838 (2013).
22. N. M. Markovic, P. N. Ross, *Surf. Sci. Rep.* **45**, 117–229 (2002).
23. J. Zhang, H. Yang, J. Fang, S. Zou, *Nano Lett.* **10**, 638–644 (2010).
24. J. Wu, A. Gross, H. Yang, *Nano Lett.* **11**, 798–802 (2011).
25. S.-I. Choi *et al*., *Nano Lett.* **13**, 3420–3425 (2013).
26. C. Cui, L. Gan, M. Heggen, S. Rudi, P. Strasser, *Nat. Mater.* **12**, 765–771 (2013).
27. L. Gan *et al*., *Science* **346**, 1502–1506 (2014).
28. B. Han *et al*., *Energy Environ. Sci.* **8**, 258–266 (2015).

ACKNOWLEDGMENTS

The syntheses were supported by start-up funds from the Georgia Institute of Technology (to Y.X.). As jointly supervised PhD students from Xiamen University, L.Z. and X.W. were also partially supported by fellowships from the China Scholarship Council. The theoretical modeling work at University of Wisconsin–Madison was supported by the U.S. Department of Energy (DOE)–Basic Energy Sciences (BES), Office of Chemical Sciences, grant DE-FG02-05ER15731. Calculations were performed at supercomputing centers located at the Environmental Molecular Sciences Laboratory, which is sponsored by the DOE Office of Biological and Environmental Research at the Pacific Northwest National Laboratory; Center for Nanoscale Materials at Argonne National Laboratory, supported by DOE contract DE-AC02-06CH11357; and National Energy Research Scientific Computing Center, supported by DOE contract DE-AC02-05CH11231. Part of the electron microscopy work was performed through a user project supported by the Oak Ridge National Laboratory's Center for Nanophase Materials Sciences, which is a DOE Office of Science User Facility. J.L. gratefully acknowledges the support by Arizona State University and the use of facilities in the John M. Cowley Center for High Resolution Electron Microscopy at Arizona State University. Data described can be found in the main figures and supplementary materials. The authors declare no conflict of interests.

SUPPLEMENTARY MATERIALS

www.sciencemag.org/content/349/6246/412/suppl/DC1
Materials and Methods
Figs. S1 to S8
Tables S1 to S3
References (*29–37*)

8 March 2015; accepted 15 June 2015
10.1126/science.aab0801

EVOLUTION

A four-legged snake from the Early Cretaceous of Gondwana

David M. Martill,[1] Helmut Tischlinger,[2] Nicholas R. Longrich[3]

Snakes are a remarkably diverse and successful group today, but their evolutionary origins are obscure. The discovery of snakes with two legs has shed light on the transition from lizards to snakes, but no snake has been described with four limbs, and the ecology of early snakes is poorly known. We describe a four-limbed snake from the Early Cretaceous (Aptian) Crato Formation of Brazil. The snake has a serpentiform body plan with an elongate trunk, short tail, and large ventral scales suggesting characteristic serpentine locomotion, yet retains small prehensile limbs. Skull and body proportions as well as reduced neural spines indicate fossorial adaptation, suggesting that snakes evolved from burrowing rather than marine ancestors. Hooked teeth, an intramandibular joint, a flexible spine capable of constricting prey, and the presence of vertebrate remains in the guts indicate that this species preyed on vertebrates and that snakes made the transition to carnivory early in their history. The structure of the limbs suggests that they were adapted for grasping, either to seize prey or as claspers during mating. Together with a diverse fauna of basal snakes from the Cretaceous of South America, Africa, and India, this snake suggests that crown Serpentes originated in Gondwana.

Snakes are among the most diverse groups of tetrapods, with >3000 extant species exploiting a remarkable range of niches (*1*). Snakes inhabit deserts and rainforests, mountains and oceans; and despite lacking limbs, employ an extraordinary range of locomotor styles, including crawling, burrowing, climbing, swimming, and even gliding (*1*). All snakes are predators, but they consume a wide range of prey, from insects to large mammals (*1*). This diversity is made possible by a specialized body plan, including an elongate body with reduced limbs, a flexible skull and ribs to swallow large prey (*2*), and a specialized forked tongue and vomeronasal organ to detect chemical gradients (*1*). The origins of this body plan remain unclear, however (*1*). One scenario holds that it originated in a marine environment, whereas others argue that it results from adaptation for a fossorial lifestyle. New fossils (*2–4*), including snakes with hindlimbs (*5*, *6*), have shed light on the lizard-to-snake transition, but no snake has been reported with four limbs. The ecology of early snakes is also uncertain. Although alethinophidians are primarily carnivorous (*1*), Typhlopidae and Anomalepididae, which are basal with respect to Alethinophidia (*7–9*), are insectivorous (*1*). This suggests that early snakes were insectivores, although adaptations for carnivory in stem snakes (*2*) suggest that carnivory may be primitive (*2*, *5*).

Here we report a fossil snake from the Early Cretaceous of Gondwana, which sheds light on these issues. *Tetrapodophis amplectus* gen. et sp. nov. (holotype BMMS BK 2-2) is distinguished from all other snakes by the following combination of characters: 160 precaudal and 112 caudal vertebrae, short neural spines, four limbs, metapodials short, penultimate phalanges hyperelongate and curved, phalangeal formula 2?-3-3-3-3? (manus) 2-3-3-3-3 (pes).

The fossil (Fig. 1) comes from the Nova Olinda Member of the Early Cretaceous (Aptian) Crato Formation, Ceará, Brazil (*10*). The specimen is preserved on laminated limestone as part and counterpart. The matrix is typical of the Nova Olinda Member in being composed of fine-grained laminated micrite with elongated pellets on the surface of the slab representing coprolites of the fish *Dastilbe*. As is typical of Crato vertebrates, the skeleton is articulated and the bones are a translucent orange-brown color; soft tissues are also preserved.

The snake affinities of *Tetrapodophis* are demonstrated by derived features of the skull, axial

[1]School of Earth and Environmental Sciences, University of Portsmouth, Portsmouth PO1 3QL, UK. [2]Tannenweg 16, 85134 Stammham, Germany. [3]Department of Biology and Biochemistry and Milner Centre for Evolution, University of Bath, Claverton Down, Bath BA2 7AY, UK.

skeleton, limbs, integument, and even behavior (Figs. 2 to 4) (* = snake autapomorphy). Snake-like features of the skull include a short rostrum, a long braincase, and a nasal descending lamina. The mandible is bowed, with a deep subdental ridge and an intramandibular joint formed by a concave splenial cotyle contacting the angular, as in *Dinilysia* (*11*). Teeth exhibit the ophidian condition, being unicuspid and hooked, with expanded bases. Implantation is subacrodont, with teeth separated by interdental ridges; replacement teeth are oriented subhorizontally.* Snake-like features of the axial skeleton include an elongate trunk with over 150 vertebrae,* zygosphene-zygantrum articulations, a vaulted neural arch with posterolateral tuberosities,* short neural spines, haemal keels, large subcentral fossae/foramina, tubercular processes of the ribs, and lymphapophyses. The ilium is long and slender as in other snakes; the fibula is bowed as in *Najash* (*5*) and Simoliophiidae (*12*). Transverse belly scales* are preserved, and the presence of a vertebrate in the gut suggests a snake-like feeding strategy in which proportionately large prey are ingested whole. Although many of these features occur in other long-bodied squamates, only snakes exhibit all of them, and many of these characters are uniquely ophidian.

Tetrapodophis exhibits a number of primitive characters, however. The nasal is L-shaped, as in *Dinilysia* (*11*) and Simoliophiidae. The maxilla's facial process is reduced as compared to those of lizards but tall relative to those of crown snakes, as in *Coniophis* (*2*). The subdental ridge is shallow posteriorly, a primitive feature shared with *Najash* (*5*) and *Coniophis* (*2*). Unlike crown snakes, in which a convex splenial condyle articulates with the angular, the splenial exhibits a concave cotyle, as in *Dinilysia* (*11*). Prezygapophyseal processes are absent as in other stem snakes; synapophyses are kidney-shaped, lacking the distinct condyle and planar cotyle of alethinophidians. Strikingly, *Tetrapodophis* retains reduced but apparently functional forelimbs and hindlimbs.

Fig. 1. *T. amplectus*, holotype part and counterpart. (**A**) Counterpart, showing skull and skeleton impression. (**B**) Main slab, showing skeleton and skull impression.

To test *Tetrapodophis*' ophidian affinities, we used a morphological matrix (*13*, *14*) to conduct four phylogenetic analyses: with and without molecular backbone constraint (*8*) and with equal and implied weighting (*15*). In each analysis, *Tetrapodophis* emerges as a basal snake (Fig. 5) but is closer to modern snakes than the putative Jurassic-Cretaceous stem ophidians *Parviraptor*, *Diablophis*, *Portugalophis*, and *Eophis*. When a molecular backbone is used (Fig. 5), *Tetrapodophis* emerges as sister to *Coniophis*, and snakes emerge as sister to the Mosasauria; i.e., Pythonomorpha, as in a recent combined analysis (*7*).

As the only known four-legged snake, *Tetrapodophis* sheds light on the evolution of snakes from lizards. *Tetrapodophis* lacks aquatic adaptations (such as pachyostosis or a long, laterally compressed tail) and instead exhibits features of fossorial snakes and lizards: a short rostrum and elongation of the postorbital skull, a long trunk and short tail (*16*, *17*), short neural spines (*18*), and highly reduced limbs (*16*, *17*). *Tetrapodophis* therefore supports the hypothesis that snakes evolved from burrowing (*2*, *5*, *6*) rather than marine (*19*) ancestors. Although the current analysis suggests a sister-group relationship between Mosasauria and Serpentes, Cretaceous aquatic snakes (Simoliophiidae) are recovered nested within crown Serpentes, and aquatic habits are therefore derived (*2*, *7*).

Tetrapodophis also sheds light on the evolution of snake feeding. *Tetrapodophis* exhibits adaptations for carnivory, including recurved claw-like teeth to seize large prey and an intramandibular joint allowing the gape to expand to swallow large prey. Along with the presence of a vertebrate in the gut, these feature show that *Tetrapodophis* preyed on vertebrates. Similar adaptations occur in other early snakes (*2*, *11*), suggesting that snakes made the transition to carnivory early in their history and that the insectivorous lifestyle of typhlopids and anomalolepidids is derived.

The structure of the spine may represent another such adaptation for carnivory. Elongate bodies and reduced limbs evolved many times among squamates (*13*, *17*), occurring in burrowing

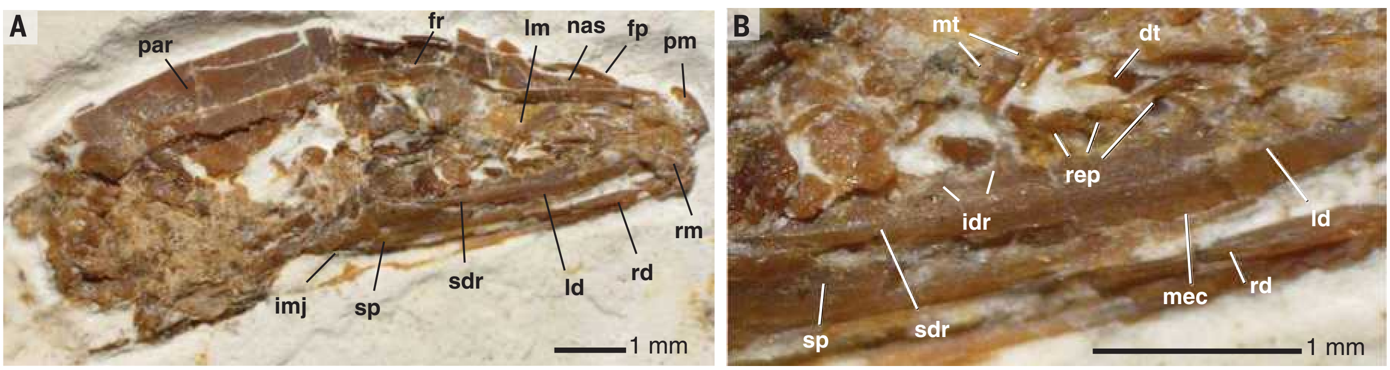

Fig. 2. *T. amplectus*, skull and jaws. (**A**) Skull. (**B**) Left mandible in medial view. Abbreviations: dt, dentary tooth; fp, facial process of maxilla, fr, frontal; idr, interdental ridges; imj, intramandibular joint lm, left maxilla, ld, left dentary; mt, maxillary teeth; nas, nasal, par, parietal; pm, premaxilla; rd, right dentary; rd, right dentary; rep, replacement teeth; sdr, subdental ridge; sp, splenial.

and terrestrial forms (*17*) as well as in aquatic mosasaurs. Yet snakes are unique among long-bodied squamates in having over 150 precaudal vertebrae. This permits extreme flexibility of the spinal column, so that the entire body can coil into tight loops. The fact that other long-bodied squamates lack this feature suggests that it is not related to locomotion. We propose that the increased number of trunk vertebrae may be an adaptation allowing the body to be used to constrict prey. *Tetrapodophis* exhibits both an increased number of precaudal vertebrae and a high degree of flexibility, with the body forming a tight coil anteriorly and a series of sinuous curves posteriorly, suggesting that constriction was developed even in the earliest snakes.

The structure of the limbs may represent another predatory adaptation. The snake-like spine and reduced limbs of *Tetrapodophis* suggest that the animal engaged in characteristic serpentine locomotion, with the limbs playing little or no role in locomotion. However, the specialized structure of the limbs suggests that they were functional. Given *Tetrapodophis*' presumed fossorial or semifossorial habits, digging is a plausible function, but the limbs lack fossorial specializations. Instead, the manus and pes exhibit slender isodactyl digits with hyperelongate penultimate phalanges and abbreviated proximal phalanges. This suite of characters recalls the prehensile feet of scansorial birds, sloths (*20*), and bats, suggesting a grasping or hooking function. The limbs may have functioned for grasping prey, or perhaps mates. Climbing is another possibility, although the low neural spines seem inconsistent with this function. Regardless, *Tetrapodophis* shows that after the initial evolution of serpentine locomotion, the limbs were repurposed for another function.

Finally, *Tetrapodophis* sheds light on the geographic origin of snakes. The Serpentes, Iguania, and Anguimorpha form the Toxicofera (*7*–*9*), with the oldest iguanian and anguimorph fossils coming from Laurasia (*13*). These patterns suggest that the center of toxicoferan diversification is Laurasia and that the ancestors of snakes probably originated there. The identification of possible stem ophidians from the Jurassic and Early Cretaceous of Laurasia (*4*) would support this hypothesis. However, the most basal divergences within crown Serpentes, including Anomalolepididae and Typhlopidae, Aniliidae and Tropidophiidae,

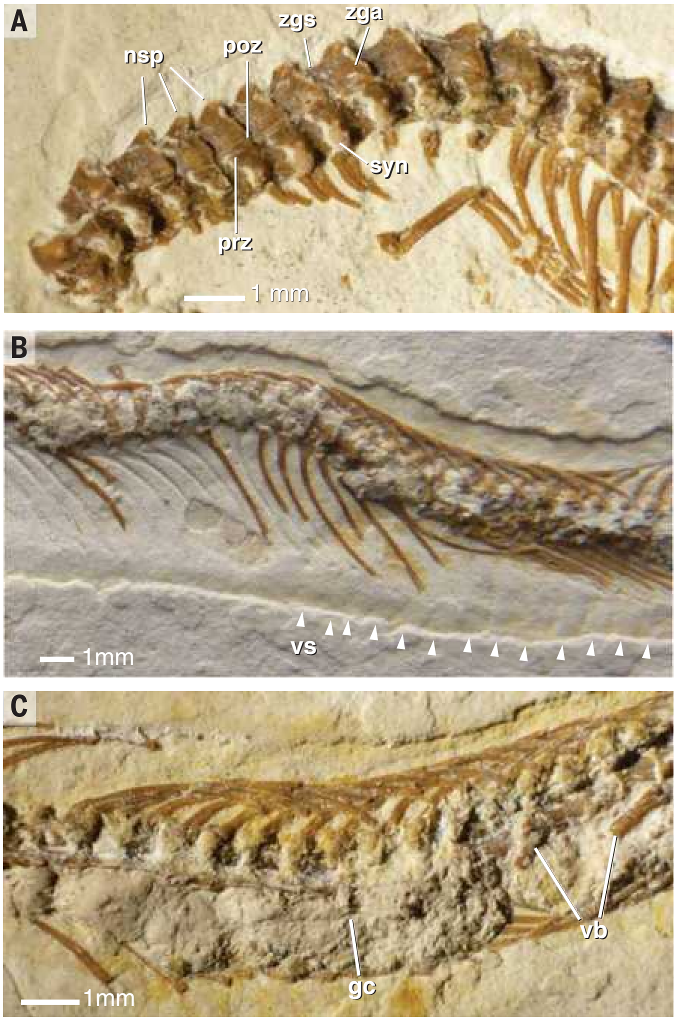

Fig. 3. *T. amplectus* axial column. (**A**) Cervicals and anterior presacrals. (**B**) Midthorax, showing ventral scales. (**C**) Posterior thorax, showing gut contents. Abbreviations: gc, gut contents; nsp, neural spines; poz, postzygapophysis; prz, prezygapophysis; syn, synapophyses vb, vertebrate bone; vs, ventral scales; zga, zygantrum; zgs, zygosphene.

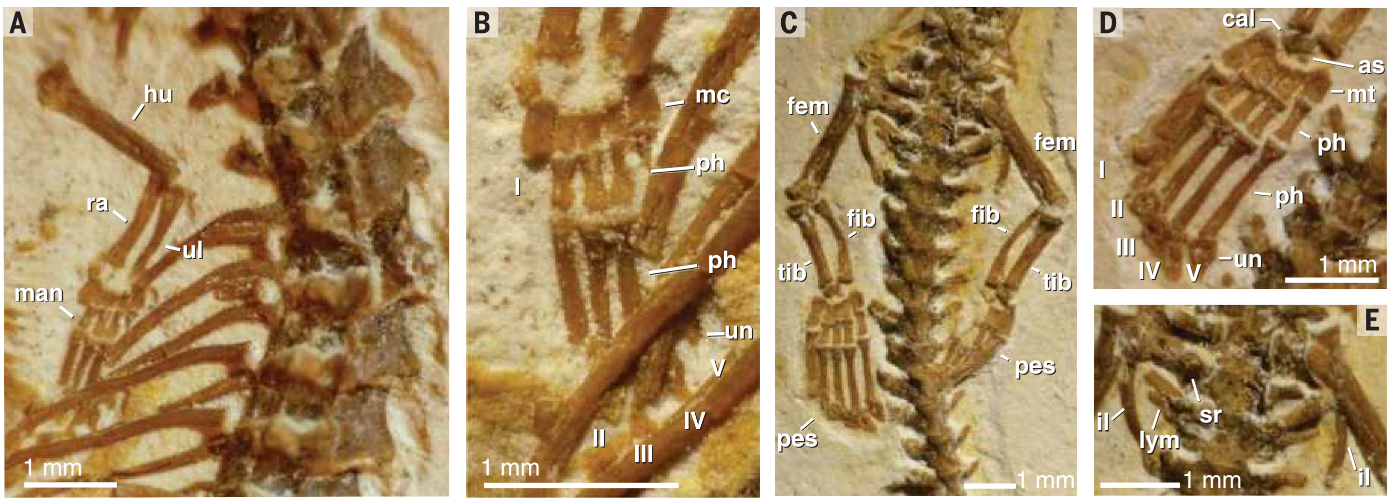

Fig. 4. *T. amplectus* appendicular morphology. (**A**) Forelimb. (**B**) Manus. (**C**) Hindlimbs and pelvis. (**D**) Pes. (**E**) Pelvis. Abbreviations: fem, femur; fib, fibula; hu, humerus; il, ilium; lym, lymphapophysis; man, manus; mc, metacarpal; mt, metatarsals; ph, phalanges; ra, radius; sr, sacral rib; tib, tibia; ul, ulna; un, ungual.

are endemic to or originate in South America and Africa, hinting at Gondwanan origins (*1*). Furthermore, during the middle Cretaceous, Gondwana was home to a diverse fauna of basal snakes, including Coniophiidae, Russellophiidae, Madtsoiidae (*21*), and Simoliophiidae (*22*) in the Cenomanian of Africa, the Cenomanian-Turonian *Najash* (*18*, *23*) in South America, and now *Tetrapodophis* from the Aptian of South America. Snakes are far less diverse in the Cretaceous of Laurasia, with a single lineage appearing in the Cenomanian (*24*) of North America; alethinophidians do not appear until the Maastrichtian in North America (*14*) and Europe (*25*). These patterns suggest that the Serpentes represent an endemic Gondwanan radiation that saw limited dispersal to Laurasia during the Cretaceous.

Snakes appear to have been part of a highly endemic herpetofauna that evolved in the Cretaceous in Gondwana. In this fauna, notosuchian crocodiles (*26*) and rhynchocephalians (*27*) played a major role, whereas squamates appear to have been less diverse and disparate than in Laurasia. The exception is the snakes, which radiated to produce small burrowers, large constrictors, and aquatic forms (*21*, *22*). Much of this herpetofauna appears to have become extinct during the Cretaceous-Paleogene extinction (Notosuchia) or was greatly reduced in diversity in the Cenozoic (Rhynchocephalia). Snakes, meanwhile, not only survived but became diverse and widespread in the Paleogene (*14*), perhaps in response to ecological release provided by the end-Cretaceous mass extinction (*14*).

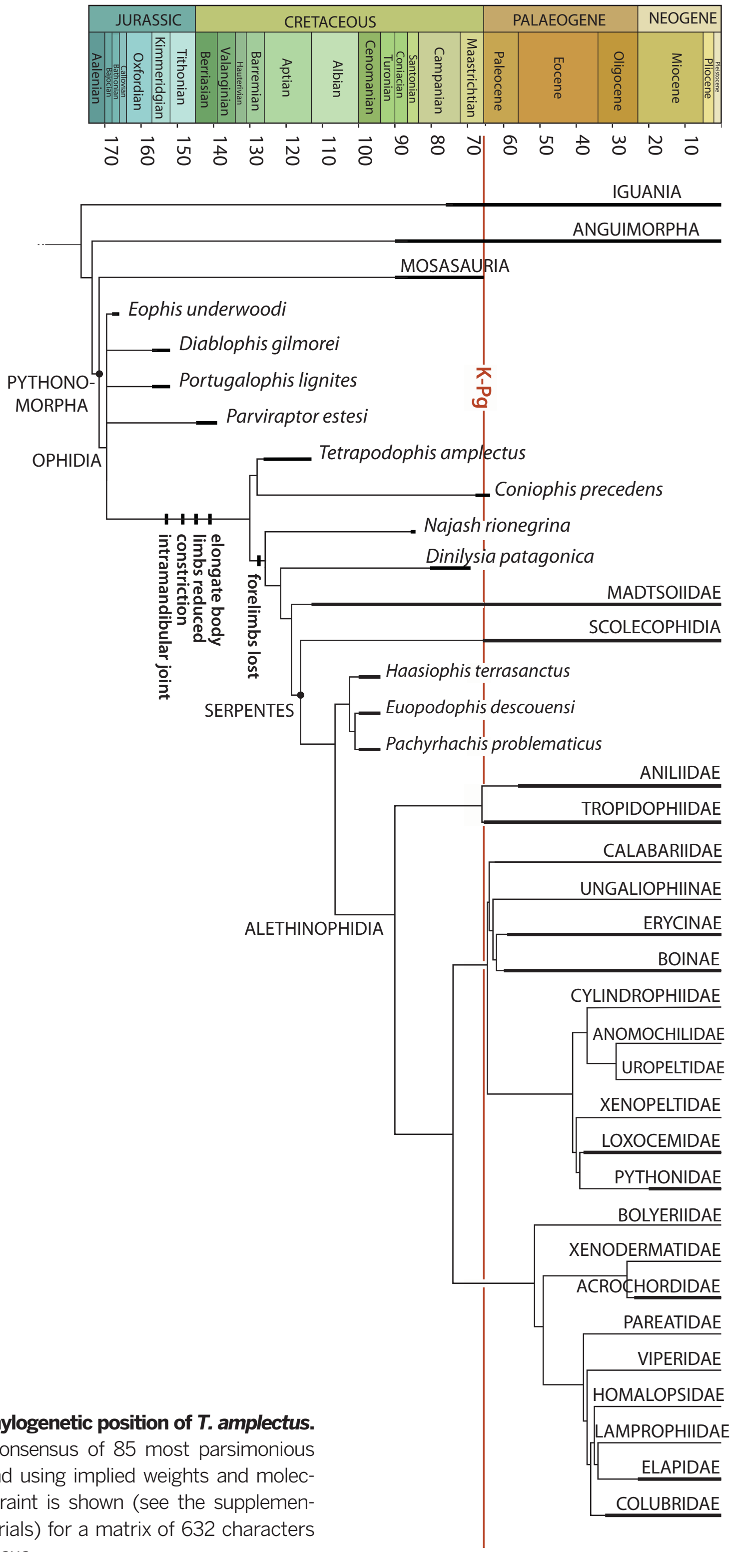

Fig. 5. Phylogenetic position of *T. amplectus*. A strict consensus of 85 most parsimonious trees found using implied weights and molecular constraint is shown (see the supplementary materials) for a matrix of 632 characters and 205 taxa.

REFERENCES AND NOTES

1. H. W. Greene, *Snakes: the Evolution of Mystery in Nature* (Univ. of California Press, Berkeley, 1997).
2. N. R. Longrich, B.-A. S. Bhullar, J. A. Gauthier, *Nature* **488**, 205–208 (2012).
3. J. D. Scanlon, M. S. Y. Lee, *Nature* **403**, 416–420 (2000).
4. M. W. Caldwell, R. L. Nydam, A. Palci, S. Apesteguía, *Nat. Commun.* **6**, 5996 (2015).
5. S. Apesteguía, H. Zaher, *Nature* **440**, 1037–1040 (2006).
6. E. Tchernov, O. Rieppel, H. Zaher, M. J. Polcyn, L. L. Jacobs, *Science* **287**, 2010–2012 (2000).
7. T. W. Reeder *et al*., *PLOS ONE* **10**, e0118199 (2015).
8. R. A. Pyron, F. T. Burbrink, J. J. Wiens, *BMC Evol. Biol.* **13**, 93 (2013).
9. J. J. Wiens *et al*., *Biol. Lett.* **8**, 1043–1046 (2012).
10. U. Heimhofer, D. M. Martill, in *The Crato Fossil Beds of Brazil*, D. M. Martill, G. Bechly, R. F. Loveridge, Eds. (Cambridge Univ. Press, Cambridge, 2007), pp. 44–62.
11. H. Zaher, C. A. Scanferla, *Zool. J. Linn. Soc.* **164**, 194–238 (2012).
12. M. S. Lee, M. W. Caldwell, *Philos. Trans. R. Soc. London Ser. B* **353**, 1521–1552 (1998).
13. J. Gauthier, M. Kearney, J. A. Maisano, O. Rieppel, A. Behlke, *Bull. Yale Peabody Mus.* **53**, 3–308 (2012).
14. N. R. Longrich, B. A. Bhullar, J. A. Gauthier, *Proc. Natl. Acad. Sci. U.S.A.* **109**, 21396–21401 (2012).
15. P. A. Goloboff, J. M. Carpenter, J. S. Arias, D. R. M. Esquivel, *Cladistics* **24**, 758–773 (2008).
16. J. J. Wiens, J. L. Slingluff, *Evolution* **55**, 2303–2318 (2001).
17. J. J. Wiens, M. C. Brandley, T. W. Reeder, *Evolution* **60**, 123–141 (2006).
18. H. Zaher, S. Apesteguía, C. A. Scanferla, *Zool. J. Linn. Soc.* **156**, 801–826 (2009).
19. M. W. Caldwell, M. S. Y. Lee, *Nature* **386**, 705–709 (1997).
20. M. Hildebrand, G. Goslow, *Analysis of Vertebrate Structure* (Wiley, New York, 2001).
21. J.-C. Rage, C. Werner, *Palaeontol. Africana* **35**, 85–110 (1999).
22. J.-C. Rage, D. B. Dutheil, *Palaeontographica Abteilung A*, 1–22 (2008).
23. J.-C. Rage, A. M. Albino, *Neues Jahrb. Geol. Palaontol. Monatsh.* **1989**, 433–447 (1989).
24. J. D. Gardner, R. L. Cifelli, *Spec. Pap. Palaeontol.* **60**, 87–100 (1999).
25. J.-C. Rage, *C. R.'Acad.Sc. Sér. 2 Sci.Terre Planètes* **322**, 603–608 (1996).
26. P. M. O'Connor *et al*., *Nature* **466**, 748–751 (2010).

ACKNOWLEDGMENTS

Thanks to B. A. S. Bhullar, J. A. Gauthier, and J. C. Rage for discussions and to the anonymous reviewers whose comments improved this paper. The holotype (BMMS BK 2-2) is housed at the Bürgermeister-Müller-Museum, Solnhofen, Germany.

SUPPLEMENTARY MATERIALS

www.sciencemag.org/content/349/6246/416/suppl/DC1
Supplementary Text
Figs. S1 to S7
Table S1
References (*27*–*44*)
Character-Taxon Matrix
Constraint Tree

23 February 2015; accepted 16 June 2015
10.1126/science.aaa9208

DEEP BIOSPHERE

Exploring deep microbial life in coal-bearing sediment down to ~2.5 km below the ocean floor

F. Inagaki,[1,2]* K.-U. Hinrichs,[3]* Y. Kubo,[4,5] M. W. Bowles,[3] V. B. Heuer,[3] W.-L. Hong,[6]† T. Hoshino,[1,2] A. Ijiri,[1,2] H. Imachi,[2,7] M. Ito,[1,2] M. Kaneko,[2,8] M. A. Lever,[9]‡ Y.-S. Lin,[3]§ B. A. Methé,[10] S. Morita,[11] Y. Morono,[1,2] W. Tanikawa,[1,2] M. Bihan,[10] S. A. Bowden,[12] M. Elvert,[3] C. Glombitza,[9] D. Gross,[13] G. J. Harrington,[14] T. Hori,[15] K. Li,[10] D. Limmer,[12]|| C.-H. Liu,[16] M. Murayama,[17] N. Ohkouchi,[2,8] S. Ono,[18] Y.-S. Park,[19]¶ S. C. Phillips,[20] X. Prieto-Mollar,[3] M. Purkey,[21]# N. Riedinger,[22]** Y. Sanada,[4,5] J. Sauvage,[23] G. Snyder,[24]†† R. Susilawati,[25] Y. Takano,[2,8] E. Tasumi,[7] T. Terada,[26] H. Tomaru,[27] E. Trembath-Reichert,[28] D. T. Wang,[18] Y. Yamada[5,29]

Microbial life inhabits deeply buried marine sediments, but the extent of this vast ecosystem remains poorly constrained. Here we provide evidence for the existence of microbial communities in ~40° to 60°C sediment associated with lignite coal beds at ~1.5 to 2.5 km below the seafloor in the Pacific Ocean off Japan. Microbial methanogenesis was indicated by the isotopic compositions of methane and carbon dioxide, biomarkers, cultivation data, and gas compositions. Concentrations of indigenous microbial cells below 1.5 km ranged from <10 to ~10^4 cells cm^{-3}. Peak concentrations occurred in lignite layers, where communities differed markedly from shallower subseafloor communities and instead resembled organotrophic communities in forest soils. This suggests that terrigenous sediments retain indigenous community members tens of millions of years after burial in the seabed.

Microbial life has been found in marine sediments as deep as 1922 m below the seafloor (mbsf) (*1*), with cell numbers decreasing logarithmically as burial depth increases (*2*). However, the extent of the deep subseafloor biosphere and the factors limiting or stimulating life at its lower boundaries remain largely unknown, partly because of the technological challenges associated with obtaining pristine scientific samples from great depths. The deepest microbial signatures measured thus far come from the biodegradation of heavy oils in fossil fuel reservoirs down to subsurface depths of ~4 km (*3*, *4*).

We studied the microbial communities associated with deep subseafloor coal beds, which are widespread along the Western Pacific continental margins (*5*). During Integrated Ocean Drilling Program (IODP) Expedition 337 in 2012, we drilled and recovered sediments down to 2466 mbsf using the riser-drilling vessel *Chikyu* at Site C0020, located along the northwestern Pacific margin (41°10.5983′N, 142°12.0328′E, 1180 m water depth) (fig. S1) (*6*). The top 365 mbsf of the borehole had been drilled in 2006 during the *Chikyu* cruise CK06-06 (*6*, *7*). The site is located in the forearc basin offshore from the Shimokita Peninsula, Japan, where terrigenous sediments rich in organic matter were deposited in coastal environments during the late Paleogene to early Neogene periods, before the depositional environment became marine in the course of subsidence (*5*). The series of buried lignite coal beds at depths of ~1.5 to 2.5 km are 0.3 to 7.3 m thick (*6*). Because of the relatively low geothermal temperature gradient of 24°C km^{-1} (*6*), the deepest horizons, with in situ temperatures of <60°C, are well within the thermal limits of microbial life.

We detected intact microbial cells throughout the entire drilled sediment column, down to the deepest sample at 2458 mbsf. Cell concentrations decreased with depth but in an unexpected fashion. In the "shallow" subseafloor (above 365 mbsf), concentrations decreased steadily from ~10^9 to ~10^7 cells cm^{-3} (*8*) and exceeded predictions based on the global regression line from previous surveys of cell concentrations at ocean margins (*2*) (Fig. 1A and table S1). In contrast, raw cellular concentrations were substantially lower in the "deep" subseafloor (below ~1.5 km), ranging from ~10^2 to 10^3 cells cm^{-3}, but they exceeded this range in coal-bearing horizons and adjacent sediment layers (Fig. 1A).

The low cell concentrations required the implementation of rigorous contamination tests to characterize indigenous microbial communities in the deep coal-bed biosphere. To minimize and quantify contamination potentially introduced during drilling, we (i) investigated whole round core sections by x-ray computed tomography before selecting sediment samples, (ii) took microbiological samples only from the center part of undisturbed core intervals, and (iii) quantified the intrusion of drill fluids into the cores by perfluorocarbon tracer assays (*6*, *7*). As additional validation, we sequenced the V1 to V3 region of 16*S* ribosomal RNA genes in all sediment samples (*7*) obtained by riser drilling. We compared these to control samples consisting of drill mud and lab experimental blanks to differentiate indigenous microbial communities from contaminant cells (fig. S2) (*7*). We applied a probabilistic approach, incorporating taxon variability across samples to identify the likelihood that each taxon would be consistently sampled, either exclusively from the control or sediment sample sets or from both sample sets (*7*). In this way, we identified likely indigenous taxa, which were either (i) exclusive to sediment samples ("most conservative") (figs. S2 to S4 and table S1) or (ii) consistently found in sediment samples in significant abundance and only occasionally found in

[1]Kochi Institute for Core Sample Research, Japan Agency for Marine-Earth Science and Technology (JAMSTEC), Nankoku, Kochi 783-8502, Japan. [2]Research and Development Center for Marine Resources, JAMSTEC, Yokosuka 237-0061, Japan. [3]MARUM Center for Marine Environmental Sciences, University of Bremen, D-28359 Bremen, Germany. [4]Center for Deep-Earth Exploration, JAMSTEC, Yokohama 236-0061, Japan. [5]Research and Development Center for Ocean Drilling Science, JAMSTEC, Yokohama 236-0001, Japan. [6]College of Earth, Ocean, and Atmospheric Sciences, Oregon State University, Corvallis, OR 97331, USA. [7]Department of Subsurface Geobiological Analysis and Research, JAMSTEC, Yokosuka 237-0061, Japan. [8]Department of Biogeochemistry, JAMSTEC, Yokosuka 237-0061, Japan. [9]Center for Geomicrobiology, Department of Bioscience, Aarhus University, DK-8000 Aarhus C, Denmark. [10]Department of Environmental Genomics, J. Craig Venter Institute, Rockville, MD 20850, USA. [11]Geological Survey of Japan, National Institute of Advanced Industrial Science and Technology (AIST), Tsukuba, Ibaraki 305-8567, Japan. [12]Department of Geology and Petroleum Geology, School of Geosciences, University of Aberdeen, Aberdeen AB2A 3UE, UK. [13]Department of Applied Geosciences and Geophysics, Montanuniversität, 8700 Leoben, Austria. [14]School of Geography, Earth and Environmental Sciences, University of Birmingham, Birmingham B15 2TT, UK. [15]Environmental Management Research Institute, AIST, Tsukuba, Ibaraki 305-8569, Japan. [16]The State Key Laboratory of Pharmaceutical Biotechnology, School of Life Science, Nanjing University, Nanjing, Jiangsu 210093, China. [17]Center for Advanced Marine Core Research, Kochi University, Nankoku, Kochi 783-8502, Japan. [18]Department of Earth, Atmospheric and Planetary Sciences, Massachusetts Institute of Technology, Cambridge, MA 02139, USA. [19]Petroleum and Marine Resources Research Division, Korea Institute of Geoscience and Mineral Resources, Yuseong-gu, Daejeon 305-350, Korea. [20]Department of Earth Sciences, University of New Hampshire, Durham, NH 03824, USA. [21]Department of Earth and Atmospheric Sciences, University of Nebraska–Lincoln, Lincoln, NE 68588, USA. [22]Department of Earth Sciences, University of California Riverside, Riverside, CA 92521, USA. [23]Graduate School of Oceanography, University of Rhode Island, Narragansett, RI 02882, USA. [24]Department of Earth Science, Rice University, Houston, TX 77005, USA. [25]School of Earth Science, University of Queensland, Brisbane Queensland 4072, Australia. [26]Marine Works Japan, Yokosuka 237-0063, Japan. [27]Department of Earth Sciences, Graduate School of Science, Chiba University, Chiba 263-8522, Japan. [28]Geological and Planetary Sciences, California Institute of Technology, Pasadena, CA 91125, USA. [29]Department of Urban Management, Graduate School of Engineering, Kyoto University, Kyoto 615-8540, Japan.
***Corresponding author. E-mail: inagaki@jamstec.go.jp (F.I.); khinrichs@uni-bremen.de (K.-U.H.)** †Present address: CAGE - Centre for Arctic Gas Hydrate, Environment and Climate, Department of Geology, UiT The Arctic University of Norway, N-9037 Tromsø, Norway. ‡Present address: Department of Environmental Systems Science, ETH Zurich, 8092 Zurich, Switzerland. §Present address: Department of Oceanography, National Sun Yat-Sen University, Kaohsiung 80424, Taiwan. ||Present address: Adrok, Edinburgh, Scotland EH6 5NX, UK. ¶Deceased. #Present address: Noble Energy, 1625 Broadway, Suite 2200, Denver, CO 80202, USA. **Present address: Boone Pickens School of Geology, 105 Noble Research Center, Oklahoma State University, Stillwater, OK 74078-3031, USA. ††Present address: Gas Hydrate Research Laboratory, Meiji University, Tokyo 101-8301, Japan.

contamination controls in low abundance ("most likely") (figs. S5 and S6 and table S1). From this approach, we derived correction factors (table S1) to the raw cell concentrations to estimate the corresponding population sizes. We used the results of taxonomy-based sequence filtration and the probability-based relationship analysis for 16*S* sequences to estimate the "most conservative" and "most likely" indigenous cell concentrations, respectively (Fig. 1A, figs. S5 to S7, and table S1) (*7*). These estimated cell concentrations are much lower than predicted by the slope of the global regression line (fig. S7) (*2*) and are even lower than previously reported values from the most oligotrophic subseafloor setting on Earth, the South Pacific Gyre (*9*).

Despite the very low cell numbers, geochemical data indicated microbial activity even in the deepest horizons sampled. Carbon isotopic compositions of methane ($\delta^{13}C\text{-}CH_4$) and ratios of methane over ethane (C_1/C_2) (Fig. 1, B and C), both continuously monitored in circulating mud gas during riser drilling (*6*), point to microbial methanogenesis as the predominant source of methane (*10*) throughout the entire drilled sequence. Positive inflections of C_1/C_2 ratios between 1700 and 2000 mbsf suggest that biological methanogenesis is stimulated in coal-bearing horizons (Fig. 1C), where contamination-corrected cell concentrations reached ~10^2 to 10^4 cells cm^{-3} (Fig. 1A), as well as in the overlying 200 m of sediment. Hydrogen isotopic compositions of methane ($\delta D\text{-}CH_4$) ranged from –200 to –150 per mil (‰) (Fig. 1B), consistent with its production by hydrogenotrophic carbon dioxide (CO_2) reduction (*10*). Locally increased $\delta^{13}C\text{-}CO_2$ values in coal-bearing horizons provide further evidence that the CO_2 pool was isotopically fractionated by microbial methanogenesis (Fig. 1C). Moreover, in situ production of methane is indicated by the abundance of $^{13}CH_3D$ (a rare "clumped" isotopologue of methane with two heavy isotopes) in formation fluids sampled in two discrete coal-bed horizons (Fig. 1B and table S2) (*6*, *7*). These analyses returned low $\Delta^{13}CH_3D$-based temperatures of 70^{+9}_{-9}°C and 70^{+24}_{-21}°C (table S2), providing evidence against major contributions of more deeply sourced thermogenic methane, which would be expected to carry clumped-isotope temperatures >150°C (*11*). In addition, we detected coenzyme F_{430} in core samples, providing biomarker evidence for methanogenesis in coal beds ~2 km below the seafloor (Fig. 2A and table S3) (*12*, *13*). Coenzyme F_{430} is a key prosthetic group of methyl-coenzyme M reductase that catalyzes the last step of methanogenesis. Its concentrations in deep sediments were about two orders of magnitude lower than in shallow sediments (table S3), suggesting the presence of a small but persistent community of methanogens in deep coal-bearing layers.

In a continuous-flow bioreactor (*14*) at near in situ temperature (40°C), we enriched methanogenic communities from ~2-km-deep coal-bed samples amended with powdered coal as the major energy source (*7*) (Fig. 2, B to G). Analysis of methyl-coenzyme M reductase gene (*mcrA*) sequences in this enrichment culture indicated the growth of hydrogenotrophic methanogens closely related to *Methanobacterium subterraneum* and *M. formicicum* (fig. S8). These species have previously been detected in terrestrial coal beds (*15*)

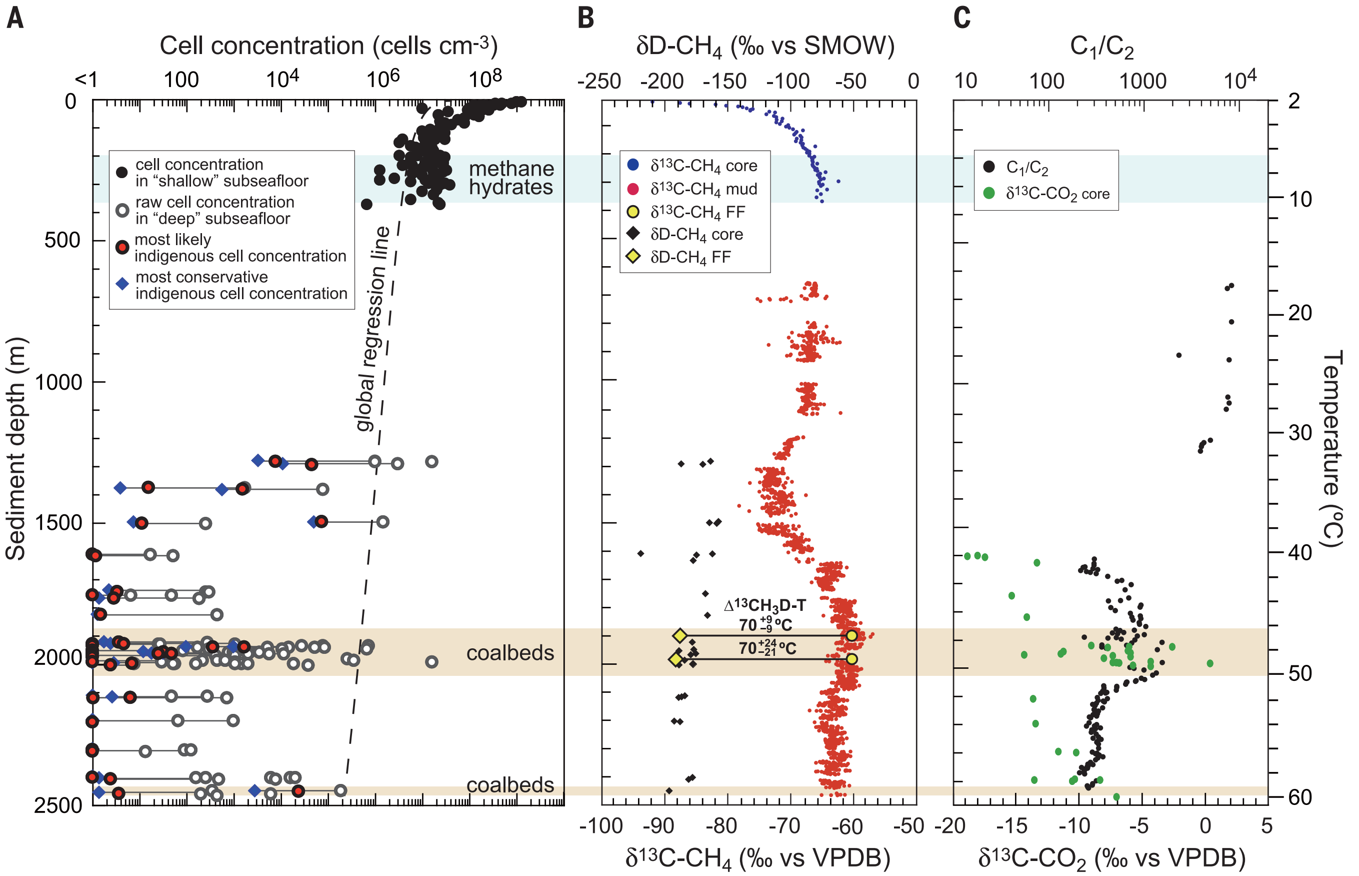

Fig. 1. Depth profiles of microbial cell counts and geochemical data at Site C0020. (**A**) Microbial cell concentrations, (**B**) $\delta^{13}C$ and δD of methane, and (**C**) C_1/C_2 ratios and $\delta^{13}C$ of CO_2. (A) For cell concentrations in the deep subseafloor, raw data of fluorescence image-based cell counts (*8*), the most likely indigenous cell concentrations based on the probability-relationship set analysis (*7*), and the most conservative indigenous cell concentrations estimated based on the taxonomic classification (*7*) are shown (figs. S6 and S7 and table S1). The correction factor is the proportion of sequences estimated to be indigenous (table S1). The minimal quantification limit for raw cell counts was 1.43×10^2 cells cm^{-3} (i.e., the upper 95% confidence interval of the negative background). All $\delta^{13}C$ and δD in (B) and (C) are in per mil versus the Vienna Pee Dee Belemnite (VPDB) and Standard Mean Ocean Water (SMOW) standards, respectively. The $\Delta^{13}CH_3D$-T values in (B) designate the apparent equilibrium temperatures derived from measurements of $^{13}CH_3D$, a clumped isotopologue of methane (table S2) in discrete formation fluid (FF) samples (*6*, *7*). Temperature is based on the temperature gradient of 24°C km^{-1} determined by downhole logging (*6*).

and in shallower, methane hydrate–bearing sediments at Site C0020 (*14*). Using nanoscale secondary ion mass spectrometry (NanoSIMS) (*7*, *16*), we detected the incorporation of ^{13}C-labeled bicarbonate into cellular biomass (Fig. 2, E to G). Collectively, these microbiological and geochemical findings indicate that microbial communities are stimulated within coal-bed environments and that hydrogenotrophic methanogens act as terminal remineralizers.

Despite these multiple lines of evidence for the activity of methanogenic archaea, we could only amplify one archaeal 16*S* sequence related to *Methanosarcina barkeri* (from a ~2-km-deep coal sample) and one *mcrA* sequence related to *Methanococcus maripaludis* (from ~1-km-deep cuttings samples) (fig. S8) (*7*). Archaeal 16*S* genes were neither quantifiable by digital polymerase chain reaction (dPCR) (*17*) nor stably amplifiable using multiple primer sets, indicating that this deep subseafloor microbial ecosystem harbors substantially lower proportions of archaea than shallower sediments at this and other ocean margin sites (*18*). The difficulty in detecting methanogenic archaea using multiple molecular assays is not unexpected, given their generally low relative abundance of <1%, even in methane-laden subseafloor sediments (*19*).

The taxonomic distribution based on 16*S* sequences of the most conservative indigenous community members showed a marked difference between bacterial communities in deeper layers (1279.1 to 2458.8 mbsf) and those in shallower layers (9.5 to 364.0 mbsf) (Fig. 3, figs. S3 and S4, and table S4). For example, in deeper layers, sequences affiliated with the phyla Chloroflexi or

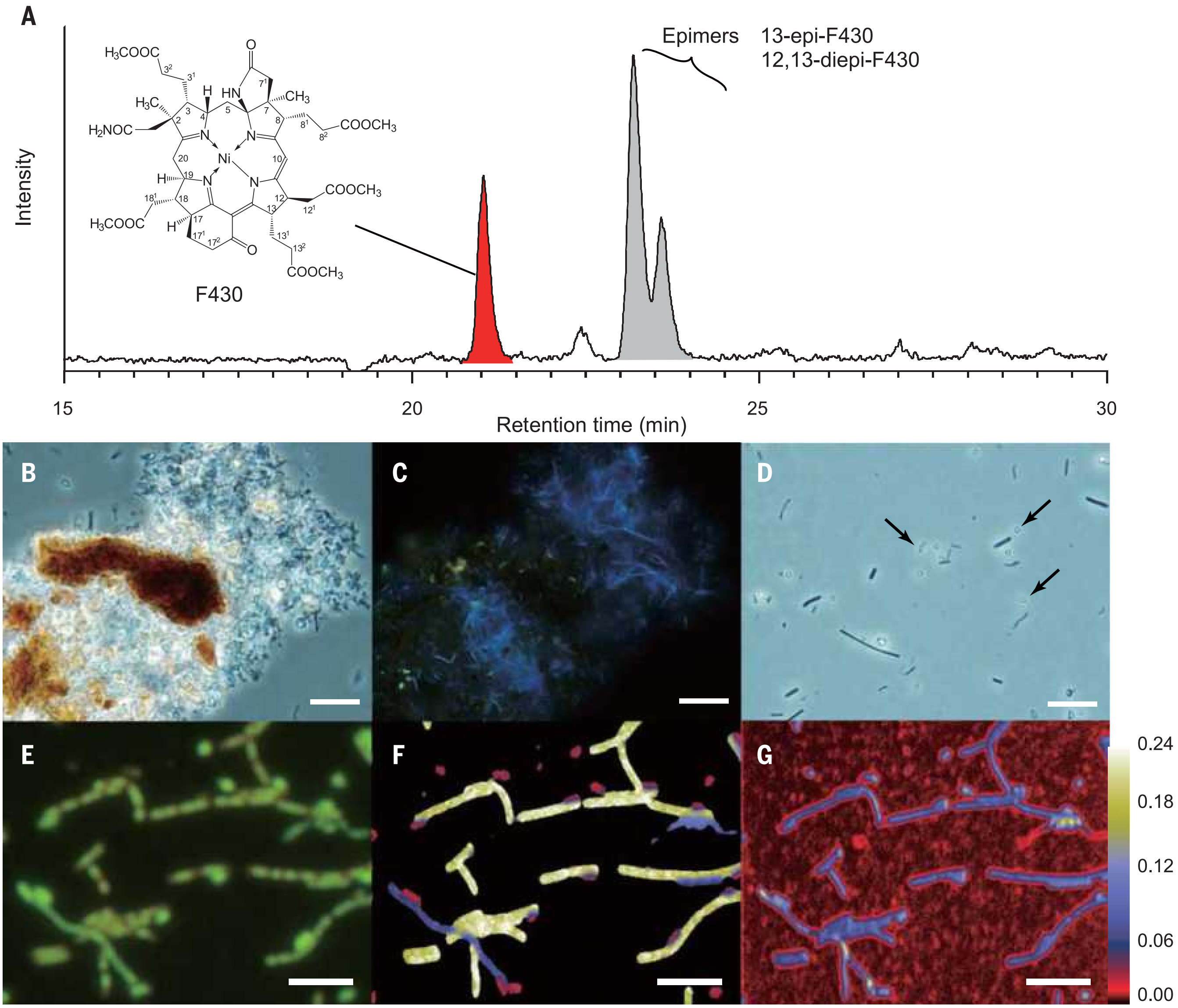

Fig. 2. Geochemical and microbiological indications for methanogenic microbial communities in ~2-km-deep subseafloor coal beds at Site C0020. (**A**) A representative chromatogram of the diagnostic methanogen biomarker F_{430} (as methyl ester) and its epimers from a coal sample (core 18R-2, 1946 mbsf) (table S3). (**B**) to (**D**) Photomicrographs of microbial cells in an enrichment culture from ~2-km-deep coal-bed samples using a continuous-flow bioreactor with powdered coal as the major energy source (*7*). (B) Phase-contrast micrograph of microbial cells attached to mineral particles. (C) Fluorescent micrograph of the same field shown in (B) showing the growth of methanogens that produce autofluorescence derived from coenzyme F_{420}. (D) Phase-contrast micrograph showing spherical spore-like particles, indicated by arrows. (**E**) to (**G**) NanoSIMS analysis of cells in the reactor enrichment culture incubated with ^{13}C-labeled bicarbonate (*7*). (E) Fluorescent micrograph of SYBR Green I–stained cells. (F) and (G) NanoSIMS ion images of $^{13}C/^{12}C$ (F) and ^{12}C (G). The color gradient indicates the relative abundance of ^{13}C expressed as $^{13}C/^{12}C$. The length of the bars is 10 μm.

"Atribacteria" [candidate division JS1 (20, 21)], which are both globally abundant groups in subseafloor sediments at ocean margins (22, 23), were detected in lower proportions than in shallower layers (Fig. 3A, fig. S3, and table S4). The indigenous sequence assemblage in deeper layers was dominated instead by bacterial groups known to dominate a wide range of terrestrial soil environments (Actinobacteria, Proteobacteria, Firmicutes, Bacteroidetes, and Acidobacteria) (24). In fact, many operational taxonomic units (OTUs) from deeper layers showed high sequence similarity to those from forest soils (figs. S3 and S4). Deeper layers also included microbial phyla that were not or were only barely detectable in shallower layers (such as Gemmatimonadetes and Synergistetes) (fig. S9) (7). Clustering and Bray-Curtis dissimilarity analyses (Fig. 3B and fig. S10), as well as multidimensional scaling and permutational analysis of variance based on genus-level classification (fig. S11), further support the notion that deep communities in coal-associated sedimentary environments on the former forearc basin off Shimokita differ compositionally from those found in shallow diatom-rich marine sediments.

Our combined microbiological and geochemical data set provides an opportunity to examine the potential energy sources of life at depths greater than ~1.5 km below the seafloor. The concentration of dissolved hydrogen (H_2), a key intermediate in the anaerobic degradation of organic matter, is an important gauge of the bioenergetic status of anaerobic microbial ecosystems (25, 26). At Site C0020, high H_2 concentrations of ~1 to ~500 μM in sediments below 1.5 km (fig. S12 and table S5) resulted in Gibbs free energy yields of hydrogenotrophic methanogenesis that were much more negative than those previously documented from energy-rich surface environments (fig. S13 and tables S6 and S7) (25). These high H_2 concentrations suggest very low H_2 turnover rates, possibly due to low concentrations of microorganisms with low viabilities and consequently low cell-specific energy turnover. Under these circumstances, the coupling between substrate production and substrate uptake may be severely delayed, resulting in long residence times and the accumulation of H_2 to high concentrations in sediment porewater. These substrates are probably generated from lignite (15), microbial necromass (27), and/or adsorbed organic matter. In addition to enzymatic hydrolysis, chemical degradation of recalcitrant organic matter (28, 29) in situ and in deeper, warmer strata bearing Cretaceous coal beds (30) may supply monomeric substrates and contribute to the accumulation of H_2. Despite the high H_2 concentrations, a range of organotrophic reactions involving the breakdown of lignin phenols, cellular building blocks, and anaerobic degradation intermediates are likely to be thermodynamically favorable and thus could explain the presence of alive and active microbial populations (fig. S13).

In addition to energy availability from organotrophic and hydrogenotrophic reactions, an important factor controlling the viability and size of microbial communities buried deeper than 1.5 km could be the increase in energy expended on the repair of biomolecules as a function of depth. The rates of abiotic amino acid racemization and DNA depurination increase exponentially with temperature (31), and substantial increases in their modeled rates coincided with a dramatic drop in cell numbers at Site C0020 (fig. S14). The relatively increased energetic cost of biomolecule repair

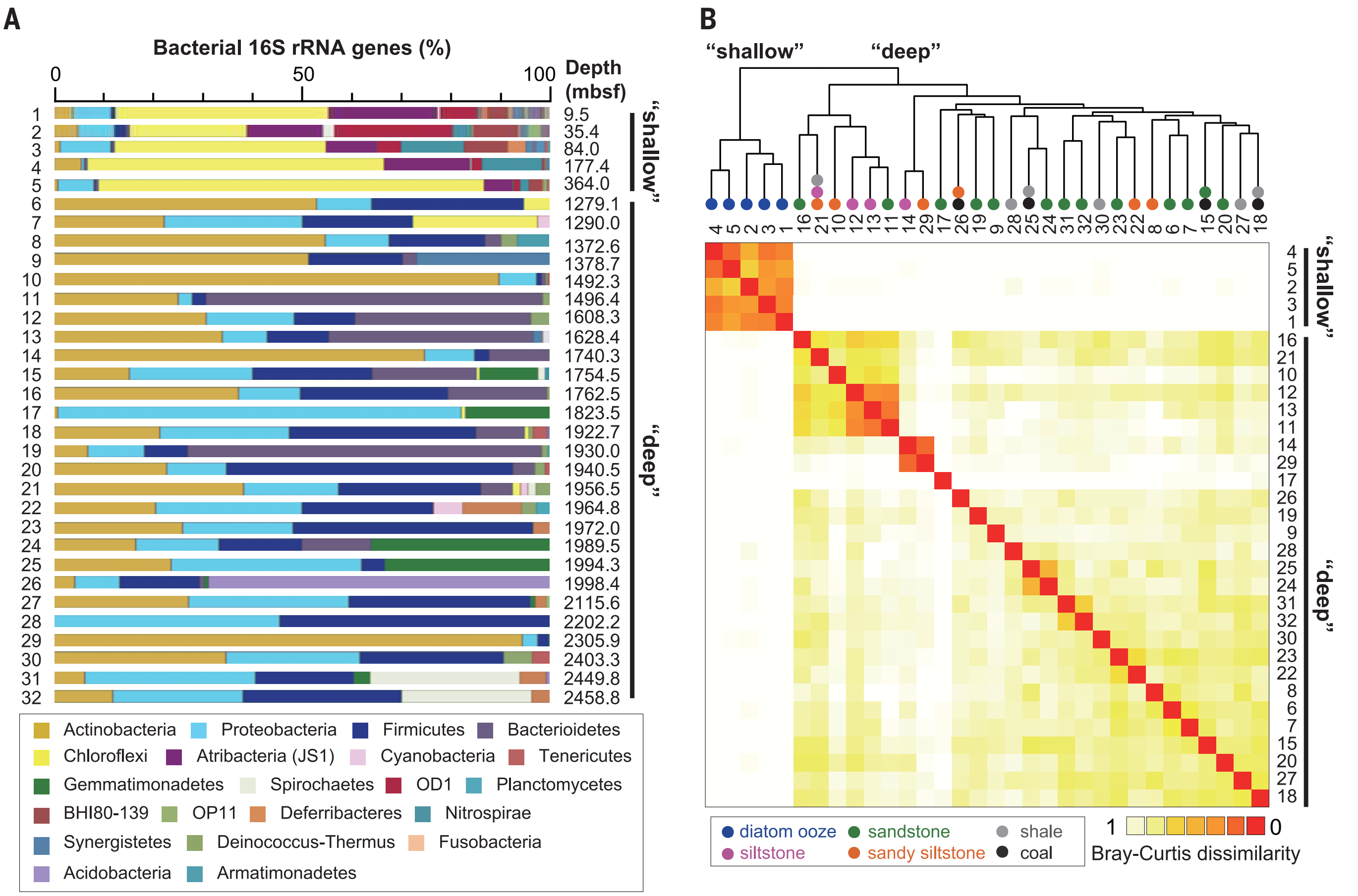

Fig. 3. Taxonomic distribution of the most conservative indigenous bacterial communities in sediments at Site C0020. (**A**) Phylum-level taxonomic composition of bacterial 16*S* gene-tagged sequences (i.e., V1–V3 region) in shallow (sample numbers 1 to 5, 9.5 to 364 mbsf, from *Chikyu* cruise CK06-06) and deep (sample numbers 6 to 32, 1279.1 to 2458.8 mbsf, from IODP Expedition 337) subseafloor sediment samples (7). (**B**) Cluster and Bray-Curtis dissimilarity analyses of bacterial community structure based on the genus-level classification of the same sequence assemblages used in (A). Colored dots on the cluster tree represent the sedimentological characteristics of each sample horizon (6). The OTU-based analysis for the most likely indigenous bacterial communities in deep subseafloor sediment samples is shown in fig. S10.

could result in a higher cell-specific energy demand in the deeper layers at Site C0020 and may explain why microbial abundance was only a small fraction of the size predicted by the global regression line (Fig. 1A and figs. S7 and S14).

Our findings provide a comprehensive view of the deep subseafloor biosphere associated with coal beds. Despite energetic challenges, this environment appears to have maintained some of the taxonomic groups that populated the original shallow depositional setting and have contributed to carbon cycling ever since.

REFERENCES AND NOTES

1. M.-C. Ciobanu *et al.*, *ISME J.* **8**, 1370–1380 (2014).
2. R. J. Parkes, B. A. Cragg, P. Wellsbury, *Hydrogeol. J.* **8**, 11–28 (2000).
3. I. M. Head, D. M. Jones, S. R. Larter, *Nature* **426**, 344–352 (2003).
4. D. M. Jones *et al.*, *Nature* **451**, 176–180 (2007).
5. A. I. Konyukhov, *Lithol. Miner. Resour.* **45**, 465–485 (2010).
6. Expedition 337 Scientists, in *Proceedings of the Integrated Ocean Drilling Program*, F. Inagaki, K.-U. Hinrichs, Y. Kubo, Eds. (IODP Management International, Tokyo, vol. 337, 2013); http://publications.iodp.org/proceedings/337/103/103_.htm.
7. Materials and methods are available as supplementary materials on *Science* Online.
8. Y. Morono, T. Terada, N. Masui, F. Inagaki, *ISME J.* **3**, 503–511 (2009).
9. S. D'Hondt *et al.*, *Nat. Geosci.* **8**, 299–304 (2015).
10. M. J. Whiticar, *Chem. Geol.* **161**, 291–314 (1999).
11. D. A. Stolper *et al.*, *Science* **344**, 1500–1503 (2014).
12. M. Kaneko *et al.*, *Anal. Chem.* **86**, 3633–3638 (2014).
13. Y. Takano *et al.*, *Org. Geochem.* **58**, 137–140 (2013).
14. H. Imachi *et al.*, *ISME J.* **5**, 1913–1925 (2011).
15. D. Strąpoć *et al.*, *Annu. Rev. Earth Planet. Sci.* **39**, 617–656 (2011).
16. Y. Morono *et al.*, *Proc. Natl. Acad. Sci. U.S.A.* **108**, 18295–18300 (2011).
17. T. Hoshino, F. Inagaki, *Syst. Appl. Microbiol.* **35**, 390–395 (2012).
18. J. S. Lipp, Y. Morono, F. Inagaki, K.-U. Hinrichs, *Nature* **454**, 991–994 (2008).
19. F. S. Colwell *et al.*, *Appl. Environ. Microbiol.* **74**, 3444–3452 (2008).
20. G. Webster, R. J. Parkes, J. C. Fry, A. J. Weightman, *Appl. Environ. Microbiol.* **70**, 5708–5713 (2004).
21. J. A. Dodsworth *et al.*, *Nat. Commun.* **4**, 1854 (2013).
22. F. Inagaki *et al.*, *Proc. Natl. Acad. Sci. U.S.A.* **103**, 2815–2820 (2006).
23. A. P. Teske, *Geomicrobiol. J.* **23**, 357–368 (2006).
24. N. Fierer, M. A. Bradford, R. B. Jackson, *Ecology* **88**, 1354–1364 (2007).
25. T. M. Hoehler, M. J. Alperin, D. B. Albert, C. S. Martens, *Geochim. Cosmochim. Acta* **62**, 1745–1756 (1998).
26. B. Schink, *Microbiol. Mol. Biol. Rev.* **61**, 262–280 (1997).
27. B. A. Lomstein, A. T. Langerhuus, S. D'Hondt, B. B. Jørgensen, A. J. Spivack, *Nature* **484**, 101–104 (2012).
28. B. Horsfield *et al.*, *Earth Planet. Sci. Lett.* **246**, 55–69 (2006).
29. R. J. Parkes *et al.*, *Org. Geochem.* **38**, 845–852 (2007).
30. M. Osawa, S. Nakanishi, M. Tanahashi, H. Oda, *J. Japan. Assoc. Pet. Technol.* **67**, 38–51 (2002).
31. M. A. Lever *et al.*, *FEMS Microbiol. Rev.* 10.1093/femsre/fuv020 (2015).

ACKNOWLEDGMENTS

The authors are grateful to IODP and the Ministry of Education, Culture, Sports, Science and Technology of Japan for providing an opportunity to explore the deep coal-bed biosphere off Shimokita during Expedition 337. We thank all crews, drilling team members, lab technicians, and scientists on the drilling vessel *Chikyu* for supporting core sampling and onboard measurements during *Chikyu* shakedown cruise CK06-06 and IODP Expedition 337. The authors thank J. A. McKenzie and K. H. Nealson for useful discussions during project design; S. Fukunaga, S. Hashimoto, A. Imajo, Y. Saito, S. Tanaka, K. Uematsu, and N. Xiao for assistance in microbiological analyses; and D. Gruen for technical assistance during clumped isotope analysis. This work was supported in part by the Japan Society for the Promotion of Science (JSPS) Strategic Fund for Strengthening Leading-Edge Research and Development (to F.I. and JAMSTEC), the JSPS Funding Program for Next Generation World-Leading Researchers (grant no. GR102 to F.I.), the JSPS Grants-in-Aid for Science Research (no. 26251041 to F.I., no. 24770033 to T.H., no. 24687011 to H.I., no. 26287142 to M.I., no. 25610166 to M.K., and nos. 24651018 and 24687004 to Y.M.), the European Research Council (Advanced Grant no. 247153 to K.-U.H.), the Deutsche Forschungsgemeinschaft trough project HI 616/16 (to K.-U.H.) through MARUM–Cluster of Excellence 309, and NSF (no. EAR-1250394 to S.O). All shipboard and shore-based data presented in this manuscript are archived and publicly available online in the IODP Expedition 337 Proceedings (6) through the J-CORES database (http://sio7.jamstec.go.jp/j-cores.data/337/C0020A/) and the PANGAEA database (http://doi.pangaea.de/10.1594/PANGAEA.845984). This is a contribution to the Deep Carbon Observatory.

SUPPLEMENTARY MATERIALS

www.sciencemag.org/content/349/6246/420/suppl/DC1
Materials and Methods
Figs. S1 to S14
Tables S1 to S7
References (*32*–*83*)

23 January 2015; accepted 10 June 2015
10.1126/science.aaa6882

NEURODEVELOPMENT

Adult cortical plasticity depends on an early postnatal critical period

Stuart D. Greenhill,[1]* Konrad Juczewski,[2]* Annelies M. de Haan,[1] Gillian Seaton,[1] Kevin Fox,[1] Neil R. Hardingham[1]†

Development of the cerebral cortex is influenced by sensory experience during distinct phases of postnatal development known as critical periods. Disruption of experience during a critical period produces neurons that lack specificity for particular stimulus features, such as location in the somatosensory system. Synaptic plasticity is the agent by which sensory experience affects cortical development. Here, we describe, in mice, a developmental critical period that affects plasticity itself. Transient neonatal disruption of signaling via the C-terminal domain of "disrupted in schizophrenia 1" (DISC1)—a molecule implicated in psychiatric disorders—resulted in a lack of long-term potentiation (LTP) (persistent strengthening of synapses) and experience-dependent potentiation in adulthood. Long-term depression (LTD) (selective weakening of specific sets of synapses) and reversal of LTD were present, although impaired, in adolescence and absent in adulthood. These changes may form the basis for the cognitive deficits associated with mutations in DISC1 and the delayed onset of a range of psychiatric symptoms in late adolescence.

Disrupted in schizophrenia 1 (DISC1) is a protein that, when mutated, predisposes the human carrier for a number of mental disorders including schizophrenia, bipolar disorder, recurrent major depression, and autism (*1*, *2*). DISC1 interacts with a surprisingly large number of signaling molecules, including phosphodiesterase 4, glycogen synthase kinase 3, kalirin-7, fasciculation and elongation protein ζ 1, kendrin, lissencephaly 1 (Lis1), and nudE neurodevelopment protein 1–like 1 (Nudel) (*3*–*8*). DISC1 affects diverse aspects of neuronal development, such as proliferation, migration, and neurite extension. In addition, DISC1 is known to be expressed in cortical neurons during both development and adulthood (*9*) and to reside at the postsynaptic density (*6*, *10*–*12*), although very little is understood of the role it plays there. In this study, working with mice, we asked whether DISC1 protein-protein interactions early in development are critical for synaptic plasticity in adulthood. We disrupted transiently DISC1's interaction with Lis1 and Nudel during early development, at a time after cortical neurogenesis and cell migration [which are complete by about postnatal day 7 (P7) in the mouse] but before synaptogenesis and dendrite formation dominate.

We studied adult plasticity in the mouse barrel cortex, a primary sensory cortical area that receives tactile information from a normal array of 40 large whiskers. We removed all but one whisker on one side of the face of adult mice (*13*) to invoke cortical plasticity. The single-whisker experience normally leads to expansion of the cortical territory responding to the spared whisker (Fig. 1A). To manipulate DISC1 interactions with Lis1 and Nudel, we used a conditional transgenic mouse expressing the DISC1 C-terminal domain (DISC1cc; residues 671 to 852), which interacts with Lis1 and Nudel (*14*–*16*) in a tamoxifen-sensitive construct. Within this system, a single tamoxifen injection affects DISC1 signaling for 6 to 48 hours (P7 to P9) (*15*). Spatial expression of DISC1cc is restricted to excitatory neurons in the forebrain by the calcium/calmodulin-dependent protein kinase II subunit α (αCaMKII) promoter, and its activity is controlled by tamoxifen. We studied

[1]School of Biosciences, Cardiff University, Cardiff, CF23 3AX, UK. [2]National Institute on Alcohol Abuse and Alcoholism, NIH, Rockville, MD 20852, USA.
*These authors contributed equally to this work. **†Corresponding author. E-mail: sbinrh@cardiff.ac.uk**

the effect of a single subcutaneous injection of tamoxifen at P7 on single-whisker plasticity in adulthood (age range P70 to P130).

We found that adult DISC1cc mice injected with tamoxifen at P7 and with whiskers intact developed a normal barrel pattern, as well as normal cortical layers, cell density, and receptive fields (fig. S1). However, experience-dependent potentiation invoked by whisker loss was absent in DISC1cc mice injected with tamoxifen [$F_{7,51}$ = 6.9, P < 0.001, three-way analysis of variance (ANOVA)] (see Fig. 1). Plasticity in cortical layers 2 and 3 (L2/3) was normal in wild-type mice receiving tamoxifen, which indicated that tamoxifen only acted in conjunction with the mutant

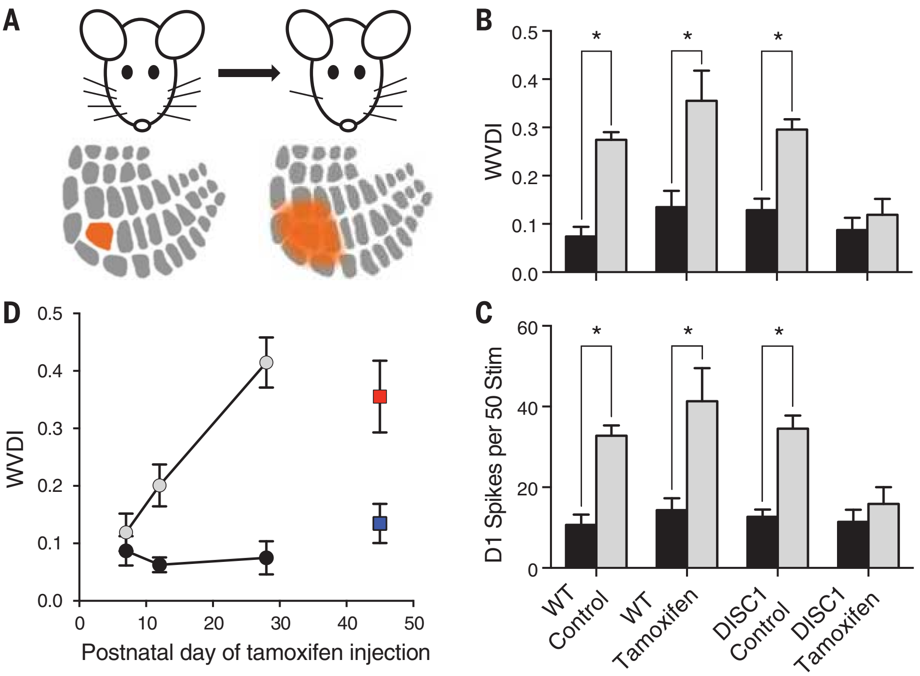

Fig. 1. Plasticity is impaired in adults by transient impairment of DISC1 C-terminal interactions at P7. (**A**) Whisker deprivation and expansion of spared whisker domain (orange area) (*13*). (**B**) Weighted vibrissae dominance index (WVDI) for spared versus principal whiskers across experimental groups (total n = 52 mice, 496 cells; naïve mice, black bars; deprived mice, gray bars). WVDI increases with deprivation except for in DISC1cc mice injected with tamoxifen at P7 [$F_{7,51}$ = 10.6, P < 0.001, three-way analysis of variance (ANOVA)]. Tamoxifen only affected plasticity in DISC1cc mice and not wild types [interaction between genotype and tamoxifen (P < 0.0005)]. (**C**) Spared (D1) whisker response increased with deprivation (gray bars), directly correlated with WVDI [correlation coefficient (R) = 0.93; P < 0.0001]. (**D**) The WVDI increases in DISC1cc mice injected with tamoxifen on P11 to P13 [t_{12} = 4.97, P < 0.05; black, naïve; gray, deprived) but only attains levels seen in wild types (red square) when injected at P28]; WT mice injected on P7 were not different from DISC1cc mice injected on P28 (t_{12} = 0.61, P = 0.45) (interaction between age and deprivation $F_{2,2}$ = 10.46, P < 0.0003, ANOVA). The WT control data are plotted at P45 for clarity (red, deprived; blue, naïve), but all mice were injected with tamoxifen on P7. All plasticity values were measured in adulthood.

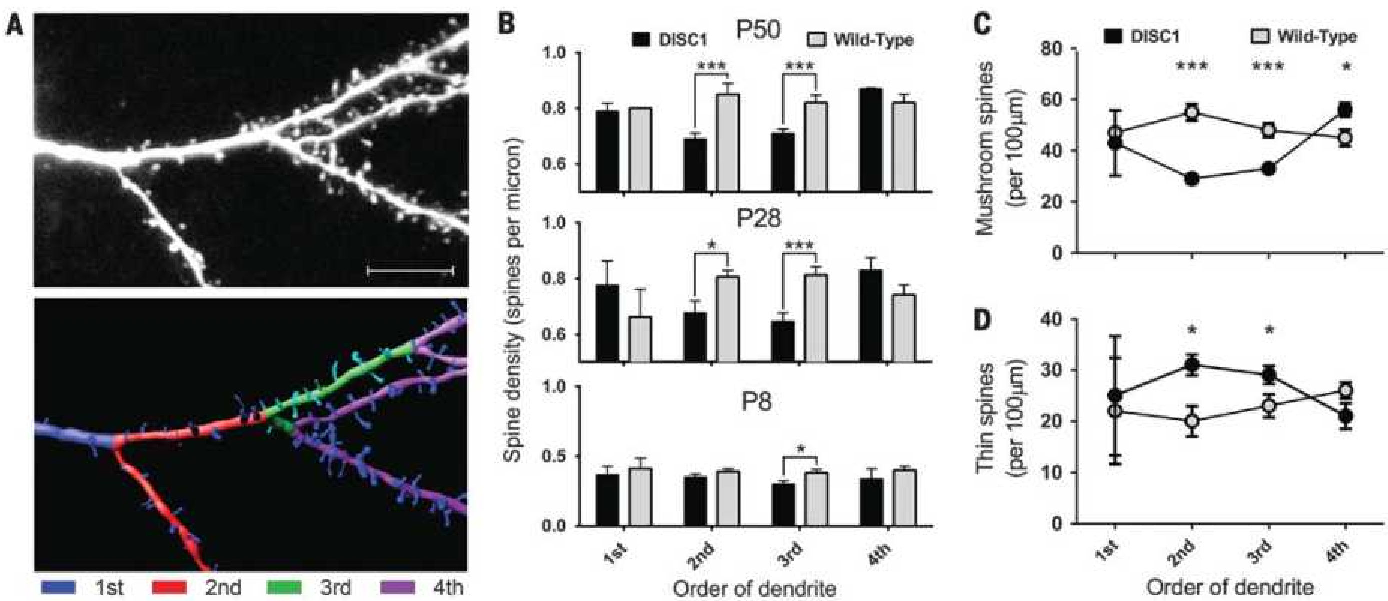

Fig. 2. Enduring effects of transient impairment of DISC1 C-terminal interactions at P7 on dendritic spines. (**A**) Example of L2/3 dendrites showing spines and dendritic order. Scale bar, 10 µm. (**B**) DISC1cc mice had lower spine density on second- and third-order dendrites at P28 and P50. Spine density was lower at P8 on third-order dendrites in DISC1cc mice. (*P < 0.05, **P < 0.01, ***P < 0.001.) (**C** and **D**) DISC1cc mice had a lower density of mushroom spines and a higher density of thin spines on second- and third-order dendrites. (ANOVA: interaction between dendrite order and genotype for mushroom spines: $F_{1,124}$ = 58.64, P < 0.0001 and for thin spines $F_{1,124}$ = 7.40, P < 0.01).

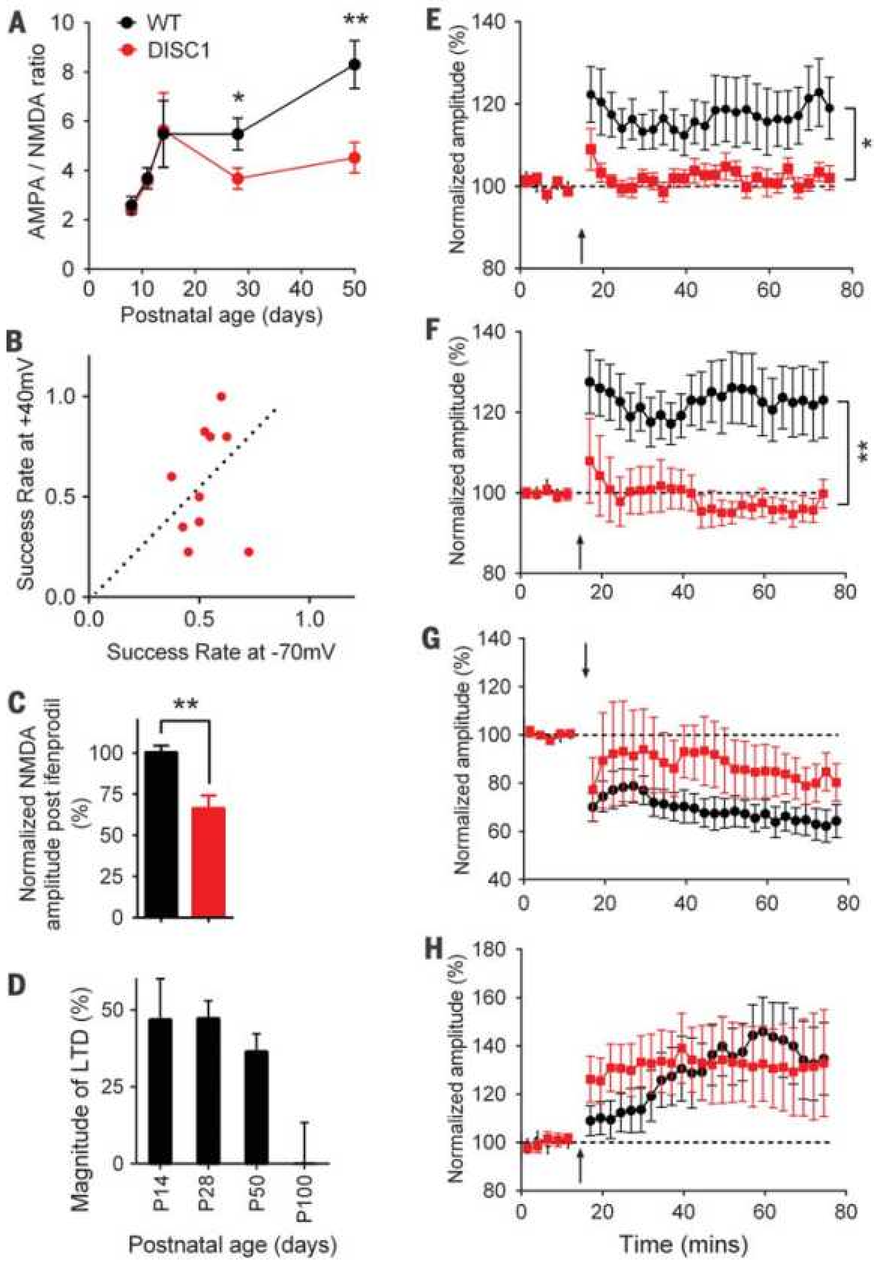

Fig. 3. Persistent functional consequences of transient impairment of DISC1 C-terminal interactions at P7. (**A**) The AMPA/NMDA ratio of WT and DISC1cc mice diverge after P14, and this ratio in DISC1cc mice remains at a low level into adulthood (P50 WT ratio is 8.29 ± 0.97; DISC1 ratio is 4.52 ± 0.61; and $t_{15} = 3.29$, $P < 0.01$). (**B**) Of P50 DISC1cc recordings, 50% had minimal-stimulus excitatory postsynaptic current success rates at +40mV higher than rates at –70mV, indicative of the presence of silent synapses. (**C**) NMDA currents in adult DISC1cc mice (red bar) showed enhanced sensitivity to ifenprodil application when compared with WT mice (black bar; DISC1cc 0.67 ± 0.08, WTs 1.01 ± 0.04, $t_{10} = 3.9$, $P < 0.005$). (**D**) LTD in WT mice was consistent at P14, P28, and P50 but was absent at P100 [average depression of 47 ± 13% at P14 ($P < 0.01$), 47 ± 6% at P28 ($P < 0.001$), 36 ± 6% at P50 ($P < 0.001$), and –1 ± 14% at P100 ($P > 0.05$)]. (**E**) Normalized peak excitatory postsynaptic potential amplitude is plotted versus time. Transient expression of mutant DISC1 at P7 abolishes the capability for intercolumnar LTP in L2/3 at P28 and (**F**) at P50 (effect of genotype $F_{1,74} = 14.27$, $P < 0.0003$ and not age $F_{1,74} = 0.13$, $P < 0.71$, ANOVA). The percentage of cells showing statistically significant LTP drops from 33% in WT mice to 5% in DISC1cc mice (P28) and 43% in WT mice to 9% in DISC1cc mice at P50. (**G**) Average LTD values are similar in WT and DISC1cc mice ($F_{1,18} = 3.44$, $P < 0.08$, ANOVA), although the percentage of cells showing LTD drops from 90% in wild types to 40% in DISC1cc mice. (**H**) Complete whisker deprivation unmasks the reversal of LTD that depends on adenosine 3′,5′-monophosphate–dependent protein kinase (*26*), and this is unaffected in the adult mouse by P7 DISC1cc activation ($F_{1,19} = 0.16$, $P < 0.87$, ANOVA).

protein and not by perturbing estrogen signaling ($t_{11} = 2.9$, $P < 0.02$). Plasticity was also normal in DISC1cc mice given just vehicle at P7, which indicated that background levels of DISC1cc availability are effectively zero (Fig. 1) ($t_{11} = 2.4$, $P < 0.05$). (Note that the mutated ligand-binding domain fused to DISC1cc does not bind natural estrogen, only tamoxifen.) The weighted vibrissae dominance index was unchanged in whisker-deprived DISC1cc animals receiving tamoxifen, because the spared whisker responses did not potentiate (Fig. 1 and fig. S2), and consequently, the spared whisker domain did not expand into the deprived barrels surrounding the D1 barrel (fig. S3). The lack of plasticity in the DISC1cc mice was robust across two background strains (Fig. 1 and fig. S4). These results show that normal DISC1 interaction with Lis1 and Nudel is vital during a brief period in neonatal development for the adult animal to exhibit experience-dependent plasticity.

Transient disruption of DISC1/Lis1/Nudel interactions later in development had a smaller effect on L2/3 plasticity. Disrupting DISC1 C-terminal interactions at P11 to P13 reduced plasticity less than it did at P7 and had no effect at P28 (Fig. 1D). This indicates that a critical period exists in early development with long-lasting consequences for plasticity expressed much later in adulthood.

We studied the early development of the DISC1cc mice to see where the defect originated. We found that disrupting DISC1 C-terminal signaling at P7 retarded dendritic elongation and elaboration of dendritic branching (figs. S5 and S6), but both had recovered by P21. The paired-pulse ratio, which is a measure of presynaptic maturation in the L4 to 2/3 pathway (*17*) was also delayed (fig. S7). Retardation of neuronal development demonstrates the immediate effect of disrupting DISC1 C-terminal interactions at P7 but does not explain the long-lasting loss of adult plasticity.

The long-lasting effects of transient disruption of DISC1/Lis1/Nudel interactions were to be found at the level of the spines rather than the dendrites. At the start of the critical period for adult plasticity, the neurons highest-order basal dendrites are mainly second- and third-order branches and are destined to become 50% of adult basal dendrites (Fig. 2 and figs. S5 and S6). We found lower spine density on second- and third-order dendritic spines in DISC1cc mice at P28 ($t_{31} = 2.36$, $P < 0.03$; and $t_{41} = 3.82$, $P < 0.0005$, respectively) and P50 ($t_{30} = 4.78$, $P < 0.0001$; and $t_{43} = 4.66$, $P < 0.0001$, respectively). The fourth- and higher-order dendrites, which mainly develop after the period during which we impaired DISC1 C-terminal interactions, showed normal spine density at P28 ($t_{20} = 0.96$, $P = 0.35$; interaction between dendrite order and genotype $F_{4,104} = 4.48$, $P < 0.005$) and at P50 ($t_{30} = -1.318$, $P = 0.20$; interaction between dendrite order and genotype $F_{4,117} = 7.29$, $P < 0.0001$). The spine density deficit was only found on basal dendrites, not on apical dendrites ($F_{4,131} = 0.86$, $P = 0.49$).

The period when DISC1 C-terminal signaling is critical for adult plasticity (P7 to P13)

corresponds to a period of rapid synaptogenesis across the brain, as well as in L2/3 of barrel cortex (*18*), when experience is necessary for AMPA insertion within synapses (*19*). Altered neonatal experience during this period leads to defocused receptive fields in adulthood (*20*). As the size of spine heads are correlated with their AMPA receptor content (*21*, *22*), we investigated spine head size and classification. At P50, there were fewer mushroom spines (both as a percentage of the whole and in absolute terms) on the second- and third-order dendrites of DISC1cc mice than on their first-, fourth-, and fifth-order dendrites ($t_{35.8}$ = 8.76, $P < 0.0001$), and fewer than on the second- and third-order dendrites of wild-type mice ($t_{49.9}$ = 8.72, $P < 0.0001$). Furthermore, there were more thin spines on the second- and third-order dendrites in the DISC1cc mice ($t_{75} = 3.07$, $P < 0.005$ compared with wild types, and $t_{68} = 4.10$, $P < 0.0005$ compared with other dendrite orders within the DISC1cc mice). Finally, the spine heads were smaller on the thin spines in the DISC1cc mouse second- and third-order dendrites than in the wild types ($t_{76} = 3.31$, $P < 0.01$) (Fig. 2). These findings imply a lower level of AMPA receptor insertion in DISC1 mutants.

We investigated synaptic function further in DISC1 mutants and found that, whereas the AMPA/*N*-methyl-D-aspartate (NMDA) ratio followed a normal developmental trajectory up to P14, it diverged at P28 ($t_{18} = 2.33$, $P < 0.05$) and did not recover by P50 ($t_{18} = 3.29$, $P < 0.01$) (Fig. 3A). Consistent with this finding, silent synapses were present in DISC1 L2/3 cells at P50 (Fig. 3B), whereas in wild types they had converted to functional synapses by this age (*23*). The NMDA component of the synaptic response was also immature and contained a higher proportion of GluN2B versus GluN2A subunits than normal ($t_{10} = 3.9$, $P < 0.005$) (Fig. 3C) (*24*, *25*). In contrast, inhibition appeared to be unaffected in DISC1cc mice (fig. S8). Low levels of GluN2A and AMPA receptors are consistent with the spine size defects, which implies that glutamate receptor insertion is affected by transient disruption of DISC1 C-terminal interactions in early development. These factors predict that synaptic plasticity should also be deficient in DISC1cc mice (*21*, *22*, *25*).

On investigation, we found that long-term potentiation (LTP) was absent in the P7 tamoxifen-treated DISC1cc mice at P28 and P50 (Fig. 3, E and F), which indicated that development of LTP was abolished rather than delayed. Long-term depression (LTD) was affected although not abolished: The time-course of LTD was slower and the probability of LTD induction was lower in DISC1cc mice (fig. S9), although it was possible to induce LTD in the mutants as in the wild types (Fig. 3G). This suggested that it might be possible to reverse LTD in these synapses despite their lack of LTP. Previous studies had shown that 7 days of complete bilateral whisker deprivation can occlude LTD in the barrel cortex and reset the synapses to a state that favors LTD reversal (*26*). We found that it was possible to reverse LTD in the completely whisker-deprived DISC1cc mouse (Fig. 3H). These results show that developmental disruption of DISC1 signaling blocks or impairs selective aspects of synaptic plasticity.

Adult plasticity is different from many forms of developmental plasticity (*27*, *28*). In the somatosensory and visual cortex, adult plasticity is dependent on CaMKII and closely related to LTP (*29*, *30*). Developmental forms of synaptic plasticity, such as tumor necrosis factor-α–dependent synaptic scaling, experience-dependent depression, and LTD are gradually reduced with age (*30*, *31*). We found that the normal period of LTD expression in the barrel cortex ends between P50 and P100 (Fig. 3D), after which LTD and reversal of LTD are not available modes of plasticity. Therefore, the loss of adult LTP only becomes critical at an age when developmental forms of plasticity have decreased to low levels. The latent effect of ablating prospective adult plasticity during an early critical period may therefore help explain the late onset of some schizophrenia symptoms.

How might a loss of LTP affect psychiatric conditions? Working memory is defective in schizophrenia and relies on persistent modes of network firing (*32*). Persistent neuronal activity requires formation of attractor states in neuronal networks, as has recently been shown in monkey prefrontal cortex during context-dependent integration of visual information (*33*). Therefore, a loss of plasticity such as we describe here is likely to disrupt working memory function by preventing formation of stable attractor states.

The C-terminal domain of DISC1 expressed in the DISC1cc mouse is known to reduce wild-type DISC1-Nudel and DISC1-Lis interactions (*15*). DISC1-Nudel interactions are thought to depend on the C-terminal domain's ability to form dimeric and tetrameric states (*16*). DISC1 and Nudel interact strongly at P7, less so by P16, and negligibly by 6 months (*14*). The DISC1-Nudel complex is therefore available to be disrupted only when spines form rapidly on cortical neurons during the critical period we describe here for adult plasticity. Nudel and DISC1 also both bind to Lis1 (*14*), and Lis1 haploinsufficiency has been shown to decrease spine density, specifically on second- and third-order dendrites (*34*), in striking similarity to the present results. Human induced pluripotent stem cells from schizophrenia and depression sufferers carrying a DISC1 C-terminal mutation also exhibit deficits in synapse formation (*35*). By restricting DISC1 C-terminal dysfunction to a short period of development, we have been able to show that adult plasticity (i) depends on synapse formation during this early critical period, (ii) cannot be recovered despite continued expression of normal DISC1, and (iii) is independent of DISC1-Nudel interactions in adulthood.

REFERENCES AND NOTES

1. J. K. Millar *et al.*, *Hum. Mol. Genet.* **9**, 1415–1423 (2000).
2. N. J. Bradshaw, D. J. Porteous, *Neuropharmacology* **62**, 1230–1241 (2012).
3. K. Miyoshi *et al.*, *Biochem. Biophys. Res. Commun.* **317**, 1195–1199 (2004).
4. S. Taya *et al.*, *J. Neurosci.* **27**, 15–26 (2007).
5. K. E. Burdick *et al.*, *Hum. Mol. Genet.* **17**, 2462–2473 (2008).
6. A. Hayashi-Takagi *et al.*, *Nat. Neurosci.* **13**, 327–332 (2010).
7. E. Kang *et al.*, *Neuron* **72**, 559–571 (2011).
8. T. V. Lipina, M. Wang, F. Liu, J. C. Roder, *Neuropharmacology* **62**, 1252–1262 (2012).
9. I. L. Schurov, E. J. Handford, N. J. Brandon, P. J. Whiting, *Mol. Psychiatry* **9**, 1100–1110 (2004).
10. B. Kirkpatrick *et al.*, *J. Comp. Neurol.* **497**, 436–450 (2006).
11. H. J. Carlisle *et al.*, *J. Neurosci.* **31**, 16194–16207 (2011).
12. Q. Wang *et al.*, *Mol. Psychiatry* **16**, 1006–1023 (2011).
13. S. Glazewski, C. M. Chen, A. Silva, K. Fox, *Science* **272**, 421–423 (1996).
14. N. J. Brandon *et al.*, *Mol. Cell. Neurosci.* **25**, 42–55 (2004).
15. W. Li *et al.*, *Proc. Natl. Acad. Sci. U.S.A.* **104**, 18280–18285 (2007).
16. D. C. Soares *et al.*, *J. Biol. Chem.* **287**, 32381–32393 (2012).
17. C. E. Cheetham, K. Fox, *Neuroscience* **30**, 12566–12571 (2010).
18. K. D. Micheva, C. Beaulieu, *J. Comp. Neurol.* **373**, 340–354 (1996).
19. J. A. Wen, A. L. Barth, *J. Neurosci.* **31**, 4456–4465 (2011).
20. E. A. Stern, M. Maravall, K. Svoboda, *Neuron* **31**, 305–315 (2001).
21. Z. Nusser *et al.*, *Neuron* **21**, 545–559 (1998).
22. C. D. Kopec, E. Real, H. W. Kessels, R. Malinow, *J. Neurosci.* **27**, 13706–13718 (2007).
23. N. Hardingham, K. Fox, *J. Neurosci.* **26**, 7395–7404 (2006).
24. G. Carmignoto, S. Vicini, *Science* **258**, 1007–1011 (1992).
25. C. Bellone, R. A. Nicoll, *Neuron* **55**, 779–785 (2007).
26. N. Hardingham, N. Wright, J. Dachtler, K. Fox, *Neuron* **60**, 861–874 (2008).
27. K. Fox, *Neuroscience* **111**, 799–814 (2002).
28. M. Sato, M. P. Stryker, *J. Neurosci.* **28**, 10278–10286 (2008).
29. N. Hardingham *et al.*, *J. Neurosci.* **23**, 4428–4436 (2003).
30. A. Ranson, C. E. Cheetham, K. Fox, F. Sengpiel, *Proc. Natl. Acad. Sci. U.S.A.* **109**, 1311–1316 (2012).
31. D. E. Feldman, R. A. Nicoll, R. C. Malenka, J. T. R. Isaac, *Neuron* **21**, 347–357 (1998).
32. D. Durstewitz, J. K. Seamans, T. J. Sejnowski, *Nat. Neurosci.* **3** (suppl.), 1184–1191 (2000).
33. V. Mante, D. Sussillo, K. V. Shenoy, W. T. Newsome, *Nature* **503**, 78–84 (2013).
34. A. Sudarov, F. Gooden, D. Tseng, W. B. Gan, M. E. Ross, *EMBO Mol. Med.* **5**, 591–607 (2013).
35. Z. Wen *et al.*, *Nature* **515**, 414–418 (2014).

ACKNOWLEDGMENTS

We acknowledge the support of the UK Medical Research Council and U.S. National Institute of Mental Health, NIH, to K.F. for this work. We also thank T. Gould for histology, A. Siva for discussions on DISC1cc, and S. Butt for suggestions on methods of tamoxifen delivery. Supplement contains additional data.

SUPPLEMENTARY MATERIALS

www.sciencemag.org/content/349/6246/424/suppl/DC1
Materials and Methods
Figs. S1 to S9
References (*36*–*46*)

5 February 2015; accepted 23 June 2015
10.1126/science.aaa8481

INTRACELLULAR TRANSPORT

PI4P/phosphatidylserine countertransport at ORP5- and ORP8-mediated ER–plasma membrane contacts

Jeeyun Chung,[1] Federico Torta,[2] Kaori Masai,[1] Louise Lucast,[1] Heather Czapla,[1] Lukas B. Tanner,[2]* Pradeep Narayanaswamy,[2] Markus R. Wenk,[2] Fubito Nakatsu,[1]†‡ Pietro De Camilli[1]‡

Lipid transfer between cell membrane bilayers at contacts between the endoplasmic reticulum (ER) and other membranes help to maintain membrane lipid homeostasis. We found that two similar ER integral membrane proteins, oxysterol-binding protein (OSBP)–related protein 5 (ORP5) and ORP8, tethered the ER to the plasma membrane (PM) via the interaction of their pleckstrin homology domains with phosphatidylinositol 4-phosphate (PI4P) in this membrane. Their OSBP-related domains (ORDs) harbored either PI4P or phosphatidylserine (PS) and exchanged these lipids between bilayers. Gain- and loss-of-function experiments showed that ORP5 and ORP8 could mediate PI4P/PS countertransport between the ER and the PM, thus delivering PI4P to the ER-localized PI4P phosphatase Sac1 for degradation and PS from the ER to the PM. This exchange helps to control plasma membrane PI4P levels and selectively enrich PS in the PM.

Membrane lipids can be exchanged between bilayers at contact sites between the endoplasmic reticulum (ER) and other membranes (*1–7*). One class of molecules mediating these contacts are oxysterol-binding proteins (OSBP) and the closely related OSBP-related proteins (ORPs) (Osh proteins in yeast), which harbor lipids in a hydrophobic cavity of their OSBP-related domain (ORD) (fig. S1) (*3*, *7–13*). Members of this protein family (more than 10 in mammals) have been thought to function selectively as sterol sensors or transport proteins (*12*, *13*), but recent studies show that they can also harbor different lipids (*3*, *7*, *9–11*). OSBP and Osh4/Kes1function in a lipid countertransport between the Golgi complex and membranes of the ER by delivering cholesterol to the Golgi in exchange for phosphatidylinositol 4-phosphate (PI4P), which is degraded by the Sac1 phosphatase in the ER (*9*, *14*). Whether other ORPs also function in lipid countertransport reactions to help maintain membrane heterogeneity, such as a selective concentration of phosphatidylserine (PS) in the plasma membrane (PM) (*15*), is unclear. We focused on two very similar mammalian ORPs, ORP5 and ORP8, which are anchored to the ER membrane, where they reside via a hydrophobic tail sequence (*12*, *16*, *17*). Their ORDs are the mammalian ORDs most closely related to the ORDs of Osh6 and Osh7, which transport PS to the PM in yeast, although ORP5/8 and Osh6/7 are otherwise different in domain organization (fig. S2A) (*3*, *8*, *11*, *12*).

Green fluorescent protein (GFP)–ORP5 and GFP-fusions of the two splice variants of ORP8 (*17*), which differ by the inclusion (ORP8L) or exclusion (ORP8S) of an N-terminal 42 amino acids sequence (fig. S5), were independently expressed in HeLa cells and analyzed by means of confocal microscopy. ORP5 predominantly accumulated in small patches at the cell periphery in a pattern reminiscent of ER-PM contacts (*18*, *19*): a row of peripheral dots in mid-cell optical sections and tightly apposed patches in optical sections of the flat base of the cell (Fig. 1A). More numerous and longer ER-PM contacts were detected as a result of excess ORP5 expression (Fig. 1, C to E). In contrast, GFP-ORP8L had a broad reticular distribution throughout the cell (Fig. 1A) that overlapped with that of the ER marker Sec61β (fig. S3), with only a faint puncta at the cell periphery. GFP-ORP8S had a somewhat intermediate localization pattern (Fig. 1A). Coexpressed GFP-ORP5 and mCherry-ORP8L partially colocalized at the cell cortex (Fig. 1F), and ORP8L coimmunoprecipitated with ORP5 (Fig. 1G), indicating that ORP5 may help mediate ORP8 recruitment to ER-PM contacts via heteromerization.

Because both ORP5 and ORP8 contain a PH domain, we next investigated whether their tethering function depended on phosphoinositides in the PM. The cortical pool of GFP-ORP5 and GFP-ORP8S, and even the very weak cortical accumulation of GFP-ORP8L, increased upon overexpression of phosphatidylinositol 4-kinase IIIα (PI4KIIIα) and its associated factors [the enzyme complex responsible for PI4P synthesis in the PM (*20–23*)] (Fig. 1, A and B). In cells treated with the PI4KIIIα inhibitor A1 (*25*), both ORP5 and ORP8S dissociated from the PM and dispersed throughout the ER (Fig. 1H and movies S1 and S2). This redistribution correlated with the dissociation from the PM of near-infrared fluorescent protein (iRFP)–P4M, a PI4P reporter (*24*), but not of $PH_{PLC\delta}$, a phosphatidylinositol 4,5-bisphosphate [$PI(4,5)P_2$] reporter (movie S3) (*25*). Thus, PI4P is required for the binding of ORP5 and ORP8 to the PM.

ORP5 and ORP8L constructs lacking their PH domains were localized throughout the ER even upon coexpression of PI4KIIIα (Fig. 1, I and J, and fig. S4). Constructs lacking the transmembrane region or comprising the PH domain and upstream N-terminal sequences mimicked the properties of the full-length proteins (cortical localization of ORP5 constructs and strong dependence on PI4KIIIα overexpression for the cortical accumulation of ORP8L constructs) (Fig. 1, I and J). Both PH domain-only constructs were similarly targeted to the PM and more prominently upon PI4KIIIα overexpression (Fig. 1, I and J). Thus, differences in the PM recruitment of ORP5 and ORP8L are dictated by their N-terminal amino acid sequences that differ substantially in the two proteins and confer an overall more negative charge to ORP8L. Most of this negative charge is accounted for by the ORP8L-specific extension (fig. S5), which explains the greater accumulation of ORP8S at ER-PM contacts. The ORD is dispensable for cortical localization (fig. S4).

The PI4P-dependent cortical accumulation of ORP5 was supported by studies of tamoxifen-inducible PI4KIIIα-conditional knockout embryonic fibroblasts (MEFs) (*20*). In sham-treated MEFs, GFP-ORP5 was concentrated at ER-PM contacts, but in knockout (tamoxifen-treated) cells, in which global PI4P levels are 70% lower than in controls with dramatic loss of PM PI4P (*20*), GFP-ORP5 was dispersed throughout the ER (Fig. 2A). ORP5 and ORP8 expression was up-regulated in knockout MEFs, pointing to a functional link between ORP5/ORP8 function and PI4KIIIα (Fig. 2B). This phenotype, as well as the loss of cortical localization of ORP5, was rescued by expression of PI4KIIIα in the knockout MEFs (Fig. 2, A and B). PI4KIIIα knockout MEFs also had lower PS levels (about 50% reduction) (Fig. 2C and fig. S6) but no major changes in levels of phosphatidylethanolamine (PE) and phosphatidylcholine (PC), the precursors of PS (Fig. 2C) (*15*, *26*).

If ORP5 and ORP8 operate in a countertransport mechanism, they should contain more than one lipid in their ORD domains, which are the most similar to each other in their portion defining the lipid-harboring cavity (fig. S2A). Because only the ORD of ORP8 (amino acids 370 to 809) could be purified in sufficient yield (Fig. 3A), we focused on this domain. Mass spectrometry comparison between the denatured ORD [apo form, molecular weight (MW) 53,865 daltons] and the native ORD (mixture of native apo and holo forms) revealed two main ORD-lipid complexes: MW 54,654 daltons (apo form + 789 daltons) and MW 54,808 daltons (apo form + 943 daltons) (Fig. 3B). These mass increments correspond

[1]Department of Cell Biology, Howard Hughes Medical Institute, Kavli Institute for Neuroscience, and Program for Cellular Neuroscience, Neurodegeneration, and Repair, Yale School of Medicine, New Haven, CT 06520, USA. [2]Department of Biochemistry, Yong Loo Lin School of Medicine, National University of Singapore, 117456 Singapore.
*Present address: Lewis-Sigler Institute for Integrative Genomics, Princeton University, Princeton, NJ 08544, USA. †Present address: Department of Neurochemistry and Molecular Cell Biology, Graduate School of Medical and Dental Sciences, Niigata University, Niigata 951-8510, Japan. **‡Corresponding author. E-mail: pietro.decamilli@yale.edu (P.D.C.); nakatsu@med.niigata-u.ac.jp (F.N.)**

well to the mass of PS 36:1 (789.55 daltons) and phosphatidylinositol phosphate (PIP) 36:1 or 36:2 (944.5 or 942.5), respectively. PS and PIP were also found in a quantitative analysis of the lipid fraction extracted from the purified ORD construct (Fig. 3, C and D). The PIP species presented in ORD_{ORP8} is most likely PI4P because the cluster of amino acids that mediate specific binding of PI4P in other ORDs (His[143], His[144], Lys[336], and Arg[344] in Osh4) (*9*, *10*) is conserved in this ORD as well as in ORD_{ORP5} (fig. S2, B and C). Other phospholipids, sphingolipids, and cholesterol were not detected in appreciable amounts, indicating that reported effects of ORP5 and ORP8 on cholesterol dynamics (*16*, *17*) result from indirect actions of these proteins.

On the basis of these findings, we examined whether ORD_{ORP8} could exchange PS and PI4P between artificial bilayers in vitro. "Heavy" and "light" liposomes composed of 90% PC and either 10% PI4P or 10% PS, respectively, were incubated (*27*) with wild-type (WT) ORD_{ORP8}- and ORD_{ORP8}-harboring mutations in the PI4P binding motif (H514A,H515A) (fig. S2B) (*9*, *10*) (or with

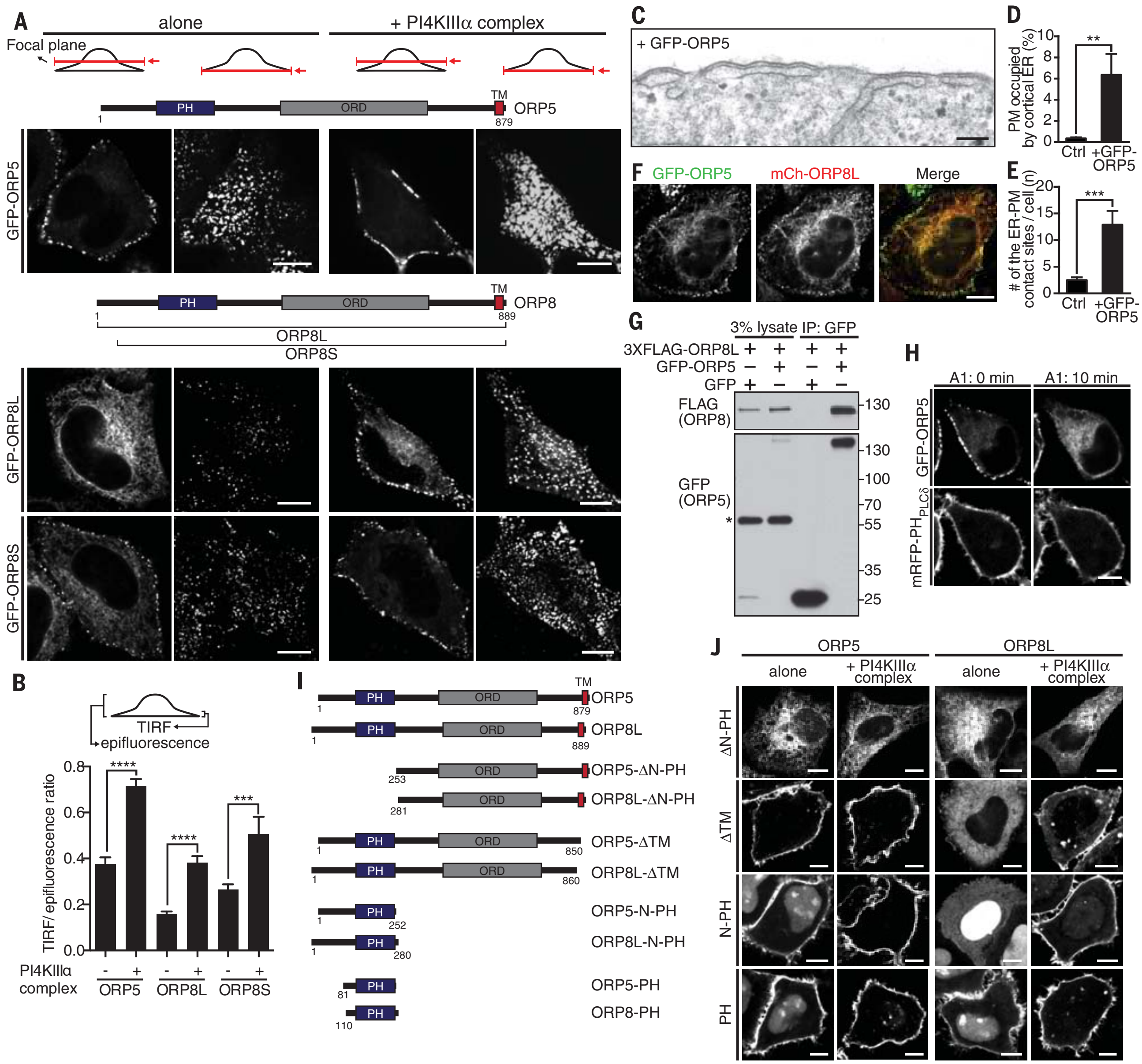

Fig. 1. PI4P-dependent accumulation of ORP5 and ORP8 at ER-PM contact sites. (**A**) Confocal images of the middle or of the basal PM focal planes (illustrations at top) of HeLa cells expressing GFP-ORP5, GFP-ORP8L, or GFP-ORP8S either alone (left) or together with the PI4KIIIα complex (right). Scale bars, 10 μm. (**B**) Ratio of GFP fluorescence visible in the total internal reflection fluorescence (TIRF) (basal PM-associated fluorescence) versus epifluorescence fields (total fluorescence) of cells transfected as in (A) (mean ffl SEM; $P < 0.0001$, *t* test, $n = 8$ to 20 cells). (**C** to **E**) Increase of ER-PM contacts produced by GFP-ORP5 expression as revealed with electron microscopy and accompanying morphometric analysis: contact length per unit PM length in (D) (mean ffl SEM; $P < 0.01$, *t* test, $n = 10$ cells) and number of contacts per PM length in (E) (mean ffl SEM; $P < 0.001$, *t* test, $n = 10$ cells). Scale bar, 200 nm. (**F**) Confocal live imaging of HeLa cells transfected with GFP-ORP5 and mCh-ORP8, showing partial recruitment of ORP8 under these conditions. Scale bar, 10 μm. (**G**) Co-immunoprecipitation of 3XFLAG-ORP8 with GFP-ORP5 in HeLa cells. Asterisk points to an nonspecific band. (**H**) Dissociation from the PM of GFP-ORP5 but not of mRFP-$PH_{PLC\delta}$ upon acute treatment of cells with the specific PI4KIIIα inhibitor A1 (100 nM) induces. (**I**) ORP5 and ORP8 deletion constructs used for the experiments shown in (J). (**J**) Confocal live imaging of HeLa cells expressing the deletion constructs depicted in (I) and with a C-terminal GFP tag revealing that the PI4P-dependent PM recruitment of ORP5 and ORP8 is mediated by their PH domains. The smallest constructs show a partial accumulation in nuclei, as reported previously for other PH domains. Scale bars, 10 μm.

no proteins as a control) and then separated by centrifugation. (Single-letter abbreviations for the amino acid residues are as follows: A, Ala; C, Cys; D, Asp; E, Glu; F, Phe; G, Gly; H, His; I, Ile; K, Lys; L, Leu; M, Met; N, Asn; P, Pro; Q, Gln; R, Arg; S, Ser; T, Thr; V, Val; W, Trp; and Y, Tyr. In the mutants, other amino acids were substituted at certain locations; for example, H514A indicates that histidine at position 514 was replaced by alanine.) The supernatant (light liposomes) contained no PI4P in the absence of protein, 20% PI4P in samples incubated with WT ORD_{ORP8}, and much reduced PI4P levels in samples incubated with mutant ORD_{ORP8} (Fig. 3E). Conversely, a greater specific amount of PS was recovered in the heavy liposomes pellets when WT ORD_{ORP8} was used instead of H514A,H515A ORD_{ORP8} (Fig. 3E). A similar assay in which transfer of either PI4P or PS from heavy liposomes to light liposomes was tested in the presence or absence of the other lipid in the light liposomes demonstrated

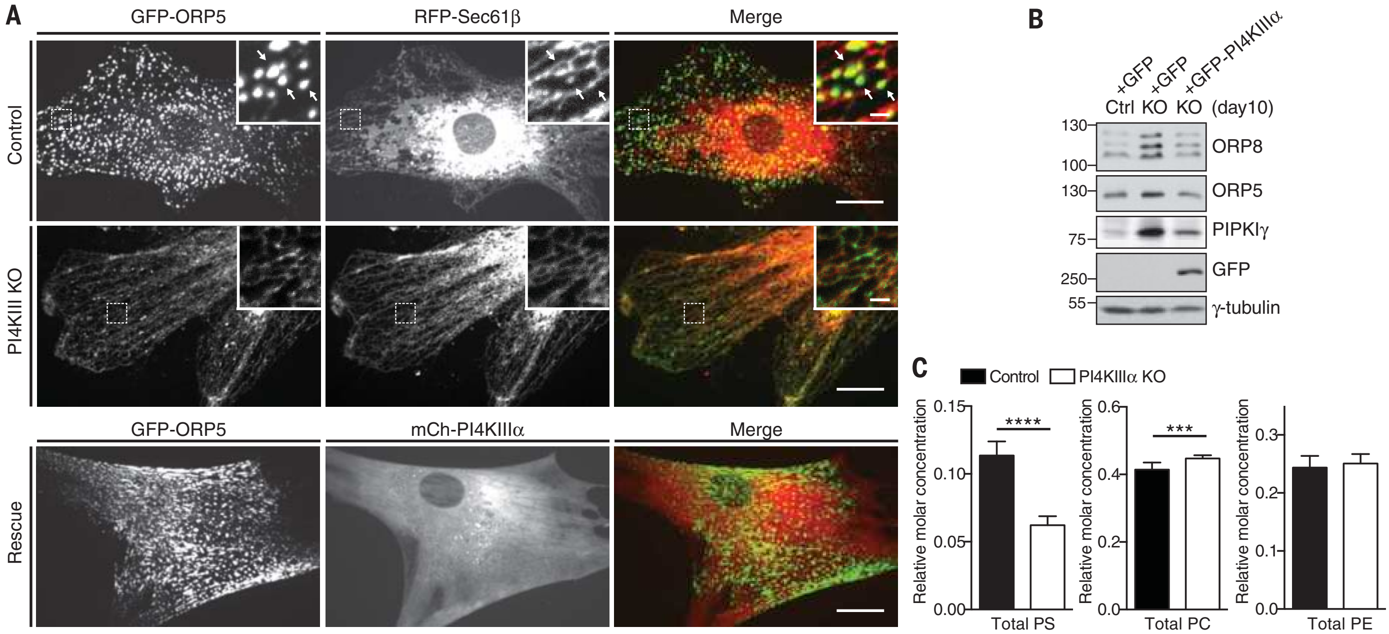

Fig. 2. PI4KIIIα KO cells shows defects in PS metabolism. (**A**) Confocal live imaging of control (top) or PI4KIIIα KO MEFs (middle) coexpressing GFP-ORP5 and RFP-Sec61β showing ER-PM contacts at base of the cell and their absence in knockout cells. mCh-PI4KIIIα expression in the knockout cells rescues the phenotype (bottom). Regions enclosed by rectangles are shown at higher magnification in the insets. Scale bars, main fields, 10 μm; insets, 2 μm. (**B**) Immunoblot of the proteins indicated in lysates from control MEFs, PI4KIII knockout MEFs, and knockout MEFs expressing GFP-PI4KIIIα. (**C**) Lipidomics analysis of PI4KIIIα knockout and control MEFs (mean ± SEM; *****P* < 0.0001, ****P* < 0.001, *t* test, *n* = 3 cells).

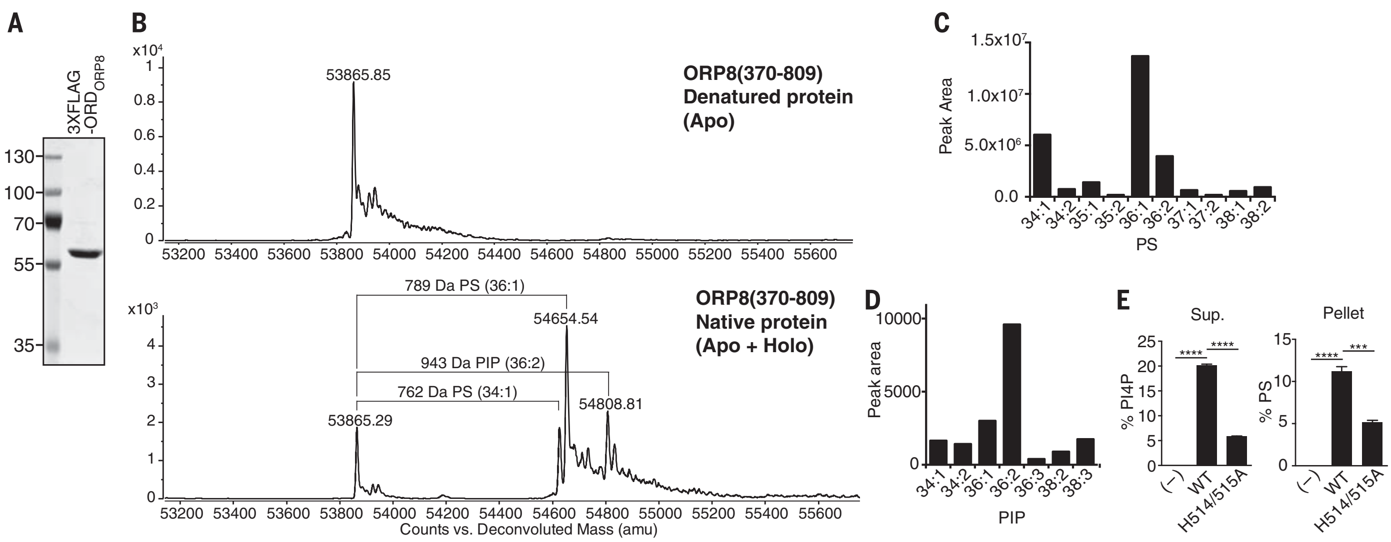

Fig. 3. Detection of PS and PIP in the ORD of ORP8. (**A**) Coomassie blue–stained SDS–polyacrylamide gel electrophoresis gel of purified 3XFLAG-ORD_{ORP8} used for the mass spectrometry studies. (**B**) Mass spectrometry analysis of 3XFLAG-ORD_{ORP8} showing the occurrence of apo and holo forms (with PS and PIP bound) in native conditions (bottom) and, for comparison, of the apo protein alone in denatured conditions (top). (**C** and **D**) Relative abundance of PS (C) and PIP (D) species (different acyl chain lengths) recovered after extraction from 3XFLAG-ORD_{ORP8}. (**E**) Sucrose-loaded heavy PC/PI4P liposomes (90:10 mol/mol, 2 mM lipids, 400 nm diameter) and light PC/PS liposomes (90:10 mol/mol, 2 mM lipids, 100 nm diameter) were incubated with no protein (−) or with 5 μM either WT ORP_{ORP8} or H514A,H515A mutant ORP_{ORP8} for 15 min at 25°C. After centrifugation, supernatant (left) and pellet (right) fractions were collected, and the percentages of PI4P and PS recovered in the two fractions were assessed by means of high-performance liquid chromatography–based lipid analysis (mean ± SEM; *****P* < 0.0001, ****P* < 0.001, *t* test, *n* = 3 cells). Pellet fractions were normalized by PS recovery of (−) sample.

that presence of the other lipid accelerated transfer (fig. S7). This effect was more prominent for PS transport (fig. S7). Thus, PI4P/PS countertransport occurs in vitro.

We next investigated a potential role of ORP5/ORP8 in a countertransport of PI4P and PS between the PM and the ER aimed at delivering PM PI4P to the ER for degradation by Sac1 (*28*) and PS from its site of synthesis in ER (*15*) to the PM. Overexpression of ORP5 reduced PI4P in the PM, as detected by the dissociation of the PI4P biosensor P4M (Fig. 4, A and B). Residual PI4P in this membrane was implied by the PI4P-dependent cortical localization of ORP5 (Figs. 1A and 4A, inset) (binding of multiple ER-localized ORP5 molecules to PM PI4P likely accounts for increased avidity) and by the PM localization of a tandem PH_{ORP5} (fig. S8). Conversely, ORP5 overexpression also resulted in increase of PM-localized PS, as revealed by two PS biosensors, evt2-2XPH (tandem PH domains of evectin-2) (*29*) or LactC2 (C2 domain of lactadherin) (*30*), respectively (Fig. 4, C and D, and fig. S9). These effects were not observed upon expression of ORP5-harboring mutations that impair the lipid-binding properties of its ORD domain: the double H478A,H479A mutation (impaired PI4 binding) (fig. S2B) (*9*) and the L to D mutation at position 389 (L389D) (*11*), which corresponds to a leucine critical for PS binding in yeast Osh6 (Leu^{69}) and Osh7 (fig. S2D) (*11*). In fact, these mutant constructs were even more enriched in the cortical ER than was WT ORP5 (fig. S10), most likely reflecting higher levels of PI4P in the PM. Knockdown of ORP5 and ORP8 resulted in prominent PM accumulation of N-PH_{ORP8}, which is normally retained in the cytosol and nucleus but relocates to the PM in response to increased PI4P in this membrane (Figs. 1J and 4E). Likewise, the PS sensor evt2-2XPH was no longer enriched at the PM in ORP5/ORP8 double-knockdown cells (fig. S11). The requirement of PI4P in the PM for the delivery of PS to this membrane was supported by the lack of enrichment of the PS sensor evt2-2XPH at the PM in PI4KIIIa knockout MEFs (fig. S12).

Because ORP overexpression could result in indirect chronic effects, ORP-mediated PI4P/PS exchange at the ER-PM contacts was further analyzed by means of the acute PM recruitment of ORP constructs by using an FK506/rapamycin-inducible FK506 binding protein (FKBP)–FKBP12-rapamycin-binding (FRB) heterodimerization system (*31*). A monomeric red fluorescent protein (mRFP) fusion of ORP5 in which its PH domain had been replaced by FKBP12 (mRFP-FKBP-ΔPH-ORP5) was transfected in HeLa cells along with a PM membrane bait [PM-FRB-CFP (*32*)] and together with PI4P and PS reporters (fig. S13). Upon the addition of rapamycin (fig. S13), this fusion protein was rapidly recruited to the PM, leading to dissociation of iRFP-P4M (PI4P) but not of GFP-$PH_{PLC\delta}$ [PI(4,5)P_2] and to PM recruitment of GFP-evt2-2XPH (PS) (Fig. 4, F to H). Similar results were observed by replacing the ORP5 portion of the FKBP12 fusion proteins with the corresponding portion of ORP8 (Fig. 4I). In contrast, acute PM recruitment of FKBP12-ORP5 fusion proteins with mutations in the ORD that affect PI4P or PS binding (fig. S2, B to E) had no effect on the localization of PI4P and PS reporters (Fig. 4I and fig. S14), and depletion of PI4P in the PM by prior A1 treatment nearly abolished PS increase in this membrane (Fig. 4J).

Physical tethering of the ER to the PM by mRFP-FKBP-ΔPH-ORPs was required for the PI4P/PS exchange to occur. Thus, an mRFP-FKBP-ΔPH-$ORP5_{WT}$ construct in which the C-terminal

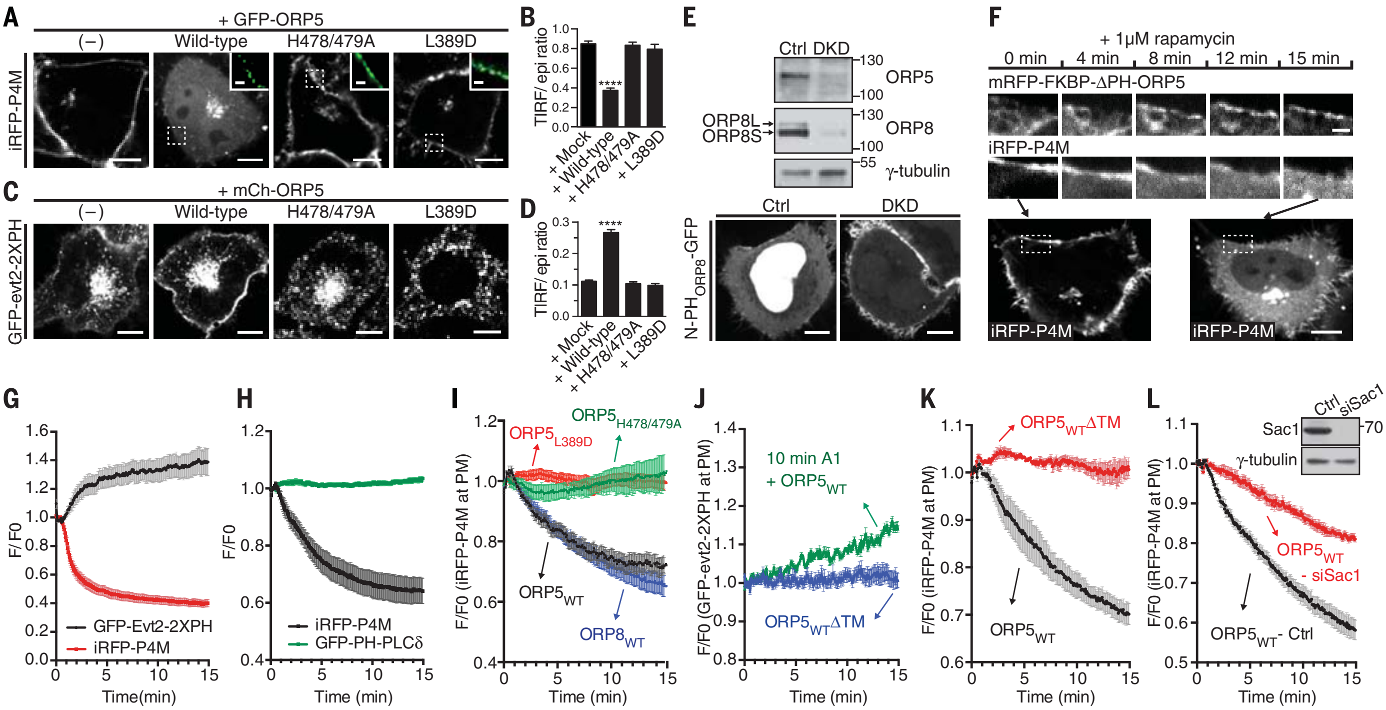

Fig. 4. ORP5 and ORP8 mediate PS/PI4P exchange at the ER-PM contact sites. (**A** to **D**) Confocal live imaging of HeLa cells expressing iRFP-P4M [(A) and (B)] or GFP-evt2-2XPH [(C) and (D)] either alone (–) or together with WT or mutant ORP5, as indicated. The main fields show the fluorescence of iRFP-P4M and GFP-evt2-2XPH, respectively. The insets of (A) shows at high magnification the GFP-ORP5 fluorescence in the regions indicated in the main fields. The ratio of iRFP (A) or GFP (C) fluorescence visible in the TIRF versus epifluorescence fields is shown in (B) and (D) (mean ± SEM; $P < 0.0001$, t test, n = 14 to 25 cells). Scale bars, 10 μm; insets, 2 μm. (**E**) Effect of the double knockdown of ORP5 and ORP8 on the subcellular localization of the N-PH domain of ORP8. Scale bars, 10 μm. (**F**) Confocal live microscopy showing that recruitment of ΔPH-ORP5 to the PM with 1 μm rapamycin induces dissociation of iRFP-P4M. Scale bar, 10 μm for the main fields; 2 μm for the time sequence. (**G** to **L**) Quantification of fluorescent signals in the TIRF fields upon rapamycin-induced PM recruitment of FKBP12 fused to the ΔPH-ORP proteins (mean ± SEM). (G) Loss of iRFP-P4M and increase of GFP-evt2-2XPH upon recruitment of ΔPH-$ORP5_{WT}$ (n = 6 cells). (H) Loss of iRFP-P4M, but not of GFP-PH-PLCδ, upon recruitment of ΔPH-$ORP5_{WT}$ (n = 8 cells) (I) Loss of iRFP-P4M upon ΔPH-$ORP5_{WT}$ or ΔPH-$ORP8_{WT}$ recruitment, but not upon recruitment of ΔPH-$ORP5_{H478/479A}$ or ΔPH-$ORP5_{L389D}$ (n = 6 to 10 cells). (J) GFP-evt2-2XPH fluorescence upon recruitment of ΔPH-$ORP5_{WT}$ΔTM (blue, n = 18 cells) or ΔPH-$ORP5_{WT}$ pretreated with 100nM A1 (10 min) (green, n = 10 cells) (K) Loss of iRFP-P4M only if the ΔPH-ORP_{WT} construct is tethered to the ER by its transmembrane region (n = 4 cells). (L) The knockdown of Sac1 (inset, immunoblot) impairs the decrease of iRFP-P4M fluorescence upon recruitment of ΔPH-$ORP5_{WT}$ (n = 6 to 9 cells).

transmembrane anchor had been deleted, mRFP-FKBP-ΔPH-ORP5$_{WT}$ΔTM (fig. S13), was recruited to the PM in response to rapamycin (much faster than the ER-anchored construct because this protein is a cytosolic protein) (fig. S15) but failed to dissociate the PI4P marker P4M (Fig. 4K) and to recruit the PS marker evt2-2XPH to the PM (Fig. 4J). Furthermore, the knockdown of Sac1 strongly reduced the dissociation of iRFP-P4M from the PM upon acute recruitment of mRFP-FKBP-ΔPH-ORP5$_{WT}$ (Fig. 4L), implicating PI4P consumption by Sac1 for efficient countertransport, most likely by allowing the ORD to favor PS binding over PI4P binding at the ER membrane interface. These findings support the importance of Osh/ORP–family proteins in the negative regulation of PM PI4P via an action that involve Sac1, as suggested (*28*), but favor an action of Sac1 "in cis" in ER membrane after delivery of PI4P to this membrane by the ORPs.

Collectively, our results demonstrate that ORP5 and ORP8 function as ER-PM tethers that, via a countertransport mechanism, negatively regulate PI4P in the PM (where the two ORPs are recruited in a PI4P-dependent way) and accounts, at least in part, for the enrichment of PS in this membrane (fig. S16). Thus, a PI4P-dependent countertransport mechanism first proposed to mediate cholesterol delivery from the ER to the Golgi complex by Osh4/OSBP (*14*) may apply to at least some other ORP/Osh family members [von Filseck *et al.* (*33*) provide a similar countertransport by Osh6/Osh7 in yeast], mediate export of another lipid from the ER, and operate at the contact sites of the ER with other membranes. Last, our results suggest a role for plasma membrane PI4P as a homeostatic regulation of PM lipid composition independent from its role as a precursor of PI(4,5)P_2.

REFERENCES AND NOTES

1. C. J. Stefan, A. G. Manford, S. D. Emr, *Curr. Opin. Cell Biol.* **25**, 434–442 (2013).
2. J. C. M. Holthuis, A. K. Menon, *Nature* **510**, 48–57 (2014).
3. J. Moser von Filseck, B. Mesmin, J. Bigay, B. Antonny, G. Drin, *Biochem. Soc. Trans.* **42**, 1465–1470 (2014).
4. A. Toulmay, W. A. Prinz, *Curr. Opin. Cell Biol.* **23**, 458–463 (2011).
5. T. Levine, C. Loewen, *Curr. Opin. Cell Biol.* **18**, 371–378 (2006).
6. Y. Elbaz, M. Schuldiner, *Trends Biochem. Sci.* **36**, 616–623 (2011).
7. C. T. Beh, C. R. McMaster, K. G. Kozminski, A. K. Menon, *J. Biol. Chem.* **287**, 11481–11488 (2012).
8. S. Raychaudhuri, W. A. Prinz, *Annu. Rev. Cell Dev. Biol.* **26**, 157–177 (2010).
9. M. de Saint-Jean *et al.*, *J. Cell Biol.* **195**, 965–978 (2011).
10. J. Tong, H. Yang, H. Yang, S. H. Eom, Y. J. Im, *Structure* **21**, 1203–1213 (2013).
11. K. Maeda *et al.*, *Nature* **501**, 257–261 (2013).
12. V. M. Olkkonen, S. Li, *Prog. Lipid Res.* **52**, 529–538 (2013).
13. Y. J. Im, S. Raychaudhuri, W. A. Prinz, J. H. Hurley, *Nature* **437**, 154–158 (2005).
14. B. Mesmin *et al.*, *Cell* **155**, 830–843 (2013).
15. P. A. Leventis, S. Grinstein, *Annu. Rev. Biophys.* **39**, 407–427 (2010).
16. X. Du *et al.*, *J. Cell Biol.* **192**, 121–135 (2011).
17. D. Yan *et al.*, *J. Biol. Chem.* **283**, 332–340 (2008).
18. F. Giordano *et al.*, *Cell* **153**, 1494–1509 (2013).
19. J. Liou *et al.*, *Curr. Biol.* **15**, 1235–1241 (2005).
20. F. Nakatsu *et al.*, *J. Cell Biol.* **199**, 1003–1016 (2012).
21. D. Baird, C. Stefan, A. Audhya, S. Weys, S. D. Emr, *J. Cell Biol.* **183**, 1061–1074 (2008).
22. X. Wu *et al.*, *Dev. Cell* **28**, 19–29 (2014).
23. A. Balla, G. Tuymetova, A. Tsiomenko, P. Várnai, T. Balla, . *Mol. Biol. Cell* **16**, 1282–1295 (2005).
24. G. R. V. Hammond, M. P. Machner, T. Balla, *J. Cell Biol.* **205**, 113–126 (2014).
25. N. Bojjireddy *et al.*, *J. Biol. Chem.* **289**, 6120–6132 (2014).
26. J. E. Vance, R. Steenbergen, *Prog. Lipid Res.* **44**, 207–234 (2005).
27. T. A. Schulz *et al.*, *J. Cell Biol.* **187**, 889–903 (2009).
28. C. J. Stefan *et al.*, *Cell* **144**, 389–401 (2011).
29. Y. Uchida *et al.*, *Proc. Natl. Acad. Sci. U.S.A.* **108**, 15846–15851 (2011).
30. T. Yeung *et al.*, *Science* **319**, 210–213 (2008).
31. S. K. Muthuswamy, M. Gilman, J. S. Brugge, *Mol. Cell. Biol.* **19**, 6845–6857 (1999).
32. P. Varnai, B. Thyagarajan, T. Rohacs, T. Balla, *J. Cell Biol.* **175**, 377–382 (2006).
33. J. Moser von Filseck *et al.*, *Science* **349**, 432–436 (2015).

ACKNOWLEDGMENTS

We thank Y. Cai, X. Wu, C. Schauder, Y. Saheki, J. Park, and X. Bin for discussion and critical technical suggestions; T. Melia for discussion and advice for lipid experiments; and F. Wilson for outstanding technical support. We thank T. Balla for the kind gift of A1 compound. Generous gifts of plasmids are acknowledged in the materials and methods section of the supplementary materials. This work was supported in part from grants from the NIH (DK082700, R37NS036251, DK45735, and DA018343) to P.D.C., grants from the National University of Singapore via the Life Sciences Institute and a Biomedical Research Council (BMRC)–Science and Engineering Research (SERC) joint grant (BMRC-SERC 112 148 0006) from the Agency for Science, Technology and Research to M.R.W, and grants from the Medical Research Internship program of Okayama University and Japan Student Service Organization to K.M.

SUPPLEMENTARY MATERIALS

www.sciencemag.org/content/349/6246/428/suppl/DC1
Materials and Methods
Figs. S1 to S16
Table S1
References (*34*–*39*)
Movies S1 to S3

16 March 2015; accepted 1 July 2015
10.1126/science.aab1370

INTRACELLULAR TRANSPORT

Phosphatidylserine transport by ORP/Osh proteins is driven by phosphatidylinositol 4-phosphate

Joachim Moser von Filseck,[1]* Alenka Čopič,[2]* Vanessa Delfosse,[3,4]* Stefano Vanni,[1] Catherine L. Jackson,[2] William Bourguet,[3,4] Guillaume Drin[1]†

In eukaryotic cells, phosphatidylserine (PS) is synthesized in the endoplasmic reticulum (ER) but is highly enriched in the plasma membrane (PM), where it contributes negative charge and to specific recruitment of signaling proteins. This distribution relies on transport mechanisms whose nature remains elusive. Here, we found that the PS transporter Osh6p extracted phosphatidylinositol 4-phosphate (PI4P) and exchanged PS for PI4P between two membranes. We solved the crystal structure of Osh6p:PI4P complex and demonstrated that the transport of PS by Osh6p depends on PI4P recognition in vivo. Finally, we showed that the PI4P-phosphatase Sac1p, by maintaining a PI4P gradient at the ER/PM interface, drove PS transport. Thus, PS transport by oxysterol-binding protein–related protein (ORP)/oxysterol-binding homology (Osh) proteins is fueled by PI4P metabolism through PS/PI4P exchange cycles.

Membranes of eukaryotic cells vary in their lipid composition, a feature essential to organelle identity (*1*, *2*). It is unclear how lipids are conveyed across the cytosol or at organelle junctions and precisely distributed in the cell (*3*–*5*). The plasma membrane (PM) is highly enriched in the anionic phospholipid phosphatidylserine (PS), which recruits and activates various signaling proteins (*6*). How PS, synthesized in the endoplasmic reticulum (ER) (*7*, *8*), reaches its final destination remains unclear. In yeast, PS is transferred from the ER to the PM by Osh6p or Osh7p (*9*), two members of the oxysterol-binding protein (OSBP)–related protein (ORP)/oxysterol-binding homology (Osh) family (*10*). What drives this directional process is unknown.

Osh6p and Osh7p contain a lipid-binding domain—called ORD (OSBP-related domain)—for transferring PS (*9*), with a short upstream region (fig. S1). Other ORP/Osh proteins have an ORD specific for sterol (*10*–*12*), and two of them, OSBP and Osh4p, exchange sterol with a second lipid, phosphatidylinositol 4-phosphate (PI4P) (*13*, *14*). Like other phosphoinositides, PI4P is confined to specific organelles via the local activity of PI kinases and phosphatases (*15*). PI4P levels are higher in the trans-Golgi and PM than in the ER. OSBP and Osh4p, by sterol/PI4P exchange, use this PI4P gradient to ensure ER-to-

[1]Institut de Pharmacologie Moléculaire et Cellulaire, Université de Nice Sophia-Antipolis and CNRS, 660 route des lucioles, 06560 Valbonne, France. [2]Institut Jacques Monod, CNRS, UMR 7592, Université Paris Diderot, Sorbonne Paris Cité, F-75013 Paris, France. [3]Inserm U1054, 29 rue de Navacelles, 34090 Montpellier, France. [4]CNRS UMR5048, Centre de Biochimie Structurale, 29 rue de Navacelles, 34090 Montpellier, France.
*These authors contributed equally to this work. †**Corresponding author. E-mail: drin@ipmc.cnrs.fr**

Golgi sterol transport (*14*, *16*). Presumably, PI4P is a ligand for all ORP/Osh proteins (*13*, *17*). We thus looked for a link between PI4P and Osh6p/Osh7p transport function.

First, we investigated whether purified Osh6p/Osh7p extracted PI4P from model membranes. We used a PI4P sensor, NBD-PH$_{FAPP}$ (PH domain of the four-phosphate-adaptor protein 1) (*16*), bearing a polarity-sensitive (7-nitrobenz-2-oxa-1,3-diazol) NBD fluorophore, whose emission intensity depends on whether it is soluble or membrane-bound. In the absence of Osh proteins, NBD-PH$_{FAPP}$ was fully bound to PI4P-containing liposomes. Adding Osh6p or Osh7p resulted in a decrease in fluorescence, indicating that they extracted PI4P from liposome (80 to 95% of accessible PI4P) (Fig. 1A). In control experiments, wild-type (WT) Osh4p removed PI4P, whereas Osh4p(H143A/H144A), deficient in binding PI4P (*16*), did not. Unlike Osh4p, Osh6p and Osh7p did not extract dehydroergosterol (DHE), a fluorescent ergosterol (fig. S2).

Consequently, we hypothesized that Osh6p/Osh7p might be lipid exchangers like Osh4p but specific for PS and PI4P. Because Osh6p and Osh7p are close homologs, we focused the rest of our study on Osh6p. With the PI4P extraction assays, we first investigated whether PS competes with PI4P for binding Osh6p using lipids (16:0/18:1 PS and 16:0/16:0 PI4P) that most closely resemble the major yeast PS and PI4P species (*18*). When liposomes contained PI4P and a 2.5-fold excess of PS, the extraction of PI4P by Osh6p was inhibited (Fig. 1B). DHE at the same concentration did not block extraction. Conversely, DHE, but not PS, prevented Osh4p from extracting PI4P. Thus, Osh6p binds PS and PI4P specifically in a mutually exclusive manner.

Next, we examined whether Osh6p exchanged PS with PI4P between membranes. To measure PS transport, we created a fluorescent sensor (NBD-C2$_{Lact}$), based on the lactadherin C2 domain (*19*), selective for PS (fig. S3). NBD-C2$_{Lact}$ was mixed with two liposome populations, one (L$_A$) containing 5% PS and 2% rhodamine-phosphatidylethanolamine (Rhod-PE) and the other (L$_B$) only made of phosphatidylcholine. The signal of NBD-C2$_{Lact}$, bound to L$_A$ liposomes, was quenched due to fluorescence resonance energy transfer with Rhod-PE. Adding Osh6p provoked dequenching because it transported PS to L$_B$ liposomes, thereby promoting the translocation of NBD-C2$_{Lact}$ (Fig. 1C). The initial transport rate (calculated from the signal converted into PS amount in L$_B$ liposomes) was 0.9 ± 0.7 PS/min per Osh6p (mean ± SEM, N = 3 experiments). Osh4p was almost inactive (0.14 ± 0.02 PS/min). When L$_B$ liposomes contained PI4P, Osh6p transported PS 10 times faster (15.4 ± 1.5 PS/min), whereas only a slight increase was seen with Osh4p (Fig. 1C). Osh6p moved short and saturated PS species faster (fig. S4).

Using a similar assay with NBD-PH$_{FAPP}$, we followed PI4P transport in the back direction, from L$_B$ liposomes with 4% PI4P and 2% Rhod-PE to L$_A$ liposomes (containing or not containing 5% PS). In the absence of PS, Osh6p transferred PI4P at an initial velocity of 8 PI4P/min (Fig. 1D). Transport increased by a factor of about 2 in the presence of PS. In control assays, PI4P transport by Osh4p was slightly enhanced by PS but was much faster when L$_A$ liposomes contained the proper counterligand DHE. Thus, Osh6p transported PS and PI4P along opposite routes. Both lipids were transported faster, with similar velocities, when they were initially in distinct membranes, suggesting that Osh6p is a PS/PI4P exchanger.

Next, we solved the crystal structure of Osh6p in complex with PI4P to define how it binds this lipid (Fig. 2A, fig. S5A, and table S1). The structure (at 2.55 Å resolution) is similar to that of PS-bound Osh6p (root mean square deviation = 0.36 Å for 403 residues) (fig. S5, B and C). The electron density of ligand corresponds to 18:0/20:4 PI4P (main PI4P species used for crystallization). The stearate (18:0 chain) at the *sn*-1 position of the glycerol backbone of PI4P is deeply inserted into the binding pocket, whereas the *sn*-2 arachidonate (20:4) is twisted, pointing its end to the lid (residues 35 to 69) that closes the pocket (Fig. 2A). The 4-phosphate group makes hydrogen bonds with H157, H158, and R359 side chains and water-mediated hydrogen bonds with R66 and E355 main chains. The 1-phosphate group interacts with the backbone amide of L69, K126, N129, and K351. Free hydroxyl groups of inositol interact with T65, N129, and E355. As seen for other ORD structures (*13*, *17*), PI4P recognition relies on residues conserved in ORP/Osh family members, like the histidine pair, reinforcing the idea that PI4P is a ligand common to all ORP/Osh proteins.

Molecular dynamics (MD) simulations were carried out to compare how PS or PI4P bind to Osh6p. Both lipids had limited motion in the binding pocket (fig. S6, A and B). The mobile parts of Osh6p (except loops) were the lid and α7 helix. No differences in the amplitude and/or opening of the lid were seen between the complexes (fig. S6C). The interaction energy between PI4P and Osh6p was ~50% higher (–1029.6 kJ/mol) than that between PS and Osh6p (–628 kJ/mol). In both cases, the contribution of acyl chains to the

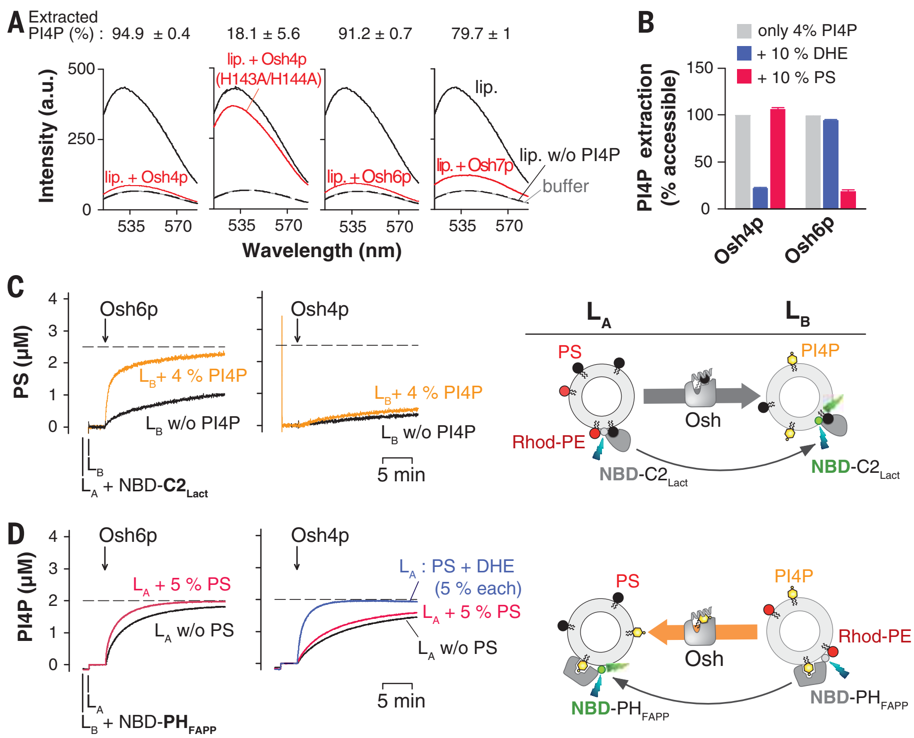

Fig. 1. Osh6p is a PS/PI4P exchanger. (**A**) Fluorescence spectra of NBD-PH$_{FAPP}$ (250 nM) mixed with liposomes (150 µM lipid, 4% PI4P) in the absence or presence of Osh protein (3 µM). Normalized signal gives the percentage of extracted PI4P. (**B**) PI4P extraction by Osh protein from liposomes containing 4% PI4P and, additionally, 10% PS or DHE. (**C**) PS transport by Osh protein (200 nM) injected into a suspension of L$_A$ liposomes containing 5% PS and 2% Rhod-PE, mixed with NBD-C2$_{Lact}$ (250 nM) and L$_B$ liposomes (with 0 or 4% PI4P). (**D**) PI4P transport by Osh protein added to L$_B$ liposomes containing 4% PI4P and 2% Rhod-PE, mixed with NBD-PH$_{FAPP}$ (250 nM) and L$_A$ liposomes (with or without PS). [L$_A$] = [L$_B$] = 200 µM total lipids. NBD signals were converted into PS and PI4P amount (µM) in L$_B$ and L$_A$ liposomes, respectively. Dashed line, equilibrium. All values are means ± SEM (N = 3 experiments).

interaction was similar (about –300 kJ/mol) (Fig. 2B). In contrast, some residues (R66, H157, H158, and R359) made strong and almost exclusive contacts with PI4P (Fig. 2C and fig. S7), accounting for the differential interaction energy calculated for PS and PI4P. The binding of the 4-phosphate group to Osh6p (–517 kJ/mol) represented 50% of the Osh6p-PI4P interaction energy.

Based on our structural analysis, we designed Osh6p mutants deficient in binding PI4P and/or PS: a H157A/H158A mutant lacking the histidines that recognize PI4P, a reverse-charge mutant K351E (K351 binds PI4P and, as suggested by simulation, PS), and a Δ69-Osh6p mutant (residues 70 to 448) lacking the N-terminal region and ORD lid. We tested the transport activity of these mutants and of Osh6p(L69D), deficient in binding PS (*9*). Like Osh6p WT, all mutants slowly transported PS or PI4P in the absence of counterligand, with Δ69-Osh6p showing no PS transport. In assays with both lipids, all mutants had a slower PS and PI4P transport activity compared with Osh6p WT. Whereas Osh6p(L69D) was defective for both PI4P and PS transport, Osh6p(K351E) and Osh6p(H157A/H158A) did not transfer PI4P while transporting PS at a moderate rate, and Δ69-Osh6p transported some PI4P but no PS (Fig. 2D). The mutants that still transport lipid into acceptor membranes without transporting back the counterligand likely retain some affinity for this latter, allowing them to better target these membranes. Our assays, showing that PS and PI4P transport rates appeared linked and were maximal only when Osh6p could properly recognize both lipids, confirmed that Osh6p is a PS/PI4P exchanger.

These data suggested that the transport of PS mediated by Osh6p at the ER/PM interface might depend on PI4P. To test this hypothesis in vivo, we expressed Osh6p-mCherry WT or mutants in a *cho1*Δ strain lacking endogenous Osh6p and Osh7p to compare their PS-transport ability. The *cho1*Δ mutation blocks PS synthesis, greatly diminishing PS levels and leading to cytosolic localization of $C2_{Lact}$-GFP (green fluorescent protein) (*20*, *21*). Lyso-PS added to *cho1*Δ cells is converted into PS and rapidly transferred from the ER to the PM when Osh6p is expressed (*9*), as indicated by $C2_{Lact}$-GFP redistribution (Fig. 2E). Analysis of $C2_{Lact}$-GFP fluorescence profiles showed a large increase of peripheral intensity peaks compared with internal intensity peaks (Fig. 2F and fig. S8). In contrast, when Osh6p was missing or replaced by Osh6p(L69D), the

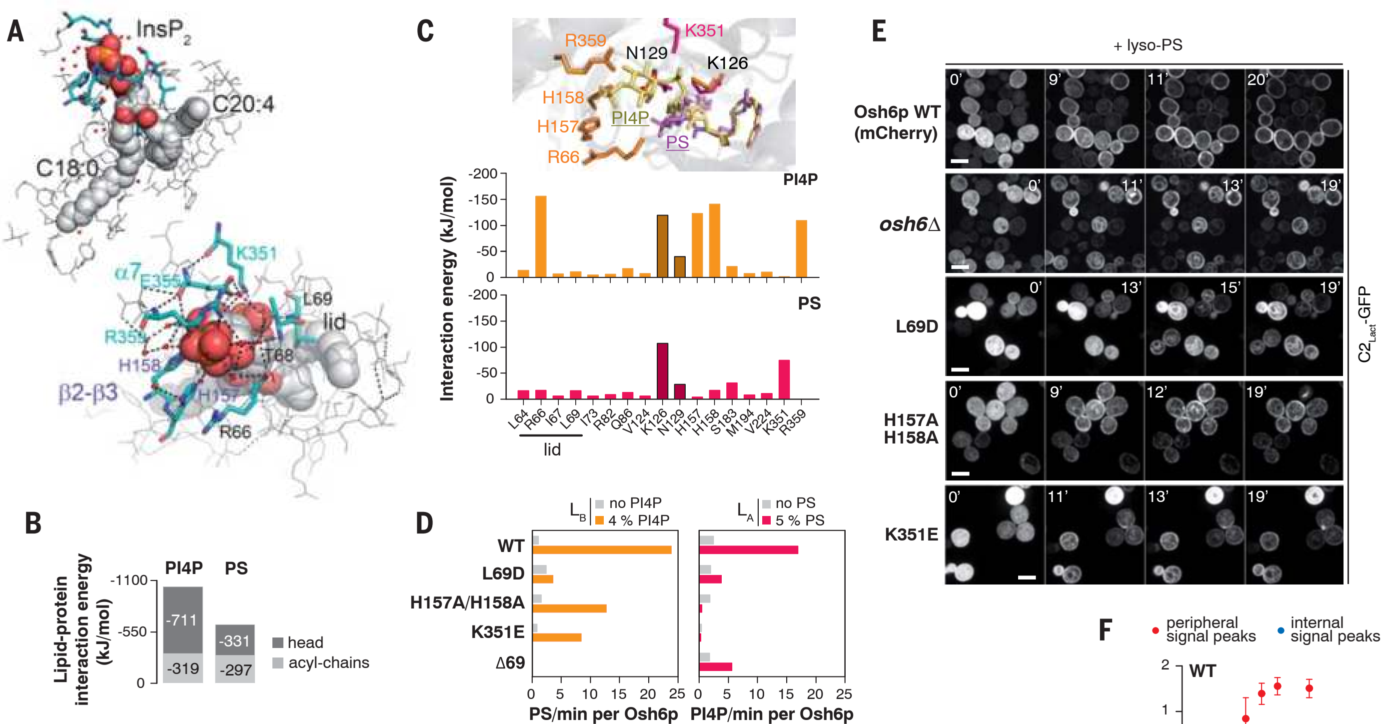

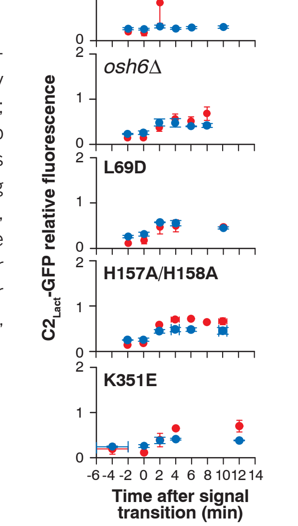

Fig. 2. Cellular Osh6p activity depends on PI4P recognition. (**A**) Structure of PI4P-bound Osh6p (PI4P in sphere). Close-up view: key residues coordinating the head group. Red dots, water molecules; dashed lines, H bonds. (**B**) Interaction energy of 16:0/18:1-PS or 18:0/20:4-PI4P with Osh6p. (**C**) Main interaction energy between PS or PI4P and Osh6p residues (mean; *N* = 2 experiments). K126 and N129 are key interacting residues for both lipids. (**D**) PS and PI4P transport activity of Osh6p WT or mutants (200 nM) when, initially, the second lipid is absent or the two lipids are present in distinct liposomes (mean; *N* = 2 experiments). (**E**) Redistribution of $C2_{Lact}$-GFP in PS-depleted yeast cells (*osh6*Δ*osh7*Δ*cho1*Δ) expressing Osh6p-mCherry WT or mutants after adding 18:1 lyso-PS. Time points: lyso-PS injection (0 min), first transition in signal, maximal ER signal, end of time course. Scale bar, 5 μm. (**F**) Quantification of $C2_{Lact}$-GFP localization showing relative levels in peripheral (red) and internal (blue) membrane signal peaks (mean ± SD, *N* = 3 experiments, ~20 cells per experiment). Internal peaks = mostly ER; peripheral = ER + PM. Time is adjusted (see fig. S8). (Single-letter abbreviations for the amino acid residues are as follows: A, Ala; C, Cys; D, Asp; E, Glu; F, Phe; G, Gly; H, His; I, Ile; K, Lys; L, Leu; M, Met; N, Asn; P, Pro; Q, Gln; R, Arg; S, Ser; T, Thr; V, Val; W, Trp; and Y, Tyr.)

intensities of internal and peripheral signal peaks increased concomitantly, indicating that PS mostly remained at the ER. Compared with Osh6p(L69D), in agreement with our in vitro data, Osh6p(H157A/H158A) and Osh6p(K351E) seemed somewhat less defective in transporting PS to the PM, because the peripheral intensity peaks increased slightly more than the internal peaks (Fig. 2, E and F, and figs. S8 and S9). However, the transport efficiencies were lower than that of Osh6p WT by about an order of magnitude. The mutant Osh6p(H157A/H158A/K351E) displayed a similar phenotype (figs. S8 and S9). Thus, recognizing PI4P is critical for Osh6p to mediate the ER-to-PM PS transport.

To move PS from the ER to the PM, Osh6p should transport PI4P down its gradient in the reverse direction and would be active only if ER PI4P levels remain low. Dephosphorylation of PI4P by the ER-resident Sac1p, the major yeast PI4P phosphatase (*22*, *23*), should thus be critical for Osh6p activity. PS was mislocalized to internal membranes in *sac1Δ* cells (*24*) (fig. S10A). We probed whether the lack of Sac1p affected PS transport directly using a *cho1Δ sac1Δ* strain and following $C2_{Lact}$-GFP redistribution after adding lyso-PS. $C2_{Lact}$-GFP remained blocked at the ER in *sac1Δ* cells, although Osh6p was present (Fig. 3, A and B, and fig. S10B). The ER-to-PM transport of PS was also blocked in *cho1Δ sac1-23* cells at the nonpermissive temperature (Fig. 3, C and D). In vitro, the PS-transport activity of Osh6p was stimulated when a PI4P gradient preexisted between membranes (as in Fig. 1C) but not when PI4P was equilibrated (Fig. 3E). Sac1p might act in trans between the ER and PM (*25*). We rather propose that it acts in cis, hydrolyzing the PI4P delivered by Osh6p and maintaining a PI4P gradient at the ER/PM interface mandatory for its transport activity.

Deciphering the mechanism of lipid transport is key to understanding how organelle identity is maintained (*3*–*5*). Osh6p/Osh7p colonize ER-PM junctions, which might contain high PS levels due to concentration of Cho1p/Pss1p at these sites, allowing PS to be transported along its gradient to the PM (*9*, *26*). Instead, we propose that Osh6p and Osh7p extract PS from the ER, exchange PS with PI4P at the PM, and transport PI4P to the ER. Given the key contribution of the 4-phosphate group for the Osh6p-PI4P interaction, PI4P hydrolysis might facilitate PS uptake from the ER. Maintenance of a PI4P gradient by Sac1p (and Stt4p producing PM PI4P) would sustain PS/PI4P exchange cycles, and thereby PS delivery to the PM, against its concentration gradient (Fig. 3F). These results, along with those obtained with sterol/PI4P exchangers (*13*, *14*, *16*) and ORP5/ORP8 (*27*), suggest a general mechanism by which ORP/Osh proteins use PI4P metabolism to build distinct intracellular lipid gradients.

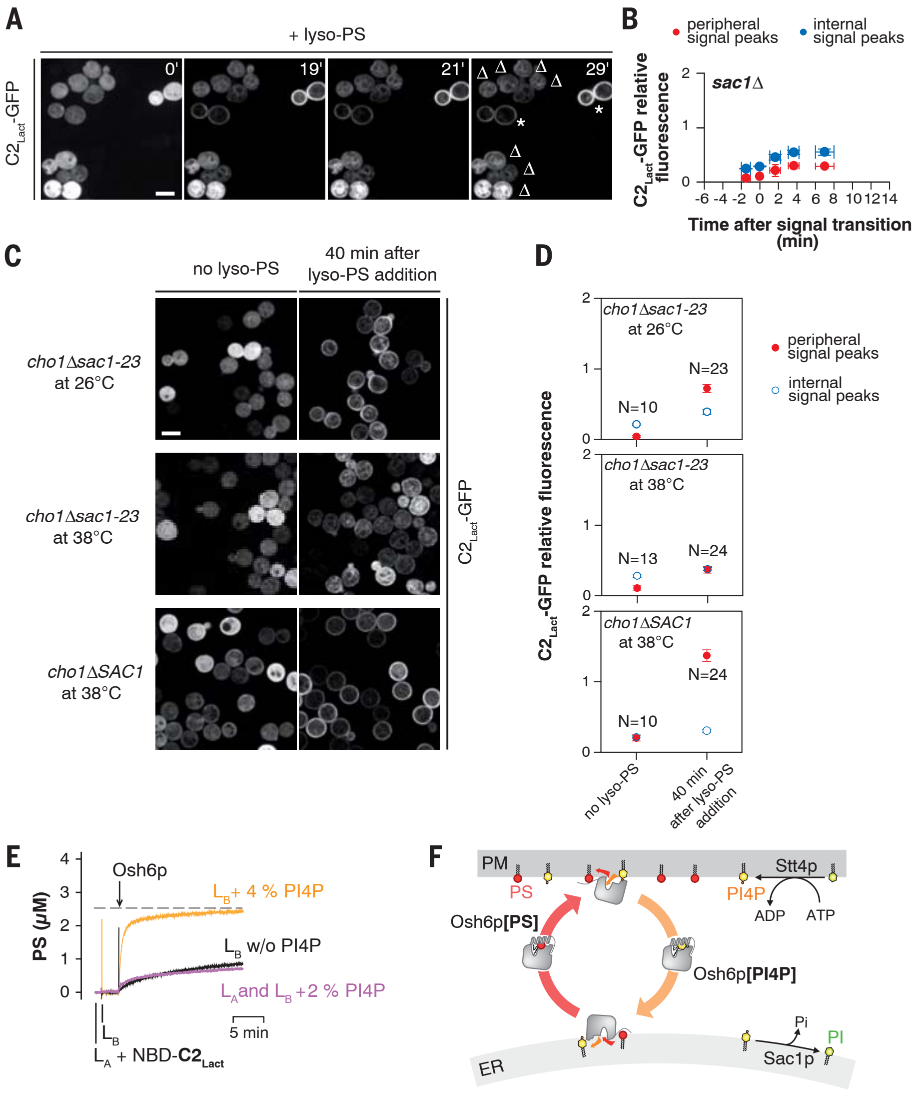

Fig. 3. Sac1p maintains PS transport by Osh6p. (**A**) $C2_{Lact}$-GFP redistribution in *SAC1* (*) and *sac1Δ* cells (Δ), depleted for PS and expressing Osh6p-mCherry, after adding lyso-PS. Scale bars, 5 μm. (**B**) Quantification of $C2_{Lact}$-GFP localization as in Fig. 2F (mean ± SD, *N* = 3 experiments). (**C**) $C2_{Lact}$-GFP distribution in *cho1Δsac1-23* or *cho1Δ* cells at permissive (26°C) or nonpermissive temperature (38°C) for the *sac1* allele before and after a 40-min incubation with lyso-PS. The experiment was repeated twice; representative images from one experiment are shown. (**D**) Quantification (mean ± SEM, *N* = number of cells) of the experiments shown in (C). (**E**) PS transport assays with L_B liposomes containing 0 or 4% PI4P or with L_A and L_B liposomes, both containing 2% PI4P. L_A liposome contains 5% PS. (**F**) Model for the coupling between PI4P metabolism and Osh6p-mediated PS/PI4P exchange.

REFERENCES AND NOTES

1. J. Bigay, B. Antonny, *Dev. Cell* **23**, 886–895 (2012).
2. G. Drin, *Annu. Rev. Biochem.* **83**, 51–77 (2014).
3. W. A. Prinz, *Cell* **143**, 870–874 (2010).
4. T. Levine, *Trends Cell Biol.* **14**, 483–490 (2004).
5. J. C. Holthuis, A. K. Menon, *Nature* **510**, 48–57 (2014).
6. P. A. Leventis, S. Grinstein, *Annu. Rev. Biophys.* **39**, 407–427 (2010).
7. J. E. Vance, R. Steenbergen, *Prog. Lipid Res.* **44**, 207–234 (2005).
8. E. Zinser *et al.*, *J. Bacteriol.* **173**, 2026–2034 (1991).
9. K. Maeda *et al.*, *Nature* **501**, 257–261 (2013).
10. S. Raychaudhuri, W. A. Prinz, *Annu. Rev. Cell Dev. Biol.* **26**, 157–177 (2010).
11. Y. J. Im, S. Raychaudhuri, W. A. Prinz, J. H. Hurley, *Nature* **437**, 154–158 (2005).
12. N. D. Ridgway, *Subcell. Biochem.* **51**, 159–182 (2010).
13. M. de Saint-Jean *et al.*, *J. Cell Biol.* **195**, 965–978 (2011).
14. B. Mesmin *et al.*, *Cell* **155**, 830–843 (2013).
15. G. Di Paolo, P. De Camilli, *Nature* **443**, 651–657 (2006).
16. J. Moser von Filseck, S. Vanni, B. Mesmin, B. Antonny, G. Drin, *Nat. Commun.* **6**, 6671 (2015).
17. J. Tong, H. Yang, H. Yang, S. H. Eom, Y. J. Im, *Structure* **21**, 1203–1213 (2013).
18. C. S. Ejsing *et al.*, *Proc. Natl. Acad. Sci. U.S.A.* **106**, 2136–2141 (2009).
19. T. Yeung *et al.*, *Science* **319**, 210–213 (2008).
20. G. D. Fairn *et al.*, *J. Cell Biol.* **194**, 257–275 (2011).
21. W. R. Riekhof *et al.*, *J. Biol. Chem.* **282**, 36853–36861 (2007).
22. M. Foti, A. Audhya, S. D. Emr, *Mol. Biol. Cell* **12**, 2396–2411 (2001).
23. F. Faulhammer *et al.*, *Traffic* **8**, 1554–1567 (2007).
24. M. Tani, O. Kuge, *Yeast* **31**, 145–158 (2014).
25. C. J. Stefan *et al.*, *Cell* **144**, 389–401 (2011).
26. H. Pichler *et al.*, *Eur. J. Biochem.* **268**, 2351–2361 (2001).
27. J. Chung *et al.*, *Science* **349**, 428–432 (2015).

ACKNOWLEDGMENTS

We thank B. Antonny, M. Dauvois, M. de Saint-Jean, L. d'Esposito, K. Eudes, C. La Torre, N. Leroudier, S. Léon, the staff of the

European Synchrotron Radiation Facility (Grenoble, France), and the imaging facility of the Institut Jacques Monod (ImagoSeine) for help. This work was supported by the CNRS, the Agence Nationale de la Recherche (ANR-2010-1503-01), the European Research Council (ERC advanced grant 268888), the French Infrastructure for Integrated Structural Biology (FRISBI, ANR-10-INSB-05-01), and a Marie Curie Grant to A.C. (6319977). J.M.v.F. was supported by the ERC. Osh6p-PI4P structure is available under the Protein Data Bank code 4PH7.

SUPPLEMENTARY MATERIALS

www.sciencemag.org/content/349/6246/432/suppl/DC1
Materials and Methods
Figs. S1 to S10
Table S1
References (*28*–*39*)

16 March 2015; accepted 1 July 2015
10.1126/science.aab1346

AUTOIMMUNE DISEASE

Patients with LRBA deficiency show CTLA4 loss and immune dysregulation responsive to abatacept therapy

Bernice Lo,[1,2]* Kejian Zhang,[3]* Wei Lu,[1,2] Lixin Zheng,[1,2] Qian Zhang,[2,4] Chrysi Kanellopoulou,[1,2] Yu Zhang,[2,4] Zhiduo Liu,[5] Jill M. Fritz,[1,2] Rebecca Marsh,[6] Ammar Husami,[3] Diane Kissell,[3] Shannon Nortman,[3] Vijaya Chaturvedi,[6] Hilary Haines,[7] Lisa R. Young,[8] Jun Mo,[9] Alexandra H. Filipovich,[6] Jack J. Bleesing,[6] Peter Mustillo,[10] Michael Stephens,[11] Cesar M. Rueda,[12] Claire A. Chougnet,[12] Kasper Hoebe,[12] Joshua McElwee,[13] Jason D. Hughes,[13] Elif Karakoc-Aydiner,[14] Helen F. Matthews,[1,2] Susan Price,[1,2] Helen C. Su,[2,4] V. Koneti Rao,[1,2] Michael J. Lenardo,[1,2]† Michael B. Jordan[6,12]†‡

Mutations in the *LRBA* gene (encoding the lipopolysaccharide-responsive and beige-like anchor protein) cause a syndrome of autoimmunity, lymphoproliferation, and humoral immune deficiency. The biological role of LRBA in immunologic disease is unknown. We found that patients with *LRBA* deficiency manifested a dramatic and sustained improvement in response to abatacept, a CTLA4 (cytotoxic T lymphocyte antigen-4)–immunoglobulin fusion drug. Clinical responses and homology of LRBA to proteins controlling intracellular trafficking led us to hypothesize that it regulates CTLA4, a potent inhibitory immune receptor. We found that LRBA colocalized with CTLA4 in endosomal vesicles and that *LRBA* deficiency or knockdown increased CTLA4 turnover, which resulted in reduced levels of CTLA4 protein in FoxP3$^+$ regulatory and activated conventional T cells. In LRBA-deficient cells, inhibition of lysosome degradation with chloroquine prevented CTLA4 loss. These findings elucidate a mechanism for CTLA4 trafficking and control of immune responses and suggest therapies for diseases involving the CTLA4 pathway.

Common variable immune deficiency (CVID) is a heterogeneous primary immunodeficiency characterized by antibody deficiency, infections, autoimmunity, and lymphoproliferation (*1*, *2*). Lymphocytic interstitial lung disease (ILD) causes substantial morbidity and mortality in CVID, and there is no effective treatment (*3*–*6*). CVID can be caused by "lipopolysaccharide (LPS)–responsive vesicle trafficking, beach- and anchor-containing" (*LRBA*) gene defects (*7*). The LRBA protein has domains homologous to vesicle trafficking proteins, but its function and relation to disease pathogenesis are unknown (*8*, *9*).

Cytotoxic T lymphocyte–associated protein 4 (CTLA4) is an inhibitory checkpoint protein, expressed on activated T cells and FoxP3$^+$ regulatory T cells (T_{regs}) (*10*). CTLA4 inhibits immune responses by negative signaling, by competition with the costimulatory molecule CD28 for the ligands CD80 and CD86, or by removing these ligands from antigen-presenting cells by transendocytosis (*11*, *12*). CTLA4 resides in endocytic vesicles that are released to the cell surface after T cell receptor (TCR) stimulation (*13*). The clinical effectiveness and adverse effects of CTLA4 modulation are revealed by three approved drugs that mimic or target CTLA4: abatacept for rheumatoid arthritis, belatacept for prevention of rejection after renal transplantation, and ipilimumab for the immunotherapy of melanoma (*14*–*16*).

We identified nine patients with immune deficiency and/or autoimmunity from eight unrelated kindreds with biallelic loss-of-function mutations in *LRBA* that have not been previously reported (Fig. 1A). All mutations decreased or abolished LRBA protein expression as assessed by immunoblotting and flow cytometry (Fig. 1, B and C, and fig. S1).

The clinical features of these patients are described in detail in the supplementary text and table S1. Most patients were diagnosed in early childhood with CVID, and all patients experienced substantial inflammatory and/or autoimmune complications. Notably, *LRBA* deficiency was associated with interesting phenotypic characteristics in several patients, including type 1 diabetes mellitus (patients 1 and 2), Burkitt's lymphoma (patient 6), and exocrine pancreatic insufficiency (patient 1). Patients 1 to 3 experienced severe ILD—consisting of dense, predominantly T cell interstitial infiltrates—which was refractory to multiple medications and led to progressive impairment of lung function (Fig. 1D). Note that, when patients were treated with abatacept [a CTLA4-immunoglobulin (CTLA4-Ig) fusion protein that inhibits T cell responses by competing for costimulatory ligands], their overall clinical status, computed tomography (CT) scans, and pulmonary function showed rapid and dramatic improvement (Fig. 2). Treatment also halted ongoing inflammatory and/or autoimmune conditions (Fig. 2A); decreased levels of soluble CD25 (sCD25, a biomarker of T cell–mediated inflammation) (*17*); increased naïve:effector (CD45RA:RO) T cell ratios (fig. S2); and improved functional antibody responses to polysaccharide vaccine antigens in patient 2. In the three patients treated initially, the improvements in lung disease were maintained when abatacept was continued for 5 to 8 years. This treatment had minimal infectious or autoimmune complications. Patients 1 and 3 acquired norovirus infection (see supplementary text), which can cause chronic enteritis

[1]Molecular Development of the Immune System Section and Clinical and Molecular Genomics Unit, Laboratory of Immunology, National Institute of Allergy and Infectious Diseases, National Institutes of Health, Bethesda, MD, USA. [2]NIAID Clinical Genomics Program, National Institute of Allergy and Infectious Diseases, National Institutes of Health, Bethesda, MD, USA. [3]Division of Human Genetics, Department of Pediatrics, Cincinnati Children's Hospital Medical Center, University of Cincinnati, Cincinnati, OH, USA. [4]Human Immunological Diseases Unit, Laboratory of Host Defenses, National Institute of Allergy and Infectious Diseases, National Institutes of Health, Bethesda, MD, USA. [5]Lymphocyte Biology Section, Laboratory of Systems Biology, National Institute of Allergy and Infectious Diseases, National Institutes of Health, Bethesda, MD, USA. [6]Division of Bone Marrow Transplantation and Immune Deficiency, Department of Pediatrics, Cincinnati Children's Hospital Medical Center, University of Cincinnati, Cincinnati, OH, USA. [7]Division of Pediatric Hematology and Oncology, Department of Pediatrics, University of Alabama at Birmingham, AL, USA. [8]Division of Allergy, Immunology, and Pulmonary Medicine, Department of Pediatrics, and Division of Allergy, Pulmonary, and Critical Care, Department of Medicine, Vanderbilt University School of Medicine, Nashville, TN, USA. [9]Departments of Pathology and Pediatrics, University of California, San Diego and Rady Children's Hospital, San Diego, CA, USA. [10]Section of Allergy and Immunology, Nationwide Children's Hospital, Columbus, OH, USA. [11]Department of Pediatrics and Adolescent Medicine, Mayo Clinic, Rochester, MN, USA. [12]Division of Immunobiology, Department of Pediatrics, Cincinnati Children's Hospital Medical Center/ University of Cincinnati, Cincinnati, OH, USA. [13]Merck Research Laboratories, Merck & Co, Boston, MA, USA. [14]Marmara University, Division of Pediatric Allergy and Immunology, Istanbul, Turkey.
*These authors contributed equally to this work. †These authors contributed equally to this work. **‡Corresponding author. E-mail: michael.jordan@cchmc.org**

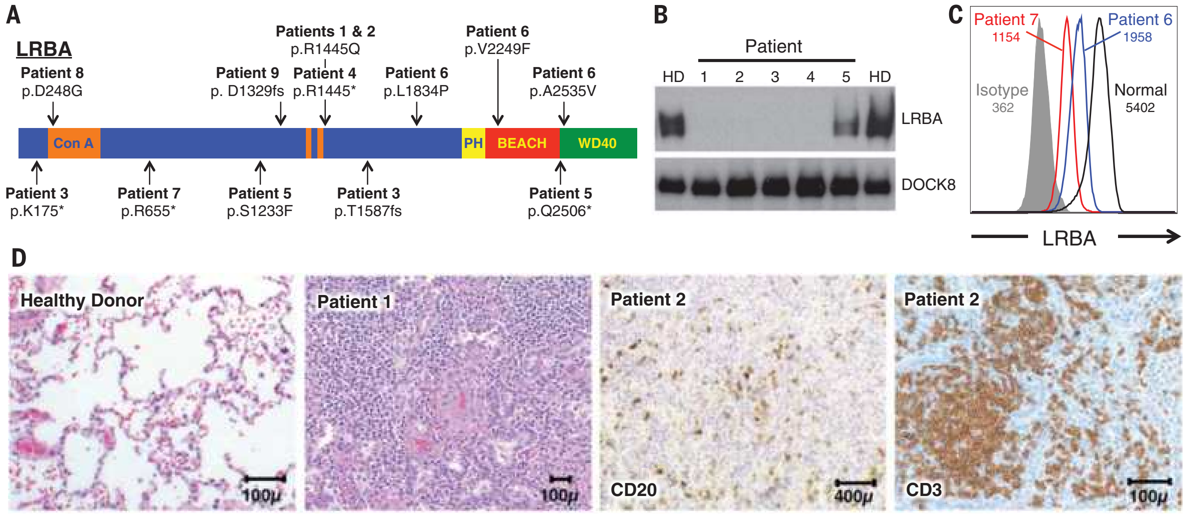

Fig. 1. LRBA deficiency and interstitial lung disease. (**A**) Shown are the novel biallelic *LRBA* mutations of nine patients from eight unrelated kindreds mapped onto a schematic representation of LRBA illustrating the protein domains. Amino acid changes are referred to by their single letter code. Asterisk (*) indicates a premature stop codon. Orange thin double bars indicate the A-kinase–anchoring protein (AKAP) motif. Con A, Con A–like lectin domain. Patients 3 and 5 are compound heterozygous for the two mutations indicated. Patient 6 is compound heterozygous for p.V2249F mutation from father and p.A2535V and p.L1834P mutations from mother. Patient 8 is compound heterozygous for the mutation indicated and an intronic mutation c.8502-1G>C, which is predicted to affect mRNA splicing. (**B**) Immunoblotting for patients 1 to 5 and (**C**) flow cytometry for patients 6 and 7 show loss of LRBA compared with a healthy donor (HD). DOCK8 is included as a loading control. Mean fluorescence intensity for LRBA is indicated in histogram. (**D**) Hematoxylin and eosin staining of healthy donor lung and lung from patient 1. Also shown are immunostains for CD20 (B cells) and CD3 (T cells) on lung from patient 2. Scale bars are indicated in microns.

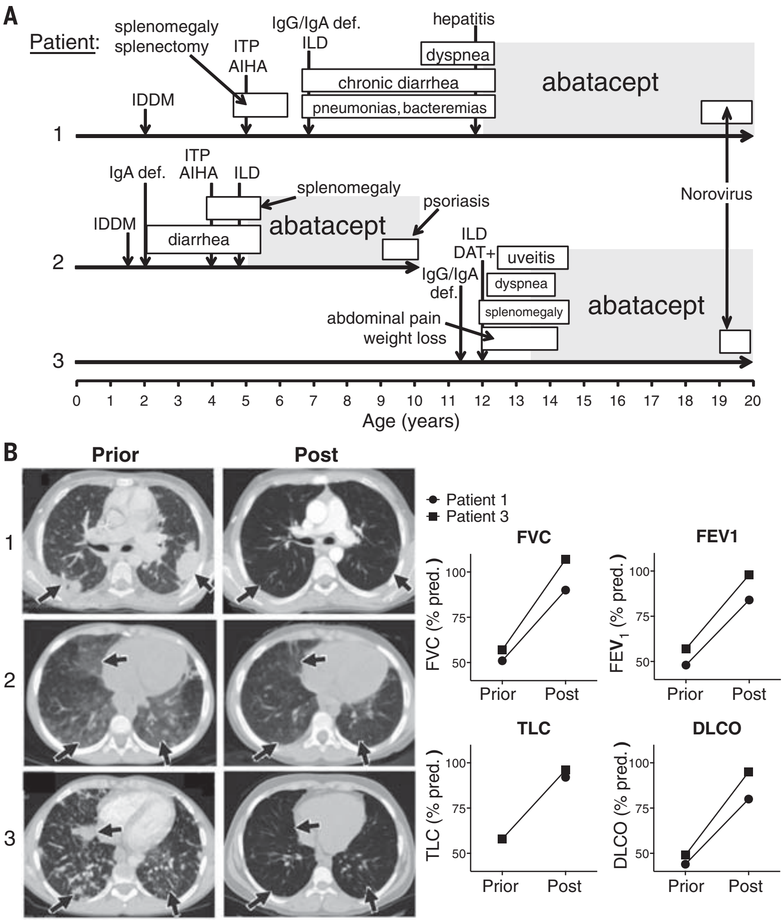

Fig. 2. Sustained response to abatacept in three *LRBA*-deficient patients. (**A**) Timeline showing multiple clinical features and therapy with abatacept in patients 1 to 3. Gray shading indicates time of therapy with abatacept with dosing initially 20 mg/kg of body weight intravenously (i.v.) every 2 weeks for patients 1 and 3, and 20 mg/kg i.v. every 4 weeks in patient 2. "Norovirus" indicates onset of intermittent abdominal symptoms associated with acquisition of chronic norovirus infection. (**B**) High-resolution CT scans (patients 1 to 3) and pulmonary function tests (patients 1 and 3) before and after abatacept. Arrows highlight examples of lung disease improvement before and after abatacept. FVC, forced vital capacity; FEV1, forced expiratory volume; TLC, total lung capacity; DLCO, diffusing capacity of the lungs for carbon monoxide.

in patients with CVID (*18*). Patient 1 also developed *Legionella pneumophila* pneumonia, and patient 2 developed psoriasis. Patients 4, 8, and 9 were started on abatacept within the last 6 months for the treatment of intractable enteritis and other features of autoimmunity and have begun to show improvement (see supplementary text).

Given the dramatic clinical improvement of *LRBA*-deficient patients with a CTLA4 immunomodulator, we hypothesized that LRBA might control the expression, function, or trafficking of CTLA4. In healthy donors, CTLA4 is mainly in intracellular vesicles of T_{regs} (*19*). CTLA4 can be mobilized to the cell surface by TCR stimulation (fig. S3A). We found that the abundance of total (intracellular) and mobilized (cell surface) CTLA4 was substantially depressed in T_{regs} from *LRBA*-deficient patients (Fig. 3A and fig S3, A to C). Note that *CTLA4* mRNA levels were normal in these patients, which suggested that *LRBA* posttranslationally regulates CTLA4 protein (fig. S3C). After stimulation with CD3-specific antibody and interleukin 2 (IL-2), conventional ($FoxP3^-$) T cells express CTLA4, but this response was also deficient in patient cells (fig. S3D). Patients 5 and 6, who have residual LRBA protein (Fig. 1, B and C), had the highest residual CTLA4 levels in $FoxP3^+$ T cells (Fig. 3A, triangles), which suggests an LRBA dose-dependent effect on CTLA4 expression. Even so, patient samples showed normal mobilization of other endosomal proteins, including CD154 and CD107 (*20*), which indicated that LRBA-deficient T cells were not globally defective in vesicle trafficking (fig. S4). We also found that CTLA4-dependent cellular functions were impaired in patient cells: $CD4^+$ and $CD8^+$ T cells were hyperproliferative in vitro; patient T_{regs} showed impaired trans-endocytosis of CD80 and had decreased suppressive function in a CTLA4-dependent assay (fig. S5). Consistent with these functional defects and the reported phenotypes of CTLA4-haploinsufficient patients and the original description of *LRBA*-deficient patient T_{regs} by Charbonnier and colleagues (*21*, *22*), we found that patient T_{regs} expressed lower levels of CD25 and Foxp3 along with CTLA4 (fig. S6).

To verify that *LRBA* deficiency was sufficient to impair CTLA4 expression, we performed small interfering RNA (siRNA)–mediated knockdown of *LRBA* in normal donor T cells. This treatment lowered the abundance of CTLA4 protein to levels comparable to those in patient samples but had no effect on *CTLA4* mRNA (Fig. 3B and fig. S7B). Further, when protein synthesis was inhibited with cycloheximide (CHX), CTLA4 protein was rapidly lost in *LRBA* knockdown cells, which indicated accelerated degradation (Fig. 3C). Thus, decreased LRBA protein caused an apparent posttranslational loss of CTLA4 protein in T cells. CTLA4 trafficking to the cell surface was apparently not impaired by LRBA deficiency, because the amount of CTLA4 that mobilized to the cell surface was proportional to the total intracellular levels of CTLA4 (Fig. 3, A and B). We also found that CTLA4 endocytosis was normal after *LRBA* knockdown using previously described techniques. The majority of CTLA4 was internalized whether or not *LRBA* was knocked down (fig. S8).

These results, especially the rapid loss of CTLA4 after CHX treatment, led us to hypothesize that LRBA regulates the lysosomal degradation of

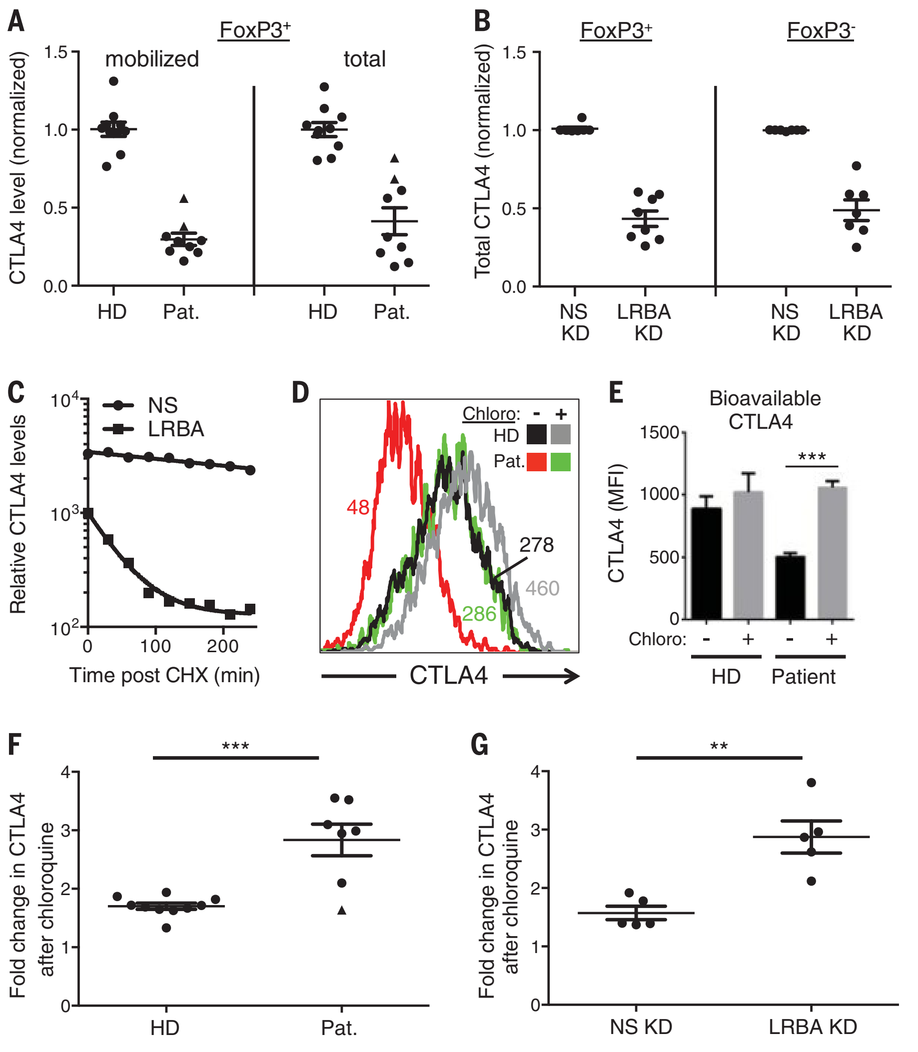

Fig. 3. LRBA regulates CTLA4 protein turnover. (**A**) The quantification of total and surface mobilized CTLA4 in $FoxP3^+$ T cells from healthy donors (HD) and *LRBA*-deficient patients (Pat.). $FoxP3^+$ cells were assessed fresh or after overnight culture in medium alone. Triangles represent the two patients (5 and 6) with residual LRBA protein expression. Data are normalized as described in Materials and Methods and represented as means ± SEM. $P < 0.001$, for all displayed comparisons of healthy donors and patients (unpaired *t* test). (**B**) siRNA-mediated KD of *LRBA* in T cells from healthy donors suppressed CTLA4 levels in $FoxP3^+$ and $FoxP3^-$ T cells compared with nonspecific (NS) siRNA-transfected cells. $P < 0.001$, for comparisons of NS and *LRBA* knockdown (unpaired *t* test). (**C**) CTLA4 turnover kinetics were evaluated. NS or *LRBA* KD cells from normal donors were cultured for varying amounts of time with cycloheximide (CHX) to block protein synthesis, then total amounts of CTLA4 protein were assessed by flow cytometry. Relative CTLA4 levels were calculated as the geometric mean fluorescence of CTLA4 staining minus that of the isotype control. Data are representative of three or more independent experiments. (**D** and **F**) Healthy donor and patient-derived T cells were cultured overnight with or without chloroquine, and total CTLA4 levels were assessed by flow cytometry. Mean fluorescence intensities of CTLA4 staining are indicated on histogram. Fold change in CTLA4 levels after chloroquine exposure for the individual control and patient samples is shown. Means ± SEM are shown. $***P < 0.001$ (unpaired *t* test). Triangular point represents patient 5 (with residual LRBA expression). (**E**) T cells from HD and patients were cultured with or without chloroquine and CTLA4 staining within $CD4^+Foxp3^+$ cells was assessed by mean fluorescence intensity (MFI). "Bioavailable" refers to signal not associated with Golgi (58k), lysosomes (CD107a), or autophagosomes (LC3) and, hence, includes CTLA4 available for mobilization to the cell surface. $***P < 0.01$, as determined by *t* test (unpaired, two-tailed) (**G**) NS or *LRBA* KD cells from normal donors were cultured with or without chloroquine, and total CTLA4 was assessed by flow cytometry. $**P = 0.003$ (unpaired *t* test).

CTLA4. Indeed, when we examined the subcellular localization of CTLA4 using a flow microscopy technique (Imagestream), we found that more CTLA4 localized to CD107⁺ lysosomes in patient T cells than in T cells from healthy donors (fig. S9). Furthermore, when we treated T cells from patients and healthy donors with chloroquine to inhibit lysosomal degradation, we found that CTLA4 protein levels rose sharply in patient T cells but only modestly in healthy donor (HD) T cells (Fig. 3, D to F, and fig. S10). We also observed rescue of CTLA4 in *LRBA* knockdown cells with chloroquine and other agents that inhibit lysosomal acidification, fusion, or protein degradation, including brefeldin A, monensin, NH_4Cl, and a cocktail of protease inhibitors (Fig. 3G and figs. S10 and S11).

Although the function of LRBA has been unclear, related BEACH domain–containing proteins regulate trafficking of intracellular vesicles (*8*, *23*). Consistent with our hypothesis that LRBA controls CTLA4-containing vesicles, we observed that CTLA4 and LRBA colocalized within recycling endosomes and the trans-Golgi network in normal T cells indicated by their coincidence with the Rab11 and Syntaxin 6 (STX6) markers, respectively (Fig. 4, A and B). It is interesting that the transferrin receptor (CD71), which traffics through recycling endosomes, was also reduced in *LRBA* knockdown cells, which suggests that LRBA may specifically regulate recycling endosomes (fig. S12 and S13). CD28 family members and molecules known to traffic through other vesicles, including CD28, ICOS, PD-1, and CD154 were unaffected in *LRBA* knockdown cells (fig. S12). Consistent with their cellular colocalization, we found that CTLA4 and LRBA coimmunoprecipitate (Fig. 4C) and that this interaction required the concanavalin A (Con A)–like lectin

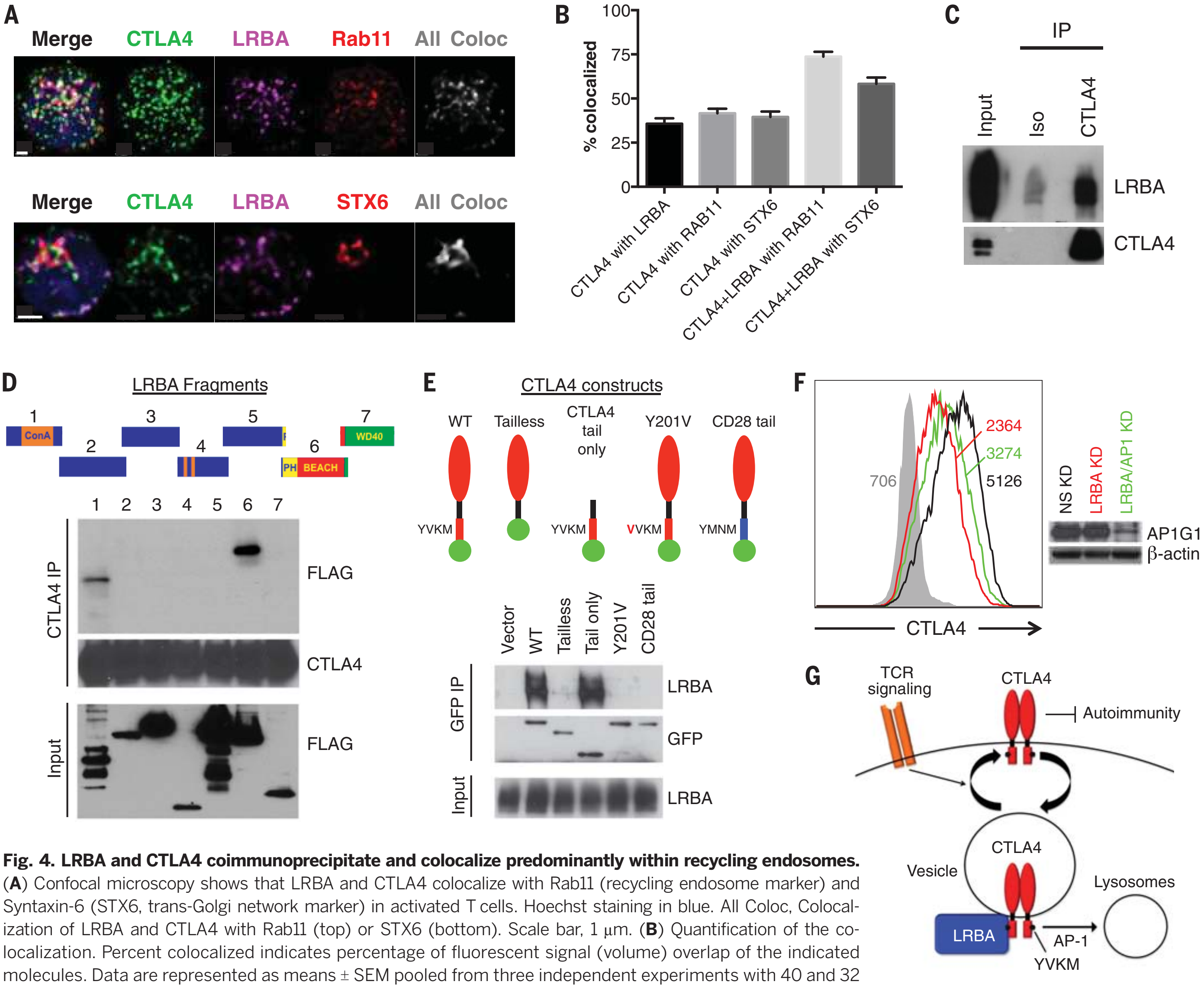

Fig. 4. LRBA and CTLA4 coimmunoprecipitate and colocalize predominantly within recycling endosomes. (**A**) Confocal microscopy shows that LRBA and CTLA4 colocalize with Rab11 (recycling endosome marker) and Syntaxin-6 (STX6, trans-Golgi network marker) in activated T cells. Hoechst staining in blue. All Coloc, Colocalization of LRBA and CTLA4 with Rab11 (top) or STX6 (bottom). Scale bar, 1 μm. (**B**) Quantification of the colocalization. Percent colocalized indicates percentage of fluorescent signal (volume) overlap of the indicated molecules. Data are represented as means ± SEM pooled from three independent experiments with 40 and 32 images total, respectively, for Rab11 and STX6 analyses. (**C**) LRBA and CTLA4 immunoblots of CTLA4-specific antibody or isotype control (iso) immunoprecipitates from lysates of activated T cells. (**D**) Human embryonic kidney (HEK) 293T cells were transfected with DNA encoding wild-type (WT) CTLA4 and FLAG-tagged fragments 1 to 7 of LRBA as indicated. CTLA4 immunoprecipitates from the transfected cells were immunoblotted with antibodies against FLAG and CTLA4. (**E**) HEK 293T cells were transfected with constructs of green fluorescent protein (GFP) fused to WT CTLA4, tailless CTLA4, YVKM mutant CTLA4 (Y201V), CTLA4 tail only, and CTLA4 with CD28 tail. GFP immunoprecipitates from the transfected cells were immunoblotted with antibodies against LRBA and GFP. CTLA4 extracellular domain as a red oval; transmembrane domain, black bar; cytoplasmic tail, red (CTLA4) or blue (CD28) rectangle; GFP, green circle. (**F**) CTLA4 intracellular staining of NS KD, LRBA KD, or LRBA and AP1G1 (subunit of AP-1) double-KD T cells. Mean fluorescence intensities of CTLA4 staining are indicated on graph. Shaded gray histogram is isotype control. Data are representative of at least three independent experiments. Immunoblot on right shows AP1G1 KD efficiency. (**G**) Model depicting the regulation of CTLA4 vesicle trafficking by LRBA.

domain and the pleckstrin homology (PH)–like BEACH domain of LRBA and the cytoplasmic tail of CTLA4 (Fig. 4, D and E). CTLA4 with its cytoplasmic tail substituted with the corresponding CD28 tail could not bind LRBA (Fig. 4E). Note that we found that mutating the conserved tyrosine residue in the Tyr-Val-Lys-Met (YVKM) motif present in the tail of CTLA4 led to loss of binding (Fig. 4E). These experiments established that the CTLA4 tail—and the YVKM motif specifically—are necessary for LRBA association. We next investigated whether the tail of CTLA4 is sufficient for the LRBA interaction. If so, this would be consistent with the topology of CTLA4 (tail facing the cytoplasm) and would allow LRBA to use the tail as a handle to guide the movement of CTLA4-bearing recycling endosomes. We found that addition of the CTLA4 tail to GFP could coimmunoprecipitate LRBA, which confirmed that the CTLA4 tail is necessary and sufficient to mediate the interaction (Fig. 4E).

Finally, to further understand how the loss of LRBA leads to CTLA4 degradation, we assessed the role of AP-1, the clathrin-associated adaptor protein complex previously implicated in the shuttling of CTLA4 to lysosomes (*24*). Knockdown of AP-1, but not AP-2 nor AP-3 (other trafficking adaptors), could partially rescue the loss of CTLA4 and CD71 in *LRBA* knockdown cells (Fig. 4F and fig. S13). Note that the YVKM motif of CTLA4, which is critical for the interaction with LRBA, is also known to bind to AP-1, which suggests that LRBA may block CTLA4 trafficking to lysosomes by competing with AP-1 for binding to this motif. Taken together, these data indicate that LRBA plays a major immunoregulatory role by protecting CTLA4 from being sorted to and degraded within lysosomes.

In summary, therapy targeting CTLA4 was highly effective in reversing life-threatening infiltrative and autoimmune disease in *LRBA*-deficient patients. Molecular investigation of this effect revealed LRBA as an important control point for the lysosomal turnover of CTLA4 protein in T lymphocytes. LRBA is a 300-kD protein, one of the largest intracellular proteins, with a structure suggesting an adaptor function (*8*, *9*). It harbors a BEACH domain that has been implicated in intracellular vesicle regulation. A previous investigation suggested that lysosomal processes involving autophagy were defective in LRBA-deficient cells (*7*). By contrast, our data indicate that, at least for CTLA4, lysosomal degradation is enhanced when LRBA is absent. Thus, LRBA helps maintain intracellular stores of CTLA4, which allows the protein to mobilize rapidly to the cell surface where it can perform its inhibitory function in T_{regs} and memory T cells. This posttranslational mechanism for regulating CTLA4 expression in human T cells is depicted schematically in Fig. 4G.

Early investigations of CTLA4 deficiency in mice revealed fatal lymphoproliferative and autoimmune disease (*25*–*27*). Also, CTLA4 haploinsufficiency with autoimmune infiltration (CHAI) disease due to genetic haploinsufficiency of CTLA4 has been described (*21*, *28*). Patients with CHAI disease exhibit a clinical phenotype similar to that of people with *LRBA* deficiency, which underscores the disease connection between CTLA4 and LRBA (*7*, *29*, *30*). Our findings provide a clear rationale for the prospective study of CTLA4-targeted therapies for *LRBA* deficiency and other disorders that lead to reduced CTLA4 levels. Recent reports have confirmed the long-term safety and efficacy of abatacept in patients with rheumatoid arthritis, although treatment is associated with increased infections (*31*, *32*). Because abatacept will reinforce the immune checkpoint on T cells, it could hypothetically blunt antitumor responses, and this will need to be monitored with long-term use. Our studies also suggest that chloroquine or hydroxychloroquine, relatively inexpensive drugs that inhibit lysosomal degradation, may merit investigation as therapies for diseases with LRBA or CTLA4 deficiency. Note that hydroxychloroquine has shown therapeutic efficacy in systemic lupus erythematosus (*33*), which we now postulate might stem from an enhancement of CTLA4.

REFERENCES AND NOTES

1. C. Cunningham-Rundles, *Hematology (Am Soc Hematol Educ Program)* **2012**, 301–305 (2012).
2. H. Chapel *et al*., *Blood* **112**, 277–286 (2008).
3. C. A. Bates *et al*., *J. Allergy Clin. Immunol.* **114**, 415–421 (2004).
4. E. S. Resnick, E. L. Moshier, J. H. Godbold, C. Cunningham-Rundles, *Blood* **119**, 1650–1657 (2012).
5. H. Chapel, C. Cunningham-Rundles, *Br. J. Haematol.* **145**, 709–727 (2009).
6. N. M. Chase *et al*., *J. Clin. Immunol.* **33**, 30–39 (2013).
7. G. Lopez-Herrera *et al*., *Am. J. Hum. Genet.* **90**, 986–1001 (2012).
8. N. de Souza, L. G. Vallier, H. Fares, I. Greenwald, *Development* **134**, 691–702 (2007).
9. J. W. Wang, J. Howson, E. Haller, W. G. Kerr, *J. Immunol.* **166**, 4586–4595 (2001).
10. T. Takahashi *et al*., *J. Exp. Med.* **192**, 303–310 (2000).
11. K. Wing, T. Yamaguchi, S. Sakaguchi, *Trends Immunol.* **32**, 428–433 (2011).
12. L. S. Walker, D. M. Sansom, *Nat. Rev. Immunol.* **11**, 852–863 (2011).
13. K. I. Mead *et al*., *J. Immunol.* **174**, 4803–4811 (2005).
14. F. Atzeni *et al*., *Autoimmun. Rev.* **12**, 1115–1117 (2013).
15. D. Wojciechowski, F. Vincenti, *Curr. Opin. Organ Transplant.* **17**, 640–647 (2012).
16. J. D. Wolchok *et al*., *Ann. N.Y. Acad. Sci.* **1291**, 1–13 (2013).
17. L. A. Chakrabarti *et al*., *AIDS* **28**, 1593–1602 (2014).
18. J. M. Woodward *et al*., *Am. J. Gastroenterol.* **110**, 320–327 (2015).
19. O. S. Qureshi *et al*., *J. Biol. Chem.* **287**, 9429–9440 (2012).
20. Y. Koguchi, T. J. Thauland, M. K. Slifka, D. C. Parker, *Blood* **110**, 2520–2527 (2007).
21. H. S. Kuehn *et al*., *Science* **345**, 1623–1627 (2014).
22. L. M. Charbonnier *et al*., *J. Allergy Clin. Immunol.* **135**, 217–227 (2015).
23. D. Gebauer *et al*., *Biochemistry* **43**, 14873–14880 (2004).
24. H. Schneider *et al*., *J. Immunol.* **163**, 1868–1879 (1999).
25. P. Waterhouse *et al*., *Science* **270**, 985–988 (1995).
26. E. A. Tivol *et al*., *Immunity* **3**, 541–547 (1995).
27. C. A. Chambers, T. J. Sullivan, J. P. Allison, *Immunity* **7**, 885–895 (1997).
28. D. Schubert *et al*., *Nat. Med.* **20**, 1410–1416 (2014).
29. A. Alangari *et al*., *J. Allergy Clin. Immunol.* **130**, 481–8.e2 (2012).
30. S. O. Burns *et al*., *J. Allergy Clin. Immunol.* **130**, 1428–1432 (2012).
31. J. M. Kremer *et al*., *Ann. Rheum. Dis.* **70**, 1826–1830 (2011).
32. R. Westhovens *et al*., *J. Rheumatol.* **36**, 736–742 (2009).
33. N. Costedoat-Chalumeau, B. Dunogué, N. Morel, V. Le Guern, G. Guettrot-Imbert, *Presse Med.* **43**, e167–e180 (2014).

ACKNOWLEDGMENTS

We thank R. Sills for patient referrals and collaborative patient care; J. Davis, E. Smoot, and M. Similuk for clinical support; E. Jaffe and K. Dunleavy for help with diagnosis and management of lymphoma; J. Tabacof for patient care; I. Barlan and A. Ozen for patient referrals; S. Ganesan, A. Morawski, and K. Lampe for technical assistance; and C. Lucas for advice. Supported by an American Society of Hematology Bridge award, the Cincinnati Children's Hospital Medical Center Gap Award, and Divisional Funds from Immunobiology and Bone Marrow Transplantation and Immune Deficiency, as well as the Intramural Research Program of the National Institute of Allergy and Infectious Diseases (NIAID), NIH, and Merck, Inc. The Next Generation Mendelian Genetics project support was provided by NIH grant 1RC2 HG005608 to D. Nickerson, J. Shendure, M. Bamshad, and W. Raskind. The Autoimmune Lymphoproliferative Syndrome project is also supported through the Division of Intramural Research, NIAID, NIH, under project 1ZIAAI000769-14. The content of this publication does not necessarily reflect the views or policies of the U.S. Department of Health and Human Services, nor does mention of trade names, commercial products, or organizations imply endorsement by the U.S. government.

SUPPLEMENTARY MATERIALS

www.sciencemag.org/content/349/6246/436/suppl/DC1
Materials and Methods
Supplementary Text
Figs. S1 to S14
Table S1
Reference (*34*)

28 October 2014; accepted 8 June 2015
10.1126/science.aaa1663

Thermo Scientific invitrogen gibco

ThermoFisher SCIENTIFIC

Multiplexing PCR Amplicons

Direct polymerase chain reaction (PCR) amplification of a specific region is a powerful technique to perform targeted sequencing. When combined with multiplexing capability, PCR amplification is an efficient manner to study many samples. PacBio offers two barcoding strategies for multiplexing up to ninety-six 10 kb amplicons. In the first approach, barcodes are added to the end of the amplicon during PCR and the standard SMRTbell adapter is subsequently ligated onto the barcoded amplicon. In the second approach, the barcode is added to the SMRTbell adapter and the amplicon is ligated to the SMRTbell barcoded adapter. The second approach is recommended for validated PCR systems since the amplicon is generated with the unmodified primers. The first approach provides researchers more cost savings because the barcode is added to the amplicon and samples can be pooled prior to the SMRTbell template preparation steps.

PacBio

For info: 877-920-7222

www.pacb.com

ChIRP RNA Interactome Kits

Magna ChIRP RNA Interactome Kits allow researchers to more easily identify, recover, and analyze regions of chromatin that interact with chromatin-associated RNAs such as long noncoding RNA (lncRNA). The highly effective multiprobe-based capture strategy uses cross-linked chromatin to provide reliable detection and discovery of RNA-associated genomic DNA sequences, RNA sequences, and proteins. The new kits use the ChIRP method (Chromatin Isolation by RNA Purification) to isolate chromatin complexes using RNA as the target, allowing researchers to pinpoint specific sites of genomic interaction for chromatin-associated RNAs. The kits simplify the ChIRP method, providing all necessary buffers, enzymes, and reagents in one validated kit as well as a negative control probe set and detailed protocol with capture probe design guidelines. In addition, first-time users can opt for the EZ-Magna ChIRP kit, which includes a positive control capture probe set and detection primers that make it easier to validate an experiment's success.

EMD Millipore

For info: 800-645-5476

www.emdmillipore.com/chirp

Real-Time PCR Systems

New real-time polymerase chain reaction (PCR) systems that fully integrate with cloud computing technology mark a new era in data sharing and global research collaboration. Designed for low to mid throughput laboratories conducting real-time PCR experiments, QuantStudio 3 and 5 are the first to connect to the Thermo Fisher Cloud computing platform, allowing researchers to learn, analyze, share, collaborate, and obtain support within a single platform. Researchers worldwide can now collaborate online in real-time, and access their data wherever and whenever necessary. Laboratories can also share experimental conditions and results with their partners, while providing a uniform experience for every user, and helping minimize training and errors. With the Applied Biosystems QuantStudio 3 and QuantStudio 5 Real-Time PCR systems hosted on Amazon Web Services (AWS), these PCR systems benefit from the inherent security of the AWS Cloud. The new instruments seamlessly integrate with existing analysis workflows, syncing with next generation sequencing, capillary electrophoresis, and qPCR applications to create a customized data ecosystem.

Thermo Fisher Scientific

For info: 800-678-5599

www.thermofisher.com

GeneChip Whole-Transcriptome Arrays

The GeneChip WT Pico Kit is designed for gene expression array target preparation from as little as 100 pg of total RNA input. Working with as few as 10 cells, the new kit offers a high degree of flexibility and precision, enabling analyses of samples too small for other methods as well as the interrogation of small subpopulations of cells within larger samples. For use with Affymetrix' GeneChip Whole-Transcriptome Arrays, the new WT Pico Kit is compatible with small sample isolation techniques, including flow cytometry, laser capture microdissection, and fine needle aspiration. The kit prepares targets from multiple sample types, including fresh and fresh frozen tissues, cultured cells, FFPE specimens, and whole blood samples without a globin mRNA reduction step. The use of a single kit for multiple sample types improves the ability to better compare data from different samples, especially important for translational research.

Affymetrix

For info: 888-362-2447

www.affymetrix.com

NGS Software Analysis Templates

Customized analysis workflow templates have been incorporated into the NextGENe NGS software providing users of the ThunderBolts Cancer and Myeloid Panels with predefined settings for detecting minor allele frequencies at different sensitivity settings (1% and 5%). Use of the predefined NextGENe settings for the ThunderBolts panels provides a simple, automated, accurate, and rapid NGS bioinformatics workflow solution on the analysis of important oncogenes of clinical relevance to cancer diseases, with important results visualization provided by NextGENe software. Through the NextGENe AutoRun, a template for the ThunderBolts Cancer or Myeloid Panel can now be selected. With a single click of the template, our users will have configured a project to automatically trim the adapters and primer sequences from the ends of reads, set the appropriate read alignment settings, chosen an appropriate variant detection sensitivity and selected useful quality and variant reports to be generated.

SoftGenetics

For info: 888-791-1270

www.softgenetics.com

Electronically submit your new product description or product literature information! Go to www.sciencemag.org/products/newproducts.dtl for more information.

Newly offered instrumentation, apparatus, and laboratory materials of interest to researchers in all disciplines in academic, industrial, and governmental organizations are featured in this space. Emphasis is given to purpose, chief characteristics, and availability of products and materials. Endorsement by *Science* or AAAS of any products or materials mentioned is not implied. Additional information may be obtained from the manufacturer or supplier.

invitrogen

TOPO™ technology delivers 95% clone recovery in 5 minutes

A revolution in the science of high-performance cloning, TOPO technology delivers simplicity, efficiency, speed and unparalleled yield—no matter how difficult the sample or downstream application.

Choose a cloning technology you can trust at
thermofisher.com/topo

ThermoFisher SCIENTIFIC

There's only one Science

Science Careers Advertising

For full advertising details, go to ScienceCareers.org and click For Employers, or call one of our representatives.

Tracy Holmes
Worldwide Associate Director
Science Careers
Phone: +44 (0) 1223 326525

THE AMERICAS

E-mail: advertise@sciencecareers.org

Fax: +1 (202) 289 6742

Tina Burks
Phone: +1 (202) 326 6577

Nancy Toema
Phone: +1 (202) 326 6578

Online Job Posting Questions
Phone: +1 (202) 312 6375

EUROPE / INDIA / AUSTRALIA / NEW ZEALAND / REST OF WORLD

E-mail: ads@science-int.co.uk

Fax: +44 (0) 1223 326532

Sarah Lelarge
Phone: +44 (0) 1223 326527

Kelly Grace
Phone: +44 (0) 1223 326528

Online Job Posting Questions
Phone: +44 (0) 1223 326528

JAPAN

Katsuyoshi Fukamizu (Tokyo)
E-mail: kfukamizu@aaas.org
Phone: +81 3 3219 5777

Hiroyuki Mashiki (Kyoto)
E-mail: hmashiki@aaas.org
Phone: +81 75 823 1109

CHINA / KOREA / SINGAPORE / TAIWAN / THAILAND

Ruolei Wu
Phone: +86 186 0082 9345
E-mail: rwu@aaas.org

ScienceCareers
FROM THE JOURNAL SCIENCE AAAS

ScienceCareers.org

Perelman School of Medicine
UNIVERSITY of PENNSYLVANIA

Assistant/Associate/Full Professor of Radiation Oncology, Tenure-Track

The Department of Radiation Oncology at the Perelman School of Medicine at the University of Pennsylvania seeks candidates for a Full, Assistant, or Associate Professor position in the tenure track. Rank will be commensurate with experience. The successful applicant will have experience in the field of Tumor or Radiation Biology. Applicants must have a Ph.D. or M.D./Ph.D. degree and have demonstrated excellent qualifications in research, education, and clinical care.

Candidates with evidence of significant extramural funding and a strong publication record in any area of Tumor or Radiation Biology are encouraged to apply. We are particularly interested in individuals with research interests in normal tissue radiobiology, tumor microenvironment or tumor stem cells and immuno-radiotherapy. The Division of Radiation Research is comprised of 14 faculty engaged in innovative, translational research with a focus on the study of the tumor microenvironment, radiation response modifiers, photodynamic therapy and proton therapy. Research in the Division is supported by multiple grants from the NIH, DoD, private foundations and industry. Faculty in the Division can have cross-appointments to other Departments and can belong to different graduate groups such as Cell and Molecular Biology and Pharmacology. The majority of the Division faculty are located in new, contiguous laboratory space in the Smilow Center for Translational Research Building (SCTR), in very close proximity to the clinic. State-of-the- art shared instrumentation includes a 3-D conformal irradiator for small animals, live cell microscopy, hypoxia chambers, multiple PDT lasers, etc. The SCTR building has its own barrier and non-barrier animal facility and small animal imaging facilities which include optical, MR and CT imaging. A competitive start-up package and laboratory space will be provided. For more information about the Department of Radiation Oncology, and the Division of Radiation Research please visit: http://www.xrt.upenn.edu/index.shtml

Interested candidates should send a curriculum vitae, a one page summary of their future research goals and the names of three references via the online form at **https://www.med.upenn.edu/apps/faculty_ad/index.php/g/d4017**.

Information about the position may be obtained from the Administrator to the Chair of the Search Committee: **Corrinne Fahl, Department of Radiation Oncology, School of Medicine, University of Pennsylvania; corrinne.fahl@uphs.upenn.edu**

ETH zürich

Professor of Molecular Plant Breeding

→ The Department of Environmental Systems Science (www.usys.ethz.ch) at ETH Zurich and Agroscope (www.agroscope.ch) invite applications for the above-mentioned position to establish a research group in molecular plant breeding. The successful candidate should have an excellent background in agricultural sciences and will be expected to develop an internationally recognized research programme. Her or his research should be oriented around developing molecular technologies to breed plants suitable for the Swiss agricultural setting, supporting the development of new cultivars with novel traits that can contribute to a sustainable intensification of Swiss agriculture.

→ The successful candidate will teach undergraduate and graduate courses within the study programme in Agricultural Sciences. The professorship will be expected to collaborate with diverse stakeholders to improve plant breeding related networks within Switzerland. The new professor will be expected to teach undergraduate level courses (German or English) and graduate level courses (English).

→ **Please apply online at www.facultyaffairs.ethz.ch**

→ Applications should include a curriculum vitae, a list of publications, a statement of future research and teaching interests, and the names and contact details of three referees. The letter of application should be addressed **to the President of ETH Zurich, Prof. Dr. Lino Guzzella. The closing date for applications is 30 September 2015**. ETH Zurich is an equal opportunity and family friendly employer and is further responsive to the needs of dual career couples. We specifically encourage women to apply.

Dartmouth

Faculty Position in Ecology
Department of Biological Sciences
Hanover, NH USA

The Department of Biological Sciences at **Dartmouth College** seeks applicants for an **open-rank** tenure-track/tenured Professorship in **Ecology**. We seek highly qualified candidates working in any area of ecology, but especially welcome applicants whose research would include field studies in local ecosystems to address broadly relevant conceptual issues in ecology. The successful candidate will be expected to supervise an independent research program that will attract extramural funding, provide research training for graduate and undergraduate students, and teach biology courses at the undergraduate and graduate levels. The new hire will contribute to our newly expanded graduate program in Ecology, Evolution, Ecosystems and Society and offer exceptional courses in one or more of the following areas: population biology, species interactions, disease ecology, community ecology, ecosystem science, field ecology, and biostatistics. Application materials should include a cover letter, curriculum vitae, three representative publications, statements of research and teaching interests, and the names and contact information for at least three letters of reference. Please submit materials electronically to: **apply.interfolio.com/30338**.

Application review will begin on **15 September 2015** and continue until the position is filled. For further information about the department and graduate programs, see http://biology.dartmouth.edu

Dartmouth College combines a commitment to innovative scholarship with dedication to excellent teaching. One of the most diverse institutions of higher education in New England, Dartmouth College is an Equal Opportunity/Affirmative Action Employer, has a strong commitment to diversity, and in that spirit encourages applications from all individuals regardless of gender, race, religion, color, national origin, sexual orientation, age, disability, or veteran status.

CELEBRATING 250 YEARS 1765–2015 Perelman School of Medicine UNIVERSITY of PENNSYLVANIA

Assistant/Associate Professor of Physiology

The Department of Physiology at the Perelman School of Medicine at the University of Pennsylvania seeks candidates for Assistant or Associate Professor positions in the tenure track. Rank will be commensurate with experience. Responsibilities include establishing and conducting an independent research program, and supervising, mentoring and teaching students. Applicants must have an M.D. or Ph.D. or equivalent degree and have demonstrated excellent qualifications in research.

The successful candidate will have experience in any aspect of physiology or a related field, including neuroscience and cardiovascular science. Candidates working at any or all ranges of physiology (molecular, cellular, and organismal) will be considered. Special attention will be given to investigators using state-of-the-art techniques with research programs that leverage molecular and cellular insights to inform physiological and pathophysiological functions. Research areas of particular interest include signaling, membrane transport physiology, organelle biology, metabolism and structural biology. Applicants at the Associate Professor level are expected to have funding and an internationally recognized track record of creative research productivity and excellence.

Highly competitive lab space and start-up funds are available. The Perelman School of Medicine, one of the top ranked medical schools in the nation for research and NIH funding, is a highly collaborative environment with strong core facilities. It is located on the campus of the University of Pennsylvania, a world-class institution located near the center of Philadelphia.

We seek candidates who embrace and reflect diversity in the broadest sense.

The University of Pennsylvania is an EOE. Minorities/Women/Individuals with disabilities/Protected Veterans are encouraged to apply.

Apply for this position online at:
https://www.med.upenn.edu/apps/faculty_ad/index.php/g311/d3686

wellcometrust

Wellcome Trust funding committee members

The Wellcome Trust is a global charitable foundation dedicated to improving health. We support bright minds in science, the humanities and the social sciences, as well as education, public engagement and the application of research to medicine.

To do this, we need to select the best research proposals and fund the best researchers. These decisions depend on our funding committees - including expert review groups, interview committees, selection panels and scheme specific committees - to review grant applications and make funding recommendations. Members of our funding committees are drawn from leading universities, research institutes, pharma and biotech companies, and policy organisations, both within the UK and internationally.

We are now seeking to recruit a pool of prospective committee members with expertise throughout our Science, Innovations, and Humanities and Social Science portfolios. We will draw from this pool to create new committees, to refresh membership of existing committees and to co-opt members to specific meetings.

You should have:

- international standing in your field, with an outstanding track record in research
- extensive success in securing competitive funding or resourcing for your research programmes
- significant experience in the review and assessment of research proposals or publications
- the ability to consider and critique research outside your immediate area
- experience in conducting interviews, and the ability to question and solicit discussion in a fair manner.

For full details of the commitment required, remuneration and how to apply, visit **www.wellcome.ac.uk/committeerecruitment**

The closing date for applications is 9 September 2015.

The Wellcome Trust is a charity registered in England and Wales, no. 210183.

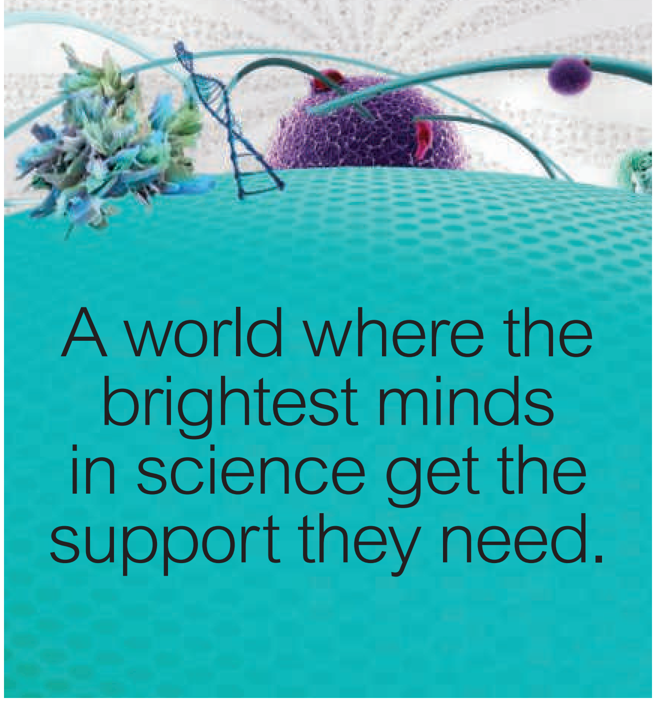

TEXAS TECH UNIVERSITY HEALTH SCIENCES CENTER. EL PASO
Paul L. Foster School *of* Medicine

Department of Medical Education
Basic Science and/or Clinician Medical Educators
(Multiple disciplines, with emphasis on anatomy, microbiology, physiology and pharmacology)

The Paul L. Foster School of Medicine is seeking full-time medical science educators to contribute to the University's mission through teaching, research and service, with some variation in roles and responsibilities according to credentials and experience.

Minimum Qualifications:

- Ph.D. or equivalent terminal degree in physiology, human anatomy, medical microbiology, pharmacology, or a related biomedical science (Basic Science Medical Educator option); or alternatively, an M.D., D.O., or equivalent medical degree with additional relevant credentials relating to advanced scientific training and scholarship (Clinician Medical Educator option).
- Physician candidates applying for the Clinician Medical Educator option must be Board Certified (ABMS recognized), qualify for an unrestricted Texas Medical License, and must agree to obtain an unrestricted Texas Medical License as a condition for employment.

Preferred Qualifications:

- Experience with development and delivery of a course or major course components in physiology, human anatomy, pharmacology, medical microbiology or related biomedical science at an LCME accredited medical school.

These positions are salaried and fully funded. Salary, academic rank and tenure option are commensurate with experience. A comprehensive benefits package is included. All candidates must apply online at **http://www.texastech.edu/careers/**. The position requisition numbers are: 4045BR, 4051BR and 4245BR.

For additional information applicants may contact: Richard D. Brower, M.D.; Associate Professor and Chair, Department of Medical Education (richard.brower@ttuhsc.edu)

Texas Tech University Health Sciences Center is an Equal Opportunity/Affirmative Action Employer.

MONTANA STATE UNIVERSITY
Mountains & Minds

Environmental Microbiology Faculty
Assistant, Associate, or Full Professor
Department of Microbiology & Immunology

The Department of Microbiology & Immunology at Montana State University-Bozeman (http://www.montana.edu.mbi) invites candidates with a PhD in Microbiology or related area to apply for a full-time, nine-month tenure-track position in Environmental Microbiology (Assistant/Associate/Full Professor) beginning January 2016. The successful candidate will have postdoctoral and/or Assistant Professor experience and will be responsible for developing/growing an extramurally funded, nationally recognized research program within the broad field of environmental microbiology. Scientists that use interdisciplinary approaches that include biochemical, cellular, physiological, ecological, genomic, and/or molecular tools to investigate areas including microbe-environment interactions, microbial biology/ecology, and/or microbial engineering are encouraged to apply. We are seeking an individual with a research program to complement and expand expertise in the Department. The Department, which is nationally recognized for its strengths in both environmental and human-related microbiology, includes state-of-the-art core facilities both in the department and campus research centers. The Department strives to maintain a diverse faculty group, and women and underrepresented minorities are encouraged to apply. The position includes a competitive institutional salary (9-months) and generous start-up package. While a funded research program is preferred, it is not required.

Full details about the position and application procedure are available at **https://jobs.montana.edu/postings/2601**. Potential candidates are encouraged to contact the Search Committee Chairperson, Dr. Matthew Fields, (**matthew.fields@biofilm.montana.edu**) for more details. Screening will begin **September 10, 2015** and will continue until a suitable applicant is hired.

ADA/EO/AA/Veterans Preference.

Los Alamos
NATIONAL LABORATORY
EST. 1943

Los Alamos National Laboratory (LANL), a multidisciplinary research institution engaged in strategic science on behalf of national security, has an opportunity available in their Theory, Simulation & Computation Directorate.

THEORETICAL DIVISION LEADER

The Theoretical (T) Division at Los Alamos National Laboratory has a storied history of discovery and mission impact dating back to the Manhattan Project and today is focused on advancing the frontiers of theoretical science across a broad range of disciplines. T Division is a 250-person organization with an annual budget greater than $100 M. The Division Leader has responsibility for leading, managing, setting strategic direction, and cultivating the careers of the Division's workforce. The successful candidate will have an outstanding record of scientific research or programmatic accomplishment in an area of Theoretical Division-relevant research as evidenced by publications, citations, presentations, grants or programmatic support, and/or leadership of large technical projects. A Ph.D. in physics, materials science, chemistry, life sciences or a related discipline, or an equivalent combination of education and experience in related areas that are relevant to the mission of the Division, is required.

To apply and learn more about this position and others, please visit **careers.lanl.gov** – **Job IRC41175 (R&D Manager 6).** EOE

By **C. Neal Stewart Jr.**

Songwriting and science

Each week, articles in *Science* and friends in science-related careers remind me how competitive the grant and paper scenes have gotten. One National Science Foundation (NSF) panelist, for example, recently told me that the panel's funding rate in the last competition was 3%. I don't need these reminders; my own steady diet of rejections from prospective funders and journal editors keeps the message vivid and personal.

So 3 years ago, when I rebooted my songwriting "career" after a 30-year hiatus, I felt battle-hardened enough to think big. Not only did I dive right into writing and recording my songs, but I became enamored with breaking into the Nashville market as a songwriter. I naively thought that my songs were at least as good as what I heard on country radio, and on my most optimistic days, I judged my tunes better than average. Certainly, I reasoned, my experience with rejection in science would steel my resolve to get my songs recorded by the latest country stars.

ILLUSTRATION: ROBERT NEUBECKER

Songwriting "has been good for my soul as well as my science."

What I didn't realize then was that rejection in science is nothing compared to the Fort Knox–like exclusion that the Nashville fortress foists on newcomer-wannabes. I gained an appreciation for NSF: At least it reviews my grant proposals and tells me if I win or lose. The agency even gives me feedback. In contrast, the music industry is a sort of black hole where songs disappear forever. I haven't been totally unsuccessful; I've had a few cuts on small record labels. But between the minor triumphs, it's discouraging not knowing the outcome of a pitch most of the time and not hearing from publishers and producers—the reviewers—about how I can improve a song. Science is much kinder than the music business in this regard.

Pitching songs, however, has taught me a few practical lessons about pitching papers and grant proposals:

You have to tell your story in 3 minutes. If the paper or proposal (or song) doesn't grab the audience's attention pretty quickly, it won't be a hit. This is especially true for grant proposals: If the first page doesn't compel the reviewer's interest in 3 minutes, the proposal is toast.

You need a memorable hook. In a song, the hook is the phrase or melodic line that the listener hums and sings in the shower. A science story also needs a memorable hook that relays a simplified message about why a piece of science is important.

Keep it fresh. Most hit songs have predictable structure but include surprises and interesting turns. Similarly, the best papers are well structured but include unexpected and novel results.

Don't go solo. Although I would like to think I can do all the songwriting, playing, and singing to express a song in a pitch, for me that is almost never the right decision. Most hit songs have two or more co-writers, and the demos are played by extraordinarily fine musicians. In science, collaborators bring unique expertise and make a project stronger. Science and commercial music are both so competitive that the right team is needed to produce winners.

Inspiration isn't everything. Supposedly, Jimmy Buffett wrote most of "Margaritaville" in a few minutes, but most songs are rewritten several times. The same should be true for papers and grant proposals. When I'm reviewing proposals, it's usually obvious when the principal investigator thinks he's Jimmy Buffett. Most hits are the product of close examination and rewriting.

Finally, in music, it goes without saying that the most successful songs are those that people like the most. It's less obvious in science, but it's equally true. I now pay more attention to which papers are cited most and which talks my audiences react best to. It helps to know what works and what doesn't.

I don't plan to give up my day job anytime soon, but I also don't intend to give up songwriting. It has been good for my soul as well as my science. ■

C. Neal Stewart Jr. holds the Ivan Racheff chair of excellence in plant molecular genetics at the University of Tennessee, Knoxville, which is about a 3-hour drive from Nashville. His song demos can be found at bit.ly/Neal-Stewart. For more on life and careers, visit sciencecareers.org. Send your story to SciCareerEditor@aaas.org.

Published by AAAS